Hydrodynamic modelling of the shock ignition scheme for inertial confinement fusion

Alexandra Vallet

université de BORDEAUX

THÈSE PRÉSENTÉE

POUR OBTENIR LE GRADE DE

DOCTEUR DE

L'UNIVERSITÉ DE BORDEAUX

ÉCOLE DOCTORALE DES SCIENCES PHYSIQUES ET DE L'INGÉNIEUR
SPÉCIALITÉ ASTROPHYSIQUE, PLASMAS, NUCLÉAIRE

Par Alexandra VALLET

Modélisation hydrodynamique du schéma d'allumage par choc pour la fusion par confinement inertiel

Sous la direction de : Vladimir TIKHONCHUK
co-directeur : Xavier RIBEYRE

Soutenue le 20 Novembre 2014

Membres du jury :

M. BATANI, Dimitri	Professeur	Université de Bordeaux	Président
M. ATZENI, Stefano	Professeur	Université de Rome La Sapienza	Rapporteur
M. BOUQUET, Serge	Directeur de recherche	CEA Bruyères Le Châtel	Rapporteur
M. LEFEBVRE, Erik	Directeur de recherche	CEA Bruyères Le Châtel	Examinateur
M. NORREYS, Peter	Professeur	Université d'Oxford	Examinateur
M. TIKHONCHUK, Vladimir	Professeur	Université de Bordeaux	Directeur de thèse
M. RIBEYRE, Xavier	Chercheur	CEA,CELIA	Co-directeur de thèse

THÈSE

présentée à

L'UNIVERSITÉ DE BORDEAUX

ÉCOLE DOCTORALE DES SCIENCES PHYSIQUES ET DE L'INGÉNIEUR

par Alexandra VALLET

POUR OBTENIR LE GRADE DE

DOCTEUR

SPÉCIALITÉ : ASTROPHYSIQUE, PLASMAS, NUCLÉAIRE

Hydrodynamic modeling of the shock ignition scheme for inertial confinement fusion

---

Soutenue le : 20 Novembre 2014.

Après avis des Rapporteurs :

M. Stefano ATZENI,	Professeur,	Université Roma La Sapienza.
M. Serge BOUQUET,	Directeur de recherches CEA,	CEA Bruyères Le Châtel.

Devant la commission d'examen formée de :

M. Dimitri BATANI, Professeur, Université de Bordeaux,	Président.
M. Stefano ATZENI, Professeur, Université de Rome La Sapienza,	Rapporteur.
M. Serge BOUQUET, Directeur de recherches CEA, CEA Bruyères Le Châtel,	Rapporteur.
M. Erik LEFEBVRE, Directeur de recherches CEA, CEA Bruyères Le Châtel,	Examinateur.
M. Peter NORREYS, Professeur, Université d'Oxford,	Examinateur.
M. Vladimir TIKHONCHUK, Professeur, Université de Bordeaux,	Directeur de thèse.
M. Xavier RIBEYRE, Chercheur, CEA-CELIA,	Co-directeur de thèse.

À mes parents,

Remerciements

J'adresse mes respectueux remerciements à mes rapporteurs de thèse, Serge Bouquet et Stefano Atzeni, pour leur lecture détaillée et leurs remarques constructives, qui m'ont permis d'améliorer la qualité de ce présent manuscrit. Je remercie également les autres membres de mon jury : Dimitri Batani, président, Erik Lefebvre et Peter Norreys, rapporteurs, pour l'intérêt qu'ils ont porté à mon travail et pour les discussions issues de ma soutenance de thèse.

Ces trois années de ma vie furent extrêmement riches. Une thèse, c'est un peu comme un périple le long d'un chemin dont le tracé se dévoile au fur et à mesure. Tout au long de ce voyage, j'ai vécu de nombreuses expériences et j'ai côtoyé des personnes qui ont eu une part d'influence sur mes travaux. Il s'agit aussi bien de personnalités marquantes rencontrées durant mon parcours que de personnes qui ont toujours été là. Je profite de cette section pour les remercier.

Je remercie tout d'abord mes directeurs de thèses Xavier Ribeyre et Vladimir Tikhonchuk à qui je dois beaucoup. Je vous remercie pour m'avoir fait confiance en me confiant ce sujet de thèse, pour les opportunités que vous m'avez offertes, pour votre soutien ainsi que pour les nombreux échanges que nous avons eus. Ces trois années ont été un tremplin pour ma carrière scientifique et je vous remercie de tout cœur pour cet élan que vous m'avez donné.

J'ai eu également la chance d'avoir passé ces trois années de travail au sein du laboratoire CELIA, qui en mon sens est un environnement idéal pour effectuer une thèse. Ainsi je remercie, Phillipe Balcou, directeur du laboratoire, pour son accueil.

Alexis Casner, je te remercie pour les opportunités que tu m'as offertes. J'ai été heureuse de pouvoir participer à la préparation et à l'interprétation de tirs sur OMEGA. Je te remercie pour ton aide, nos discussions, les données expérimentales et ce lien que tu as permis avec l'équipe outre atlantique !

Lorsque je dis que ma thèse a été un voyage, ce n'est pas juste au sens figuré. J'ai eu l'occasion de partir en mission au laboratoire LLE à Rochester aux Etat-Unis, et de participer à des conférences et écoles d'été en Europe et aux États-Unis. C'est une vrai chance en tant que doctorant de pouvoir valoriser ainsi son travail dans un contexte international. Je le dois au laboratoire et à mes directeurs de thèses, donc encore une fois, merci !

Je remercie sincèrement Riccardo Betti pour son accueil chaleureux au Laboratoire LLE à Rochester. Ce séjour de deux mois fut très profitable aussi bien pour ma thèse, ma carrière et mon épanouissement personnel. Je remercie grandement Ryan Nora pour les échanges que nous avons eus à propos des expériences OMEGA. Je remercie également tous les doctorants et post-doc du groupe qui m'ont accueillie.

Marion, je suis ravie d'avoir pris la suite de ton travail. Je te remercie pour ton aide lors de mon arrivée au CELIA, et au LLE ! Merci aussi pour les sorties à ces occasions. Décidément, je te suis de près ! (Et ce n'est pas fini a priori !)

Je n'aurais pas été bien loin sans le soutien moral et scientifique de toute l'équipe du laboratoire. Ainsi je remercie Jérome Breil, pour ta patience face à mes questions sur le code et pour ton aide avec mes cas un peu farfelus; Philippe pour les discussions sur mes travaux, mon avenir et l'organisation des repas de labos sur le bassin d'Arcachon ! ; Jean-Luc pour nos discussions philosophiques sur le sens et la légitimité de l'expression artistique ou scientifique, et sur les électrons chauds ; Rachel pour ton soutien (lorsque qu'il n'y avait plus d'eau chez moi, mais pas que) et tes conseils concernant mon avenir ; Edouard, pour ton temps et tes conseils sur mes travaux de thèse, pour tes encouragements lors mes démarches pour rentrer au CEA; je remercie aussi Marina, Emmanuel, Benoît, Guillaume, Bruno, Henry, Gérard, pour leur soutien et bonne humeur. Un grand merci à l'équipe informatique, Loic et Elodie, pour m'avoir sauvée plus d'une fois d'un naufrage informatique. Joao, l'évasion musicale est importante pour moi, je suis ravie d'avoir découvert le fado Portugais en la présence d'un connaisseur ! Je remercie chaleureusement Emmanuelle, Céline et Sophie, pour leur aide dans les démarches administratives et leur patience.

Un grand merci à tous les nouveaux docteurs ou bientôt docteurs du CELIA : pour votre bonne humeur, votre soutien dans les moments difficiles et toutes ces bonnes soirées à Bordeaux ou ailleurs. Merci à Dario, Sebastien (colloque d'un mois, pas toujours de tout repos n'est ce pas ?) , Pierre (et tes tiramisus), Nesrinne, Witold (je n'oublie pas la mythique fête de la musique), Rémy (j'attends toujours de te voir jouer), Jessy, Mokrane, Yohan, Mathieu et Mathieu, Arnaud (je n'aurais pas réussi à faire des graphs plus beaux que les tiens finalement), Luca, Xavier (grâce à toi j'ai une photo avec Dévin !), Aurore , Igor (il arrive de drôles d'aventures quand on te rejoint au restaurant !).

Emma, je te remercie du fond du cœur pour ta patience, ton écoute et ton support durant ce parcours du combattant. Tu m'as aidée jusqu'au bout ! Je suis heureuse de t'avoir rencontrée, et ton arrivée au labo a été une grande chance ! J'espère que cette amitié continuera en dehors du CELIA.

Barth, toi aussi tu as été un pilier pour moi. Je te remercie pour tous ces bons moments, forums ILP, New-York (chez notre ami Edgar ;)), Rochester, ton jardin aux mille plantes aromatiques, le Lucifer, déménagement/emménagement et j'en passe. Impossible de ne pas avoir le sourire en ta présence !

Mika, co-bureau, co-thésard,mais surtout ami. Finalement, j'ai gagné avec l'allumage par choc, puisque tu t'y es mis , n'est ce pas ? Nos soirées tapas/vin en sortant à pas d'heure le vendredi soir du labo, les virées à la plage, et les café reggae étaient de vraies bouffées d'air frais ! Que de fous rires avec toi ! Tout cela au milieu de discussions physico-phylosophiques bien sûr. Bon vent en Californie !

Alex, pour ces longues discussions, tes conseils pour tous les choix difficiles, et aussi les restos du vendredi qui me redonnaient de la force sur la fin. Tu as toujours été là quand j'avais besoin

de toi ! Merci !

Je remercie aussi Giovanni, mathématicien proche du CELIA, pour nos pauses midi musicales. Je suis heureuse d'avoir joué un peu de la fameuse sonate de Franck avec toi !

Le voyage de thèse ne reste pas confiné au laboratoire. Il s'étend bien plus loin, si bien qu'on en rêve parfois (souvent). Autant dire qu'une thèse, cela se vit 24h/24h, 7J/7J, et ce, peut être au désarroi de ses proches.

Ainsi je tiens à remercier les amis en dehors du labo qui m'ont également soutenue dans cette aventure.

Léo, Hadrien, Ben, Johan, Arthur, Alexis, merci pour toutes ces soirées musicales, les sorties, le voyage à Barcelone, les concerts ! La DT team, j'ai eu beaucoup de chance de jouer avec vous ! C'était un vrai plaisir ! Merci pour le soutien et pour être venus à ma soutenance.

Ibby, meilleur prof d'anglais, pour m'avoir fait partager ton incroyable périple et tes réflexions !

Florine, pour nos Dimanches musicaux et l'opéra Ophée et Euridice. Que de bons souvenirs !

Alban, pour m'avoir poussée et accompagnée dans le début de cette aventure. Ton soutien dans mes choix a été important pour moi.

Laure et Cervoise, pour votre soutien, vos visites régulières et.. pour les provisions de nouilles chinoises !

Violette, pour ton soutien et tes encouragements, pour nos séjours au Wacken ou à Madrid qui m'ont bien changé les idées !

Nasta, même en étant à l'autre bout de la France, tu es toujours là pour me soutenir et m'aider dans mes choix difficiles. Et quelle professionnelle en gestion de soutenance de thèse ! On se faisait la course aux examens de math au collège... nous voilà maintenant toutes les deux docteurs ! Je te remercie pour tout.

Enfin, je remercie ma famille pour son intérêt et sa présence. Je dois tout ce que je suis à mes parents. Je les remercie de leur soutien inaltérable, de leur écoute si importante, et de m'avoir poussée jusqu'ici. Merci aussi de supporter une fille qui passe son temps à travailler ou à jouer du violon, même pendant les vacances.

Quand je vois la longueur de mes remerciements, je me dis que j'ai de la chance d'avoir été autant entourée durant ces années.

Le voyage de thèse est terminé mais je compte bien continuer à partager les prochaines aventures avec ces personnes qui m'ont accompagnée jusqu'ici !

Encore un grand merci à tous !

Abstract

The shock ignition concept in inertial confinement fusion uses an intense power spike at the end of an assembly laser pulse. The key features of shock ignition are the generation of a high ablation pressure, the shock pressure amplification by at least a factor of a hundred in the cold fuel shell and the shock coupling to the hot-spot. In this thesis, new semi-analytical hydrodynamic models are developed to describe the ignitor shock from its generation up to the moment of fuel ignition.

A model is developed to describe a spherical converging shock wave in a pre-heated hot-spot. The self-similar solution developed by Guderley is perturbed over the shock Mach number $M_s >> 1$. The first order correction accounts for the effects of the shock strength. An analytical ignition criterion is defined in terms of the shock strength and the hot-spot areal density. The ignition threshold is higher when the initial Mach number of the shock is lower. A minimal shock pressure of 20 Gbar is needed when it enters the hot-spot.

The shock dynamics in the imploding shell is then analyzed. The shock is propagating into a non inertial medium with a high radial pressure gradient and an overall pressure increase with time. The collision with a returning shock coming from the assembly phase enhances further the ignitor shock pressure. The analytical theory allows to describe the shock pressure and strength evolution in a typical shock ignition implosion. It is demonstrated that, in the case of the HiPER target design, a generated shock pressure near the ablation zone of the order of 300-400 Mbar is needed.

An analysis of experiments on the strong shock generation performed on the OMEGA laser facility is presented. It is shown that a shock pressure close to 300 Mbar near the ablation zone has been reached with an absorbed laser intensity up to 2×10^{15} W.cm^{-2} and a laser wavelength of 351 nm. This value is two times higher than the one expected from collisional laser absorption only. That significant pressure enhancement is explained by contribution of hot-electrons generated by non-linear laser/plasma interaction in the corona.

The proposed analytical models allow to optimize the shock ignition scheme, including the influence of the implosion parameters. Analytical, numerical and experimental results are mutually consistent.

Keywords: shock ignition, inertial confinement fusion, spherical shock wave, self-similar solution, perturbative approach, shock dynamics, ablation pressure, hot-electrons

Résumé

Le schéma d'allumage par choc pour la fusion par confinement inertiel utilise une impulsion laser intense à la fin d'une phase d'assemblage du combustible. Les paramètres clefs de ce schéma sont la génération d'une haute pression d'ablation, l'amplification de la pression du choc généré par un facteur supérieur à cent et le couplage du choc avec le point chaud de la cible. Dans cette thèse, de nouveaux modèles semi-analytiques sont développés afin de décrire le choc d'allumage depuis sa génération jusqu'à l'allumage du combustible.

Tout d'abord, un choc sphérique convergent dans le cœur pré-chauffé de la cible est décrit. Le modèle est obtenu par perturbation de la solution auto-semblable de Guderley en tenant compte du nombre de Mach du choc élevé mais fini. La correction d'ordre un tient compte de l'effet de la force du choc. Un critère d'allumage analytique est exprimé en fonction de la densité surfacique du point chaud et de la pression du choc d'allumage. Le seuil d'allumage est plus élevé pour un nombre de Mach faible. Il est montré que la pression minimale du choc, lorsqu'il entre dans le cœur de la cible, est de 20 Gbar.

La dynamique du choc dans la coquille en implosion est ensuite analysée. Le choc se propage dans un milieu non inertiel avec un fort gradient de pression et une augmentation temporelle générale de la pression. La pression du choc est amplifiée plus encore durant la collision avec une onde de choc divergente provenant de la phase d'assemblage. Les modèles analytiques développés permettent une description de la pression et de la force du choc dans une simulation typique de l'allumage par choc. Il est démontré que, dans le cas d'une cible HiPER, une pression initiale du choc de l'ordre de 300 Mbar dans la zone d'ablation est nécessaire.

Il est proposé une analyse des expériences sur la génération de chocs forts avec l'installation laser OMEGA. Il est montré qu'une pression du choc proche de 300 Mbar est atteinte près de la zone d'ablation avec une intensité laser absorbée de l'ordre de 2×10^{15} W.cm^{-2} et une longueur d'onde de 351 nm. Cette valeur de la pression est deux fois plus importante que la valeur attendue en considérant une absorption collisionnelle de l'énergie laser. Cette importante différence est expliquée par la contribution d'élétrons supra-thermiques générés durant l'interaction laser/plasma dans la couronne.

Les modèles analytiques proposés permettent une optimisation de l'allumage par choc lorsque les paramètres de la phase d'assemblage sont pris en compte. Les diverses approches analytiques, numériques et expérimentales sont cohérentes entre-elles.

Mots clefs : allumage par choc, fusion par confinement inertiel, choc sphérique, solution auto-semblable, dynamique du choc, pression d'ablation, éléctrons chauds

Résumé détaillé

Lors de la fusion par confinement inertiel (FCI), une cible millimétrique contenant un milligramme de combustible deutérium - tritium est exposée à un rayonnement laser d'une dizaine de nanosecondes avec une énergie de l'ordre du mégajoule. La cible, alors comprimée, subit en son centre une augmentation de la densité puis une augmentation de la température lorsque l'énergie cinétique est convertie en énergie interne. Dès lors que les conditions d'allumage des réactions de fusion sont atteintes au centre de la cible, des particules hélium 4 (particules alpha) ainsi que des neutrons de 14 MeV sont émis. Si la densité surfacique de la cible (ρR) est suffisamment élevée, les particules alpha sont ralenties et elles déposent leur énergie dans le combustible. La température du combustible continue d'augmenter et les réactions sont alors auto-entretenues. Les neutrons, plus énergétiques, sont arrêtés plus loin dans l'installation. Leur énergie est récupérée sous forme de chaleur. Le gain de l'implosion est le rapport de l'énergie dégagée par les réactions de fusion avec l'énergie laser injectée.

L'onde de combustion thermonucléaire est limitée par l'expansion hydrodynamique de la cible. Pour atteindre un gain de cible assez élevé, l'onde de combustion doit être maintenue pendant un temps suffisamment long. Cela est possible si l'inertie de la cible en implosion est assez élevée pour confiner la matière. La FCI peut être envisagée pour un réacteur nucléaire si le gain est supérieur à 100.

De grandes installations laser telles que le Laser Mégajoule (LMJ) en France ou le National Ignition Facility (NIF) aux États-Unis sont construites afin de démontrer la faisabilité de l'allumage de réactions de fusion en laboratoire. Le dimensionnement actuel des implosions devrait permettre d'atteindre un gain de 15 ce qui est loin du gain nécessaire à l'échelle d'une centrale. Aujourd'hui, le chauffage auto-entretenu du combustible par les particules alpha a été obtenu en laboratoire. Mais un gain dépassant l'unité n'a pas encore été atteint et la faisabilité de l'allumage n'est pas encore démontrée. Le principal facteur limitant est la croissance des instabilités hydrodynamiques qui dégradent l'implosion.

Le gain de la cible et le taux de croissance des instabilités hydrodynamiques dépendent de la vitesse d'implosion. En réduisant cette vitesse, l'implosion est plus stable et des gains supérieurs peuvent être potentiellement atteints. Seulement la température dans le cœur de la cible dépend également de cette vitesse d'implosion et si cette dernière est trop faible, aucune réaction n'a lieu et le gain est nul. Dans le schéma d'implosion conventionnel, la compression et l'allumage de la cible se font en même temps. Des schémas d'implosion alternatifs proposent d'imploser la cible à faible vitesse d'implosion puis d'allumer les réactions de fusion à l'aide d'une source d'énergie supplémentaire en fin d'implosion. Dans le schéma d'allumage par choc, cette source d'énergie est apportée par un choc convergeant généré par une impulsion laser d'intensité élevée.

Ce schéma semble plus robuste vis à vis des instabilités hydrodynamiques et devrait permettre d'atteindre des gains supérieurs à 100. De plus l'énergie et la puissance laser requises sont envisageables sur les installations laser actuelles (NIF ou LMJ).

L'allumage par choc

La cible est constituée d'une coquille de deutérium-tritium cryogénique remplie du même combustible à l'état gazeux. Le tout est compris dans un ablateur en plastique. La cible est tout d'abord comprimée par une impulsion laser similaire à celle utilisée dans le schéma d'implosion conventionnel. Durant cette première phase, deux paramètres clefs de l'implosion sont imposés : l'adiabat de la coquille (il s'agit d'une mesure de l'entropie et donc de la compressibilité) et la vitesse d'implosion (vitesse maximale de la coquille). Un premier choc est généré, il converge jusqu'au centre de la cible, rebondit, puis interagit avec la coquille encore en implosion. Un choc est transmis dans la coquille - le choc retour – et un autre est réfléchi vers le centre de la cible. A partir de ce temps t_d la coquille commence à décélérer. Durant la phase de décélération, la pression au centre de la cible augmente jusqu'à ce qu'un équilibre de pression se fasse dans la cible au temps t_s. La vitesse de la coquille est alors nulle et la cible est en phase de stagnation. A ce moment, si aucun choc supplémentaire n'a été généré, la température au cœur de la cible est inférieure à 4 keV et la densité surfacique de la cible est de l'ordre de 100-300 mg.cm^{-2}. Ceci est en dessous du seuil d'allumage. Pour atteindre l'allumage, un choc supplémentaire est généré de manière à ce qu'il pénètre dans le cœur de la cible un peu avant la phase de stagnation. Pour cela une impulsion laser d'intensité élevée, appelée *spike*, est utilisée à la fin de l'impulsion laser de compression. Ce choc se propage tout d'abord dans une coquille convergente en accélération. Il entre en collision avec le choc retour et se propage ensuite dans un milieu décéléré toujours en implosion. Le choc d'allumage entre ensuite dans le cœur préchauffé de la cible, rebondit en son centre, puis diverge. Les conditions de température et de densité surfacique pour l'allumage sont alors atteintes derrière le choc d'allumage.

L'objectif de cette thèse est de décrire le choc d'allumage depuis sa génération jusqu'à l'allumage des réactions de fusion. D'après les simulations numériques, le choc d'allumage est généré à l'aide d'une pression d'ablation de l'ordre de 300 Mbar avec une irradiation laser d'intensité de $5 - 10 \times 10^{15}$ W/cm^2. La pression du choc est ensuite amplifiée durant sa convergence et atteint 3-5 Gbar lorsqu'il débouche dans le point chaud. La faisabilité de l'allumage par choc repose sur la possibilité de générer une telle pression d'ablation, sur l'amplification de la pression du choc d'un facteur supérieur à dix dans la coquille et sur le couplage du choc avec le cœur de la cible.

Couplage du choc d'allumage avec le cœur de la cible

Dans l'écoulement généré par un choc convergent, le maximum de température et de densité est obtenu derrière le choc après son rebond au centre du système. Le produit $\rho RT \propto pR$ croit derrière le choc divergent et l'on s'attend à ce que l'allumage ait lieu au moment où le choc quitte le cœur chaud de la cible.

L'écoulement mis en place par le choc durant sa phase de convergence et de divergence est décrit de manière semi-analytique. La température initiale du milieu de propagation n'est pas négligeable et le nombre de Mach du choc $M_{s0} = U_{s0}/c_0$ est assez faible (avec U_{s0} la vitesse du choc et c_0 la vitesse du son amont). Le choc d'allumage est décrit dans le chapitre 4 à l'aide d'une extension de la solution auto-semblable de Guderley avec un terme correctif propositionnel à l'inverse du nombre de Mach au carré M_{s0}^{-2}. La correction obtenue pour un nombre de Mach fini montre que l'efficacité du choc à chauffer le combustible est réduite lorsque le nombre de Mach initial du choc est faible. Cela signifie que pour une vitesse de choc donnée, plus la température dans le point chaud est importante avant l'arrivée du choc, moins la pression finale dans le combustible sera élevée. Un critère d'allumage basé sur le gain en énergie par dépôt d'énergie des particules alpha et les pertes par conduction et rayonnement est exprimé dans la section 4.3. Ce critère donne une valeur minimale pour la vitesse du choc $(U_s)_{ign}$ et une densité surfacique minimale du point chaud $(\rho R)_{ign}$ au moment où le choc entre dans le cœur. Il dépend du nombre de Mach initial du choc d'allumage. Lorsque le nombre de Mach du choc est infini, les conditions d'allumage sont : $(U_s)_{ign} = 650$ km.s^{-1} et $(\rho R)_{ign} = 15$ mg.cm^{-2}. Cependant, lors d'une implosion typique pour l'allumage par choc, la température dans le cœur est de 2-4 keV lorsque le choc arrive. Le nombre de Mach du choc est alors $M_{s0} < 3$. Le modèle développé dans cette thèse n'est valide que pour des nombres de Mach $M_{s0} > 4$. Dans la limite de ce modèle, les conditions d'allumage sont $(U_s)_{ign} = 750$ km.s^{-1} et $(\rho R)_{ign} = 20$ mg.cm^{-2}. Les prédictions analytiques sont confirmées par des simulations numériques. Pour un faible nombre de Mach du choc, les conditions d'allumage sont augmentées de plus de 20 %.

Il est intéressant d'exprimer les conditions d'allumage en termes de pression du choc. En utilisant la relation $p_s \propto \rho_0 {U_{s0}}^2$, une estimation de la pression minimale du choc, lorsqu'il entre dans le cœur de la cible, est de 20 Gbar.

De nos jours, il n'est pas possible de générer une telle pression d'ablation. Ainsi une amplification de la pression du choc avant qu'il n'entre dans le cœur de la cible est nécessaire. Il s'agit du second point abordé dans cette thèse.

Amplification du choc dans la coquille en implosion

Nous faisons la distinction entre l'amplification de la pression du choc $\mathcal{X}$, qui correspond à la pression finale du choc divisée par sa pression initiale, et l'amplification de la force du choc Z, où la force est la pression du choc p_s divisée par la pression dans le milieu amont p_0.

Dans le chapitre 5, il est montré que les effets de convergence seuls ne permettent pas d'expliquer l'amplification de la pression du choc d'un facteur supérieur à dix, comme on peut le voir dans les simulations numériques. L'analyse théorique montre que l'amplification provient de trois contributions : 1) l'amplification générale de la pression de la coquille en implosion $\mathcal{X}_{imp}$, 2) l'amplification du choc dans le repère co-mobile de la coquille $\mathcal{X}_{shell}$ et 3) l'amplification au cours de la collision du choc convergeant avec un choc divergent provenant de la phase de compression $\mathcal{X}_{coll}$. Ainsi l'amplification de la pression du choc peut être exprimée à l'aide de trois facteurs : $\mathcal{X} = \mathcal{X}_{imp}\mathcal{X}_{shell}\mathcal{X}_{coll}$. En considérant une implosion homogène de la cible avec

le coefficient polytropique $\gamma = 5/3$, le rayon de la cible est décrit par un facteur d'échelle $h(t)$, la densité évolue comme h^{-3} et la pression comme h^{-5}. L'amplification de la pression dans la coquille est alors $\mathcal{X}_{imp} = (h(t_i)/h(t_f))^5$. Avec un design de cible HiPER ce facteur peut atteindre des valeurs proches de 20. Il est prédominant si le choc entre dans le cœur de la cible à des temps tardifs.

La propagation du choc dans le repère co-mobile à la coquille en implosion est décrite en négligeant l'influence de l'écoulement derrière le choc. En effet, il est considéré que le choc suit une caractéristique C+ de l'écoulement. Les relations de Rankine-Hugoniot sont injectées dans les équations de conservation de la quantité de mouvement, de l'énergie et de la masse sous leur forme caractéristique. L'évolution de la force du choc dépend des effets de convergence mais aussi du gradient de pression et de densité. Dans le cas d'une coquille en accélération, le gradient de densité est positif et le choc se propage dans le sens décroissant de la densité et de la pression. La pression du choc diminue également et $\mathcal{X}_{shell} < 1$. Au contraire, lorsque la coquille est en décélération, le signe du gradient de densité est opposé au cas précédent et la pression du choc est amplifiée. Proche du temps de stagnation, $\mathcal{X}_{shell}$ est positif mais n'est pas dominant en comparaison avec $\mathcal{X}_{imp}$. Si le choc se propage uniquement dans une coquille en accélération, sa pression diminue dans le repère co-mobile à la coquille, et le facteur $\mathcal{X}_{imp}$ n'est pas assez important pour compenser la chute de pression. Le choc d'allumage dans le repère du laboratoire n'est donc pas amplifié. Il apparait au vue de ces résultats que le choc d'allumage doit entrer dans le cœur de la cible durant la phase de décélération afin d'être amplifié dans la coquille.

Dans ce cas, le choc rencontre le choc retour issu de la phase de compression. Le facteur d'amplification du choc peut être calculé à l'aide de la loi d'échelle $\mathcal{X}_{coll} \approx \left(\frac{Z_{c1}+Z_r}{1+Z_{c1}Z_r}\right)^{\frac{1}{2}} Z_r$, où Z_r est la force du choc retour et Z_{c1} est la force du choc d'allumage avant la collision (solution approchée valide pour des forces de choc inférieures à 10). Dans les simulations typiques de l'allumage par choc, la force du choc retour est inférieure à 3. L'amplification de pression dans la collision est alors $\mathcal{X}_{coll} \simeq 2$.

Ces trois facteurs d'amplification ont été calculés de manière analytique pour un design de cible type de l'allumage par choc. L'amplification de pression derrière le choc d'allumage est très sensible au temps du spike. Il a été montré que l'amplification de la pression du choc par un facteur supérieur à 100 est possible si le spike laser est suffisamment tardif. Un bon accord entre la théorie et les résultats de simulations est obtenu.

Avec le facteur d'amplification $\mathcal{X} \simeq 50 - 100$ et la pression seuil du choc d'allumage après amplification de 20-30 Gbar, il apparait qu'une pression d'ablation de 300 Mbar est nécessaire durant le spike pour atteindre l'allumage de la cible.

La troisième partie de cette thèse considère la possibilité de générer une telle pression d'ablation de manière expérimentale.

Génération d'un choc de 300 Mbar, rôle des éléctrons chauds

Un des points les plus critiques pour l'allumage par choc est la possibilité de générer une pression de plus de 300 Mbar par irradiation laser dans un large pré-plasma (millimétrique). Le régime d'intensité requis (5 à 10×10^{15}W/cm^2) est alors tel que les instabilités paramétriques dominent la propagation et l'absorption laser. Sous ces conditions, des électrons supra-thermiques sont produits dans la couronne et influencent la génération du choc d'allumage. Il faut alors tenir compte de deux processus d'absorption de l'énergie laser et de deux processus de transport associés :

– une absorption collisionelle classique par Bremsstrahlung inverse au niveau de la densité critique et le transport thermique non local ;

– une absorption en volume en aval de la densité critique et le transport d'énergie par les électrons chauds.

Ces processus de l'absorption, du transport de l'énergie par les électrons thermiques et supra-thermiques dans la zone d'ablation et la génération du choc à l'échelle de 500 ps nécessitent une description à la fois cinétique et hydrodynamique du phénomène. Cela rend les prévisions par simulations difficiles et une question ouverte est de savoir si les électrons chauds renforcent le choc d'allumage ou au contraire nuisent à sa formation par préchauffage.

Dans le chapitre 6, sont présentés et interprétés les résultats d'expériences de mesure de pression d'ablation en géométrie sphérique réalisées sur l'installation OMEGA. Il s'agit des premières expériences de génération de choc dans un régime d'intensité pertinent pour l'allumage par choc.

Un pré-pallier dans l'impulsion laser permet de générer un pré-plasma. L'impulsion principale génère un choc convergent. La cible solide est constituée de CH dopé au Titane (4 %). Sa petite taille (D = 430 μm) permet d'atteindre une intensité laser sur cible $I_L \simeq 6 \times 10^{15}$W. cm^{-2} durant l'impulsion principale. Pour certains tirs, le lissage SSD a été retiré afin d'augmenter localement l'intensité sur cible. Lorsque le choc atteint le centre de la cible, la température atteint quelques centaines d'eV et est telle que le titane émet un flash X. Une caméra à balayage de fente mesure le flux X. Des détecteurs permettent d'évaluer l'énergie laser absorbée. Les simulations numériques permettent de déduire la pression d'ablation en retrouvant le temps d'émission du flash X et le taux d'absorption de l'énergie laser mesurés expérimentalement.

Un premier tir est réalisé avec une énergie laser de 17 kJ et un lissage SSD de la tache focale. Avec un limiteur de flux à 5 %, la simulation permet de retrouver l'énergie absorbée et le temps de convergence du choc. La pression du choc avant toute interaction avec une onde issue du pré-palier est de 160 Mbar et la pression d'ablation maximale est de 180 Mbar.

Un second tir est réalisé avec une énergie supérieure (26 kJ) sans lissage SSD de la tache focale. Alors que l'intensité sur cible est 30 % supérieure au cas précédent, l'intensité absorbée estimée par les mesures expérimentales est sensiblement la même. Ce tir ne peut pas être interprété en considérant une absorption collisionnelle de l'énergie seule. D'après les évaluations expérimentales, le taux de conversion en électrons chauds est plus élevé dans les tirs sans SSD. Leur influence est alors considérée.

Un modèle simplifié de dépôt d'énergie des électrons chauds est ajouté au code CHIC. L'énergie des électrons chauds est déposée uniformément en volume dans leur zone de propagation. Le temps de convergence du choc expérimental est retrouvé dans la simulation avec une conversion de 20 % de l'énergie absorbée en électrons chauds et avec des énergies pour les électrons chauds entre 50 et 100 keV. Ceci est en accord avec les mesures expérimentales.

Lors de l'impulsion principale, une structure à double fronts d'ablation se met en place. Le choc généré par absorption collisionelle et conduction électronique thermique est renforcé par le dépôt d'énergie des électrons chauds alors qu'il se propage dans la cible. Un second front d'ablation est créé par dépôt d'énergie des électrons chauds.

Ceci génère un second choc de plus faible amplitude qui se propage vers l'intérieur de la cible. Une onde de détente émerge également de ce front d'ablation « supra-thermique » et se propage vers l'extérieur de la cible. L'interaction de cette onde de détente avec le choc principal stoppe la montée en pression de ce dernier.

La pression maximale atteinte est de 280 Mbar. Ces résultats prometteurs montrent une voie de recherche intéressante sur la génération de choc avec deux modes de dépôt et de transport de l'énergie laser incidente dans la cible.

Les différents outils d'analyse mis en place au cours de cette thèse mettent en évidence les processus physiques mis en jeu lors de l'allumage par choc et les paramètres clefs de l'implosion. Ces travaux mettent à disposition des outils utiles pour la compréhension , l'optimisation et le design d'implosion.

Contents

1 Introduction

Mankind has a continuously increasing demand of energy. The future energy consumption depends on technological, environmental and political issues. The population is increasing and the energy demand in developing countries is rising. The global energy consumption in the future can be estimated for three scenarios of growth which are represented in the figure 1.1. The middle growth scenario is the more realistic one, it predicts a population increase by 20 % from today to 2100.

Currently the most used source of energy is the burning of fossil fuels. However, the resources are limited and the pollution is dramatically increasing, menacing our environment. The global climate change is on its way and its seems unavoidable that countries will be forced to reduce the fuel burning. Alternative sources of energy are renewable energies and fission. Replacing fuel energy with renewable energy like wind turbine, hydro dam or solar panel would require a huge amount of land impacting on the environment. Indeed, the problem with renewable energy is its low energy density. To get enough energy, huge spaces and investments are needed. There will be local opposition from the inhabitants to the building of those huge infrastructures. Thus for environmental, and technological reasons renewable energy supply could not be the main source of energy for humanity unless global consumption is strongly reduced. The nuclear fission is a good candidate to supply the world energy. It has a high energy density and a low climate impact. However, the radioactive waste is a main issue. Moreover, accidents like Chernobyl and recently Fukushima make people scared.

Therefore, we need a new source of energy. The part of this new energy source in the predicted energy supply estimates [McLean, 2005] is of 50 % in 2100 (see Figure 1.1). This source must have a lot of resources, a high energy density, a low climate impact, a low level of radioactive waste and a very low risk of accidents. This seems utopic but this source already exists in the stars : the fusion. The only problem is that we have not yet succeeded in controlling it on earth.

Fusion consists in assembling two light nuclei to form a nucleus. During this process, energy is released in the form of gamma-rays and kinetic energy of particles. The fuel reactants considered

for reactors on earth are the deuterium and the tritium, two isotopes of hydrogen. Deuterium can be extracted from the ocean's water. The reserve of deuterium on earth can supply energy for billions of years. Tritium must be artificially created by bombarding lithium with neutrons. It is unstable with a half life of twelve years. The energy produced by the fusion reactions could be collected and converted into heat, transported by water which can drive a turbine to generate electricity like in a conventional power plant. However, controlling fusion on earth is very complex and the demonstration of a gain higher than unity has not been done yet.

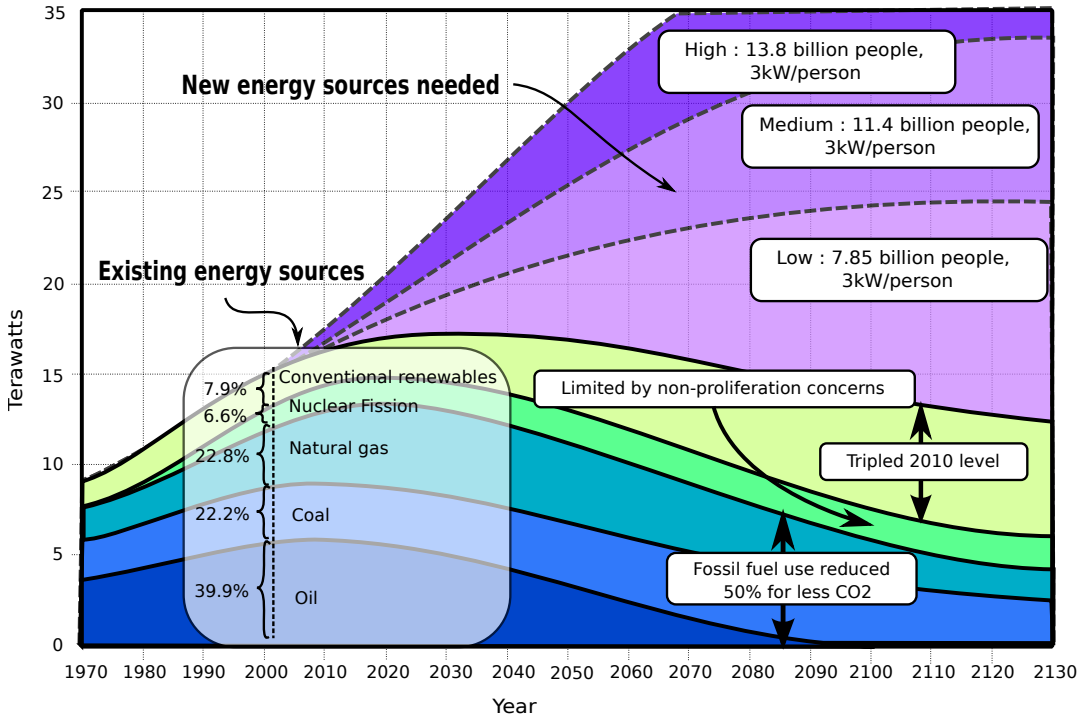

Figure 1.1: Energy supply and demand projection based on population growth, world energy consumption and plausible political strategy assumption, adapted from Ref. [McLean, 2005]

1.1 Fusion as an energy source

1.1.1 Fusion reaction

E. Rutherford, in 1911, discovered that an atom is made of a dense positively charged core and of negatively charged external electrons. The very dense region at the center of an atom, the nucleus, contains the protons and the neutrons. The proton number Z, also called the atomic number, is equal to the number of electrons surrounding the nucleus. The number of neutrons N defines the isotope state of the element. The total number of the nucleus elements is $\mathrm{A} = N + \mathrm{Z}$. All the isotopes of the same element have the same proton number Z and have the same chemical behavior, however their mass and stability are different. The hydrogen 1, with a single proton,

is the most common hydrogen isotope. The hydrogen 2, called *deuterium*, contains one proton and one neutron. The hydrogen 3, known as *tritium*, contains one proton and two neutrons. The latter is unstable and do not exist naturally. In the nucleus, protons and neutrons are bound together by the nuclear force. With the mass-energy equivalence concept, originally developed by Albert Einstein in 1905, the mass of the nucleus M is equal to the sum of the protons and neutrons masses minus the mass of the binding energy E :

$$\mathrm{M} = Nm_p + \mathrm{Z}m_n - E/c_0^2, \tag{1.1}$$

where m_p is the mass of a proton, m_n is the mass of a neutron and c_0 is the speed of light.

The figure 1.2 presents the bounding energy per nucleus E/A as a function of the mass number A. A reaction leading to a mass decrease yield to an energy emission. The iron is the most tightly bounded element. The fission of elements heavier than the iron and the fusion of elements lighter than the iron yield energy. This energy is much higher than the classical energy released by chemical reactions. Indeed the binging energy of the electrons involved in chemical reactions is much smaller than the nuclear binding energy. For example, the hydrogen oxidation in water releases an energy 2×10^7 lower than the fusion reaction between two isotopes of hydrogen.

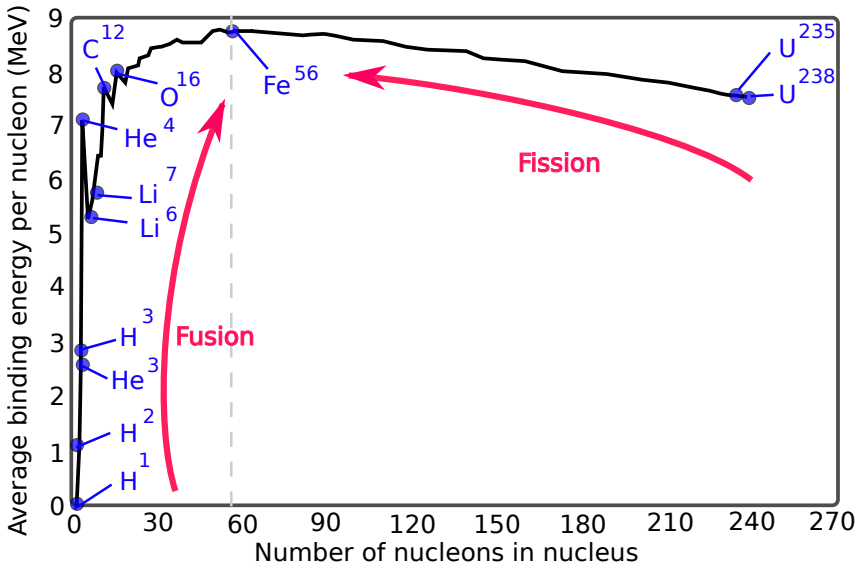

Figure 1.2: Binding energy per nucleon depending on the number of nucleons, adapted from Ref. [Atzeni and Meyer-Ter-Vehn, 2004]

To accomplish the fusion, the reactants involved have to overcome the Coulomb repulsive force. Indeed, the two nucleus are both positively charged and thus subjected to the electric repulsion. If the distance between the particles is low enough, the nuclear force dominates the electric repulsion and the fusion takes place. The energy needed for one atom to fuse with another atom at rest is of the order of 300 keV. This means that extremely high temperature

is needed. However, the quantum mechanics tells that the probability for an atom to overcome the Coulomb Barrier with a lower energy is not zero because of the tunneling effect.

The *reactivity* $< \sigma\nu >$ is the reaction probability per unit of time and unit of density averaged over the distribution of reactants over the kinetic energy. The reactivities calculated with the Maxwellian particle distribution of the most interesting fusion reactions depending on the temperature are represented on the figure 1.3. The deuterium - tritium reaction shows the higher reactivity for temperatures in the range $1 - 100$ keV. This is why this reaction is preferred.

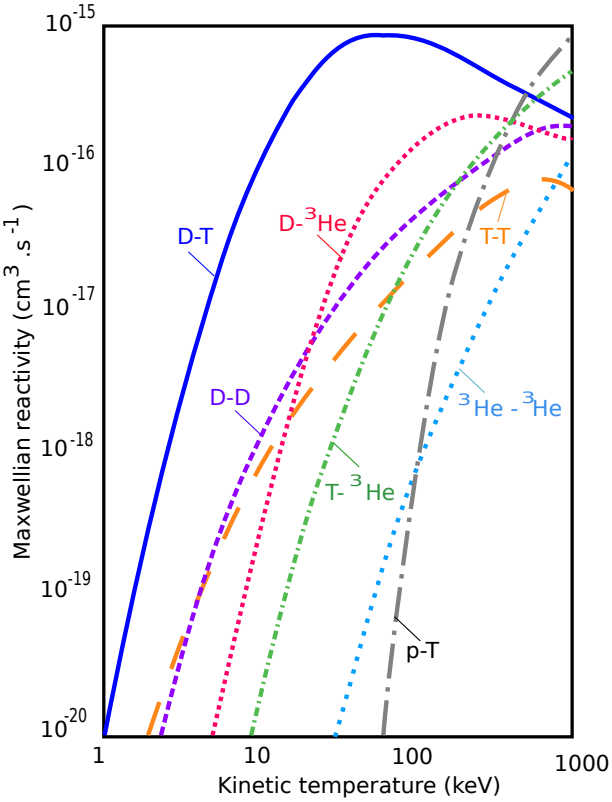

Figure 1.3: Fusion reactivity depending on the temperature, adapted from Ref. [Atzeni and Meyer-Ter-Vehn, 2004]

In the deuterium - tritium fusion reaction, two particles are released with a given amount of kinetic energy : a ^4H_e particle called the α *particle* and a neutron (figure 1.4). It writes

$$D + T \rightarrow {}^4H_e(3.5 \text{ MeV}) + n(14.1 \text{ MeV}). \tag{1.2}$$

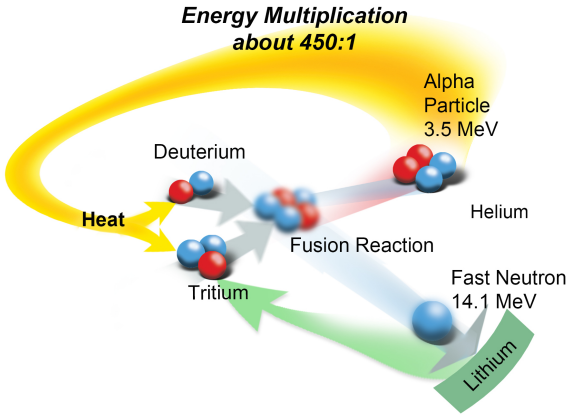

Figure 1.4: Fusion reaction between deuterium and tritium.

1.1.2 Lawson criterion

To get the maximal probability of reaction, all the reactants in the fuel must be heated to a temperature of 10-20 keV during a sufficiently long time. At this temperature the matter is under the state of *plasma*, where ions and electrons are dissociated. Maintaining the fuel at such temperature with an external source of energy would be too much costly. The idea is then to stop the alpha particles in the fuel an to use their energy to heat the fuel. This is called the *self-heating* of the fuel. The neutrons which are more energetic are used for the energy production.

However, to initiate the process, the temperature must be high enough to start the fusion reactions and the density must be high enough to stop the alpha particles. This is called the *ignition*. The ignition occurs if the fusion reaction energy production goes faster than the energy losses as radiation, conduction or mechanical work.

Figure 1.5 represents the power density losses by photo emission p_{brem} and the heating power density due to the alpha particles energy deposition p_α as a function of the temperature. The self-heating of the plasma occurs for the *Post's temperature* $T_{Post} = 4.3$ keV at which $p_{brem} = p_\alpha$.

Heating the plasma to temperatures higher T_{Post} is not sufficient. The plasma must stay confined during a sufficiently long time. The characteristic time of a reaction is $\tau = 1/(n_i < \sigma\nu >)$. It depends on the ion density of the reacting nuclei n_i and on the reactivity. A criterion on the product $n_i\tau$ was established by Lawson [Lawson, 1957] after a more detailed analysis of the energy gains and losses in the plasma. The well known *Lawson criterion* is $n_i\tau > 2\times10^{14}$ s.cm^{-3} for a temperature $T = 20$ keV.

In the stars, the confinement is due to the gravity. It requires very big masses and scales to be operational. In laboratory, two main confinement schemes are considered. The magnetic confinement fusion (MCF) scheme uses a strong magnetic field to confine the plasma with a

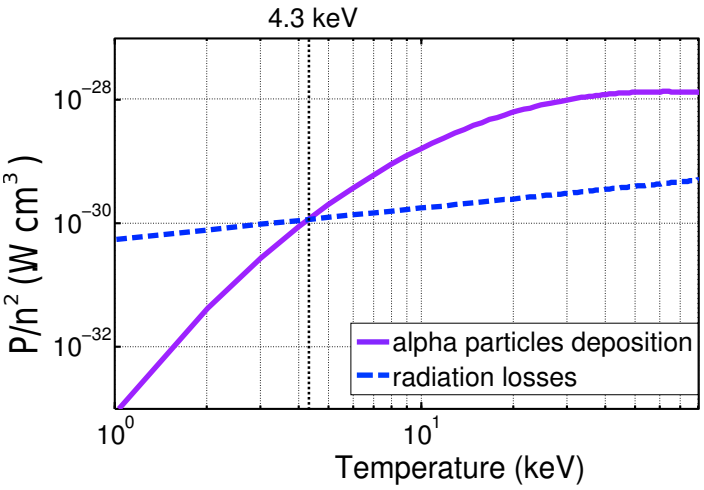

Figure 1.5: Temperature at which the self-heating by alpha particle energy deposition equals the radiation losses.

relatively low density $n_i \approx 10^{14}$ cm^{-3} and a time scale of the order of a second. In the inertial confinement scheme (ICF), a compressed and heated plasma stays confined during a finite time defined by its own inertia before it disassembles. The density in this scheme is much higher $n_i \approx 10^{26}$ cm^{-3} and the time scale is very low $\tau \approx 10^{-11}$ s.

1.1.3 Fusion for energy production

The gain is the ratio between the output energy and the driver energy E_D. Here we consider that the output energy is due to the fusion reactions E_{fus} :

$$G = \frac{E_{fus}}{E_D}. \tag{1.3}$$

The driver energy is converted from the input electric energy E_{in} with an efficiency coefficient $\eta_D = E_D/E_{in}$. The energy produced by the fusion reactions are converted into heat, transported by a fluid and converted into electric energy with a turbine with a conversion efficiency $\eta_{th} = E_{out}/E_{fus}$. A fraction fE_{out} of the output energy is used as the input electric energy to feed in the driver and the other fraction $(1-f)E_{out}$ is the final output of the reactor. The factor f is limited by the capital costs of the system. The latter depends on the cost of the installation, on the cost of its maintenance and on the electricity price. To reduce the price of the electricity, f must be small and it is usually assumed that $f < 1/4$. The systems is autonomous when

$$f\eta_D\eta_{th}G = 1. \tag{1.4}$$

In inertial confinement fusion, typically, $f = 1/4$, $\eta_D \approx 10\%$ and $\eta_{th} \approx 40\%$, which means that the gain G must be at least 100. With a driver energy of 3 MJ and a gain of 100, ten shot per second is needed to produce 1 GW of electricity.

This thesis works is conducted in the context of the inertial confinement fusion. Before focusing on this approach, let give few words on the magnetic confinement fusion in the next section. The interested reader can refer to specialized books, for example [Braams and Stott, 2002, Hazeltine and Meiss, 2003].

1.2 Magnetic confinement fusion

An approach to ignite the Deuterium Tritium fusion reactions is the magnetic confinement scheme. A strong magnetic field may confine the plasma in a steady state for a long time. In an appropriately chosen magnetic configuration the charged particles of the plasma are trapped by the magnetic field and kept away from the vessel walls. While heating this confined plasma to ignition conditions, the alpha particles are also trapped by the magnetic field and transfer their energy to the plasma. Therefore, once the ignition had occurred, the external heating can be stopped and the plasma is self heated.
The most developed device for magnetic confinement fusion is the *Tokamak*.This is a theta-pinch of a toroidal shape. It was first proposed and developed in Russia in 1951 [Tamm and Sakharov, 1959]. In this concept the plasma is confined in a toroïdally shaped vessel (see Figure 1.6). A toroidal magnetic field is generated by the external coils. However, the toroidal magnetic field itself is insufficient for particle trapping. The curvature of magnetic field lines imposes opposed drifts for the ions and the electrons leading to a charge separation and producing an electric field and a loss of the confinement. To prevent the radial drift, an additional poloidal magnetic field is induced in the plasma by generating a toroidal current with a special induction coil. Both toroidal and poloidal magnetic fields lines form globally a set of closed magnetic flux surfaces which confine the plasma inside. Thus, the Tokamak can be considered as a giant transformer. That means that the plasma confinement is a transient phenomenon during a half period of the induction current. However, in the advanced Tokamak the toroidal current is maintained by other sources such as neutral particles or electromagnetic waves. That allows to extend the plasma life time to several minutes in the present day machines and to expect a quasi-steady operation of future reactors.
The current largest tokamak is the Joint European Torus (JET) located in United Kingdom. This device has a volume of 80 cm^3, however, it is not large enough to allow energy gain because of the thermal diffusion losses across the magnetic surfaces and the plasma instabilities. The machine of next generation will be the International Thermonuclear Experimental Reactor (ITER). It should be operational in 2020 in France. The ITER device will have a plasma of 830 m^3 and will produce a fusion power of 500 MW with an energy gain of 10. The expected duration of plasma discharge is 3000 s which is a significant step toward the steady state operation. The ITER program born in 1985 by connecting European, Japanese, Russian and American scientists. Later, China and South Korea, joined the project in 2003 and also India in 2005. The place for the ITER construction was chosen to be Cadarach in 2005 and the construction is currently taking place.

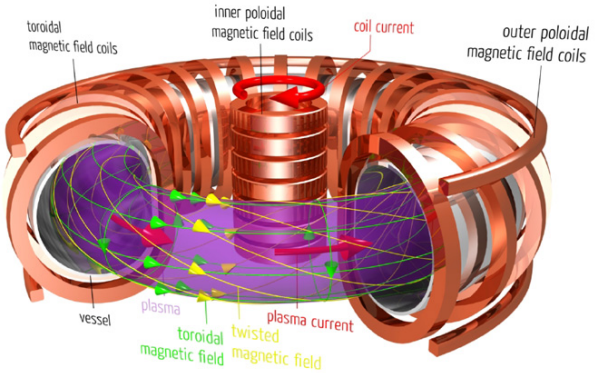

Figure 1.6: Main features of the Tokamak device for magnetic confinement. (Scheme by Abteilung Öffentlichkeitsarbeit - Max-Planck Institut für Plasmaphysik)

An alternative for the Tokamak is the *Stellarator* proposed by Lyman Spitzer in the USA in 1950. With this device, both the toroidal and the poloidal magnetic fields are generated by the coils . This device has the advantage to provide a continuous confinement of a plasma. However, the shape of the coils is much more complicated (see Figure 1.7). Currently, the largest operational Stellarator is the TJ-II in Madrid [Alejaldre et al., 1990]. An larger one, the Wendelstein 7-X [Wegener, 2009], will be operational soon in Greifswald in Germany. The aims of those devices is to demonstrate the feasibility of steady operation and a control of plasma instabilities. However the volumes (under 30 cubic meters) of those facilities will not allow to reach an energy gain higher than unity.

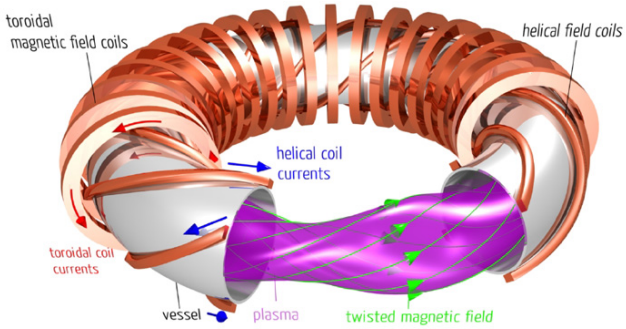

Figure 1.7: Stellarator device scheme. (Scheme by Abteilung Öffentlichkeitsarbeit - Max-Planck Institut für Plasmaphysik)

The very large size of toroidal fusion machines is explained by the fact that the maximal magnetic field which can be generated with a supra-conducting cryogenically cooled coils is 17,6 Tesla [Durrell et al., 2014].

The most important challenges for the magnetic confinement fusion are the control of plasma instabilities, the design of efficient methods of plasma heating, the removal of the reaction products and impurities and the long operation time. But even if all of these physical and technical problems may be resolved, the problem of resistant construction and plasma facing materials remains the most difficult. Indeed, the plasma being a strong neutron source, the structure must be neutron-resistant. The material must prevent the radioactive activation, the erosion and the heating.

The current design consists in a first wall made of tungsten surrounded by a blanket in a vacuum vessel. Then, superconducting magnets are enclosed in a cryostat in order to keep a low temperature. The fuel of Deuterium Tritium is injected in the Tokamak in a form of cryogenic solid pellet.

The plasma in magnetic confinement devices is unstable. The microscopic instabilities correspond to the magnetic field fluctuations that destroy the magnetic surfaces and enhance the energy and particle diffusion. However, the most dangerous instability is the large scale plasma current oscillations leading to large current disruption and ejection of plasma. Strong forces are then acting on the Tokamak structure.

Another magnetic plasma confinement scheme without external coils exists and is called Z-pinch. We chose not to go through details is this manuscript, but we invit the interested reader to look to the review paper [Haines, 2011]. Here, a strong current generated in the axial direction (Z-pinch) produces a self generated magnetic field that compresses and heat the plasma. Z-pinch is more unstable and the plasma life time is relatively short, less than a microsecond. However, with a strong current, that time could be sufficiently long to induce the fusion reactions. The fusion experiment which took place in 1958 in the Los Alamos National Laboratory was the first to demonstrate the neutrons production [Anderson et al., 1958]. The largest Z pinch device today is the Z machine at Sandia National Laboratories with the discharge current exceeding 20 MA. The current Z-pinches are the sources in hard X-rays, they allow to reach high energy density states of matter with pressures of 5-100 Mbar. The X rays generated in Z-pinch can be used as a source to drive the implosion of an ICF capsule [Haines, 2011]. The implosion scheme and the target design are similar to the indirect drive of ICF. Typically, an imploded wire array z-pinch generates up to 1.8 MJ of X-rays at power of 230 TW with an efficiency $> 15\%$. The radiation temperature in the hohlraum of 230 eV has been reached.

1.3 Inertial confinement fusion

1.3.1 Historical note

The research about nuclear reactions lasts for more than a century.

In the beginning of the 20th century, both physics and the world knew revolutions. Henry Becquerel, noticed that uranium salt self-emits radiations [Becquerel, 1896]. Pierre and Marie Curie [Curie, 1898] continued the research on those radiations and named the phenomenon as

the radioactivity. The uranium atom could be broken down (fission) with a release of energy. This reaction is spontaneous and a block of uranium ore spontaneously emits heat as fission reactions continuously take place inside it.
The discovery of the neutron in 1932 by James Chadwick [Chadwick, 1932] allowed a new conception of the atom nucleus constitution. Later, the possibility to break up a uranium nuclei under neutron bombardment had been suggested by Ida Noddack in 1934 [Noddack, 1934]:

> "When heavy nuclei are bombarded by neutrons, it is conceivable that the nucleus breaks up into several large fragments"

Later, the German team in Berlin with Otto Hahn, Lise Meitner, Otto R. Frisch and Fritz Strassmann was the first to demonstrate that the uranium nuclei can be split when bombarded with neutrons [Meitner and Frisch, 1939, Hahn and Strassmann, 1939]. The reaction is named as fission. It is evoked that the fission reaction releases energy. As the fission reaction emits neutrons, the physicist Leó Szilard proposed the idea that a chain reaction can be possible. Such a process can be the source of an enormous amount energy. This was understood by Fermi and Szilard who proposed a reactor for civilian energy (first operation in 1942). Arms based on the fission chain reaction were developped during the second wold war.
With the discovery of the radioactivity, scientists wondered if it could be the source of the sun energy [Clery, 2013]. However, the sun contains mainly hydrogen which can not be broken into lighter elements. In 1920, Francis Aston [Aston, 1920] measured that the helium mass is slightly less than four times the mass of hydrogen during his research on the existence of isotopes. Arthur Eddington [Eddington, 1920] interpreted this measurement according to Einstein's famous relation $E = mc^2$: if hydrogen atoms in the sun fuse in helium particles with a loss of mass, then this can be the energy source of the sun. However, by this time, no one was able to explain how fusion reactions can occur. In the same period, the quantum mechanics revolution arrived. George Gamow in 1928 [Gamow, 1928] stated that according to quantum mechanics, it exists a probability for two nuclei to overcome the Coulomb barrier and to fuse. Atkinson and Houtermans published a paper [Atkinson and Houtermans, 1929] in 1929 explaining that the sun's conditions predicted by Eddington are compatible with the occurrence of fusion reactions.

The first experiments of fusion reactions were done by Mark Oliphant in 1932. He used a particle accelerator to give a sufficient kinetic energy to the hydrogen particles and make them fuse. It was then proved that energy was indeed released in the reaction. But at this time, only 1 over 100 million accelerated particles fused with another particle.

> "The energy produced by the breaking down of the atom is a very poor kind of thing. Anyone who expects a source of power from the transformation of these atoms is talking moonshine." Rutherford

It was then though that if the fuel is heated, the fusion reaction rate increases. Moreover, if the temperature is high enough, a part of the energy released by the fusion reactions would maintain the process and the other part can be used as a source of energy.

Enrico Fermi has an idea to use the fission reaction to get the high density and temperature needed to ignite the fusion reactions. This leads to the concept of the "super bomb" (or bomb H) which was defended by Teller in 1942 in the Oppenheimer's summer conference. In 1957, Teller and other scientists in Livermore, presented a project of using the nuclear explosion for civilian energy production [Nuckolls, 1998]. In this context they were also looking for another possibility to get fusion reaction without the use of fission primary. Nuckolls proposed to implode a milligram of deuterium-tritium to high density and temperature with radiation coming from a gold cavity (called Hohlraum) energized by an external source. The *indirect-drive* inertial confinement fusion was born. The DT is enclosed in a thin spherical and dense shell. The target is first heated. The external matter is ablated which accelerate the shell toward the center. This drives the implosion until the ignition occurs at the center.

Nuckolls considered several external sources of energy as pulsed power machines, charged particle accelerators, plasma guns. When the first laser experiments were proceeded by T. Maiman in late 1960 [Maiman, 1960], this technology appeared as a good candidate for the external source of energy. This technical revolution allows to reproduce the state of matter and the thermal radiation similar to those found in the bomb H.

At the end of 1960, the chosen compression scheme was already close to the current conventional ICF scheme. The target shell is made of the fuel itself with cryogenic DT. The ignition occurs at the center of the target and then a burning wave propagates into the resting fuel. This allows to reach a higher gain. This scheme is called the *hot-spot ignition*.

In 1961-1962, Kidder considered the case where the laser beams ablate directly the pellet outer surface. This is called the *direct drive scheme*. The advantage of this scheme is that it avoids the energy losses through the Hohlraum. However, the laser irradiation uniformity constraints are higher.

After a decade of laser plasma production feasibility experiments and progresses in generating hight power/short pulse laser beam, inertial confinement fusion programs started. The aim was to demonstrate the DT fusion ignition. At this time, the calculation predicted the need for a laser power of a few kilo-Joules.

In URSS by the end of the 60's, the Levedev Institute is a pioneer in the ICF experimental research. The first neutrons from laser irradiated targets were announced in 1968. Then the most advanced research lasers was Kalmar built in 1971 (300 J) [Basov et al., 1975]. In USA, the first experiments took place on the 20 J laser Janus in 1974. To this laser followed the laser facility Shiva (10 kJ) in the late 70's and the laser facility Nova (100-150 kJ) in the 80's. In France, the first indirect drive experiments were performed in the early 80's using the eight beams with 5 kJ of energy of the laser Octal. The French experiments for ICF were later performed on the the Phébus laser of 20 kJ built in 1985 and on the Ligne d'Intégration Laser (LIL) of 30 kJ since 2002. In Japan, the Gekko XII laser was completed in 1983 capable of delivering 30 kJ of energy.

The indirect drive was thought as the most feasible scheme. In this scheme the non uniform laser beam irradiation is smoothed as it is converted into soft X-rays. It seemed unlikely that the

single beam smoothing techniques and the multi beams overlap with a direct irradiation scheme could lead to a sufficiently uniform irradiation on the target. Also, the laser plasma interaction at high intensity leads to parametric instabilities. Those instabilities generate hot electrons which could pre-heat the target leading to reduced compressibility. To limit the hot-electron generation, and to increase the laser absorption and the ablation pressure, it was proposed to triple the laser frequency with a wave-length of 351 nm instead of the infrared light at 1053 nm. The development of laser performance and accuracy, of sophisticated diagnostics for experiments and of computational simulation tools led to strong improvements in the next years. At the end of the 90's, hot electrons generation was reduced to acceptable level, and target conditions close to those needed for ignition were reached with the Nova laser facility (40 kJ). Then, bigger projects of Mega Joule lasers were put forward with the National Ignition facility (NIF) in the United States and the Laser Mégajoule (LMJ) in France . Whereas the LMJ will be soon operating, the NIF is the actual most powerful facility with 192 beams and an energy of 1.8 MJ. For a direct-drive irradiation, the laser beams configuration is different than in the indirect drive scheme. The OMEGA laser facility operates since 1995. It delivers 30 kJ with a 60 beams spherically symmetric configuration. Other facilities which are not aimed to reach ignition allow to study the physics of the target implosion at low scales. We mention the PALS laser (1.2 kJ) in Czech Republic, Vulcan (2.6 kJ) and ORION (5 kJ) in United Kingdom, the PHELIX laser (1 kJ) at the GSI laboratory in Germany and the laser LULI 2000 (2 kJ) at the École polytechnique in France showing that Europe is strongly involved in ICF and high energy density physics. The cooperation within Europe is promotted through projects like HiPER or COST. The aim of the HiPER project is to coordinate research related to plasma physics, targets, laser and diagnostics technologies and to develop future fusion reactor concepts.

The study of inertial confinement fusion has obviously an interest for fusion energy application but it is also related to more large scientific questions. Indeed, it allows to reproduce astrophysical processes in laboratory by means of scaling laws. It can also be related to fundamental physics as the laser experiments bring the plasma under extreme conditions. This justifies more over the construction of the intermediate (kJ) facilities.

Table 1.1 shows the ICF facilities evolution since 1974. Even if the driver technology has been continuously improved, the ignition demonstration has not been done yet. We will explain in the next part the main limitations and present where we currently are on the path to ignition.

[1]These are the announcements for the partial LMJ opening to academic research in 2017.

Year	Name	Location	Energy (wavelength)	Pulse duration	Beams
1971	Kalmar	Moscow (Russia)	300 J (1053 nm)	2 ns	9
1974	Shiva	Livermore (USA)	10 kJ (1053 nm)	0.5-1 ns	20
1978	Octal	Limeil (France)	5 kJ (1053 nm)	1 ns	2
1983	Gekko XII	Osaka (Japan)	10 kJ (532 nm) 30 kJ (1053 nm)	1-2 ns	12
1985	Nova	Livermore(USA)	40 kJ (351 nm), 100 kJ (1053 nm)	3 ns	10
1985	Phébus	Limeil (France)	6 kJ (351 nm), 20 kJ (1053 nm)	1 ns	2
1995	OMEGA	Rochester (USA)	30 kJ (351 nm)	ns	60
2002	LIL	CEA CESTA (France)	30 kJ (351 nm)	ns	8
2009	NIF	Livermore (USA)	1.8 MJ (351 nm)	ns	192
2017[1]	LMJ	CEA CESTA (France)	100kJ (351 nm)	ns	16

Table 1.1: Main high power laser devices for inertial confinement fusion research since 1971

1.3.2 Status of the conventional ignition scheme in ICF

The current conventional ignition scheme consists in imploding a target with an outer shell in plastic called the *ablator*, an inner shell made of cryogenic DT and a central part of DT gas. The target can be irradiated directly in the direct-drive scheme (Figure 1.8), or indirectly in the indirect drive scheme. In the latter, the target is enclosed in a gold cavity (the Hohlraum). The laser is absorbed by the cavity and converted in the thermal bath of X-rays which drive the implosion. The energy transfer to the target is less efficient in the indirect drive. However, this scheme is less affected by symmetry and stability issues. The fusion reactions take place at the center of the target at the end of the implosion when the kinetic energy of the shell is converted into internal energy. The implosion velocity is directly related to the final hot-spot temperature and therefore must be sufficiently high. The areal density must also be high enough to stop the alpha particles which heat further the fuel and maintain the fusion reactions.

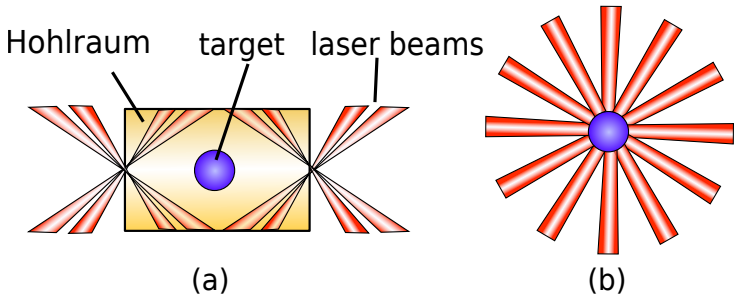

Figure 1.8: Irradiation of the target. In the indirect drive scheme (panel a), the capsule is placed inside a Hohlraum, the laser beams are arranged in two cone arrays. In the direct drive scheme (panel b), the target is directly irradiated and the laser beams come from all directions.

1.3.3 Limitations

Energy coupling to the target The direct drive scheme avoid losses of energy during the conversion of the laser light to X-rays in the Hohlraum of the indirect drive scheme. However, the current Mega-Joule laser facilities as the NIF or the LMJ are built for indirect drive, so the laser beams are arranged into rings placed on opposite poles. A direct quasi symmetric irradiation of the target with this beams configuration could be possible by re-pointing the beams, shaping the focal-spot, and increasing the intensity of the equatorial beams. This is called the *polar direct drive*. As the beams irradiate the target obliquely, the laser coupling to the target is less efficient. During the interaction, non-linear processes induce deleterious instabilities which generate hot electrons and reduce the absorbed energy. During the last years, the beam uniformity has been improved with beam smoothing techniques. The *cross beam energy transfer* coming from the overlapping of the beams reduces also the coupling efficiency (the energy of one beam is transfered to another). A *zooming* technique where the beam spot size is reduced during the implosion seems to have a positive effect.

Shell pre-heat During the compression the shell must be kept as cold as possible. Indeed the back pressure of the shell resists the compression. The heating of the shell comes from hot electrons energy deposition or from shock waves entropy deposition. The hot electrons are generated in the laser-matter coupling instabilities. The shock waves are generated to drive the implosion. The laser pulse shape must be well timed so that the shock waves do not merge in the shell and stay with a low amplitude. A mis-timing of the shocks could be dramatic for the implosion.

Implosion symmetry A non symmetric hot-spot reduces the ignition efficiency. The non uniformities coming from the target surface roughness or the beams non uniformities must be reduced.

Hydrodynamic instabilities During the implosion the shell surface perturbations are amplified by hydrodynamic instabilities. Techniques have been developed to mitigate those instabilities growth but they still are the main limitation of the implosion.

All those limitation effects become more influent when the laser intensity is increased. Thus even if huge progresses have been done on the driver power and energy, the ignition condition still have not been fulfilled.

1.3.4 Progress toward ignition

After the building of the National Ignition Facility, a National Ignition Campaign was conducted on the NIF in the US with the goal to demonstrate the feasibility of ignition. The first cryogenic implosions was performed in September 2010. Since that time, the irradiation quality, the laser pulse and the target design have been improved. To evaluate the implosion performance

according to measured parameters, the Experiment Ignition Threshold Factor (ITFx) [Haan et al., 2011] has been defined. It depends on the neutron yield and on the ratio of down-scattered neutrons to unscattered neutrons which is proportional to the fuel areal density. The ignition occur for ITFx higher than unity.

Figure 1.9 shows the progress toward ignition achieved in the NIC campaign. The progress between the shot of 2010 and the shot of February 2011 is due to the laser energy increase. The progress in 2011 was obtained by improving the shock timing, by increasing the implosion velocity with Si-doped shell ablator, and by improving the symmetry and the laser beam quality. However, the cross beam energy transfer is a phenomenon too much non linear to be well controled, and it was decided to improve the implosion by modifying the implosion hydrodynamics. Therefore, in 2012, the pre-heat of the shell is lowered by modifying the laser pulse (*low-foot* laser pulse). The target is more compressed but the hydrodynamic instabilities reduce the yield leading to an ITFx of 0.1. On the contrary, a *high-foot* laser pulse was chosen for the shot of 2013. Hydrodynamic instabilities were reduced by increasing the ablation velocity but then a higher pre-heat of the shell leads to a lower final compression. By the end of November 2013, the alpha particles self-heating has been achieved for the first time. This means that more energy was released from the fusion reactions than energy was supplied to the hot-spot. This shot reached the ITFx of 0.5. The neutron yield of 5×10^{15} was 75 % higher than any previous shot. The fusion energy released was 17.3 kJ which remains far from the 1.9 MJ laser energy input.

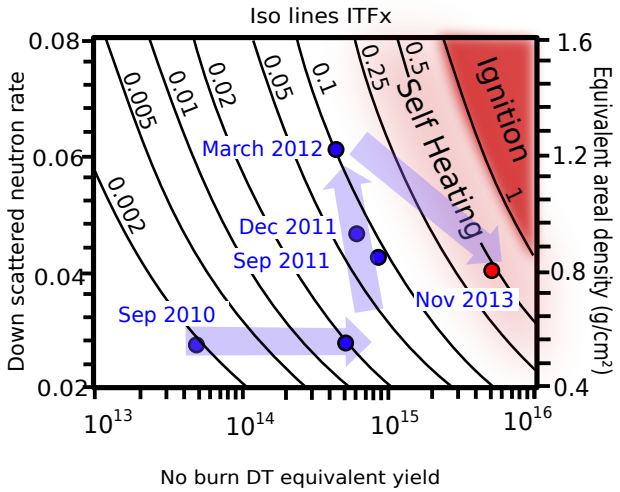

Figure 1.9: Progress toward ignition with indirect drive on NIF. Adapted from Ref. [Landen et al., 2012]. The point representing the shot of November 2013 is placed according to the data in Ref. [Hurricane et al., 2014].

The direct-drive scheme was not a part of the NIC ignition campaign. For that purpose, the laser facility OMEGA allows a spherical direct irradiation of the target with a symmetric repartition of the beams. However, its energy is limited to 30 kJ which is insufficient to reach

ignition. To evaluate the implosion performance on this facility, scaling laws has been used to extrapolate the experimental results to a future NIF direct drive implosion. A NIF equivalent ignition criterion ITFx [Sangster et al., 2013] is defined. Figure 1.10 shows the extrapolated results of direct drive implosion on OMEGA in the graph equivalent to the previous Figure 1.9. The maximum ITFx obtained between 2009 and 2013 is 0.25. This is not so far from the results obtained with the indirect drive scheme on the NIF. However, one must have in mind that this ITFx is an extrapolation of the results from implosions performed on OMEGA at the NIF scale. Uncertainties exist on this extrapolation. Indeed, the non-linear processes during the laser-plasma interaction or the hydrodynamic instabilities growth cannot be scaled in a straightforward manner from the OMEGA to NIF. Again we can see that more the target is compressed, higher is the areal density but lower is the yield. This might be related to the hydrodynamic instabilities.

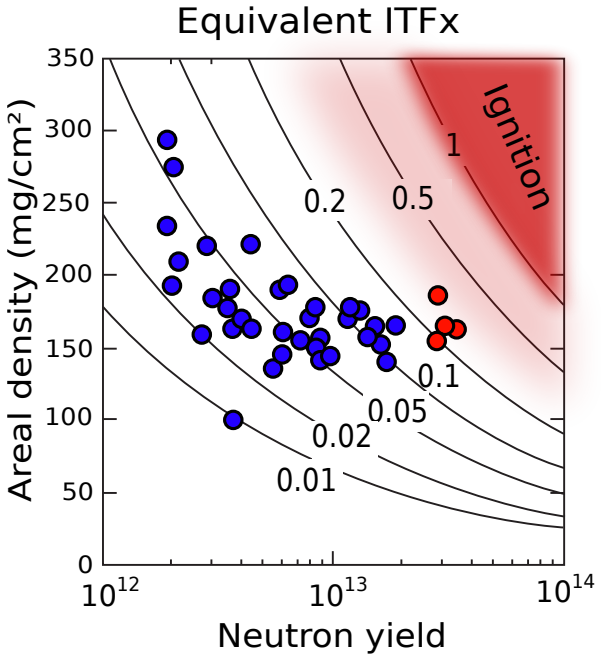

Figure 1.10: Progress toward ignition with the direct drive on OMEGA. Adapted from Ref. [Sangster et al., 2013]. The red circles are placed according to the April 2014 workshop presentation by Sangster.

1.4 Shock ignition as an alternative scheme

Faced with the conventional scheme limitations, alternative implosion schemes have been proposed. In the conventional scheme the compression and the heating of the fuel are accomplished at the same time.

Let us evaluate the energy needed for compression and for heating. We will see later that the compression is performed in a nearly isentropic way which means that $p = 2.15\alpha\rho^{5/3}$ where

α is called the shell adiabat (see Section 2.3.1), p is the pressure in Mbar and ρ is the density in g.cm^{-3}. The energy needed for compression $E_{comp} = \int_{V_f}^{V_0} p\,\mathrm{d}V$ reads

$$E_{comp}[\mathrm{MJ}] = 0.2\alpha \mathrm{M}_0 \int_{\rho_0}^{\rho_f} \rho^{-1/3}\,\mathrm{d}\rho \simeq 0.3\alpha \mathrm{M}_0 \rho_f^{2/3}, \tag{1.5}$$

where M_0 is the shell initial mass assumed constant in g, $\alpha \sim 1-3$ the dimensionless shell adiabat,ρ_f the compressed density in g.cm^{-3} and ρ_0 the initial density is neglected.
The energy needed to bring a volume V_h to the temperature T_h is $E_{heat} = 3(Z+1)n_i T_h V_h/2 = 3T_h M_h/\mathrm{A}m_p$ with M_h -the heated mass, A - the average atomic mass and m_p - the proton mass and where a perfect gas state equation is assumed. For a DT mixture we have

$$E_{heat}[MJ] = A_h M_h T_h, \tag{1.6}$$

with $A_h = 110\mathrm{MJ/keV/g}$, M_h in g and T_h in keV.
To compress 1000 times 1 mg of cryogenic DT (initially with the density 0.25 g.cm^{-3}) along with a shell adiabat of 3 , the needed compression energy is $E_{comp} = 36$ kJ. Heating one tenth of this mass to the ignition temperature 4.3 keV required an energy of $E_{heat} = 47$ kJ. One can notice that the compression is less energy demanding than heating.

Whereas the whole fuel must be compressed to stop the alpha particles and to allow the thermonuclear burn wave propagation, only the hot-spot needs to be heated to ignite the target. In the advanced schemes, the compression of the target and the heating of the hot-spot are separated into two steps. Laser intensity and energy for the compression phase are lower than in the conventional scheme. This relaxes the problem concerning the shell pre-heat, the coupling efficiency and the symmetry. Then a supplementary source of energy is brought to ignite the hot-spot. In the conventional scheme the pressure at the ignition time is equilibrated between the shell and the hot-spot. In the alternative scheme the pressure is higher in the hot-spot. This leads to a potentially higher gain. Also, the implosion velocity is reduced leading to less severe hydrodynamic instabilities.

There are two major advanced ignition schemes. In the *fast ignition scheme*, the hot-spot is created by means of energy deposition by hot electrons or energetic ions [Tabak et al., 1994]. The energetic particles are generated with a ultra-intense beam ($I \approx 10^{20}$ W.cm^{-2}) and must be focused in the hot-spot. In the *shock ignition* (SI) scheme, the ignition is triggered by a converging shock wave. This *"ignitor"* shock is generated at the end of the implosion by a laser *spike* with a high intensity ($I \approx 10^{16}$ W.cm^{-2}). When the shock converges at the center, the central pressure is strongly increased and the hot-spot temperature and areal density are raised to the ignition conditions. The advantage of this scheme is that the compression and the shock launching can be done by using the same laser beams. Thus it can be experimented on the already existing facilities as NIF or OMEGA with the same laser configuration as in the direct-drive.

Figure 1.11 presents the typical laser pulse and target used for shock ignition. The target is

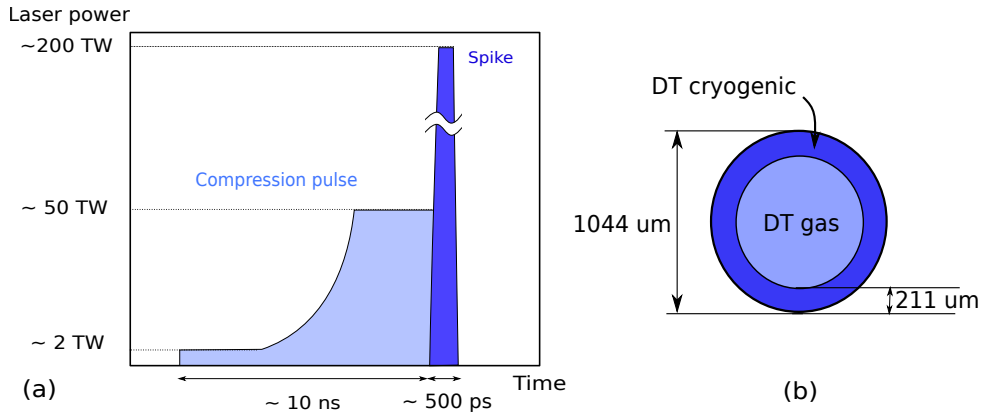

Figure 1.11: Typical laser pulse and target for the shock ignition scheme with a HiPER target design.

first imploded by the compression pulse. The implosion velocity depends on this pulse. Then the laser spike generates the ignitor shock.

We propose here a brief, non-exhaustive, review of the research done on the shock ignition topic. We recommend to the interested reader the more detailed review on the shock ignition principles and modeling proposed in Ref. [Atzeni et al., 2014]. Also, the major issues related to the shock ignition scheme, from both theoretical and experimental points of view, are summarized in Ref. [Batani et al., 2014].

Principle The idea of igniting fusion reactions with a shock wave was first proposed by Shcherbakov [Shcherbakov, 1983] in 1983.

> " First, a spherical fusion target is compressed to a comparatively high degree, and then a focusing shock wave created by an intense laser pulse heats and ignites the center of the target. [...] In this approach, the problem of achieving a high compression is separated from that of heating the center of the target, and the two problems can be addressed separately or in succession."

He proposed to first implode a target of 0.4 mg of DT with a very low velocity 20 km.s^{-1} during 40 ns, to a uniform sphere of a radius 140 μm with a density of 40 g.cm^{-3} and a temperature of 0.1 keV. Then the shock brings the hot-spot to a temperature of 5 keV needed for ignition. According to Shcherbakov, the velocity behind the shock must be $\approx$ 150 km.s^{-1} in order to reach the ignition condition. This corresponds to an initial shock velocity of 230 km.s^{-1}. The initial pressure of the shock is then 15 Gbar. To generate such a pressure the absorbed laser intensity must be at least 2×10^{18} W.cm^{-2} (by using the collisional scaling given later in (2.17)). This seems very challenging because at such intensities,the collisional laser absorption and the non-relativistic scaling for the pressure generation is no more valid.

A new approach of the shock ignition has been proposed by Betti in 2007 [Betti et al., 2007]. The target is a cryogenic shell like in the conventional scheme. The implosion brings the fuel

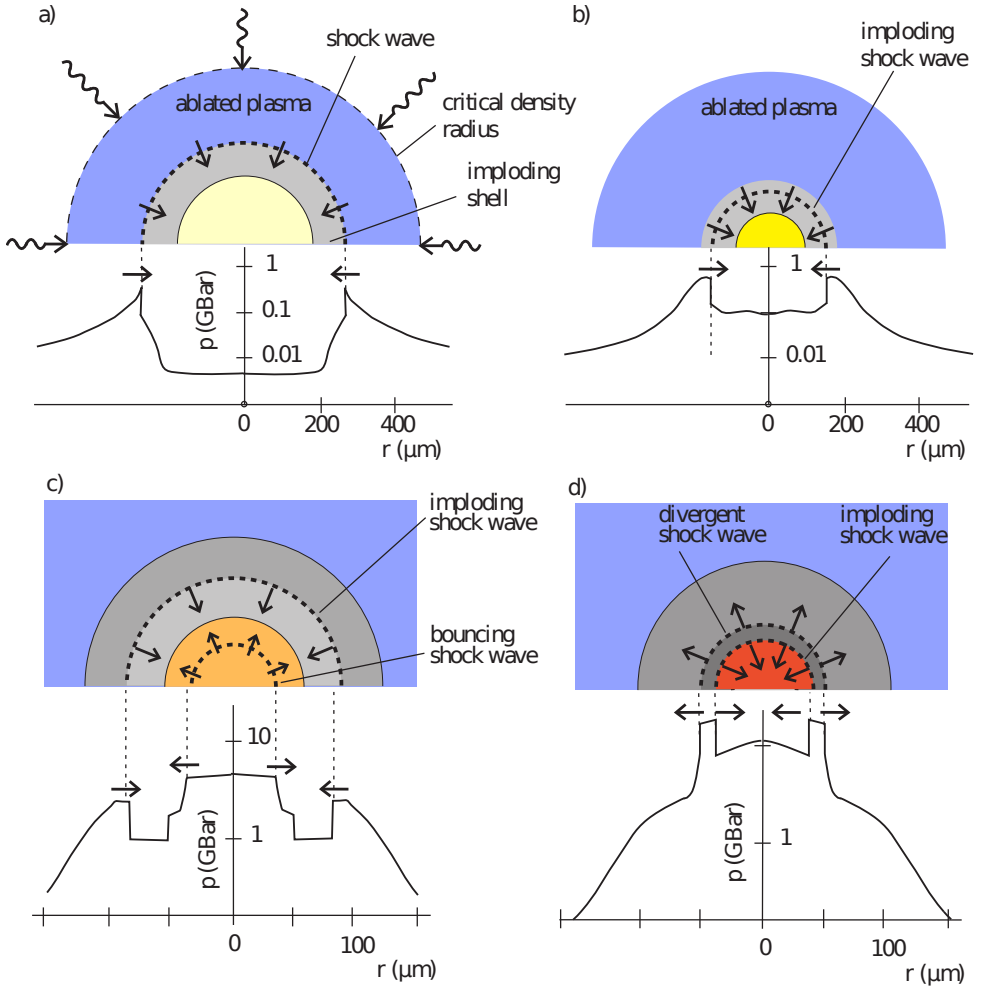

Figure 1.12: Shock ignition principle : a) The compression pulse generates a shock wave, b) this shock converges and is reflected at the center, c) at the end of the compression, a laser spike launches a shock whereas the first shock is diverging, d) the two shocks collide leading to a shock pressure increase. The amplified imploding shock ignites the fusions reactions in the hot spot (Figure from Ref. [Atzeni et al., 2013], with permission)

close to the ignition conditions and a small shock amplitude is needed. Moreover, the shock pressure is amplified in the collision with a returning shock coming from the compression phase (see Figure 1.12). Therefore, the shock ignition takes advantage of the compression phase to enhance the ignitor shock effect.

It is estimated that such a shock can be launched with the laser intensity of 6×10^{15} W.cm^{-2} which is much lower than in the Shcherbakov case. In the conventional ICF scheme of ignition, the target configuration at the end of the implosion is isobaric (see profiles (a) in Figure 1.13). In the shock ignition scheme, the ignitor shock enhance the pressure in the hot-spot and the target configuration at ignition is not isobaric (see profiles (b) in Figure 1.13). In the Ref. [Betti et al., 2007], an ignition criterion for the energy is expressed in the non isobaric case. It is shown that the energy required for ignition is reduced by a factor $\Phi^{2.5}$ where $\Phi = p/p_{\text{iso}}$ is the

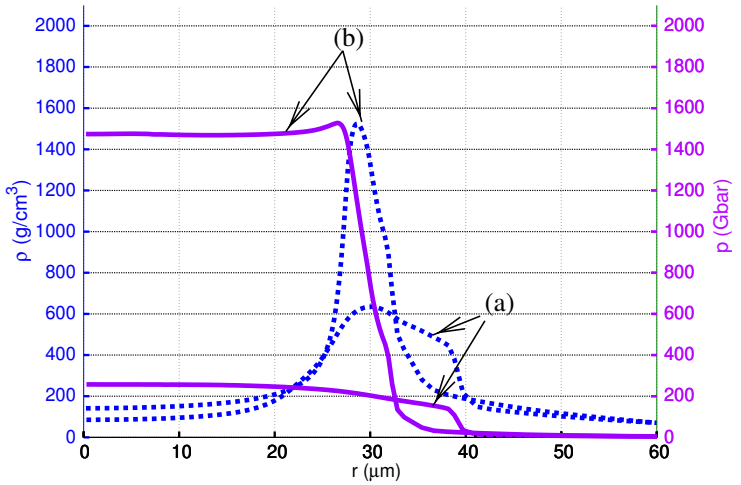

Figure 1.13: Density (dashed line) and pressure (solid line) profiles near the ignition time with (a) a conventional ignition scheme and (b) a shock ignition scheme. (From Ref. [Ribeyre et al., 2009])

ratio of the central pressure at ignition in the non isobaric case and in the isobaric case. This is under the assumption that the final pressure is achieved through an adiabatic compression which is not the case in the flow behind a converging shock. This demonstration explains why a non isobaric configuration is more economic in energy but it does not take into account the dynamics of the ignitor shock wave. It is also mentioned that hot electrons may be generated during the spike irradiation due to the high laser intensity. However, since the pre-compressed shell is dense enough, the hot electrons with energies lower than 100 keV are stopped near the shell surface and can contribute to the drive of the ignitor shock.

The principle of shock ignition is studied in further detail in Ref. [Ribeyre et al., 2009] by means of numerical simulations. The ignitor shock pressure amplification in the target shell is attributed to convergence effects and appears to be of a factor three in typical simulations. After the ignitor shock collides with the returning shock, a part of the shell has a higher pressure and a high density. This part of the shell acts like a piston on the hot-spot. The compression of the hot-spot is viewed as an adiabatic process because the ignitor strength is low when it enters the hot-spot. However, the convergence effects should increase its strength as it converges toward the origin. The flow behind a converging/diverging shock differs from the adiabatic flow driven by a piston.

Hydrodynamic studies The propagation of the shock in the hot-spot is described with the Guderley self-similar solution in the reference [Ribeyre et al., 2011]. It is used to express an ignition criterion [Ribeyre et al., 2013b]. It appears that the shock velocity when it enters the hot-spot must be higher than 600 km.s^{-1} with a hot-spot areal density higher than 10 mg.cm^{-2} at this time. This corresponds to a shock pressure of 17 Gbar for a hot-spot of 50 μm. According to the numerical simulation, an initial shock pressure of 300 Mbar is sufficient. This means that

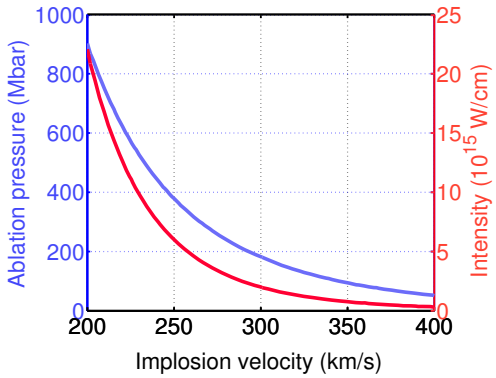

Figure 1.14: Ablation pressure and absorbed intensity needed (with $\lambda_L = 351$ nm) to ignite the target with a shock depending on the implosion velocity (according to [Lafon et al., 2013])

the ignitor shock pressure is strongly amplified in the shell.

The shock pressure amplification in the shell is studied in detail in the reference [Lafon et al., 2010]. It is modeled with the self-similar solution of Guderley. The shock pressure p_s evolves depending on the shock position R_s as $\propto R_s^{-0.9}$. This model is valid for a strong shock propagating in a uniform medium at rest. However, in the shock ignition scheme, the ignitor shock propagates in an imploding target. The medium in front of the shock is not at rest and is not uniform. Moreover, the shock strength Z (ratio of the shock downstream pressure and shock upstream pressure) is low. We will see in Section 4.1, that the shock strength is around 3 as it enters the hot-spot. This means that the shock Mach number M_s (ratio of the shock relative velocity and the upstream sound velocity) is also low as $Z \propto M_s^2$. In a later paper [Lafon et al., 2013], the Guderley's model is used to evaluate the initial shock pressure needed to ignite the hot-spot. The analytical estimate of the ablation pressure versus the implosion velocity is plotted in Figure 1.14. The ablation pressure varies between 100 and 900 Mbar. This corresponds to intensities in the range $1 - 20 \times 10^{15}$ W.cm^{-2}. It is pointed out in Refs. [Lafon et al., 2010, Lafon et al., 2013] that the Gurdeley model under estimates the shock pressure amplification compared to the simulation. A deeper study is needed to understand the ignitor shock pressure evolution in the shell.

In Ref. [Lafon et al., 2013] the final pressure at the ignition threshold is expressed as a function of the implosion velocity. For a high implosion velocity, the fuel pressure at the time of stagnation is expressed using the Kemp self-similar solution [Kemp et al., 2001]. The dense shell part downstream the ignitor shock is considered as a hollow imploding shell. This launches a shock inside the hot-spot. This shock rebounds at the center and interacts with the imploding flow during its divergence. The pressure ratio of the fuel at the time of stagnation and the time of void closure is $p_s/p_0 \simeq 3.6\mathcal{M}_0^3$ where $\mathcal{M}_0$ is the Mach number of the shell $\mathcal{M}_0 = V_p/c_{if}$ with V_p the shell velocity and c_{if} the sound velocity in the shell. In the case of a low implosion velocity, the shell material behind the ignitor shock is considered as a piston with a given mass and velocity. The final fuel pressure is evaluated assuming that all the piston kinetic energy is transfered to the fuel internal energy. This latter model does not take into account the dynamics

of the ignitor shock in the hot-spot.

The shock pressure amplification in the collision with a returning shock coming from the compression phase is studied in detail in Ref. [Lafon et al., 2013]. As no analytical solution allows to predict the shock pressure after the collision, an approximate expression is proposed. It is assumed that the density behind the converging (ignitor shock) and the diverging (returning shock) shocks is the same. This is valid for incoming shocks with the same pressure or when the pressure between the two shocks is negligible. In this paper the collision is assumed to take place at the inner face of the shell. The pressure of the shocks before the collision is expressed as a function of the implosion velocity. With the implosion velocity of 250 km.s^{-1}, the two shocks have almost the same pressure and the amplification factor through the collision is 6. Depending on the ignitor shock timing, the collision position may not be at the inner face of the shell. Moreover, the strength of the shocks is finite and may not be equal. Therefore, the shock amplification in the collision needs a deeper analysis taking into account the shock timing and the finite strengths of the shocks.

A study of the ignitor shock dynamics in a one dimensional planar model has been done by Nora [Nora and Betti, 2011]. In the conventional scheme, the final internal energy in the hot-spot is lower than the kinetic energy of the shell. This is due to a rarefaction wave created in the shell which decompresses the target and reduces the final pressure of the hot-spot. The ignitor shock, in addition to bring energy into the hot-spot, can mitigate the rarefaction wave. Depending on the shock timing and pressure, the rarefaction can be simply suppressed. Then, the maximal hot-spot pressure is increased by 80 %. Here the shock is viewed as a way to improve the coupling of the shell kinetic energy to the hot-spot internal energy.

Proof of principle of SI scheme with experiments A proof of principle campaign of experiments have been conducted on the OMEGA laser facility. In those experiments, spherical targets with a warm plastic shell were considered.

In the first campaign [Theobald et al., 2008], the 60 available laser beams of OMEGA have been used both for the shell compression and for the shock launch. The best shot with a laser spike produced a neutron yield of 8×10^9 with 18.6 kJ of laser energy (with about 5 kJ in the spike). This is four times higher than the yield obtained without spike at 19.4 kJ of laser energy. It is shown that the implosion performance depends highly on the spike timing. Also, the results suggest that the shock ignition scheme achieves a better stability and mitigates the mixing of the cold shell into the hot-spot.

In those experiments, the spike intensity was 6.5×10^{14} W.cm^{-2} which is much lower than the intensity expected in the SI implosion for ignition. To overcome this intensity limitation, a second campaign used 40 beams for the compression and 20 beams for the shock launch [Theobald et al., 2012]. The spike intensity reached 8×10^{15} W.cm^{-2}. In this configuration, the spike enhanced the neutron yield by a factor up to 2.3, which is less than in the 60 beams configuration. This may be due to the higher laser irradiation non uniformity. Nevertheless, in this campaign the laser-matter interaction at high intensity can be studied. Hot electrons of a moderate energy

(30 keV) were generated. The backscattering of laser energy was up to 36 % at the highest intensity. This population of hot-electrons can be deleterious for the compression of the target unless they are stopped by the compressed shell.

Shock pressure generation The main question for shock ignition is : what maximum ablation pressure the laser spike can create? Indeed, the laser-matter coupling in the intensity regime of $5-10\times10^{15}$ W.cm^{-2} is not well known. As this regime of intensity was not envisaged for the conventional scheme of implosion, there is a lack of experiments. It must be stressed that in the shock ignition scheme, the laser spike interaction occurs in a large scale corona which favors the occurrence of non-linear processes. Then, hot electrons can be generated and preheat the target. The laser plasma interaction in the intensity range $1-10\times10^{15}$ W.cm^{-2} has been studied numerically by Klimo [Klimo et al., 2010]. It has been shown that the dominant process of absorption changes completely in this regime. This is not included in the standard hydrodynamics simulations codes. With a kinetic approach, this paper shows that the laser spike generates hot electrons of energies in the range 20-40 keV in agreement with the experimental results presented above.

The simulation of a NIF implosion design of shock ignition [Anderson et al., 2013] shows that the hot electrons have a positive effect if their temperature is lower than 150 keV and if the conversion efficiency of the laser light is below 20 %.

Its seems that the hot electrons cannot preheat the hot-spot because the shell is enough dense at the end of the implosion to stop them [Betti et al., 2008]. However, those hot electrons energy is not well characterized and it is not obvious if they are deleterious or not for the shock generation and amplification in the shell. The Refs. [Ribeyre et al., 2013a, Gus'kov et al., 2012, Piriz et al., 2013] assess that the hot electrons can contribute to the shock generation.

We mention that during the spike irradiation, the crossbeam transfer of energy and the nonlocal heat conduction must be important. Those two features need to be better understood and their implementation in hydrodynamic codes need to be validated.

Design of implosion Since the first paper of Betti et al. [Betti et al., 2007], several authors presented design and optimization studies. The design of a SI implosion for HiPER has been studied [Ribeyre et al., 2009, Atzeni et al., 2011, Atzeni et al., 2009, Canaud and Temporal, 2010] in detail. The target is a spherical all DT cryogenic shell of external radius 1044 μm and shell thickness 211 μm. The implosion velocity is about 300 km.s^{-1}. A design for the NIF facility with a polar direct drive scheme was proposed by Perkins [Perkins et al., 2009] and Anderson [Anderson et al., 2013]. The target in the latter design is slightly larger with a radius of 1080 μm. The shell is constituted by an external plastic ablator layer of 31 μm and an internal part of cryogenic DT with a thickness of 161 μm. The implosion velocity is 300 km.s^{-1}.

It is shown that the gain is highly dependent on the time delay between the spike time and the stagnation time [Ribeyre et al., 2009, Betti et al., 2008, Schmitt et al., 2010, Atzeni et al., 2011, Atzeni et al., 2013]. If the shock is launched too early, the areal density is too low for

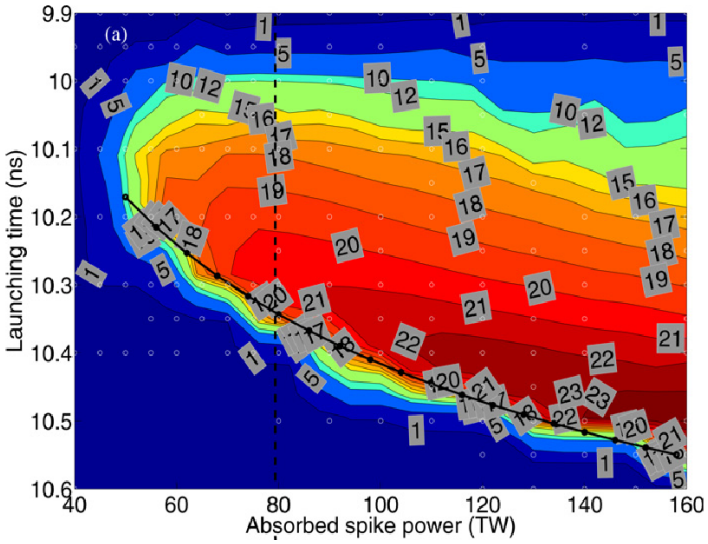

Figure 1.15: Gain contours in the plane of the spike time and the spike power for the HiPER target design [Ribeyre et al., 2009].

ignition. If the shock is launched too late, the target is already on the way to disassemble as the shock creates the hot-spot and no gain is obtained. Figure 1.15 presents the gain depending on the spike power and time. The windows of ignition seems not stringent with a width of 250 ps for the spike time.

The implosion velocity is an important parameter for the compression phase. When it exceeds a given threshold value, the target ignites without ignitor shock. Under this threshold, the laser spike is needed for ignition to take place. Figure 1.16 shows the HiPER target gain map depending the implosion velocity and on the spike power. For an implosion velocity higher than 360 km.s^{-1}, the target self-ignites. The maximal gain is then 50. For lower implosion velocities, a higher gain of 70 can be reached. For an implosion velocity under 250 km.s^{-1}, no gain is obtain. It is clearly visible here that an optimal couple implosion velocity/spike power exists for a given a target [Atzeni et al., 2011]. This has been confirmed in Ref. [Lafon et al., 2013] (see Figure 1.17). The energy of the compression pulse has been varied in order to cover an implosion velocity range from 200 to 400 km.s^{-1}. Then the spike power is adjusted to reach the ignition threshold. With the same HiPER target, no spike is needed for implosion velocities higher than 350 km.s^{-1}. The total laser energy is minimal for an implosion velocity of 250 km.s^{-1}. Under this velocity, the energy needed in the spike for ignition grows quickly thus reducing the gain.

The condition for a marginal shock ignition has been studied for both the HiPER target design and the LMJ target design in Ref. [Canaud and Temporal, 2010]. At the end of the spike, a rarefaction wave is generated and can overtake the ignitor shock. The spike duration do not seem to have any effects on the gain as far as it is long enough for the rarefaction wave not to catch up with the ignitor shock. The temporal width of the ignition windows is again 200 ps for the both targets. Designs are proposed to reach a gain of 100.

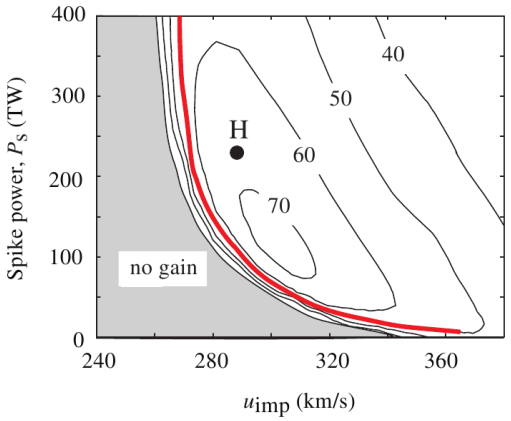

Figure 1.16: Gain contours in the plane of the implosion velocity and the spike power for the HiPER target design [Atzeni et al., 2013].

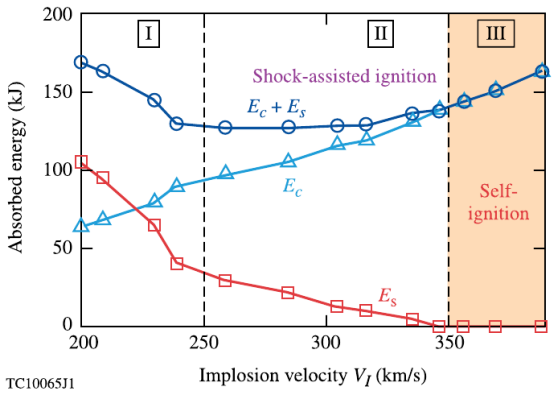

Figure 1.17: Energies in the compression pulse and in the spike depending on the implosion velocity for the HiPER target design [Lafon et al., 2013].

The reference [Atzeni et al., 2011] shows that the gain depends on the spike energy. It appears that for the HiPER target design, a threshold spike energy is about 70 kJ, independently of the spike power. Figure 1.18 presents the gain-spike energy curves for three spike powers. The three curves are almost superposed. The gain does not vary much for the energies higher than the threshold. Thus the spike duration is an important parameter near the energy threshold, its minimal value depends on the spike power.

One target design can be scaled to various target sizes whereas the implosion parameters such as the implosion velocity or the shell entropy are kept constant. This family of targets is called an *homothetic family*. The energy required to implode the target increases with the target size and so does the gain. For the full DT target, both Ref. [Canaud and Temporal, 2010] and Ref. [Schmitt et al., 2010] predict a variation of the gain from 100 to 300 with a laser energy varying from 0.1 to 2 MJ. Figure 1.19 shows the gain dependence on the laser energy. The dashed lines were obtained by scaling the targets with a shock ignition scheme and the solid line is obtained by scaling the targets without ignitor shock. With the conventional scheme, reaching a gain of 100 requires an input energy higher than 1 MJ. The shock ignition scheme allows to reach such a high gain with a lower laser energy. For the laser energies higher than 1 MJ, the two curves match. This is because no spike is needed in this range of input energy.

The robustness of an all-DT target imploded with a SI scheme with a short laser wavelength (248 nm) laser was studied in Ref. [Schmitt et al., 2010]. The parameters used in this study are the compression and ignition pulse power and the spike timing. The robustness increases as the ignitor power increases. It is confirmed that the ignitor pulse couples more efficiently its energy to the hot-spot internal energy than the compression pulse.

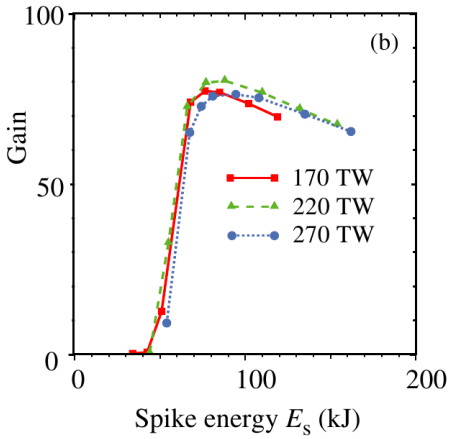

Figure 1.18: Gain versus the spike energy for three spike powers [Atzeni et al., 2011] for the HiPER baseline target SI implosions.

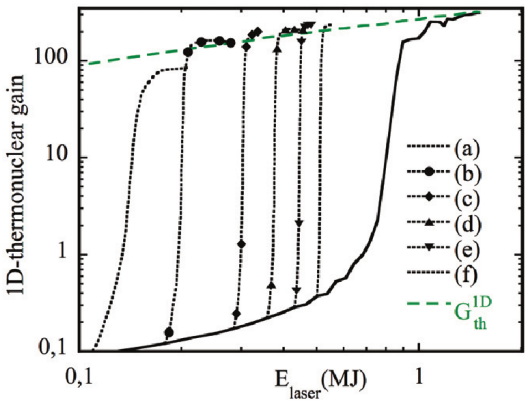

Figure 1.19: Gain versus the laser energy for homothetic target family, with spike (dashed line) without spike (full line) [Canaud and Temporal, 2010].

2D effects In the OMEGA experiments [Theobald et al., 2008], a saturation of the Rayleigh–Taylor hydrodynamic instabilities (RTI) at a high convergence ratio is observed. It seems that the shock mitigates the growth of these instabilities. In the numerical study of the SI scheme for HiPER [Ribeyre et al., 2009] the RTI growth is stopped by an impulsive acceleration driven by the shock wave and by the apparition of another stabilizing instability (Richtmyer–Meshkov instability). Figure 1.20 shows the shell density distribution obtained in simulations without spike (a) and with spike (b) at the stagnation time. The deformations are less important in the second case. The reduction of the hot-spot deformation by the ignitor shock interaction has also be seen with the DUED code [Atzeni et al., 2011]. While this effect was observed in numerical simulations, no theoretical analysis has been conducted to explain it.

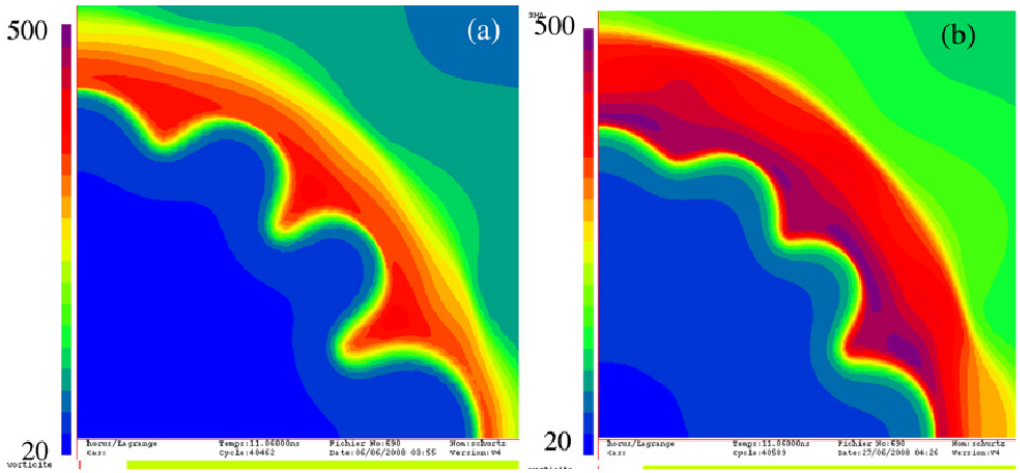

Figure 1.20: Density in the simulation or the HiPER target design without spike (a) and with spike (b) at the stagnation time [Ribeyre et al., 2009].

The 2D effects on the target performance is evaluated in Ref. [Schmitt et al., 2010]. A short laser wavelength allows to consider higher intensity in the compression pulse because the laser-matter interaction is more stable with respect to the instabilities. Then the shell target thickness can be higher which reduces the hydrodynamic instabilities growth. The 2D effects narrow the operating space of the laser pulse parameters and therefore reduce the robustness of the design. A better robustness can be recovered by increasing the laser spike power. But then the gain is reduced. In the NIF design study [Anderson et al., 2013], the 1-D gain is reduced by 15% by taking into account the laser non-uniformities. By taking into account all the uncertainties (capsule roughness, misplacement, laser non uniformities), the gain is reduced by 35%.

The target mis-positioning leads to a strong asymmetry in the implosion. The simulations of the HiPER SI implosion show a strong sensitivity to the target positioning which must be controlled within a few per cent of the target initial radius [Atzeni et al., 2011].

The possibility to use a higher laser wavelength (527 nm) has been assessed in Ref. [Atzeni et al., 2013]. The absorption efficiency and the ablation pressure are reduced hor higher laser wavelength, however, the laser inhomogeneities are also reduced with the visible light. The proposed design is scaled from the baseline HiPER design with the help of an analytical model. The wavelength is modified, but the laser irradiance $I_L\lambda_L^2$ is constrained to the value of the reference design. It is shown that the targets with this design exhibit a lower in fligth aspect ratio and a lower convergence. They should be then less sensitive to irradiation asymmetries and hydrodynamic instabilities.

Conclusions This state of the art analysis provides a snapshot of research progresses on the shock ignition scheme at the beginning of this phd study. It appears that the dynamics of the ignitor shock is mostly described with numerical simulations or simplified analytical models. The coupling of the shock with the hot-spot has been studied by neglecting the hot-spot pressure which does not agree with the results of numerical simulations. The shock propagation in the shell has been studied in a planar or a spherical geometry assuming a homogeneous upstream medium which is not the case. Therefore, the theory concerning the ignitor shock hydrodynamics needs to be developed to understand all the processes involved during the shock ignition. Moreover the key issue of the shock ignition is the generation of the ignitor shock. Both analytical and numerical studies predict that an ablation pressure of 300 Mbar during the spike would be needed. However, the generation of such a pressure had never been realized experimentally. In the intensities regime considered for shock ignition, the interaction laser/matter is strongly different from what is usually considered in the conventional scheme of ICF. We reach here the limits of the conventional hydrodynamics simulation codes. Kinetic or hybrid simulation codes are needed. Although a lack of experiments is clearly visible here.

1.5 Thesis outline

We propose in this thesis to analyze in more detail the shock dynamics in the shell and the shock coupling to the hot-spot. The approach will be mainly analytical to keep the implosion parameters well visible in the description. A comparison with simulations is systematically realized. The aim is to understand how the implosion parameters affect the shock efficiency. We also interpret experiments on the ignitor shock generation in spherical geometry with a laser intensity pertinent for shock ignition. We use both analytical and numerical tools to explain the processes involved in the experiments.

The manuscript presentation is as follows:

Chapter 1 This is a general introduction which discusses the world energy needs and presents the fusion reaction as a potential future source of energy on earth. The evolution of the inertial confinement fusion concept and of the lasers facilities during the last half century is presented. The chapter highlights the main limitations encountered in ICF and exposes the current situation on the road toward ignition. A state of the art of the shock ignition scheme is exposed.

Chapter 2 This chapter describes the main physical processes involved in the target implosion. The aim of this chapter is to explain how the ignition conditions are reached and to introduce the key implosion parameters. We take an opportunity to introduce here the basic features of the hydrodynamic simulation code CHIC used in this work. In the light of the ICF description given in this chapter, the advantages of the shock ignition scheme are reminded.

Chapter 3 This chapter recalls the basic concepts of hydrodynamics description using a perfect gas equation of state. The homogeneous compression of a target is described. Also the basic relations describing a shock are given. An overview on the existing methods describing a converging spherical shock is exposed.

Chapter 4 This chapter gives an analytical description of a spherical converging shock with taking into account the upstream pressure. Scaling laws are given in the vicinity of singular points in the flow. The solution is used to express a criterion for shock ignition. The coupling efficiency of the ignitor shock with the hot-spot is discussed.

Chapter 5 This chapter provides a detailed description of the shock pressure evolution in the imploding shell. Three amplification factors are identified and analyzed. The ignitor shock pressure evolution in a typical HiPER implosion simulation is explained according to the analytical theory.

Chapter 6 This chapter proposes an analysis of shock generation experiments relevant for the shock ignition scheme conducted on the OMEGA laser facility. The potential effects of the hot electrons are discussed.

Chapter 7 This chapter summarizes the results presented in the thesis and suggests some future research directions.

2 Physics of inertial confinement fusion

Contents

This chapter aims to present the physics of inertial confinement fusion. This will allow to define the main implosion parameters. We will also introduce the main features of the simulation code CHIC used in this work.

In Section 2.1, we introduce inertial confinement basic concepts such as the fusion reactions ignition and target burn. We will see that the target areal-density and the hot-spot temperature at the end of the implosion are key parameters. The possibility to use a laser for driving the implosion, and the laser/plasma interaction issues are exposed in Section 2.2. The implosion synopsis related to the laser pulse shape is discussed in Section 2.3. Section 2.4 gives an overview on the hydrodynamic instabilities which are one of the most constraining issues in ICF. Section 2.5, explains why the shock ignition scheme is an interesting approach for ICF by using the concepts introduced in the sections stated above.

For a more detailed introduction to ICF, we refer the reader to the review papers Ref. [Brueckner and Jorna, 1974] and Ref. [Lindl, 1995] and to the very good book [Atzeni and Meyer-Ter-Vehn, 2004].

2.1 Inertial confinement

In the inertial confinement scheme, the fusion reactions must occur during a very short time in a compressed and heated plasma confined under its own inertia. We present in this section the conditions needed for fusion reactions to take place with a significant energy gain in an inertially confined plasma.

2.1.1 Burn fraction

Let us consider that the fuel is assembled in an homogeneous sphere of radius R_f with a density ρ_f and a temperature T_f high enough to allow the fusion reactions. The particle density is expressed with the fluid density $n_i = \rho_f/\mathrm{A}m_p$ with A - the average atomic mass of a DT mixture and m_p - the proton mass. We assume that the particle densities of deuterium and tritium are equal with $n_D = n_T = n_i/2 = \rho_f/2Am_p$. The maximal number of fusion reactions in this sphere is $N_{tot} = 4\pi R_f^3 n_i/6$. In reality, the number of reactions will be only a fraction of this value. Indeed, the sphere initially at rest, expands with the sound velocity $c = \sqrt{T_f/Am_p}$, where T_f is the fuel temperature. The ignition conditions for the fusion reactions are valid only in the sphere not perturbed by the rarefaction wave. Then, the reactions occur only during the propagation time of the wave from the outer radius of the sphere to the center: $t_{max} = R_f/c$. The number of reactions during this time, in the unperturbed sphere is

$$N_f = n_D n_T < \sigma\nu > \int_0^{t_{max}} \frac{4\pi}{3}(R_f - ct)^3 \,\mathrm{d}t = \frac{1}{4}n_i^2 < \sigma\nu > \frac{1}{3}\pi\frac{R_f^4}{c}, \tag{2.1}$$

where $< \sigma\nu >$ is the reactivity of the deuterium tritium reaction which depends on the temperature (see Figure 1.3 in Chapter 1). In the range 1-100 keV, it could be approximated by the

function [Atzeni and Meyer-Ter-Vehn, 2004]

$$< \sigma\nu >_{DT} [\mathrm{cm}^3.\mathrm{s}^{-1}] = 9.10 \times 10^{-16} \exp\left(-0.572 \left| \ln \frac{T[\text{ keV}]}{64.2} \right|^{2.13}\right). \tag{2.2}$$

Looking at the equation (2.1), the number of reactions in front of the rarefaction wave is equivalent to the number of reactions that would appear in the initial sphere of radius R_f without the rarefaction wave during the time $t_{conf} = R_f/4c$. This time is called the *time of confinement*.

The burn fraction $\Phi_B = N_f/N_{tot}$ is expressed as

$$\Phi_B = \frac{1}{2} n_i < \sigma\nu > \frac{R_f}{4c} = \frac{\rho_f R_f}{H_B} \tag{2.3}$$

where $H_B = 8\sqrt{m_i T_f}/ < \sigma\nu >$ is the temperature dependent *burn parameter* which can be evaluated using the reactivity law (2.2).

Up to here, we neglected the fuel depletion during the burn time, which is possible only if $\Phi << 1$. The variation of the particle density of a fuel specie n_f is related to the reaction rate as

$$\frac{\mathrm{d}n_f}{\mathrm{d}t} = -{n_f}^2 < \sigma\nu > \tag{2.4}$$

which leads to

$$n_f(t) = \frac{n_f(0)}{1 + n_f(0) < \sigma\nu > t} \tag{2.5}$$

with $n_f(0) = n_i/2$.

Combining the expressions (2.3) and (2.5), the burn fraction $\Phi_B = 1 - n_f(t_{conf})/n_f(0)$ can then be expressed as

$$\Phi_B = \frac{\rho_f R_f}{\rho_f R_f + H_B}. \tag{2.6}$$

The product $\rho_f R_f$ is called the *areal density* of the fuel. According to the temperature dependence of H_B, the areal density must be higher than 3 $\mathrm{g.cm}^{-2}$ at the fuel temperature of 35 keV, in order to burn at least 30% of the fuel.

The energy produced by the mass m_{DT} of deuterium-tritium is expressed with the burn fraction

$$E_{fus} = \Phi_B \frac{m_{DT}}{2Am_p} 17.6 \text{ MeV} \approx 200 m_{DT(\mathrm{mg})} \mathrm{MJ} \tag{2.7}$$

where 17.6 MeV is the energy released in the fusion reaction and $\Phi = 0.3$ is assumed in the latter relation. Thus, the specific reaction energy is $2 \times 10^{11} J/g$. Let us consider a sphere of a solid DT at a cryogenic temperature with the density $\rho_f = 0.25$ $\mathrm{g.cm}^{-3}$. To reach the areal density of 3 $\mathrm{g.cm}^{-2}$ the DT mass required is 1.8 kg. Then the energy released would be $400 \times 10^{12} J$. This is equivalent to a hundred kiloton of TNT which is not thinkable for a power station purpose. The DT mass is limited by the resistance of the target chamber materials and only few milligrams of fuel could be used. Then the cryogenic DT must be compressed by a factor of 1000 to reach the needed areal density and the size of the compressed sphere is around 100 μm.

We remind that the minimum temperature to allow fusion reaction is $T_{Post} = 4.3$ keV (see Figure 1.5 in Chapter 1). This value is defined by the radiative losses. Compressing a target by a factor of 1000 and heating such a small volume to more than 4 keV shows why ICF is complicated.

Let us now evaluate the gain obtained by burning a DT sphere. The internal specific energy required to heat the fuel to the temperature T_{Post} is $\epsilon_{th} = 3\frac{T_{Post}}{Am_p} \approx 494$ MJ.g^{-1}. Let be $\eta = 10\%$, the conversion efficiency of the driver energy into the plasma internal energy. The gain is then estimated as $G = \eta E_{fus}/E_{th} = 36$. However, a gain higher than 100 is needed for an energy production purpose. A way to improve the gain, is to ignite only a part of the fuel referred to as the *hot-spot*. To be efficient, the mass of the hot-spot must be small in comparison with the mass of the surrounding cold compressed fuel. In this configuration, the fusion reactions start to ignite in the hot-spot and heat the surrounding cold region. Then, more fusion reactions occur and more energy is released thus providing the energy needed to heat the surrounded fuel. A burn wave is generated and propagates into the whole fuel. The target configuration is then a cold shell with a high density surrounding the hot-spot with a low density and a high temperature.

2.1.2 Hot spot ignition

In the conventional ICF scheme, the target configuration is isobaric at the stagnation phase. This means that the pressures in the shell and in the hot-spot are equilibrated. We consider a hot-spot of radius R_h with a homogeneous density ρ_h and a temperature T_h enclosed in a shell of a higher density and a lower temperature. Once the fusion reactions are ignited, they can be sustained only if the internal energy of the hot-spot is increasing. This condition of self-heating means that the products of fusion reactions must deposit more energy in the hot-spot per unit of time than the energy is lost by dissipative effects due to radiation and electron conduction. The stopping range of the neutrons is ≈ 4.7 g.cm^{-2}. This is much larger than the typical hot-spot areal density at the ignition time. Thus, the neutrons do not deposit their energy in the hot-spot. However, the alpha particles are less energetics and have a range comparable with the hot-spot areal density (see Section 1.1.2) . The dissipative effects are due to the heat transported by electrons and photons. When an electron is deflected by an ion (due to its charge) it decelerates. The kinetic energy of the electron is converted into a photon. This is called the electronic bremsstrahlung and this is the dominant radiative process as the photons are escaping the hot-spot. Moreover, the temperature difference between the hot and the cold fuel induces heat conduction losses. If the pressures in the cold and hot parts of the compressed target are not equal, one needs to account also for a mechanical work produced by the hot-spot.

Adding all energy production and loss processes, the internal energy E variation with time can be written

$$\frac{\mathrm{d}E}{\mathrm{d}t} = P_\alpha - P_{cond} - P_{brem} - P_{mech}, \tag{2.8}$$

with P_α the power deposited by the alpha particles, P_{mech} the mechanical work, P_{cond} the power

lost by conduction and P_{brem} the power lost by radiation.

For the self-heating to occur, the hot-spot must satisfy the condition $\mathrm{d}E/\mathrm{d}t > 0$ which means

$$P_\alpha > P_{cond} + P_{brem} + P_{mech}. \tag{2.9}$$

The energy deposited by the alpha particles depends on the reactivity $< \sigma\nu >$ of the DT reaction, on the alpha particle energy release in the DT reaction $W_\alpha = 3.5$ MeV and on the density of particles n_i [Atzeni and Meyer-Ter-Vehn, 2004]:

$$P_\alpha = \frac{1}{3}\pi W_\alpha R_h^3 n_i^2 < \sigma\nu > . \tag{2.10}$$

The electronic heat flux at the outer surface of the hot-spot is [Spitzer and Härm, 1953]

$$Q_e = \chi_e \nabla T_h, \tag{2.11}$$

with $\chi_e = K_e T_h^{5/2}/\ln\Lambda$ the *Spitzer–Härm* thermal conductivity, $K_e = 9.5{\times}10^{19}$ erg.s^{-1}.cm^{-1}.keV$^{-7/2}$ and $\ln\Lambda \simeq 6$ the Coulomb logarithm. As the gradient in this simple model is infinite, we use the approximate expression $Q_e = \alpha_e \chi_e \frac{T_h}{R_h}$ with α_e a coefficient close to unity [Atzeni and Meyer-Ter-Vehn, 2004].

The power due to the electronic conduction reads

$$P_{cond} = 4\pi R_d^2 Q_e = 4\pi\alpha_e K_e R_h \frac{T_h^{\frac{7}{2}}}{\ln\Lambda}. \tag{2.12}$$

Let us now look to the radiation losses. As the stopping range of a photon in a typical hot-spot of temperature 4 keV and density 30 g.cm^{-3} is $\rho l_\phi = 60$ g.cm^{-2}, the photons are not stopped in the hot-spot.

The radiation power is [Atzeni and Meyer-Ter-Vehn, 2004]

$$P_{brem} = \frac{4}{3}\pi A_b R_h^3 \rho_h^2 T_h^{\frac{1}{2}} \tag{2.13}$$

with $A_b = 3.05 \times 10^{23}$ erg.s^{-1}.cm^3.g^{-2}.keV$^{-1/2}$.

In the isobaric configuration, the mechanical work at the outer radius of the hot-spot is zero $P_{mech} = 0$.

By substituting the expressions (2.10), (2.12) and (2.13) in the balance equation (2.8) we obtain

$$(\rho_h R_h)^2 > \frac{\frac{3\alpha_e K_e}{\ln\Lambda} T_h^{\frac{7}{2}}}{\frac{W_\alpha}{(2Am_p)^2} < \sigma\nu > - A_b T_h^{\frac{1}{2}}}. \tag{2.14}$$

As the reactivity of deuterium tritium is a function of the temperature (2.2), the ignition criterion (2.14) is a relation between the areal density of the hot-spot $\rho_h R_h$ and the hot-spot

temperature T_h. The ignition threshold is represented in Figure 2.1. The asymptotic horizontal line corresponds to the Post's temperature $T_{Post} = 4.3$ keV where the alpha particles energy deposition is faster than the radiation losses. Indeed, for a high areal density and a low temperature, the losses are mainly due to the radiation.
The point $A = (135\ \text{mg.cm}^{-2}, 6.6\ \text{keV})$ on the threshold curve defines the condition where $E\rho_h^2 \propto (\rho_h R_h)^3 T_h$ is the lowest. By taking a margin of 20%, the hot-spot must reach the areal density $(\rho R)_{ign} = 200\ \text{mg.cm}^{-2}$ and the temperature $T_{ign} = 8$ keV to achieve an ignition of the fusion reactions.

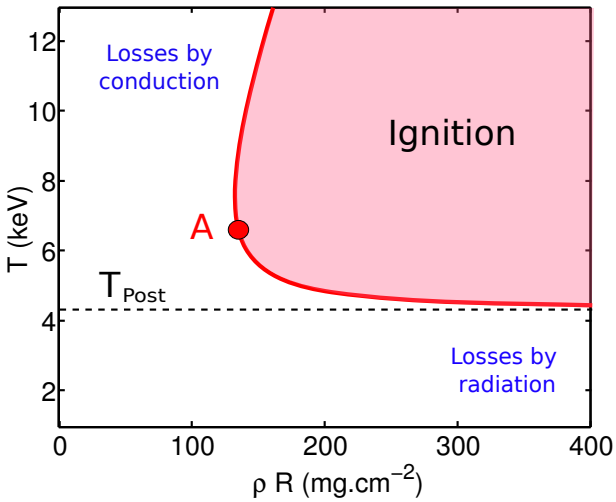

Figure 2.1: Ignition threshold in the isobare configuration at stagnation

We explain in the following parts how those conditions are reached during the implosion.

2.2 Laser driver

We saw in Section 2.1 that the inertial confinement fusion relies on a strong compression of the target and on the heating of a central hot-spot. A driver delivering an energy of the order of MJ in a time of order 10 ns is required. We mention that Z-pinches or heavy-ion accelerators can be considered but here we will only consider a laser driver. The target irradiation could be direct of indirect. In the indirect drive configuration, the laser is absorbed on the inner surface of a cylindrical gold cavity called "Hohlraum" and converted to X-rays which heat the ablator and drive the target implosion. This configuration smoothes the laser beam non-uniformities and thus reduce the hydrodynamic instabilities (see section 2.4). In a direct-drive implosion, the laser irradiates directly the target. The advantage is that the coupling efficiency is higher.

In this thesis, we restrict the discussion to the direct irradiation of the target. We describe in this part the coupling between the laser light and the target. When exposed to the irradiation by a laser light with a high intensity (higher than 10^9 W.cm^{-2}), the matter is ionized and becomes a plasma. The light of wavelength λ travels into the under dense plasma until the

critical density $n_c[\mathrm{cm}^{-3}] = 10^{21}(\lambda_L[\,\mu\mathrm{m}])^{-2}$ is attained, where the laser pulse frequency equals the plasma frequency. In this *absorption zone*, the energy of the laser light is transformed in the thermal energy of plasma electrons. The absorbed energy is transmitted to the matter with a higher density by thermal electronic conduction.

The conduction provides the energy transport to a dense zone where the solid target material is transformed in expanding plasma, which is called the *ablation front*. The pressure at this position p_a is the *ablation pressure*. At the beginning of the irradiation, the ablation front velocity v_{abl} is higher than the sound velocity c. When the laser intensity increases, the sound velocity increases faster than the ablation front velocity. As soon as $v_{abl} = c$ a shock wave is generated. This time moment is called the *hydrodynamic separation*. From this time, the target profile takes a quasi-stationary structure presented in Figure 2.2. In front of the shock wave the matter is at rest. It can be pre-heated by radiation and supra-thermal electrons.

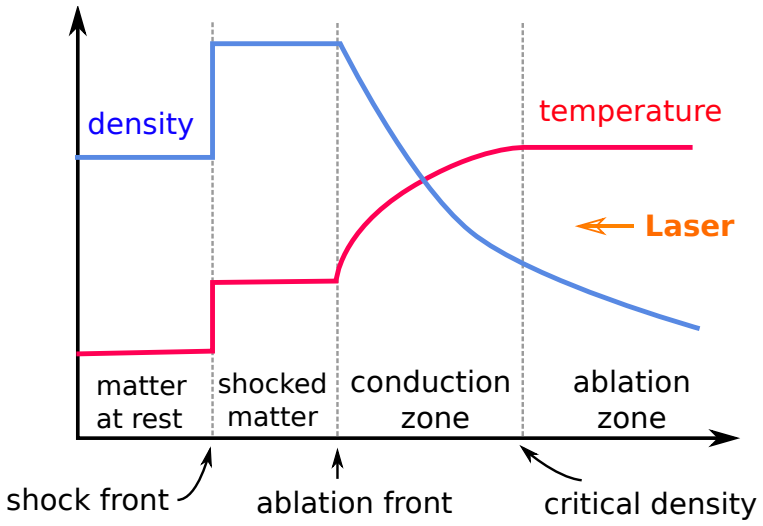

Figure 2.2: Laser energy absorption zone in the direct drive scheme. The energy is absorbed in the ablation zone. It is then transported by electrons in the conduction zone. A shock propagates upstream.

2.2.1 Absorption zone

Inverse Bremsstrahlung absorption At laser irradiance $I_L\lambda_L^2 < 10^{15}$ W.cm^{-2}.μm^2, the main absorption is the inverse bremsstrahlung due to the electron-ion collisions. In the laser electric field, the electrons oscillate and are scattered by the ions. The oscillatory energy is converted into thermal energy through the electron-ion collisions. The local absorption coefficient

depends on the plasma density n_e and temperature T_e [Atzeni and Meyer-Ter-Vehn, 2004]

$$\eta[\mathrm{cm}^{-1}] = \frac{\frac{25 Z_i}{\lambda_L^2 T_e^{\frac{3}{2}}} \left(\frac{n_e}{n_c}\right)^2}{\sqrt{1 - \frac{n_e}{n_c}}}, \tag{2.15}$$

where n_c is the critical density, Z_i the number of free electrons per ion, λ_L the laser wavelength in μm and T_e in keV. The absorption diminishes when the temperature increases and it is maximal at the critical density.

Ray-tracing simulation In the simulation code CHIC the energy deposition is calculated using the ray tracing package (illustrated in Figure 2.3). The laser beam is sampled into several rays which are propagated into the absorption zone according to geometrical optic laws. The global absorption coefficient depends on the rays paths before and after their reflection and on the local absorption coefficient given in (2.15).

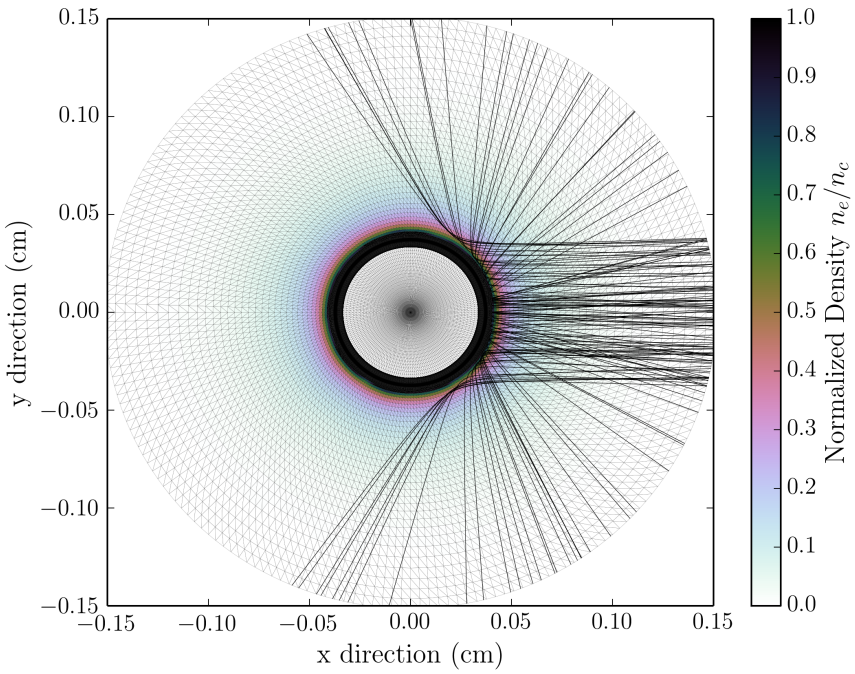

Figure 2.3: Illustration of the ray tracing simulation. The rays of one laser beam coming from the right of the target are represented. Here, this beam is divided into 80 rays which propagate in the underdense matter and are reflected at the critical density.(Personal communication A. Colaitis)

Resonant absorption Another important process is the resonant absorption. When a p-polarized light is incident obliquely in a plasma with a density gradient $\vec{\nabla} n_e$, the electric field $\vec{E}$

Instability	Condition	Coupling density	Effects
Resonance absorption	$w_0 = w_{pe}$	$\sim n_c$	Supra thermal electrons
SBS	$w_0 = w_{scatt} + w_{ai}$	$< n_c$	Reduced absorption efficiency
SRS	$w_0 = w_{scatt} + w_{pe}$	$\leq n_c/4$	Reduced absorption efficiency, supra thermal electrons
TPD	$w_0 = w_{pe} + w_{pe}$	$\sim n_c/4$	Supra thermal electrons

Table 2.1: Characteristics of the main process of light absorption by wave excitation processes

induces a charge separation $q \propto \vec{E}\vec{\nabla n}_e/(1 - n_e/n_c)$ which is maximal near the critical density, where the laser frequency w_0 is close to the plasma frequency w_{pe}. This resonance corresponds to the transfer of a part of laser energy to the plasma wave. If the collision frequency is sufficiently large, the plasma wave transmits its energy to the ions. On the contrary, if the collision frequency is too low, the absorbed energy is transfered to the resonant electrons. This generates supra thermal electrons.

Parametric instabilities At high irradiance $I_L\lambda_L^2 > 10^{15}$ W.cm^{-2}.μm^2, non-linear processes can occur which result in enhanced scattering of laser light and generation of energetic particles in the plasma. The *Stimulated Brillouin Scattering* (SBS) corresponds to the splitting of the incident laser wave into another electromagnetic wave of a smaller frequency and into an ion acoustic wave. It leads to enhanced scattering of the laser pulse. The *Stimulated Raman Scattering* (SRS) corresponds to the coupling of the incident laser light wave with a scattered electromagnetic wave and an electron plasma wave. In addition to enhanced scattering, the SRS could also be a source of energetic electrons. In those two instabilities, the scattered light wave carries energy out of plasma. This could increase the laser irradiation non-uniformity and reduce locally the collisional absorption. In the *Two Plasmon Decay* (TPD) the mother electromagnetic wave decays in two plasma waves with a frequency of about the half of the laser frequency. This process takes place near the quarter critical density. The damping of the electron plasma waves in SRS and TPD transfers the energy from the waves to the particles. This increases the population of electrons with high energy. Table 2.1 summarizes the non-linear processes in the laser plasma interaction and their properties.

2.2.2 Conduction zone

The absorbed energy in the laser matter interaction zone is transported into the target. It is essentially carried by the electrons.

In the conduction zone, the energy is transported by the electron heat flux. It depends on the temperature gradient according to (2.11) $Q_e = -\chi_e \nabla T_e$.

The electron flux maximal value $Q_{\text{lim}} = n_e T_e \nu_{the}$ can be estimated by assuming that all electrons move in the direction opposite to the temperature gradient with their thermal velocity ν_{the}. However, the expression (2.11) for the electron heat flux does not account for this limit.

Moreover, the electron kinetic theory shows that the Spitzer-Harm formula is valid only if the temperature gradient length is about 100 times larger than the electron mean free path. A simple model to account for the limitation of the heat flux in the hydrodynamic code was proposed by Malone et al. [Malone et al., 1975]. An arbitrary flux limiter f is introduced and the flux is calculated as

$$Q = \min(Q_{th}, fQ_{\lim}). \tag{2.16}$$

The numerical value of f is found from the comparison of the numerical simulation results (essentially the absorption coefficient and the shell velocity) with experimental results. Typically f is in the range 3%-10 % and the value $f = 6\%$ is often used.

More advanced methods take into account the non-local effects in the electron flux at the kinetic level. The mean free path of an electron increases with its energy. Therefore, the nonlocal effects are important for the supra-thermal electrons which transport the energy over the distances comparable with the temperature gradient scale length. In the Spizer–Harm thermal conduction model, a weak anisotropy is assumed. The heat flux is computed from the electron distribution function which is written as $f_e(\vec{p}) = f_{e0}(\vec{p}) + \frac{\vec{p}}{p}.f_{e1}(\vec{p})$. In the Spitzer model, the function $f_{e0}(\vec{p})$ is assumed to be a Maxwellian function f_{e0M}. The non-local theories are accounting for the deviation of f_{e0} from the Maxwellian distribution for the supra-thermal electrons. A corrected heat flux is computed by assuming that in the domain of high electron velocities $v >> v_{the}$ the distribution function can be presented as $f_{e0}(\vec{p}) = f_{e0M}(\vec{p}) + \Delta f_0$. The correction function Δf_0 is calculated by splitting the kinetic Fokker-Planck equation into several energy groups. For more details about the non-local model implemented in the code CHIC one can refers to Ref. [Schurtz et al., 2000].

2.2.3 Ablation pressure

The matter behind the ablation front expands in the outer region of the target. It is called the *ablated* matter. The ablation pressure can be calculated from the conservation of momentum and energy. Assuming that the conduction zone is stationary and that the absorption zone is isothermal, the ablated mass rate $\dot{m}_a$ and the ablation pressure can be expressed with the following scaling laws [Dautray and Watteau, 1993]:

$$p_a[\text{Mbar}] = 11.8 \left(I_{abs}[10^{14}\ \text{W.cm}^{-2}]\right)^{\frac{2}{3}} (\lambda_L[\,\mu\text{m}])^{-\frac{2}{3}} \left(\frac{A}{2\text{Z}}\right)^{\frac{1}{3}} \tag{2.17}$$

$$\dot{m}_a[\text{g.s}^{-1}.\text{cm}^{-2}] = 1.38 \times 10^5 \left(I_{abs}[10^{14}\ \text{W.cm}^{-2}]\right)^{\frac{1}{3}} (\lambda_L[\,\mu\text{m}])^{-\frac{4}{3}} \left(\frac{A}{2\text{Z}}\right)^{\frac{2}{3}} \tag{2.18}$$

We can notice that the coupling of the laser light to the target is more efficient for a shorter wave length.

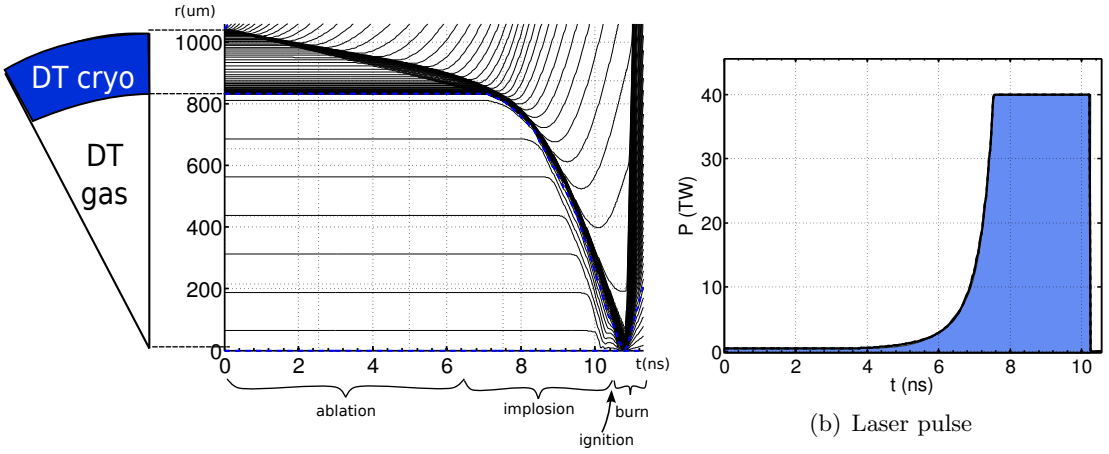

(a) Meshflow

(b) Laser pulse

Figure 2.4: Grid flow (a) and laser pulse profile (b) in the simulation of a typical ICF implosion.

2.3 Implosion and laser pulse shape

Let us consider first the conventional ICF scheme where a spherical hollow shell target is irradiated uniformly by a laser light. The implosion evolves in four steps: 1) During the ablation phase the laser light is absorbed in the outer layer of the shell. The heating and ablation of the target material generates an ablation pressure at the outer surface of the shell. 2) The work made by this pressure is transformed into the shell kinetic energy which is further converted into internal energy during the implosion. A hot-spot at the center of the target is created. 3) The ignition conditions are attained in the hot-spot. 4) A self-sustaining burn wave propagates outward and consumes the rest of the fuel.

Figure 2.4 (a) presents the grid evolution in a typical implosion simulation. As the CHIC code is Lagrangian, the grid follows the flow. The four steps of the implosion are indicated on the figure. Figure 2.4 (b) shows the laser pulse used in this simulation. The choice of its shape will be justified in the following sections.

The implosion phase consists in an acceleration phase and a deceleration phase. The sketch of the conventional implosion is presented in Figure 2.5.

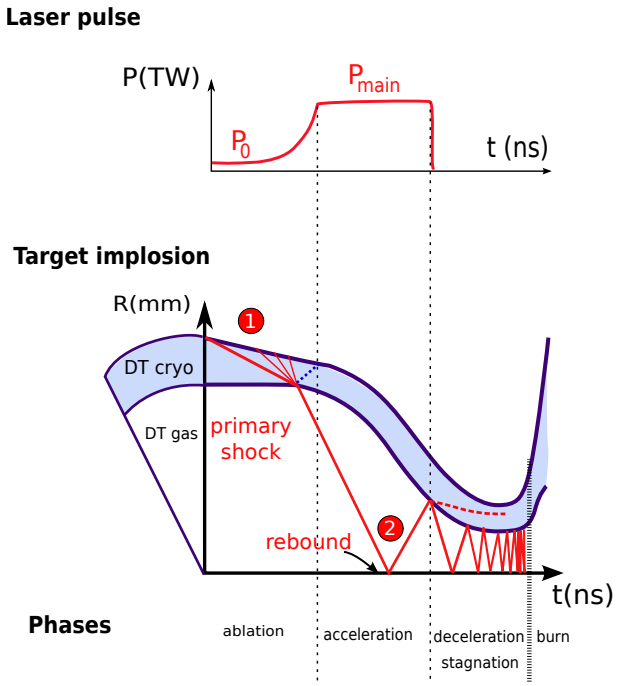

Figure 2.5: Implosion sketch of the conventional ICF scheme.

2.3.1 Ablation phase

According to the thermodynamics laws, the specific energy transmitted to the target $\mathrm{d}e$ is related to the heat transfer $T\,\mathrm{d}s$ and to the work $p\,\mathrm{d}v$ by the relation $\mathrm{d}e = T\,\mathrm{d}s - p\,\mathrm{d}v$ with s being the specific entropy, T being the temperature and v – the specific volume $v = 1/\rho$. To optimize the compression with a given energy, the specific entropy increase $\mathrm{d}s$ must be as low as possible.

The specific entropy of the shell is measured with the *adiabat* parameter $\alpha = p/p_F$ where p_F is the reference pressure of a Fermi-degenerate cold electron gas $p_F\,[\mathrm{Mbar}] = 2.15\rho^{5/3}$ for a fully ionized DT, and with ρ expressed in $\mathrm{g.cm^{-3}}$. The dimensionless adiabat parameter is therefore

$$\alpha = \frac{p}{2.15\rho^{5/3}}, \tag{2.19}$$

with the pressure p in Mbar and the DT fuel density ρ in $\mathrm{g.cm^{-3}}$.

The adiabat must be minimized to optimize the target compression. This criterion justifies the use of a cryogenic shell target. Indeed, the density must be sufficiently high to reduce the adiabat of the shell. Thus the solid density of the DT is chosen and the initial temperature of the shell must be below the hydrogen triple point $T = 19.7$ K.

An optimal compression of the shell would be an isentropic compression. As it will be explained in Section 3.2, the ablation pressure in this case increases progressively following the power low $p_a \propto \rho^{5/3}$. The compression time depends inversely on the sound velocity. As the initial temperature is low, this time is far too long. Thus the shell must be preheated in order to shorten the implosion time. For that the laser pulse starts by a pre-pulse of a power P_0. The

ablation pressure p_{a0} created by this pre-pulse launches a shock wave through the shell with a strength chosen to deposit an entropy at the level $\alpha < 3$. The matter behind the shock is compressed by a factor of about 4.

The power increases in a transition phase in such a manner that the compression is isentropic. Compression waves are generated. They must not merge into a shock as long as they are propagating through the shell in order to limit the entropy increase. The proper timing of the compression waves requires a special laser intensity profile known as the Kidder law [Kidder, 1976]. However, the laser pulse power cannot increase indefinitely because of the laser energy available and of parametric instabilities which appear at a high intensity. Thus, the power increases until a maximum value P_m and stays at this value during the *main pulse*. When the primary shock reaches the shell inner surface, a rarefaction wave is reflected in the shell and a shock wave is transmitted in the gas (see bullet 1 in Figure 2.5).We define t_{sb}, the time moment of the shock breakout at the inner surface of the shell. The compression waves, still propagating in the shell, interacts with the flow behind the rarefaction wave. Due to the density and pressure gradients in this flow, the compression waves turn faster in shock waves. Thus, to avoid any entropy deposition in the shell, the compression waves must reach the inner face of the shell just after the primary shock. When the rarefaction wave reaches the ablation front, the fast decrease in density induces a local increase in pressure. A second shock wave is reflected back into the shell. From this time the shell is accelerated and the *acceleration phase begins*. To reduce the strength of this second shock (the entropy in the shell must still be kept low), the laser power is kept constant at the level P_m after this second shock is generated. The ablation pressure is then p_{am}.

Let us introduce the *shell aspect ratio* $\mathcal{A} = R/\Delta R$ where R is the inner radius of the shell and ΔR is its thickness. During the ablation phase the shell is compressed and the shell thickness ΔR is reduced. The shell aspect ratio is thus increasing during the ablation phase. It reaches a maximal value at the time t_{sb}.

Figure 2.6 shows the pressure gradient in the shell during the ablation phase of the reference simulation. The compression and rarefaction waves trajectories are well visible.

In conclusion, during the ablation phase, a shock is launched by the foot of the laser pulse. This shock sets the shell adiabat as

$$\alpha = \frac{p_{a0}}{(4\rho_0)^{5/3}}. \tag{2.20}$$

Then the compression of the shell is isentropic and the density evolves as $\rho \propto p_a^{3/5}$. At the shock break-out time t_{sb}, the shell density is thus

$$\rho_{sb} = 4\rho_0 \left(\frac{p_{am}}{p_{a0}}\right)^{3/5}. \tag{2.21}$$

The shell aspect ratio increases during the ablation phase. At the time t_{sb}, it reaches its maximal

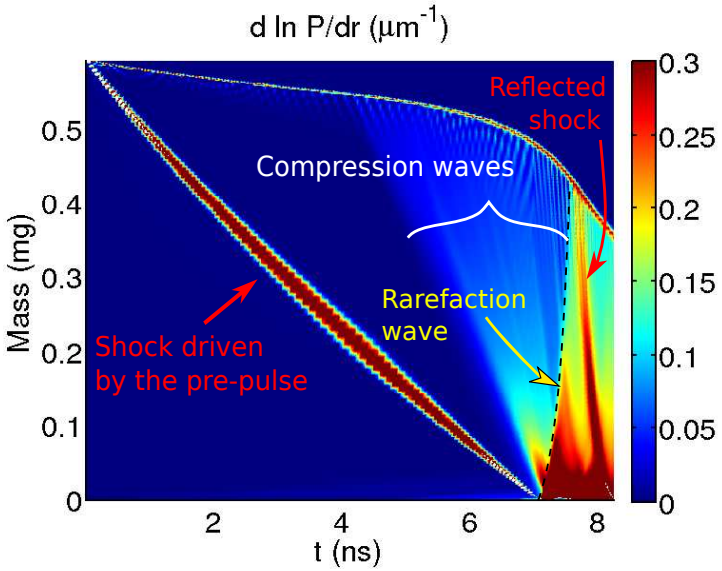

Figure 2.6: Pressure gradient in the shell during the ablation phase.

value called the *In-Flight-Aspect-Ratio* $IFAR$.

A simple estimate of the IFAR is

$$IFAR = \frac{\rho_{sb}}{\rho_0}\mathcal{A}_0, \tag{2.22}$$

where $\mathcal{A}_0$ is the initial aspect ratio of the shell.

2.3.2 Acceleration phase

The generation of compression waves at the outer part of the shell and the reflection of rarefaction waves at the inner face of the shell is repeated several times. For each shock generation at the outer edge, the shell velocity is increased. If the shell is sufficiently thin, the acceleration can be seen as a continuous process. First we express the hydrodynamic efficiency for the ablation process to accelerate the shell by using a rocket model. We will see that it depends on the shell mass variation. Then we evaluate the shell thickness and mass evolution during the acceleration. This allows to express the hydrodynamic efficiency as a function of the implosion parameters.

Rocket model The shell acceleration can be described by the rocket model. We considerer that the shell is a rigid body with a variable mass due to the ablation. Let $\mathrm{M}(t)$ be the shell mass and $U(t) = \mathrm{d}R/\,\mathrm{d}t$ its velocity. The conservation of the momentum gives

$$\frac{\mathrm{dM}(t)U(t)}{\mathrm{d}t} = 4\pi R^2(t)\dot{m}_a(u - U), \tag{2.23}$$

where u is the velocity of the ejected matter due to ablation assumed to be constant, $\dot{m}_a$ is the ablation rate and R the position of the ablation front.

The change in mass is

$$\frac{\mathrm{dM}(t)}{\mathrm{d}t} = -4\pi R^2 \dot{m}_a. \tag{2.24}$$

By combining (2.23) and (2.24)

$$\mathrm{d}U = -u\frac{\mathrm{dM}}{\mathrm{M}} \tag{2.25}$$

which leads to

$$U(t) = u \ln\left(\frac{\mathrm{M}(t)}{\mathrm{M}(0)}\right) = u \ln\left(1 - \frac{\mathrm{M}_a(t)}{\mathrm{M}_0}\right), \tag{2.26}$$

with M_0 the initial mass and $\mathrm{M}_a(t) = \mathrm{M}_0 - \mathrm{M}(t)$ the ablated mass.

From the Newton's law, the ablation pressure at the outer edge of the shell is $p_{am} = \mathrm{M}\dot{U}/4\pi R^2$. Using (2.25) and (2.24), the pressure due to the rocket effect is

$$p_{am} = u\dot{m}_a. \tag{2.27}$$

The kinetic energy of the shell writes

$$E_k = \frac{1}{2}\mathrm{M}U^2 = \frac{1}{2}\left(\mathrm{M}_0 - \mathrm{M}_a\right)u^2\left[\ln\left(1 - \frac{\mathrm{M}_a}{\mathrm{M}_0}\right)\right]^2. \tag{2.28}$$

The exhaust energy is $E_{ex} = \mathrm{M}_a u^2/2$. Thus the hydrodynamic efficiency $\eta = E_k/E_{ex}$ is [Atzeni and Meyer-Ter-Vehn, 2004]

$$\eta_{(\mathrm{ideal})} = \frac{(1-X)\left[\ln(1-X)\right]^2}{X} \tag{2.29}$$

with $X = \mathrm{M}_a/\mathrm{M}_0 = \left(1 - \frac{\mathrm{M}}{\mathrm{M}_0}\right)$. The plot of the function (2.29) is shown in Figure 2.7. We notice that η cannot exceed 60 %. In typical ICF implosion, the ratio $\frac{\mathrm{M}_a}{\mathrm{M}_0}$ does not exceed 50-60 %. In this regime we can approximate η with $\eta \simeq \left(\frac{\mathrm{M}_a}{\mathrm{M}_0}\right)$.

In this simplified discussion, the flux of the enthalpy and the energy flux needed to maintain a constant temperature in the corona are neglected. Numerical simulations [Rosen, 1999] including more detailed physics show that the overall hydrodynamic efficiency is approximately one third of the expression (2.29) $\eta = \eta_{(\mathrm{ideal})}/3$.
Here we see that the acceleration of a shell by ablation is a low efficiency process. In the direct drive the maximal efficiency is of about 20 %.

Shell aspect ratio and implosion velocity We will now express the relation between the shell aspect ratio, the ablated mass and the implosion velocity. We assume that the shell thickness is small.
The rate of mass ablation in the left hand side of (2.24) can be presented as $\mathrm{d}M/\mathrm{d}t = U\,\mathrm{d}M/\mathrm{d}R$.

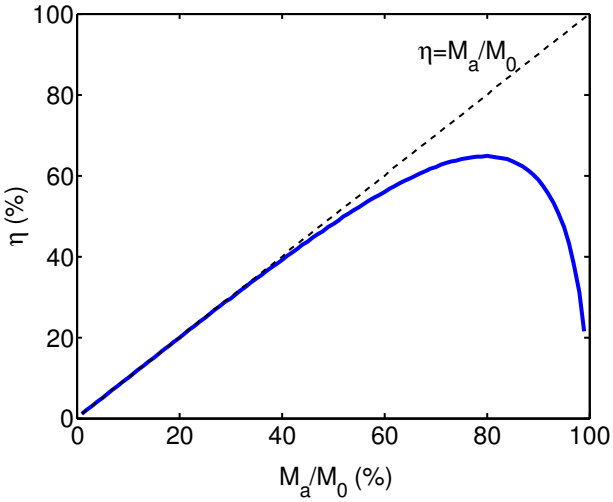

Figure 2.7: Hydrodynamic efficiency depending on the ratio of ablated mass.

Then we find

$$\int_{\mathrm{M}_0}^{\mathrm{M}} U \,\mathrm{dM} = -\int_{R_0}^{R} 4\pi \dot{m}_a R^2 \,\mathrm{d}R. \tag{2.30}$$

At the same time, by integrating the expression for the shell velocity (2.26) over the mass we have

$$\int_{\mathrm{M}_0}^{\mathrm{M}} U \,\mathrm{dM} = u \int_{\mathrm{M}_0}^{\mathrm{M}} \ln\left(\frac{\mathrm{M}}{\mathrm{M}_0}\right) \mathrm{dM} = u\mathrm{M}_0 \left[1 - \frac{\mathrm{M}}{\mathrm{M}_0}\left(1 - \ln\left(\frac{\mathrm{M}}{\mathrm{M}_0}\right)\right)\right]. \tag{2.31}$$

The initial mass of the shell is $M_0 = 4\pi\rho_0 R_0^2 \Delta R_0$. Then Equation (2.30) becomes

$$1 - \frac{\mathrm{M}}{\mathrm{M}_0}\left(1 - \ln\left(\frac{\mathrm{M}}{\mathrm{M}_0}\right)\right) = \frac{\varepsilon}{3}\left[1 - \left(\frac{R}{R_0}\right)^3\right], \tag{2.32}$$

where

$$\varepsilon = \frac{\dot{m}_a}{u\rho_0}\frac{R_0}{\Delta R_0}, \tag{2.33}$$

is the implosion parameter [Atzeni and Meyer-Ter-Vehn, 2004].
The dependence of the ablated mass on the shell radius can be seen in Figure 2.8 (a). The ablated mass increases during the shell convergence and reaches its maximal value for $R = 0$. The dependence of the ablated mass at $R = 0$ on the shell parameter ε is presented in 2.8 (b). The range of practically interesting values is $\varepsilon < 3$. Otherwise, the shell is entirely vaporized before the collapse. For $\varepsilon < 3$ one can approximate the maximal ablated mass for $R \ll R_0$ by

$$\max\left(\frac{\mathrm{M}_a}{\mathrm{M}_0}\right) \simeq \left(\frac{\varepsilon}{3}\right)^{1/3}. \tag{2.34}$$

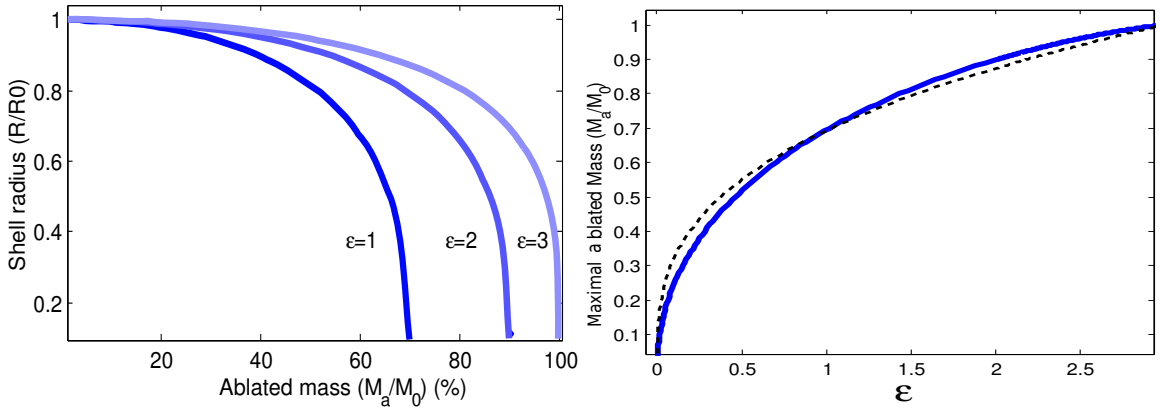

(a) (b)

Figure 2.8: Evolution of the ablated mass $\mathrm{M}_a/\mathrm{M}_0 = 1 - \mathrm{M}/\mathrm{M}_0$ during the shell convergence (panel a) and dependence of the maximal ablated mass on the implosion parameter ε (panel b). The approximate relation (2.34) is represented with a dashed line in panel (b).

Let us now find a relation between the shell velocity at the end of ablation phase $\mathrm{u}_{\mathrm{imp}} = -U$ and the aspect ratio $IFAR = R/\Delta R$. The ablation rate depends on the ablation pressure and the exhaust velocity (2.27) as $\dot{m}_a = p_a/u$. Therefore, using (2.22), the implosion parameter is proportional to IFAR:

$$\varepsilon = \frac{p_a}{\rho_{sb} u^2} IFAR. \tag{2.35}$$

At the end of the acceleration phase, the shell radius is small compared to the initial radius $(R/R_0)^3 << 1$, the shell velocity is $U = -\mathrm{u}_{\mathrm{imp}}$ and , according to (2.26), the remaining shell mass is related to its velocity as $\mathrm{M}/\mathrm{M}_0 = \exp(-\mathrm{u}_{\mathrm{imp}}/u)$. Then (2.32) reads

$$f\left(\frac{\mathrm{u}_{\mathrm{imp}}}{u}\right) = \frac{\varepsilon}{3}, \tag{2.36}$$

where the function $f(x) = 1 - \exp(-x)(1 + x)$ is represented in Figure 2.9.

In the domain of practical interest, for $x \leq 1$, the function f can be approximated by $f(x) \simeq 0.3x^2$. An implosion velocity lower than the exhaust velocity applies to direct drive for typical laser intensities of $10^{14} - 10^{16}$ W.cm^{-2} [Lindl, 1995]. Then, the IFAR can be expressed as a function of the implosion velocity:

$$IFAR = 0.9 \left(\frac{\mathrm{u}_{\mathrm{imp}}^2}{p_a/\rho_{sb}}\right). \tag{2.37}$$

The sound velocity at the outer edge of the compressed shell assuming the polytropic index $\gamma = 5/3$ is $c_{if}^2 \simeq 5p_{am}/3\rho_{sb}$. Then the dependence of IFAR on the shell maximal Mach number

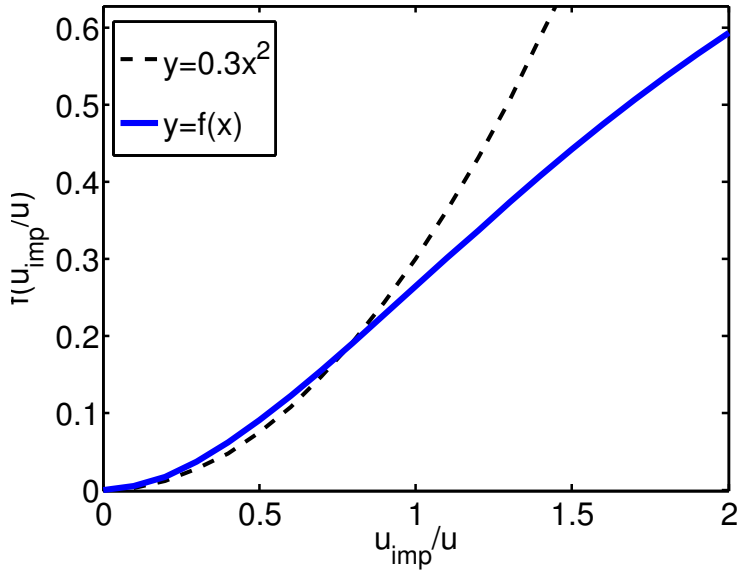

Figure 2.9: Function $f(x) = 1 - \exp(-x)(1 + x)$ and the approximate $y = 0.3x^2$.

$\mathcal{M}_0 = \mathrm{u_{imp}}/c_{if}$ can be expressed as:

$$IFAR \simeq 1.5\mathcal{M}_0^2. \tag{2.38}$$

The in-flight adiabat is $\alpha_{if} = p_{am}/\rho_{sb}^{5/3}$. Using the expression of the ablation pressure (2.17) the implosion velocity is expressed as

$$\mathrm{u_{imp}} \propto \alpha_{if}^{3/10} IFAR^{1/2} \left(\frac{I_{abs}}{\lambda_L}\right)^{2/15}. \tag{2.39}$$

The implosion velocity can be increased by increasing the IFAR and the shell adiabat. However, increasing the adiabat would reduce the target compressibility and increasing the IFAR may reduce the implosion efficiency due to hydrodynamic instabilities (see Section 2.4 below).
The mass of the shell depends on the shell aspect ratio as

$$\mathrm{M} = 4\pi\rho R^3/\mathcal{A}. \tag{2.40}$$

Therefore, the shell aspect ratio evolves in time as

$$\frac{\mathcal{A}}{IFAR} = \left(\frac{\rho_{sb}}{\rho}\right)\left(\frac{R}{R_0}\right)^3\left(\frac{\mathrm{M_0}}{\mathrm{M}}\right). \tag{2.41}$$

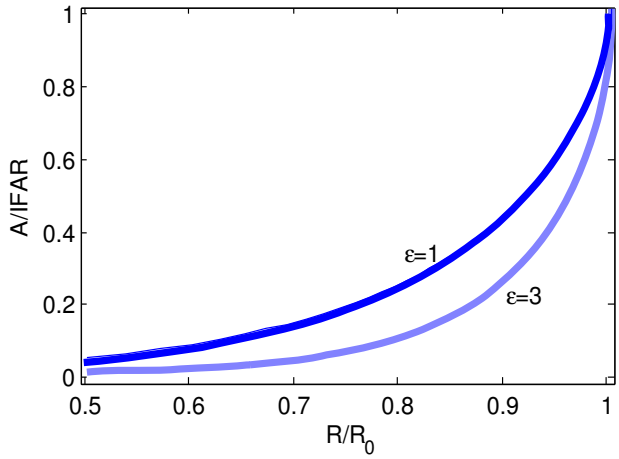

Figure 2.10: Evolution of the shell aspect ratio $\mathcal{A}/IFAR$ as a function of the shell radius R/R_0 for several values of the implosion parameter ε.

If the acceleration is nearly isentropic, the shell density $\rho \propto \alpha_{if}^{-3/5} p_{am}^{3/5}$ does not vary much and $\rho_{sb}/\rho \sim 1$. Then by inserting (2.41) into (2.32) we obtain a relation between the shell aspect ratio and the shell radius. The shell aspect ratio decreases during the target acceleration as it can be seen in Figure 2.10.

Hydrodynamic efficiency According to relations (2.34), (2.35) and (2.38), the ablated mass scales as

$$\frac{\mathrm{M}_a}{\mathrm{M}_0} \propto \mathrm{u}_{\mathrm{imp}}^{2/3} \dot{m}_a^{2/3} {p_a}^{-2/3} \tag{2.42}$$

Expressing the mass ablation rate and the ablation pressure through the laser intensity according to (2.17) and (2.18), the hydrodynamic efficiency $\eta \simeq \left(\frac{\mathrm{M}_a}{\mathrm{M}_0}\right)$ scales as

$$\eta \propto \mathrm{u}_{\mathrm{imp}}^{2/3} {I_{abs}}^{-2/9} {\lambda_L}^{-4/9} \left(\frac{\mathrm{A}}{2\mathrm{Z}}\right)^{2/9}. \tag{2.43}$$

For a given laser irradiation, the implosion velocity increases for a higher hydrodynamic efficiency. The most influencing parameter here is the laser wavelength. The hydrodynamic efficiency is reduced for higher laser wavelength.

2.3.3 Deceleration and stagnation phases

The primary shock generated by the pre-pulse is partially transmitted to the fuel gas at the end of the ablation phase. During the acceleration phase, this shock converges in the gas, rebounds at the center of the target and diverges. When the shock interacts with the incoming shell inner face

it is reflected back toward the center and the shell is in turn impulsively decelerated. This time moment t_d is the beginning of the deceleration phase. The shock rebounds again at the center and is reflected a second time from the shell. This process is repeated several times leading to an impulsive deceleration of the shell. At each reflection the shock becomes weaker. After several reflections the central gas pressure becomes uniform and the shell is decelerated continuously. The shell acts then like a piston on the hot-spot until its velocity comes to zero which is the stagnation point. During this deceleration phase the pressure, density and temperature of the hot-spot increase. The implosion is to be designed in such a way that the hot-spot reaches the ignition conditions at the stagnation time.

Let us write R_d, the radius of the hot-spot at the end of the acceleration phase t_d and $V_d = 4\pi R_d^3/3$ being its volume. The shell velocity $U = \mathrm{d}R/\,\mathrm{d}t$ is at its maximum value $\mathrm{u_{imp}}$ at that moment. When the shell stops, the final radius of the hot-spot is R_h. We define $C_d = R_d/R_h$ to be the convergence ratio during the deceleration phase. Assuming an adiabatic compression of the gas inside the piston, the pressure is linked to the density by the relation $p \propto \rho^{5/3}$ for an ideal gas. The mass conservation in the hot-spot gives $\rho \propto R^{-3}$. Therefore we have

$$p = p_d \left(\frac{R_d}{R}\right)^5. \tag{2.44}$$

Then the pressure and density at the stagnation time can be expressed as $p_h = p_d C_d^5$ and $\rho_h = \rho_d C_d^3$.

During the deceleration, the shell trajectory can be integrated from the Newton's law

$$\mathrm{M}\frac{\mathrm{d}U}{\mathrm{d}t} = 4\pi p R^2. \tag{2.45}$$

Using the relation (2.44), the shell velocity is expressed as a function of its radius

$$U^2 = \mathrm{u_{imp}^2} + \frac{4\pi p_d R_d^3}{\mathrm{M}}\left(1 - \left(\frac{R_d}{R}\right)^2\right). \tag{2.46}$$

At the stagnation time, the shell velocity $U = 0$ and the shell radius $R = R_h$. Then the convergence ratio can be expressed as

$$C_d = \sqrt{1 + \frac{E_k}{E_i}}, \tag{2.47}$$

with $E_k = \frac{1}{2}\mathrm{Mu_{imp}^2}$ the kinetic energy of the shell and $E_i = \frac{3}{2}p_d V_d$ the internal energy of the hot-spot at the end of the acceleration phase.

At the beginning of the deceleration phase, the internal energy of the hot-spot is negligible compared to the kinetic energy of the shell [LLE, 2006].

Then we can write $C_d \approx \sqrt{E_k/E_i} \propto \mathrm{u_{imp}}$. The maximal hot-spot pressure at the stagnation

is

$$p_h = p_d C_d^5 = p_d^{-3/2} \mathrm{M}^{5/2} V_d^{-5/2} \mathrm{u}_{\mathrm{imp}}^5. \tag{2.48}$$

To reach a high pressure in the hot-spot, the volume of the hot-spot and its pressure at the beginning of the deceleration phase must be low.

The temperature for an ideal monoatomic gas is proportional to the square of the sound velocity $T \propto c^2$ and $c^2 = 5p/3\rho$. Thus the hot-spot temperature scales as

$$T_h \propto \mathrm{u}_{\mathrm{imp}}^2. \tag{2.49}$$

The final pressure (2.48) and temperature (2.49) in the hot-spot are highly dependent on the implosion velocity. Here we used a rough estimate of the hot-spot pressure at the stagnation time, assuming that the shell acts on the hot-spot as a rigid piston with a given mass. In reality the electron heat conduction leads to the ablation of the shell inner part. The mass of the shell decreases as the mass in the hot-spot increases. Therefore, the hot-spot at the stagnation is denser but cooler. The pressure $p \propto T\rho$ is less sensitive to this phenomenon.

If the hot-spot pressure is high enough, the ignition occurs and the hot-spot generates a burning wave propagating in the shell.

Figure 2.11 presents a zoom of the reference simulation grid flow during the deceleration phase, ignition and burn. From the time 10.6 ns, the temperature in the hot-spot is higher than 4 keV. The hot-spot is close to the ignition conditions. The ignition starts at 10.75 ns. A burn wave is generated at 10.8 ns. It propagates in the shell in few ps.

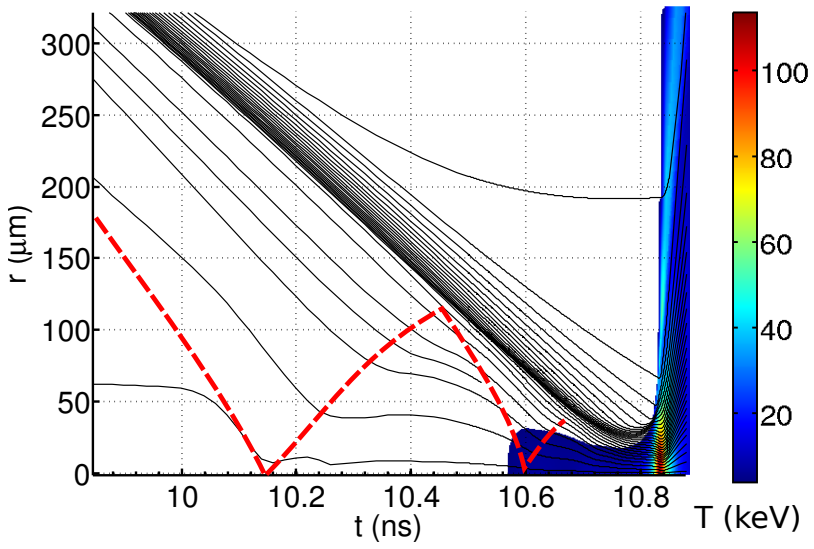

Figure 2.11: Grid flow during the deceleration phase, ignition and burn of the fuel. The dashed red line represents the trajectory of the first shock wave. The temperature is plotted when its value exceeds 4 keV.

2.4 Hydrodynamic instabilities

To reach the ignition criterion the target must be strongly compressed and the final hot-spot radius R_h is typically $20-30$ times smaller than its initial radius R_0. To conserve a spherical shape of the hot-spot the non-uniformities must be controlled. There are two kind of non-uniformities: the initial roughness of the shell and the laser irradiation non-uniformity. Even if these non-uniformities are very low, hydrodynamic instabilities during the implosion may amplify the small perturbations. This leads to dramatically asymmetric implosions with a low efficiency. Thus the non-uniformities must be controlled and the hydrodynamic instability growth mitigated.

2.4.1 Rayleigh–Taylor instability

The interface between two fluids of different densities ($\rho_2 > \rho_1$) is unstable when it is accelerated from the light fluid toward the heavy fluid. This is called the *Rayleigh–Taylor* instability. A small perturbation $h(t)$ of the interface growths exponentially with time $h(t) = h_0 \exp(\gamma t)$. The growth rate γ depends on the perturbation wave number k and is usually expressed as

$$\gamma = \sqrt{A_t k g} \tag{2.50}$$

where g is the acceleration, and $A_t = (\rho_2 - \rho_1)/(\rho_2 + \rho_1)$ is the Atwood number [Atzeni and Meyer-Ter-Vehn, 2004]. Here we see that small wavelength perturbations are most amplified.

In the ICF context, the density profile is continuous and the density gradient length $L_\rho = \rho/(\mathrm{d}\rho/\,\mathrm{d}r)$ is finite at the boundary between the two fluids. The perturbations growth is reduced for wavelengths λ smaller than L_ρ. The ablation is another phenomenon which reduces the growth rate of short wavelength perturbations. Indeed, the ablation of the heavy fluid at the interface smoothes the non-uniformities. Taking those phenomena into account, Takabe et al. [Takabe et al., 1985] proposed an empirical expression for the growth rate of the ablative Rayleigh-Taylor instability:

$$\gamma = 0.9\sqrt{kg} - \beta k v_{abl} \tag{2.51}$$

where $v_{abl} = \dot{m}_a/\rho$ is the ablation velocity and β, a numerical constant of the order of 1 which depends on the target material.

The instability evolution is qualified as linear when the perturbation amplitude is growing exponentially and is much smaller than the perturbation wavelength. When the perturbation amplitude becomes comparable to the perturbation wavelength, the perturbation profile becomes asymmetric: spikes and bubbles appear at the interface. The amplitude of the spikes and bubbles grows as a quadratic function of time $h(t) \propto t^2$. In that non-linear regime, the velocity difference at the interface between the spikes and the surrounding fluid induces the Kelvin-Helmholtz instability. Its development leads to the creation of "mushrooms". Multiple scales appear and finally the flow becomes turbulent.

During the implosion, the Rayleigh–Taylor instability occurs during the acceleration phase at the outer surface of the shell where the ablated mass is accelerated toward the dense shell, and during the deceleration phase at the inner surface of the shell where the pressure from the low density hot-spot is decelerating the shell. During the deceleration phase, the spike of dense cold matter penetrate into the hot-spot. They are reducing the effective volume of the hot-spot and compromise the ignition. Moreover, the distortion of the shell inner surface increases the surface area between the hot-spot and the cold shell and thus enhances the heat losses by heat conduction and the mass increase by ablation.

2.4.2 Kelvin–Helmholtz instability

The *Kelvin–Helmholtz* instability appears at the interface between two fluids in transversal relative motion. Initially this instability grows exponentially in time $h(t) = h_0 \exp(\gamma t)$. The growth rate γ depends on the relative velocity ν

$$\gamma = k|\nu| \tag{2.52}$$

where the wave number k corresponds to a perturbation parallel to the interface. When the perturbation amplitude becomes comparable with the wavelength, the interface rolls up pushed by the fluid flow. This occurs at different scales and leads to a mix between the two fluids.

2.4.3 Richtmyer–Meshkov instability

The passage of a shock through a perturbed interface amplifies the perturbation. This instability is known as the *Richtmyer–Meshkov* instability. The perturbation amplitude growths linearly in time $h(t) = h_0(1 + \gamma t)$. The growth rate γ depends on the interface velocity change Δu as the shock passes through

$$\gamma = A_t k \Delta u. \tag{2.53}$$

Even if the growth of the RM instability is slower than the growth of the RT instability, it can be dangerous for ICF. Indeed, it amplifies the initial perturbations of the shell surface before the shell is accelerated and the RT instability sets in.

2.4.4 Most dangerous mode

According to (2.51), the growth of RT instability can be reduced by increasing the ablation velocity. This however, requires a higher adiabat. It is possible to use a series of well timed shocks in such a way that only the adiabat at the outer part of the shell is increased. In this case, the ablation velocity is higher whereas the shell adiabat is kept low for the effective compression. This is called *the adiabat shaping* method [Anderson and Betti, 2004]. Another method uses a double ablation fronts scheme (thermal and radiative ablation fronts) with a higher Z ablator [Fujioka et al., 2004, Yañez et al., 2011]. The use of low density foams [Depierreux et al., 2009] at the

outer shell surface is also considered for mitigation of the RT instability.

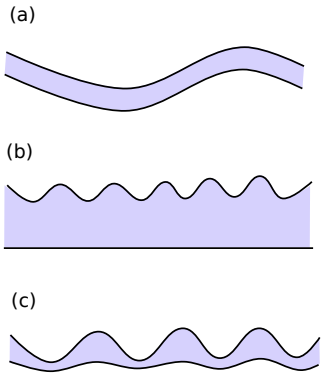

Figure 2.12: Shell perturbations scenarios: (a) $k\Delta R \ll 1$, (b) $k\Delta R \gg 1$, (c) $k\Delta R \sim 1$.

The RT instability can reduce the efficiency of the compression and of the ignition by reducing the symmetry and the effective hot-spot volume. However, the most critical scenario would be that the shell breaks during the implosion. The mode with a wavelength comparable to the shell thickness $k\Delta R \sim 1$ is the most dangerous. Indeed, the amplitude of the shell decays in space as $h(x) = h(0)e^{-kx}$. If $k\Delta R \ll 1$, the distortion of the rear side of the target follows the perturbation of the front side (panel (a) in figure 2.12). If $k\Delta R \gg 1$, the perturbations do not reach the rear side of the shell (panel (b) in figure 2.12). If $k\Delta R \sim 1$, the distortion at the rear side of the shell is low and the perturbation at the front side has an amplitude of the size of the shell. In this case, the shell can be broken easily (panel (c) in figure 2.12).

We remind that the maximal value of the aspect ratio, the IFAR, is achieved as the first shock breaks out the shell at the time t_{sb}. In the spherical geometry the mode number l is defined as $l = kR = k\Delta R\,\mathrm{IFAR}$. The most dangerous mode occurs for $k\Delta R = 1$ thus for $l = \mathrm{IFAR}$.

2.5 Separating compression and ignition

In the conventional scheme the compression and the heating of the hot-spot are achieved in the same time. It requires a large driver energy and a high implosion velocity. The idea of alternative schemes, is to separate the compression and the ignition phases [Tabak et al., 2014, Atzeni, 2013]. First, the target is isentropically compressed at a low implosion velocity in the same way as in the conventional scheme. The hot-spot is then created by a supplementary source of energy. In the fast ignition scheme, the hot-spot is created with a beam of relativistic electrons or high energy ions [Tabak et al., 1994]. In the shock ignition scheme [Betti et al., 2007], the hot-spot is created at the center of the target by a converging shock wave.

In those schemes, the final configuration is not isobaric. The pressure in the hot-spot is higher than the pressure in shell. Figure 2.13 presents schematically the thermodynamic path of the hot-spot and of the DT shell during the implosion in the conventional scheme (a) and in the shock ignition scheme (b).

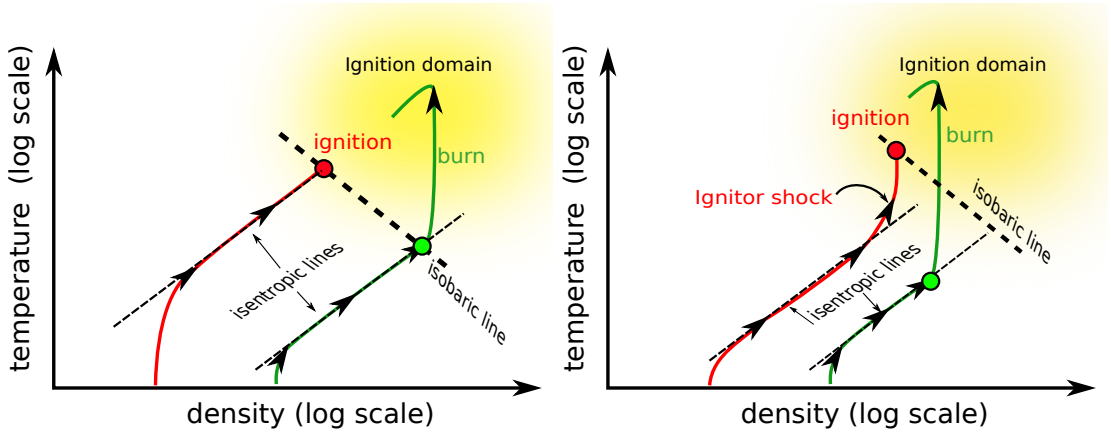

(a) Conventional scheme (b) Shock ignition scheme

Figure 2.13: Trajectories in the (ρ, T) plane of an element in the hot-spot (red line) and of an element in the shell (green line). The moment of ignition is indicated with circles. The dashed lines indicate isentropic and isobaric lines.

2.5.1 Discussion on the implosion velocity

The implosion velocity is an important parameter of the implosion. We analyze here how the implosion velocity is related to the ignition criterion, its influence on the gain of the target and on the RT instabilities. This allows us to explain the interest of the alternative schemes of ignition where the implosion velocity is lower than in the conventional ignition scheme.

Path to ignition During the implosion, the increase of internal energy in the hot-spot is dominated by the mechanical work whereas the fusion reactions are negligible. The mechanical power must be taken into account in the balance equation (2.8) [Lindl, 1995]. The shell is considered as a piston of velocity $\mathrm{u_{imp}} = \mathrm{d}R/\,\mathrm{d}t$ acting on a gas with the pressure p_h. The work done is $P_{mech} = -p_h\,\mathrm{d}V_h/\,\mathrm{d}t$ where $\mathrm{d}V_h = 4\pi R_h^2\,\mathrm{d}R_h$. Then we have

$$P_{mech} = -4\pi p_h R_h^2 \mathrm{u_{imp}}. \tag{2.54}$$

The implosion velocity appears as a parameter in this equation. The mechanical work is injected in the power balance equation (2.8). When $\mathrm{u_{imp}} = 0$ we recover the hot-spot ignition criterion expressed in (2.14). The ignition threshold for several implosion velocities are plotted in Figure 2.14. For implosion velocities below $u_{lim} = 120$ km.s^{-1} the domain $(\rho_h R_h, T_h)$ is divided into two distinct zones where the power balance is positive. In this case, during the implosion, the hydrodynamic path of the hot-spot must necessarily pass trough a negative power balance zone. Then the energy brought for compression is dissipated too quickly and the internal energy of the hot-spot cannot increase. This means that the implosion velocity must be higher than the threshold u_{lim}. It is usually said that $\mathrm{u_{imp}} > 200$ km.s^{-1} by taking a security margin into account.

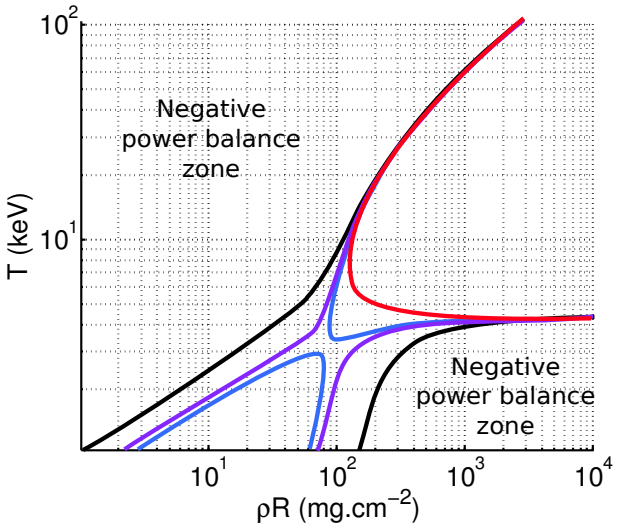

Figure 2.14: Curves where the power balance is zero (2.8). Each curve corresponds to an implosion velocity: 0 km/s in red, 100 km/s in blue, 120 km/s in purple, 200 km/s in black .

Ignition velocity Kemp [Kemp et al., 2001] expresses the stagnation pressure p_h as a function of the maximal Mach number of the imploding shell $\mathcal{M}_0$ and p_{am} the maximal ablation pressure:

$$p_h = p_{am}\mathcal{M}_0^3. \tag{2.55}$$

The maximal shell Mach number is $\mathcal{M}_0 = \mathrm{u}_{\mathrm{imp}}/c_{if}$ where c_{if} is the sound velocity at the shock break-out time t_{sb}.

We saw in Section 2.1.2 that the ignition criterion relies on the areal density and on the temperature. We consider that the ignition occurs when the product $p_h R_h$ exceeds a limit value $(pR)_{\mathrm{ign}} \propto (\rho R)_{\mathrm{ign}} T_{\mathrm{ign}}$. The hot-spot internal energy is

$$E_h = \frac{3}{2} p_h V_h = 2\pi \frac{(p_h R_h)^3}{p_h^2}. \tag{2.56}$$

At the ignition threshold, as the product $(pR)_{\mathrm{ign}}$ takes a fixed value, the hot-spot internal energy scales as $E_{\mathrm{ign}} \propto p_h^{-2}$. The entropy is assumed to be constant in the shell. Thus the density in the shell is related to the pressure as $p/\rho^\gamma = \alpha_{if}$, where $\gamma = 5/3$ for the shell considered as an ideal monoatomic gas. The sound velocity $c = \sqrt{\gamma p/\rho}$ can be related to the adiabat α_{if} and to the external pressure p_{am} by the relation $c_{if}^2 \propto p_{am}^{2/5}\alpha_{if}^{3/5}$. Then, using (2.55) and (2.56), the hot-spot energy at ignition scales as

$$E_{\mathrm{ign}} \propto p_{am}^{-4/5}\mathrm{u}_{\mathrm{imp}}^{-6}\alpha_{if}^{9/5}. \tag{2.57}$$

Let us now express the minimum implosion velocity u_{ign} needed for ignition. About 84 % of the shell kinetic energy goes to the shell compression and 16 % to the hot-spot. We consider

that the internal energy in the hot-spot is proportional to the kinetic energy of the shell at the end of the acceleration phase $E_{\rm ign} \propto \frac{1}{2}{\rm M}u_{\rm ign}^2$. The ignition velocity scales then as

$$u_{\rm ign} \propto p_{am}^{-1/10}\alpha_{if}^{9/40}{\rm M}^{-1/8}. \tag{2.58}$$

We can see that the ignition velocity is mostly affected by the shell adiabat. It is reduced for a lower shell adiabat which leads to a better compression. The shell mass and the ablation pressure should be increased to reduce the ignition velocity but their influences are weak.

Gain and implosion velocity We saw in Section 2.3.2 that the hydrodynamic efficiency scales as $\eta \propto \frac{{\rm M}_a}{{\rm M}_0} \propto {\rm u}_{\rm imp}^{2/3} {I_{abs}}^{-2/9} {\lambda_L}^{-4/9}$ (2.43). Then the gain $G = \eta E_{fus}/E_k \propto \eta {\rm u}_{\rm imp}^{-2}$ scaling is given by the relation

$$G \propto {\rm u}_{\rm imp}^{-4/3} I_{abs}^{-2/9} \lambda_L^{-4/9}. \tag{2.59}$$

This estimate gives an idea of the implosion velocity influence on the target energy gain if ignited. It is close to the scaling from the simulation data fit given in Ref. [Zhou and Betti, 2007]:

$$G \simeq \frac{73}{I_{[10^{15}\ {\rm W.cm^{-2}}]}^{0.25}} \left(\frac{3\times 10^7}{{\rm u}_{{\rm imp}[\ {\rm cm.s^{-1}}]}}\right)^{1.25} \left(\frac{\Phi_B}{0.2}\right) \left(\frac{0.35}{\lambda_{[\mu{\rm m}]}}\right)^{0.5} \tag{2.60}$$

If ignited, the target gain $G \propto {\rm u}_{\rm imp}^{-1.25}$ is higher for a lower implosion velocity. Thus the goal of an efficient target design is to achieve ignition at the minimum possible implosion velocity.

Hydrodynamic instabilities The efficiency of the shell implosion is limited by the hydrodynamic instabilities. We consider here the ablative RT instability growth dependence on the shell parameters. According to (2.51), the amplification factor reads

$$\gamma t = 0.9\sqrt{kgt^2} - \beta k v_{abl} t = 0.9\sqrt{(k\Delta R_{sb})\frac{gt^2}{\Delta R_{sb}}} - \beta(k\Delta R_{sb})\frac{v_{abl}t}{\Delta R_{sb}}, \tag{2.61}$$

where ΔR_{sb} is the shell thickness at the shock breakout time t_{sb}.

We consider the mean acceleration $\ddot{R} = g = {\rm u}_{\rm imp}^2/R_{sb}$. Then the time at the end of the acceleration phase is linked to the shell velocity as $t_d = {\rm u}_{\rm imp}/g$. Also, we consider the most dangerous mode where $k\Delta R_{sb} \sim 1$ at the maximal shell velocity ${\rm u}_{\rm imp}$. Then,

$$\gamma t_d = 0.9\sqrt{\rm IFAR} - \beta\frac{v_{abl}}{{\rm u}_{\rm imp}}{\rm IFAR}. \tag{2.62}$$

The ablation velocity reads $v_{abl} = \dot{m}_a/\rho \propto \dot{m}_a(\alpha_{out}/p_a)^{1/\gamma}$ and the IFAR $\propto {\rm u}_{\rm imp}^2 \alpha_{if}^{-3/5} p_a^{-2/5}$ (according to (2.39)). Here we assume that the shell has a uniform adiabat α_{if} except from its outer region where the adiabat α_{out} can be higher thanks to an adiabat shaping method [An-

derson and Betti, 2004]. The growth of the RT instability becomes

$$\gamma t_d = \mathrm{u_{imp}} \left(0.9 \alpha_{if}^{-3/10} p_a^{-2/10} - \beta \dot{m}_a p_a^{-1} \left(\frac{\alpha_{out}}{\alpha_{in}} \right)^{3/5} \right). \tag{2.63}$$

The growth is directly proportional to the implosion velocity. We can also notice that the adiabat shaping of the shell increases the ablative stabilization of the instability through the second term on the right hand side.

2.5.2 Shock ignition principle

In the conventional scheme the choice of the implosion velocity is limited by two conditions. During the acceleration phase the shell surface perturbation amplitude $h(t)$ scales as $\ln(h(t)/h_0) \propto \mathrm{u_{imp}}$. The implosion velocity is thus limited from the top by the RT instability. On the other side, the implosion velocity must be higher than the ignition threshold u_{ign}, otherwise the temperature of the hot-spot $T_h \propto \mathrm{u_{imp}^2}$ is too low. This criterion defines the lower limit for the implosion velocity.

The idea of the advanced ignition schemes is to work with the implosion velocity lower than the ignition limit u_{ign} (2.58). According to (2.59), reducing the implosion velocity allows to reach higher gains. Also it relaxes the hydrodynamic instability issues (2.63). The compression of the target is more efficient at a lower implosion velocity. Indeed, it requires a lower laser intensity which means that the laser-matter coupling is more efficient. Also, less danger from the parametric instabilities and less preheat is expected at a low implosion velocity. However, if $\mathrm{u_{imp}} < u_{ign}$, the hot-spot pressure at the stagnation is too low. Then, an additional source of energy is needed at the end of the implosion to raise the temperature in the hot-spot and to reach the ignition conditions. In the shock ignition scheme, this energy is brought by a converging shock driven by an intense laser spike at the end of the implosion. The laser intensity is expected to be at least one order of magnitude higher than the intensity of the compression pulse.

Figure 2.15 summarizes the implosion synopsis in the shock ignition scheme. It has to be compared to the conventional implosion scheme presented in Figure 2.5. At the beginning of the implosion, the laser radiation ablates the outer layer of the spherical target. A high pressure is created at the ablation front and a strong shock is launched inside the shell. The laser pulse intensity increases slowly at a 10 ns time scale, to generate a sequence of compression waves which compress the shell isentropically. The shock and the compression waves merge at the inner side of the shell as pointed by the bullet 1 in Figure 2.15. The entropy deposited per unit of mass in a homogeneous shell by a strong shock is constant. Thus, the shell adiabat is approximately uniform. The shock is transmitted partially into the D-T gas and a rarefaction wave is reflected into the shell. The rarefaction wave is again reflected at the ablation front and converted into a compression wave. This sequence of processes starts the acceleration phase of the shell. In the same time, the primary shock transmitted in the D-T gas converges and reflects at the center of the target. The acceleration phase is ended when the diverging primary shock collides with

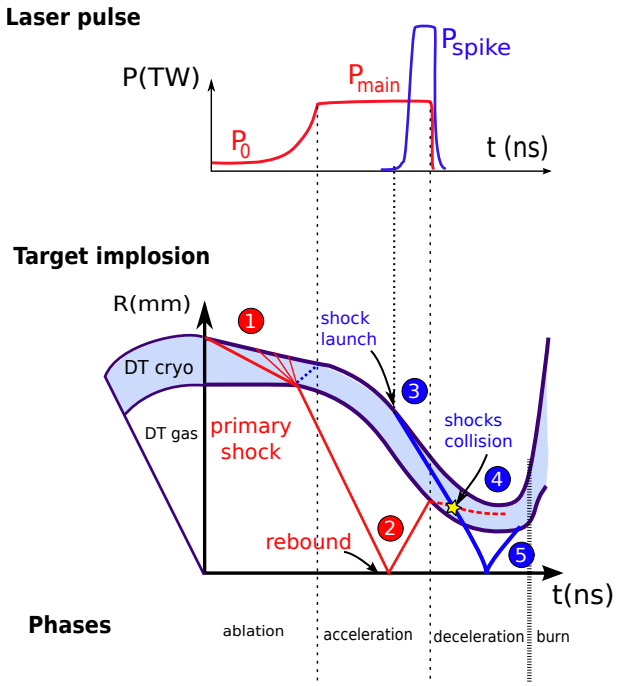

Figure 2.15: Implosion sketch of the shock ignition scheme

the shell as it shown by the bullet 2 in Figure 2.15. At this time the shell attains the maximum implosion velocity u_{imp} and starts to decelerate. The deceleration is mainly due to the increase of the pressure in the shell and in the compressed central D-T gas. The stagnation phase starts when the shell velocity comes to zero. This moment of the maximum compression is the most appropriate for ignition of the fuel in the hot-spot. However, in the shock ignition scheme, the shell implosion velocity is not sufficient to raise the compressed fuel temperature in the ignition domain. An additional energy is brought with the ignitor shock (bullet 3 in Figure 2.15). It is launched during the acceleration phase in such a way that it collides (bullet 4 in Figure 2.15) with the reflected primary shock into the shell at the beginning of the deceleration phase. It enters into the fuel (bullet 5 in Figure 2.15) and increases the fuel temperature above the ignition threshold after one or few reflections from the center.

2.6 Conclusion

In this chapter the ignition of fusion reactions by the implosion of a shell target filled with a DT fuel is presented.

To reach the ignition conditions and to obtain a sufficient energy gain, the fuel temperature and areal density must be high enough. These conditions require a strong compression of the target which is limited by the target pre-heat and the hydrodynamic instabilities.

The shock ignition scheme allows to reach a higher gain with an implosion less subjected to the hydrodynamic instability issues. In this ignition scheme, the energy used for the target compression is reduced and a shock is launched at the end of the implosion to bring the supplementary

source of energy needed for ignition.
To understand the physics of the ignitor shock, it is important to characterize the medium where it propagates. This chapter was devoted to the presentation of the conventional implosion scheme.
The implosion is characterized by the following important parameters:

Shell adiabat It is set by a shock wave launched during the pre-pulse. Lower is this parameter, higher can be the compression.

Shell IFAR This is the maximum shell aspect ratio at the time t_{sb}. This parameter must not be too high in order to limit the Rayleigh–Taylor hydrodynamic instability growth.

Implosion velocity It is the maximal velocity of the shell. The final temperature and density in the hot-spot strongly depend on this parameter which must be high to reach the ignition conditions. However, the gain is reduced as the implosion velocity is increased. The implosion is also more subjected to the hydrodynamic instability issues at high implosion velocity.

The ignitor shock depends on two parameters:

Spike time It defines the shell and the hot-spot conditions where the ignitor shock propagates.

Spike intensity It defines the initial strength and velocity of the ignitor shock. Depending on its value, strong non-linear effects can appear in the laser-matter interaction.

The interaction laser-plasma was also presented in this chapter. The laser spike intensity used to generate the ignitor shock is much higher than the laser intensity used for the compression of the target. The laser-matter interaction in this regime of intensity is strongly non-linear. It may generate a lot of hot-electrons which can pre-heat the target or enhance the shock strength if they are stopped. This issue will be assessed in the last chapter of this thesis.
In the following chapter we present the hydrodynamic tools that will be employed to describe the flow of the imploding shell and of the ignitor shock wave.

3 Hydrodynamic modeling

Contents

In a hydrodynamic description, the temporal and the spatial evolution of a plasma are described by averaged quantities such as the density, pressure and temperature in a small volume called the fluid particle. This gives a macroscopic description of the flow which is assumed to be continuous. This approach is valid if the plasma mean free path l and mean time between collisions τ are much shorter than the characteristic dimensions of the flow L and t. During the implosion, this is verified in the dense region of the target but not in the corona where the density is very low and the temperature is high. The hydrodynamic description is neither valid during the burning phase. In those two regions a kinetic description would provide better results. Here we are interested by the implosion physics in the target, before ignition. This is why the hydrodynamic description is chosen.

In this chapter, we present the theoretical background required for the following chapters. First the basic hydrodynamic equations are introduced in Section 3.1. They are used, in Section 3.2, to describe the homogeneous isentropic compression of a shell target. This model will be used in Chapter 5. The basic equations which describe a shock wave are given in Section 3.3. Lastly, a brief review of the mathematical methods to describe a converging shock wave is proposed in Section 3.4.

3.1 Basic equations

3.1.1 Conservation equations

Starting from conservation principles, one can derive general governing equations for a flow properties.

We write ρ the density, p the pressure and $\mathbf{u}$ the velocity. Those variables depend on time t and space.

The mass variation in a volume V is equal to the mass flux at its surface

$$\partial_t \int_V \rho \, \mathrm{d}V = - \oint_{\partial V} \rho \mathbf{u}. \, \mathrm{d}\mathbf{S}. \tag{3.1}$$

Using the Green–Ostrogradski theorem the conservation of mass reads

$$\partial_t \rho + \mathrm{div}(\rho \mathbf{u}) = 0. \tag{3.2}$$

Two kind of forces apply to a fluid particle. The long range forces affect all the fluid particles. They are usually proportional to the volume and called volume forces. It can be for example the gravity or the Laplace force. The second kind of forces are short range forces. The relative motion of particles generates internal forces which are called stress. We write $\mathbf{f}$ the force acting on a unit volume of fluid and $\mathbf{\Sigma}$ the stress tensor.

The resultant force acting on a volume V is

$$\mathbf{F} = \int_V \mathbf{f}\,\mathrm{d}V + \oint_{\partial V} \mathbf{\Sigma}.\,\mathrm{d}\mathbf{S}. \tag{3.3}$$

Using the local form of the force, the Newton's law gives

$$\rho\,\mathrm{d}_t\mathbf{u} = \mathbf{f} + \mathrm{div}(\mathbf{\Sigma}). \tag{3.4}$$

For an ideal fluid, the stress tensor is diagonal $\mathbf{\Sigma} = -p\mathbf{I}$. Then the momentum conservation equation reads

$$\rho\,\mathrm{d}_t\mathbf{u} = -\boldsymbol{\nabla}p + \mathbf{f}. \tag{3.5}$$

The total energy of a unit volume e is the sum of the specific internal energy ϵ and the kinetic energy $e = \epsilon + \mathbf{u}^2/2$.

The variation of energy is expressed as

$$\begin{array}{lll} \partial_t \int_V (\rho e)\,\mathrm{d}V = & -\int_{\partial V} \rho e \mathbf{u}.\,\mathrm{d}\mathbf{S}, & \textit{energy transport} \\ & +\int_V \mathcal{S}\,\mathrm{d}V, & \textit{source term} \\ & -\int_{\partial V} \mathbf{Q}.\,\mathrm{d}\mathbf{S}, & \textit{heat flux} \\ & +\int_V \mathbf{f}.\mathbf{u}\,\mathrm{d}V + \int_{\partial V} \mathbf{\Sigma}.\mathbf{u}.\,\mathrm{d}\mathbf{S}. & \textit{work done by the external forces} \end{array} \tag{3.6}$$

The local form of the energy conservation equation is

$$\partial_t \rho e + \mathrm{div}\left((\rho e + p)\mathbf{u} + \boldsymbol{Q}\right) = \mathcal{S} + \mathbf{f}.\mathbf{u}. \tag{3.7}$$

3.1.2 Ideal gas equation of state

If we consider an ideal gas without any interaction between the particles, the Boltzmann statistics leads to the famous relation between the pressure p and the temperature T

$$p = nT \tag{3.8}$$

with n being the particle density and T being the temperature in energy unit.

In a plasma totally ionized, the particles density is the sum of the ions density and the electrons density. If the plasma is neutral, $n_e = \mathrm{Z}n_i$ then $n = n_e + n_i = (\mathrm{Z}+1)n_i$. The fluid density is related to the particle density by the relation $\rho = n_i \mathrm{A} m_p$ where A is the average atomic mass of the ions and m_p the proton mass.

The pressure can then be expressed as a function of the density

$$p = \frac{(\mathrm{Z}+1)}{\mathrm{A}m_p}\rho T. \tag{3.9}$$

There is also a relation between the pressure and the internal energy

$$p = (\gamma - 1)\rho\epsilon, \tag{3.10}$$

where γ is the adiabatic index which depends on the number of freedom degrees of each particle. For an monoatomic gas $\gamma = 5/3$.

We introduce the specific entropy s which is by definition (according to the first and second laws of thermodynamics)

$$T\,\mathrm{d}s = \mathrm{d}\epsilon + p\,\mathrm{d}v, \tag{3.11}$$

where $v = 1/\rho$ is the specific volume.

By combining the equations (3.9) and (3.10) we have

$$\mathrm{d}s = \frac{(\mathrm{Z}+1)}{\gamma - 1}\left(\frac{\mathrm{d}p}{p} - \gamma\frac{\mathrm{d}\rho}{\rho}\right). \tag{3.12}$$

By integrating, the entropy has the form

$$s = \frac{(\mathrm{Z}+1)}{\gamma - 1}\ln\left(\frac{p}{\rho^\gamma}\frac{\rho_0^\gamma}{p_0}\right) + s_0, \tag{3.13}$$

with ρ_0 and p_0 being the density and pressure of the refrence state of specific entropy s_0.

The first law of thermodynamics says that

$$\mathrm{d}Q = \mathrm{d}\epsilon + p\,\mathrm{d}v, \tag{3.14}$$

with $\mathrm{d}Q$ the heat flux variation, $\mathrm{d}\epsilon$ the change in internal energy and $p\,\mathrm{d}v$ the work done by the pressure. If a process is adiabatic, $\mathrm{d}Q = 0$ and then $\mathrm{d}s = 0$ according to (3.11). Thus for an adiabatic transformation in an ideal gas, we have

$$\mathrm{d}\left(\frac{p}{\rho^\gamma}\right) = 0. \tag{3.15}$$

Let us consider the propagation of an acoustic wave in the one dimensional flow along the direction r. A homogeneous medium of density ρ_0 and pressure p_0 at rest is perturbed. The perturbed density reads $\rho = \rho_0 + \delta\rho$, the perturbed pressure is $p = p_0 + \delta p$ and the velocity of the perturbed medium is δu.

The conservation of mass (3.2) gives

$$\frac{\partial(\rho_0 + \delta\rho)}{\partial t} + \frac{\partial((\rho_0 + \delta\rho)\delta u)}{\partial r} = 0 \tag{3.16}$$

and the conservation of momentum (3.5) gives

$$(\rho_0 + \delta\rho)\frac{\partial\delta u}{\partial t} + (\rho_0 + \delta\rho)\delta u\frac{\partial\delta u}{\partial r} = -\frac{\partial(p_0 + \delta p)}{\partial r} + f. \tag{3.17}$$

At the first order, we obtain

$$\rho_0 \frac{\partial \delta u}{\partial t} + \rho_0 \frac{\partial \delta u}{\partial r} = 0 \tag{3.18}$$

$$\rho_0 \frac{\partial \delta u}{\partial t} + \frac{\partial \delta p}{\partial r} = f. \tag{3.19}$$

Then by taking the time derivative of equation (3.18) and the spatial derivative of equation (3.19), we obtain

$$\frac{\partial^2 \delta \rho}{\partial t^2} = \frac{\partial^2 \delta p}{\partial r^2}. \tag{3.20}$$

We assume that the process is adiabatic and define the *sound velocity* as

$$c = \sqrt{\left.\frac{\mathrm{d}p}{\mathrm{d}\rho}\right|_s}. \tag{3.21}$$

Then the equation (3.20) becomes

$$\frac{\partial^2 \delta \rho}{\partial t^2} = c^2 \frac{\partial^2 \delta \rho}{\partial r^2}. \tag{3.22}$$

We recognize the equation of a wave, propagating at the velocity c.
Then according to (3.15), the adiabatic sound velocity is

$$c^2 = \frac{\partial p}{\partial \rho} = \gamma \frac{p}{\rho}. \tag{3.23}$$

This will be considered as the equation of state for an ideal gas.

3.1.3 Forms of the Euler's equations

To simplify the conservation equations, we consider here a one dimensional flow without energy source nor heat flux ($\mathcal{S} = 0$ and $Q = 0$).

Eulerian form The simplified conservation laws of mass, momentum and energy are :

$$\partial_t \rho + \partial_r(\rho u) = -\frac{j\rho u}{r}, \tag{3.24a}$$

$$\partial_t u + u\partial_r u + \frac{1}{\rho}\partial_r(p) = f, \tag{3.24b}$$

$$\partial_t p + u\partial_r p - c^2(\partial_r \rho + u\partial_r \rho) = 0, \tag{3.24c}$$

where the right hand side in the mass conservation equation accounts for the symmetry of the flow ($j = 0, 1$ or 2 in a plane, cylindrical or spherical case respectively).

Lagrangian form The Lagrangian description of a flow follows the particle movement. Let us write $R_p(r_0, t)$ the trajectory of a fluid particle initially at the position r_0 at the time $t = 0$. The Lagrangian coordinate r_0 is thus defined as

$$r_0 = R_p(r_0, 0). \tag{3.25}$$

The equations (3.24) become

$$\partial_t \frac{1}{\underline{\rho}} = \frac{1}{\rho_0 r_0^j} \partial_{r_0} \left(R_p^j \underline{u} \right), \tag{3.26a}$$

$$\partial_t \left(\underline{u} \right) = -\frac{R_p^j}{\rho_0 r_0^j} \partial_{r_0} \underline{p}, \tag{3.26b}$$

$$\partial_t \underline{e} + \underline{p} \partial_t \frac{1}{\underline{\rho}} = 0. \tag{3.26c}$$

where the underline denotes a physical quantity expressed in the Lagrangian formalism. The last equation shows that if no source is considered and if the heat flux is zero, the entropy is constant along a particle path.

Characteristic form By combining the equations in (3.24), we get the characteristic form of the system :

$$\frac{\mathrm{d}p}{\mathrm{d}x} + \rho c \frac{\mathrm{d}u}{\mathrm{d}x} + \frac{\rho c}{u + c} \left[\frac{juc}{r} - f \right] = 0 \text{ on } C_+ : \frac{\mathrm{d}x}{\mathrm{d}t} = u + c \ , \tag{3.27a}$$

$$\frac{\mathrm{d}p}{\mathrm{d}x} - \rho c \frac{\mathrm{d}u}{\mathrm{d}x} + \frac{\rho c}{u - c} \left[\frac{juc}{r} - f \right] = 0 \text{ on } C_- : \frac{\mathrm{d}x}{\mathrm{d}t} = u - c \ , \tag{3.27b}$$

$$\frac{\mathrm{d}p}{\mathrm{d}x} - c^2 \frac{\mathrm{d}\rho}{\mathrm{d}x} = 0 \text{ on } P \quad : \frac{\mathrm{d}x}{\mathrm{d}t} = u \ . \tag{3.27c}$$

The flow in a general case is governed by the propagation and interaction of three wave families. The advancing and receding waves C_+ and C_- bring the pressure and velocity variations. The particle path P transports the entropy.

3.1.4 Compression waves - rarefaction waves

Riemann invariants We look at the characteristic form of the Euler's equation. By neglecting the volume force f, we define the two quantities J_+ and J_- as

$$\mathrm{d}J_+ \equiv \mathrm{d}u + \frac{1}{\rho c} \mathrm{d}p = 0, \tag{3.28}$$

$$\mathrm{d}J_- \equiv \mathrm{d}u - \frac{1}{\rho c} \mathrm{d}p = 0. \tag{3.29}$$

By integration we have

$$J_+ = u + \int c\frac{\partial\rho}{\rho}, \tag{3.30}$$

$$J_- = u - \int c\frac{\partial\rho}{\rho}. \tag{3.31}$$

Those quantities J_+ and J_- are well known as the *Riemann invariants*. The form given here is valid only for an isentropic flow. The particularity of the quantities $J_\pm$ is that they remain constant on the characteristics $C_\pm$.

For an ideal gas, the Riemann invariants read

$$J_\pm = u \pm \frac{2}{\gamma - 1}c. \tag{3.32}$$

Compression wave Let us consider a simple wave propagating into a uniform medium at rest from the left to the right. On the characteristic C_- coming from the unperturbed medium, the Riemann invariant is $J_- = -2c_0/(\gamma - 1)$ which leads to the relation

$$c(x) = c_0 + \frac{(\gamma - 1)}{2}u(x). \tag{3.33}$$

The velocity and the sound velocity have qualitatively the same profile. Figure 3.1 shows the evolution of a simple wave. The C_+ characteristics passing through the points A, B and C where $u = 0$ and $c = c_0$ are parallel lines. The C_+ characteristics emerging from the minimum and maximum points D and E have different slopes $\mathrm{d}x/\,\mathrm{d}t = u + c$. The profile of the wave is thus steepened. After some time, the characteristics cross each other. This situation is not physical as the flow quantities should be single valued. At this point the behavior of the wave becomes non-linear and the wave is transformed in a *shock wave*. The theory of shock waves will be developed later.

Rarefaction wave Let us consider a semi-infinite medium at rest. At the right boundary, a piston initially at $x = 0$ starts to move with a constant positive velocity w at the time $t = 0$. Figure 3.2 shows the characteristics C_+ and C_- in the (x, t) plane. Every C_+ characteristic comes from the initial flow $(x < x_0, t = 0)$. The Riemann invariant J_+ is the same on all those characteristics and we have

$$c(x,t) = c_0 - \frac{\gamma - 1}{2}u(x,t). \tag{3.34}$$

As the piston pulls the gas, the sound velocity decreases which means that the gas cools down.

The last C_- characteristic coming from the initial state $(x < 0, t = 0)$ is called the *trailing edge* and represented with a thick line on Figure 3.2. In the region to the left from this line, the flow stays unperturbed and the C_- characteristics are parallel.

On the piston position the relation (3.34) applies. The C_- characteristics emerging from the

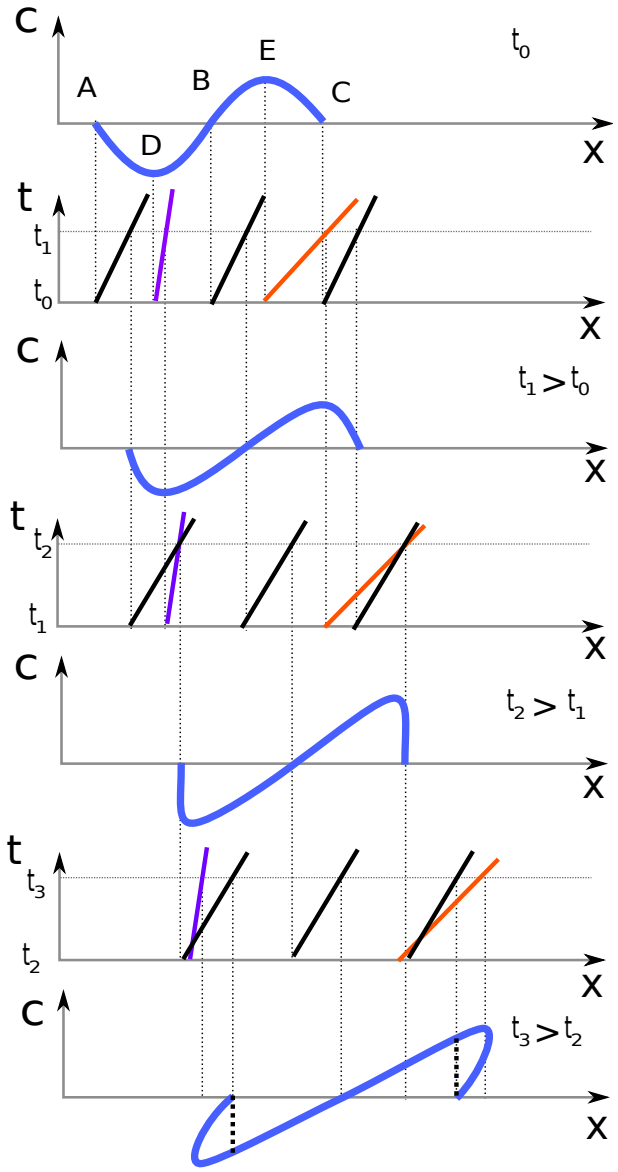

Figure 3.1: Illustration of a simple wave steepening into a non-linear wave. At the time t_3 the wave form is not physical, the dashed dots indicates discontinuities corresponding to shock waves.

piston bring therefore the Riemann invariant

$$J_- = 2w - 2c_0/(\gamma - 1). \tag{3.35}$$

The first characteristic emerging from the piston is called the *leading edge* (see figure 3.2). It delimits a zone where the C_+ and the C_- characteristics are strait lines and where the flow quantities are constants $u = w$ and $c = c_0 - w(\gamma - 1)/2$.

In the region between the trailing edge and the leading edge, the C_- characteristics are strait

lines with increasing slopes

$$\frac{\mathrm{d}x}{\mathrm{d}t} = u - c = \frac{\gamma+1}{2}u - c_0. \tag{3.36}$$

They are forming a fan. As they are coming from one common point, the wave is qualified as *centered*. By integrating equation (3.36) we obtain the expression of u :

$$u = \frac{2}{\gamma+1}\left(c_0 + \frac{x}{t}\right). \tag{3.37}$$

Then the other flow quantities are given by:

$$\frac{c}{c_0} = \left(\frac{2}{\gamma+1} - \frac{\gamma-1}{\gamma+1}\frac{x}{c_0 t}\right), \tag{3.38}$$

$$\frac{\rho}{\rho_0} = \left(\frac{2}{\gamma+1} - \frac{\gamma-1}{\gamma+1}\frac{x}{c_0 t}\right)^{\frac{2}{\gamma-1}}, \tag{3.39}$$

$$\frac{p}{p_0} = \left(\frac{2}{\gamma+1} - \frac{\gamma-1}{\gamma+1}\frac{x}{c_0 t}\right)^{\frac{2\gamma}{\gamma-1}}, \tag{3.40}$$

for $-c_0 t \leq x \leq \left(\frac{\gamma+1}{2}w - c_0\right)t \leq \frac{2}{\gamma-1}c_0 t$.

Between the leading and the trailing edge, the velocity evolves linearly between 0 and w. The pressure and density are power laws of the position for a given instant. The density and velocity profiles are represented in Figure 3.2 (b).

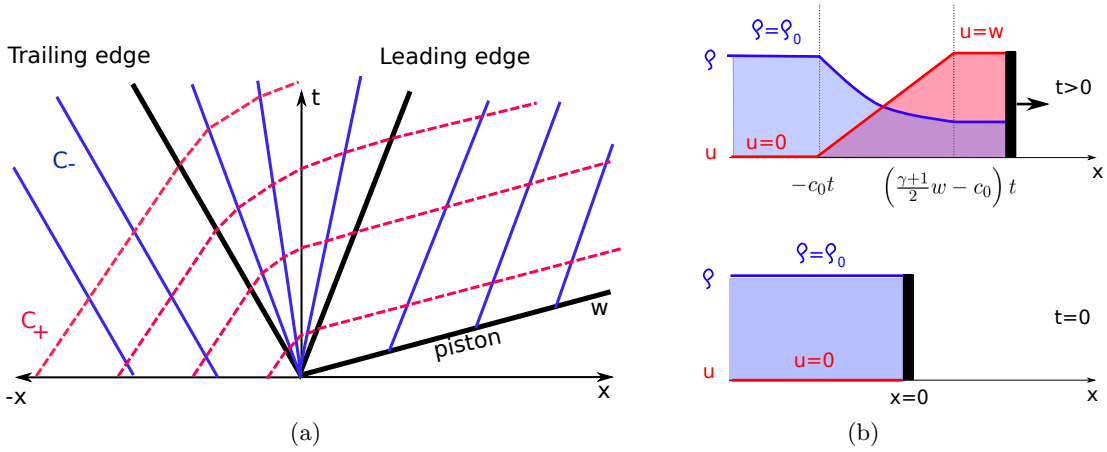

Figure 3.2: Characteristic trajectories in the problem of a centered rarefaction wave (panel a) and sketch of the density and the velocity profiles (panel b).

3.2 Homogeneous isentropic compression

Let us apply the basic hydrodynamic equations derived in Section 3.1 to the case of inertial confinement. During the implosion, the compression of the target is nearly isentropic. Therefore, the ideal case of a homogeneous isentropic compression of a shell target is of particular interest to understand the implosion.

3.2.1 Lagrangian description of the flow

Let us use in this section a Lagrangian description of the flow. We write $R_p(r_0, t)$ the position at the time t of the fluid particle initially at the position r_0 when $t = 0$.

We consider a *homogeneous* (or uniform) compression of the shell. This means that every elementary volume scales in the same way with time. Therefore,

$$R_p(r_0, t) = h(t) r_0, \tag{3.41}$$

where $h(t)$ is a time dependent dimensionless factor. This kind of assumption is often made in astrophysics to describe the expansion or the contraction of a star [Chandrasekhar, 1957].

We denote with an underscore $\underline{q}(r_0, t)$ the Lagrangian expression of a dependent variable $q(r, t)$. We also write with a subscript zero $q_0(r_0)$ the profile of the dependent variable q at the time $t = 0$. We have $q(r_0, 0) = \underline{q}(r_0, 0) = q_0(r_0)$.

According to (3.41), the particle velocity is proportional to the radius

$$\underline{u}(r_0, t) = \partial_t R_p(r_0, t) = \dot{h}(t) r_0. \tag{3.42}$$

The hydrodynamic equations in the Lagrangian formalism are given in (3.26).

The conservation of energy (3.26c) is fulfilled under the assumption that the flow is isentropic for each fluid element :

$$\frac{\underline{p}(r_0, t)}{\underline{\rho}(r_0, t)^\gamma} = \frac{p_0(r_0)}{\rho_0(r_0)^\gamma}. \tag{3.43}$$

Injecting (3.41) and (3.42) into (3.26a) we obtain the density expression

$$\underline{\rho}(r_0, t) = \frac{\rho_0(r_0)}{h(t)^{j+1}}. \tag{3.44}$$

Then using relation (3.43) we write the pressure as

$$\underline{p}(r_0, t) = \frac{p_0(r_0)}{h(t)^{(j+1)\gamma}}. \tag{3.45}$$

Now the equation of conservation of the momentum (3.26b) reads

$$h^{\gamma(j+1)-j}(t)\ddot{h}(t) = \frac{1}{\rho_0 r_0}\frac{\mathrm{d}p_0}{\mathrm{d}r_0}. \tag{3.46}$$

As the variables t and r_0 are independent, the two sides of the equation (3.46) must be constant.

3.2.2 Time evolution of the flow

The left hand side of (3.46) gives

$$h(t)^{\gamma(j+1)-j}\ddot{h}(t) = \pm\frac{1}{\tau^2}, \tag{3.47}$$

with τ an arbitrary constant time and the right hand sign determines if the flow is accelerating $\ddot{h}(t) < 0$ or decelerating $\ddot{h}(t) > 0$.

Expression of the scale factor h(t) The equation (3.47) can be written

$$\ddot{h}(t)\dot{h}(t) = \pm\frac{1}{\tau^2}h(t)^{j-\gamma(j+1)}\dot{h}(t). \tag{3.48}$$

Then considering that $h(0) = 1$ and $\dot{h}(0) = 0$ we obtain by integrating (3.48)

$$\dot{h}(t)^2 = \pm\frac{2}{(j+1-\gamma(j+1))\,\tau^2}\left[h(t)^{j+1-\gamma(j+1)} - 1\right], \tag{3.49}$$

which gives

$$\sqrt{\frac{\mu}{2}}\frac{h^{\frac{\mu}{2}}}{\sqrt{\pm(h^\mu - 1)}}\,\mathrm{d}h = -\frac{\mathrm{d}t}{\tau}, \tag{3.50}$$

where $\mu = (j+1)(\gamma-1)$.

This expression is easily integrable if $\mu/2 = \mu - 1$ which gives the condition $\gamma = \frac{2}{j+1} + 1$. In a spherical case $j = 2$, the condition is $\gamma = 5/3$. This corresponds to the equation of state of a fully ionized plasma.

For simplicity, we assume that $j = 2$ and $\gamma = 5/3$ in the following sections. The integral of (3.50) gives

$$h(t) = \sqrt{1 \pm \left(\frac{t}{\tau}\right)^2}. \tag{3.51}$$

Acceleration case The sign minus corresponds to an accelerating flow toward the center. When $t = \tau$ the target collapses and attains an infinite density and pressure. This is called a *cumulative flow*. Of course, near the collapse time, the flow is unrealistic. But for earlier times, this solution is close to the flow in ICF targets. The parameter τ represents the time of the implosion. It can be approximated by $\tau = R_{sb}/\mathrm{u_{imp}}$ where $\mathrm{u_{imp}}$ is the maximal implosion velocity and R_{sb} is the radius of the shell at the beginning of the acceleration phase $t = 0$. This time moment corresponds to the first shock breakout time t_{sb} (see Section 2.3.1).

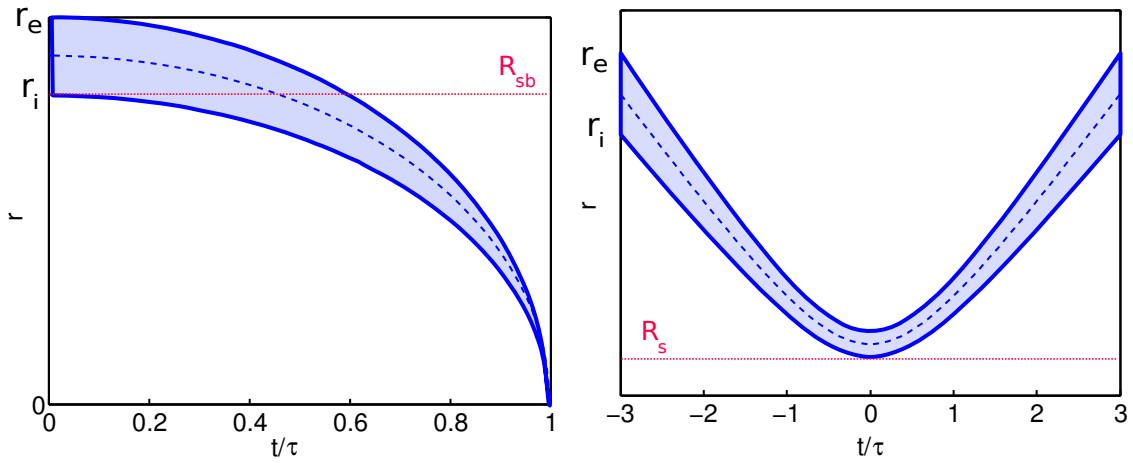

(a) (b)

Figure 3.3: Particle position evolution in an accelerating shell (a) and a decelerating shell (b).

Deceleration case The sign plus corresponds to a decelerated flow, converging if $t < 0$ and diverging if $t > 0$. At $t = 0$ the velocity is zero. This can be used to describe the deceleration and stagnation phase of the target. The time $t = 0$ corresponds thus to the stagnation time t_{stag}. One can set $\tau = R_{stag}/\mathrm{u_{imp}}$ with R_{stag} the shell radius at the stagnation time $t = 0$. Then the initial velocity of the shell for $t \mapsto -\infty$ is $\mathrm{u_{imp}}$.

Figure 3.3 presents the shell radius position as a function of time $r/r_0 = h(t)$ for the two cases.

3.2.3 Density and pressure profiles

The radial profiles of density and pressure are conserved with time. They obey to the relation issued from the right hand side of (3.46) :

$$-\frac{1}{\rho_0(r_0)r_0}\frac{\mathrm{d}p_0(r_0)}{\mathrm{d}r_0} = \pm\frac{1}{\tau^2} \tag{3.52}$$

If the shell is accelerated, then the sign of the right hand side is negative and the pressure is increasing with the radius. On the contrary, if the shell is decelerated, the pressure decreases with the radius.

To solve this equation, one more assumption is needed. We consider that the flow is radially isentropic,

$$\forall r_0, \quad \frac{p_0(r_0)}{\rho_0(r_0)^{5/3}} = \alpha_0, \tag{3.53}$$

where α_0 is a constant, called the adiabat of the shell.

Then by integrating (3.52) we get the expression

$$p_0(r_0) = p_{out}\left[1 \pm \frac{1}{3}\left(\frac{r_{out}}{c_{out}\tau}\right)^2\left(1 - \left(\frac{r_0}{r_{out}}\right)^2\right)\right]^{\frac{5}{2}} \tag{3.54}$$

where p_{out} and c_{out} are respectively the external pressure and sound velocity at the radius r_{out}.

We express τ depending on the pressure p_{in} at the inner radius of the shell r_{in}

$$\frac{1}{\tau^2} = \pm\frac{2\gamma}{\gamma+1}\left(\left(\frac{p_{in}}{p_{out}}\right)^{\frac{2}{5}} - 1\right)\frac{\frac{p_{out}}{\rho_{out}}}{r_{out}^2 - r_{in}^2}, \tag{3.55}$$

The expression of the pressure becomes

$$p_0(r_0) = p_{out}\left[1 + \left(\left(\frac{p_{in}}{p_{out}}\right)^{\frac{2}{5}} - 1\right)\left(\frac{r_0^2 - r_{out}^2}{r_{in}^2 - r_{out}^2}\right)\right]^{\frac{5}{2}}, \tag{3.56}$$

the density pressure is then

$$\rho_0(r_0) = \rho_{out}\left[1 + \left(\left(\frac{\rho_{in}}{\rho_{out}}\right)^{\frac{2}{3}} - 1\right)\left(\frac{r_0^2 - r_{out}^2}{r_{in}^2 - r_{out}^2}\right)\right]^{\frac{3}{2}}, \tag{3.57}$$

and the sound speed reads

$$c_0(r_0) = c_{out}\left[1 + \left(\left(\frac{c_{in}}{c_{out}}\right)^{2} - 1\right)\left(\frac{r_0^2 - r_{out}^2}{r_{in}^2 - r_{out}^2}\right)\right]^{1/2}. \tag{3.58}$$

Density, pressure and entropy profiles represented in Figure 3.4.

In the case of an accelerated flow, one can assume that the pressure is zero at the inner radius $p_{in} = 0$. This *hollow shell solution* was first proposed by Kidder [Kidder, 1976]. It has been studied in the early ICF research to understand the relation between an isentropic compression and the laser pulse shaping. Indeed, one can calculate the mechanical power at the outer surface of the target $P_{mech} = p(r_{out}, t)\,\mathrm{d}V/\,\mathrm{d}t$ with $\mathrm{d}V = 4\pi R^2\,\mathrm{d}R$ being the volume variation and using (3.51):

$$P_{mech} = 4\pi(R_0 h)^2(p_{out}h^{-5})R_0\dot{h} = 4\pi\frac{R_0^3 p_{out}}{\tau}\frac{(\frac{t}{\tau})}{\left(1-(\frac{t}{\tau})^2\right)^2} \tag{3.59}$$

This gives the laser pulse power law for the ramp between the pre-pulse and the main pulse allowing to maintain a constant entropy in the shell (see Section 2.3.1). This mathematical model will be used in Chapter 5 to describe the ignitor shock propagation in the imploding shell.

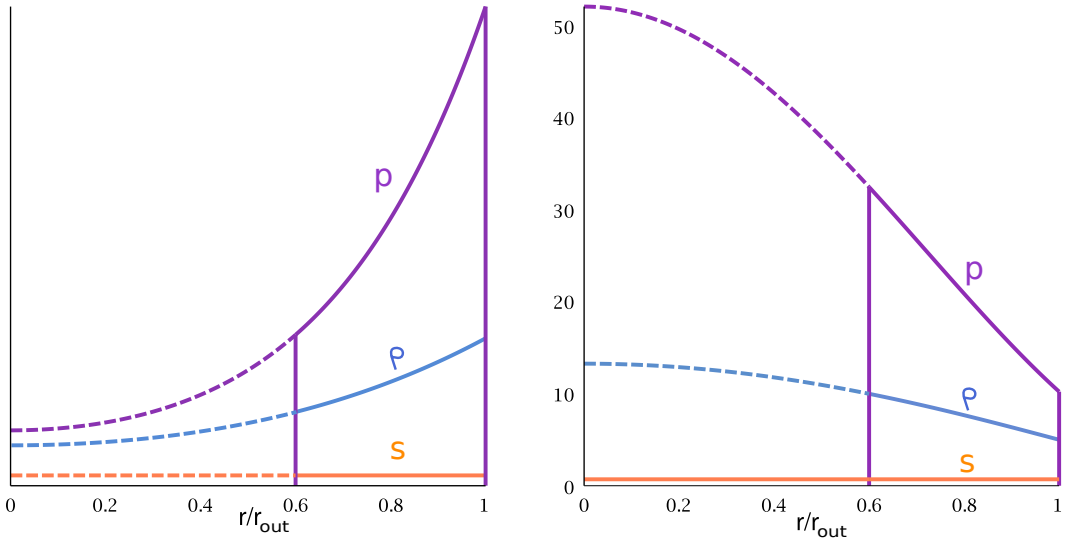

(a) (b)

Figure 3.4: Radial profiles of pressure (purple line), density (blue line) and entropy (orange line) in the isentropic case for an accelerating shell (a) and a decelerating shell (b).

3.3 Basic physics of shock waves

A shock wave is the propagation of a discontinuity of pressure, density and velocity. It appears when a compression wave breaks down as it was illustrated in Section 3.1.4. The shock velocity relative to the upstream medium velocity is then higher than the upstream sound velocity c_u.

3.3.1 Rankine–Hugoniot relations

The shock induces an increase of the pressure, the density and the velocity downstream its front. We write U_s the shock velocity in the laboratory frame. The link between the upstream quantities (subscript u) and the downstream quantities (subscript d) are obtained with the conservation laws for the mass, the impulsion and the energy:

$$\rho_d w_d = \rho_u w_u, \tag{3.60a}$$

$$p_d + \rho_d w_d^2 = p_u + \rho_u w_u^2, \tag{3.60b}$$

$$\rho_d(\epsilon_d + \frac{1}{2}w_d^2) + p_d = \rho_u(\epsilon_u + \frac{1}{2}w_u^2) + p_u, \tag{3.60c}$$

where w is the flow velocity relative to the shock velocity $w_{u/d} = u_{u/d} - U_s$.

This system of equation is known as the *Rankine–Hugoniot* relations.

In the ideal gas case, $\epsilon = \frac{p}{(\gamma-1)\rho}$. The Rankine–Hugoniot relations can then be expressed as

$$\frac{\rho_d}{\rho_u} = \frac{w_u}{w_d} = \frac{(\gamma+1)M_s^2}{(\gamma-1)M_s^2+2}, \tag{3.61a}$$

$$\frac{p_d}{p_u} = 1 + \frac{2\gamma}{\gamma+1}(M_s^2-1), \tag{3.61b}$$

where the shock *Mach number* is defined as

$$M_s = \frac{U_s - u_u}{c_u}. \tag{3.62}$$

As the Mach number tends to infinity the pressure ratio also tends to infinity. On the contrary, the ratio of densities tends to a finite limit $\lim_{M_s\to\infty} \frac{\rho_d}{\rho_u} = \frac{\gamma+1}{\gamma-1}$. Thus the compression of the fluid with a shock wave is limited. For $\gamma = 5/3$, it is not possible to compress more than four times a medium with a shock wave.

3.3.2 Hugoniot adiabat - entropy deposition

Combining equations (3.61a) and (3.61b), we express the shock strength

$$\frac{p_d}{p_u} = \frac{(\gamma+1)v_u - (\gamma-1)v_d}{(\gamma+1)v_d - (\gamma-1)v_u}. \tag{3.63}$$

with $v = 1/\rho$ the specific volume. The curve of this equation in the plane (p, v) is called the *Hugoniot adiabat*. It is the locus of all possibles states (p_d, v_d) behind the shock depending on the upstream state of the gas (p_u, v_u). The transformation through a shock wave is strongly irreversible and this leads to an entropy increase. In an isentropic transformation the state of the flow evolves on the *Poisson adiabat* $pv^\gamma = p_u v_u^\gamma$. In the same figure (Figure 3.5) the Hugoniot curve (H_a) is plotted along with the isentropic curve (S_a) for compression. These curves originate from the same point A.

In the neighborhood of the initial state (p_u, v_u) the two curves are close to each other. This means that a weak shock generates a small entropy. The state after several shocks is different from the state achieved with a single shock. Figure 3.5 shows an example of the path in the (p, v) plane with three weak shocks. We can see that it is possible to follow a quasi-isentropic compression in this way. At same final pressure, the compression is higher with several shocks than with one single shock.

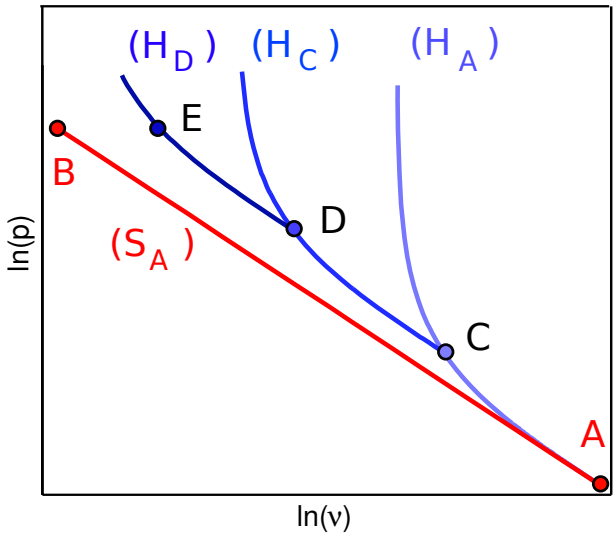

Figure 3.5: In the (p, v) plane : isentropic transformation from A to B (S_a) and Hugoniot curves starting from A, C and D (respectively (H_A), (H_C) and (H_D)).

3.3.3 Shock polar curve

After some algebraic manipulations with (3.61a) and (3.61b) it can be useful to express the Rankine–Hugoniot relations as a relation between the flow Mach numbers and the shock strength

$$\frac{u_d}{c_d} = \frac{u_u}{c_u} + s\left(\frac{2(\frac{p_d}{p_u}-1)^2}{\gamma^2(\frac{p_d}{p_u}+1)+\gamma(\frac{p_d}{p_u}-1)}\right)^{\frac{1}{2}}, \tag{3.64a}$$

where the sign of $s = \pm 1$ is the sign of the shock velocity.

The curve defined by this equation in the plane (p, u) is called a *shock polar*. It passes through the point representing the upstream state of the flow (p_u, u_u) and depends on the upstream sound velocity c_u. This representation of the shock transformation is useful to study the interaction of a shock wave with a discontinuity as we will see in the next section.

3.3.4 Interaction of a shock with a discontinuity

In this section, we discuss various interactions between a shock wave and a discontinuity.

3.3.4.1 Shocks collision

A collision between two shocks with opposite velocities generates two new shocks propagating in the opposite directions. The flow resulting from the shocks collision has a higher pressure and a lower velocity than the flow behind the two incoming shocks. The collision converts the kinetic energy of the incoming shocks into internal energy and thus enhances the transmitted shock pressure.

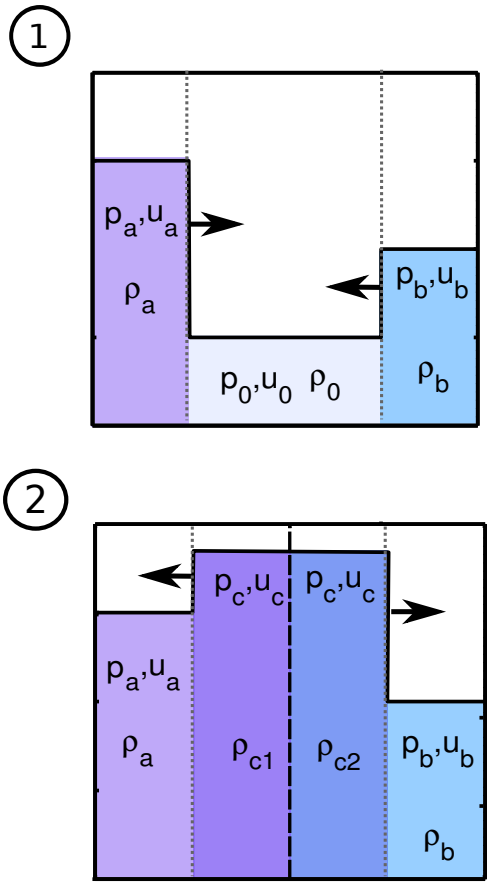

Figure 3.6: Shock pressure profiles : 1- before the collision, 2- after the collision

To simplify the problem, we assume that the two shocks propagate in a medium at rest. The theory presented below could be easily extended to the case of a moving medium by changing the reference frame. The states just before and after the collision are represented in figure 3.6. We call A the state behind the shock with the pressure p_a, the density ρ_a and the positive flow velocity u_a and B the state behind the shock with the pressure p_b, the density ρ_b and the negative flow velocity u_b. Between the two shocks, the pressure p_0 and density ρ_0 are uniform and the velocity is assumed to be zero. We introduce the dimensionless pressures $z_{a,b,c} = p_{a,b,c}/p_0$ and velocities $m_{a,b,c} = u_{a,b,c}/c_0$.

By using the Rankine–Hugoniot relations (3.64), the state in front and behind a shock wave must be on the polar curve in the plane (z, m). The polar H_o of the two shocks before the collision is given by

$$H_o \ : \ m = s\left(\frac{2(z-1)^2}{\gamma^2(z+1)+\gamma(z-1)}\right)^{\frac{1}{2}}, \tag{3.65}$$

where s equals to 1 or -1 depending on the velocity sign of the shock.

The curve H_0 shown in figure 3.7 goes through the point $O = (1, 0)$ which corresponds to the state between the shocks. The state $A = (z_a, m_a)$ and $B = (z_b, m_b)$ are placed on both branches of the curve depending on the incident shock strengths (z_a, z_b) and on the shock velocity signs

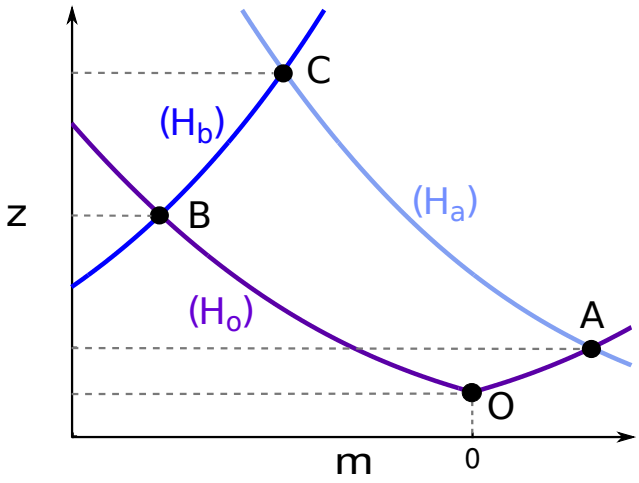

Figure 3.7: Polar curves of the collision of the shocks A and B propagating into the state O with $\gamma = 5/3$. The flow after the collision is in the state C.

(s_a, s_b).

After the collision, a discontinuity interface is created. Across this discontinuity the pressure and the velocity is continuous, whereas the density can be discontinuous. Therefore, the pressures and velocities downstream each shock after the collision must be equal. In the (z, m) plane, the states behind the two shocks after the collision are placed on the same point C. However, those shocks must rely on their own polar curves emerging from the points A and B. The state C after the collision is at the intersection of the polar curves H_a and H_b starting respectively from A and B given by the equations

$$H_{a,b} \ : \ m = -s_{a,b}\frac{c_{a,b}}{c_0}\left(\frac{z}{z_{a,b}} - 1\right)\left(\frac{2}{\gamma^2\left(\frac{z}{z_{a,b}} + 1\right) + \gamma\left(\frac{z}{z_{a,b}} - 1\right)}\right)^{\frac{1}{2}} + m_{a,b}, \tag{3.66}$$

with $m_{a,b}$ the abscissa given by (3.65) of A and B

$$m_{a,b} = s_{a,b}\left(\frac{2(z_{a,b} - 1)^2}{\gamma^2(z_{a,b} + 1) + \gamma(z_{a,b} - 1)}\right)^{\frac{1}{2}} \tag{3.67}$$

and $c_{a,b}$ the sound velocity calculated from (5.23) and $c = \sqrt{\gamma p/\rho}$

$$\frac{c_a}{c_0} = \left(z_a\frac{\gamma(z_a + 1) - (z_a - 1))}{\gamma(z_a + 1) + (z_a - 1)}\right)^{\frac{1}{2}}. \tag{3.68}$$

The equation $H_a = H_b$ where z is the unknown is of the fifth degree and is not solvable analytically. However, it can be solved graphically. An example of the graphical solution of this problem is illustrated in figure 3.7.

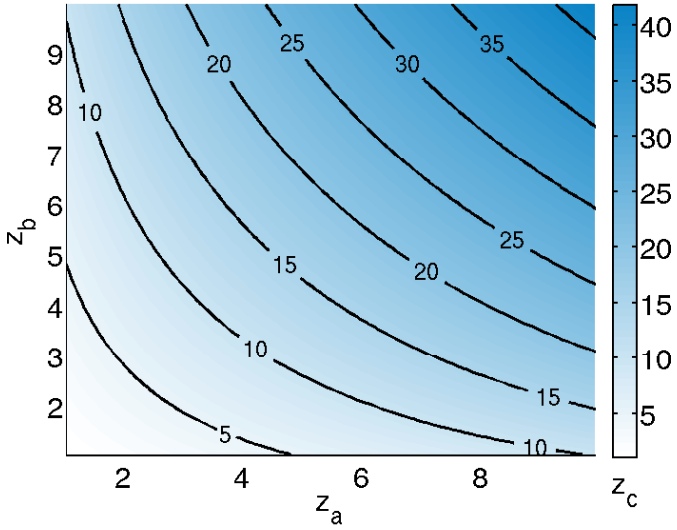

Figure 3.8: Pressure after the collision between two shocks with $\gamma = 5/3$

The calculated post collision dimensionless pressure $z_c = p_c/p_0$ depends on the incoming shock strengths (z_a, z_b) is represented in Figure 3.8. The most effective enhancement (requiring lower $z_a + z_b$) is obtained for $z_a = z_b$. Then, all the kinetic energy is converted into internal energy and the flow velocity between the shocks just after the collision is the same as before.

In this case z_c is given by

$$\left(\frac{2(\frac{z_c}{z_b} - 1)^2}{\gamma^2(\frac{z_c}{z_b} + 1) + \gamma(\frac{z_c}{z_b} - 1)} \right)^{\frac{1}{2}} = \frac{m_b}{c_b/c_0}. \tag{3.69}$$

We note that the largest gain in this case can be obtained in the limit $z_a = z_b \to \infty$. It corresponds to $z_c/z_b = (3\gamma - 1)/(\gamma - 1)$ which is equal to 6 if $\gamma = 5/3$.

The shock pressure amplification $\mathcal{X}_{coll} = z_c/z_a$ is represented on Figure 3.9.

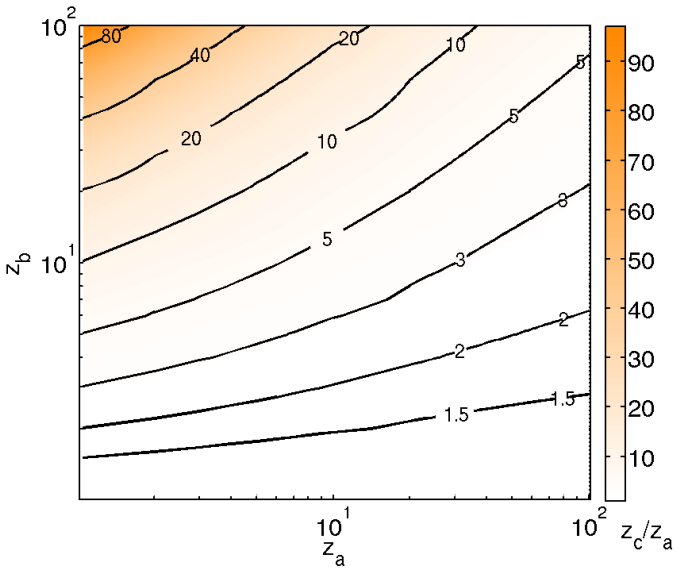

Figure 3.9: Pressure amplification in the collision $\mathcal{X}_{coll} = z_c/z_a$ with $\gamma = 5/3$. One can notice that the amplification factor tends to the limit $\mathcal{X}_{coll} = 6$ at the upper right corner of the figure where $z_b = z_a \gg 1$

3.3.4.2 Surface discontinuity

We now consider a unique shock traveling from the left to the right interacting with a contact discontinuity (CD). Before the interaction, the interaction zone is divided in three parts. The non shocked medium has a pressure p_0 and we assume that the velocity is zero.

On the left of the discontinuity the density $\rho_{0,1}$ is different from the density $\rho_{0,2}$ on the right of the discontinuity. We write

$$x = \rho_{0,1}/\rho_{0,2}, \tag{3.70}$$

the density ratio across the interface.

The polytropic index γ is assumed to be the same in the two media. Here again, we will use the dimensionless pressures $z_{a,b} = p_{a,b}/p_0$ and velocities $m_{a,b} = u_{a,b}/c_{01}$. We would like to draw the reader attention to the fact that here, the reference velocity c_{01} is the sound speed in the left medium. The point $O = (1, 0)$ represents the initial state in the plane (z, m). The downstream state of the incoming shock is given by the pressure p_a, the density ρ_a and the velocity u_a and is represented by the point $A = (p_a/p_0, u_a/c_{01})$ in the plane (z, m).

After the interaction, two final states are possible : a) a reflected and a transmitted shock waves, b) a reflected rarefaction wave and a transmitted shock wave. Figure 3.10 shows schematically the pressure profiles before and after the interaction. In any case, a shock is transmitted. At the discontinuity interface, the velocity u_b and the pressure p_b are continuous but the densities on both sides can be different ($\rho_{b1} \neq \rho_{b2}$). We write $B = (p_b/p_0, u_b/c_{01})$ the state just behind the transmitted shock.

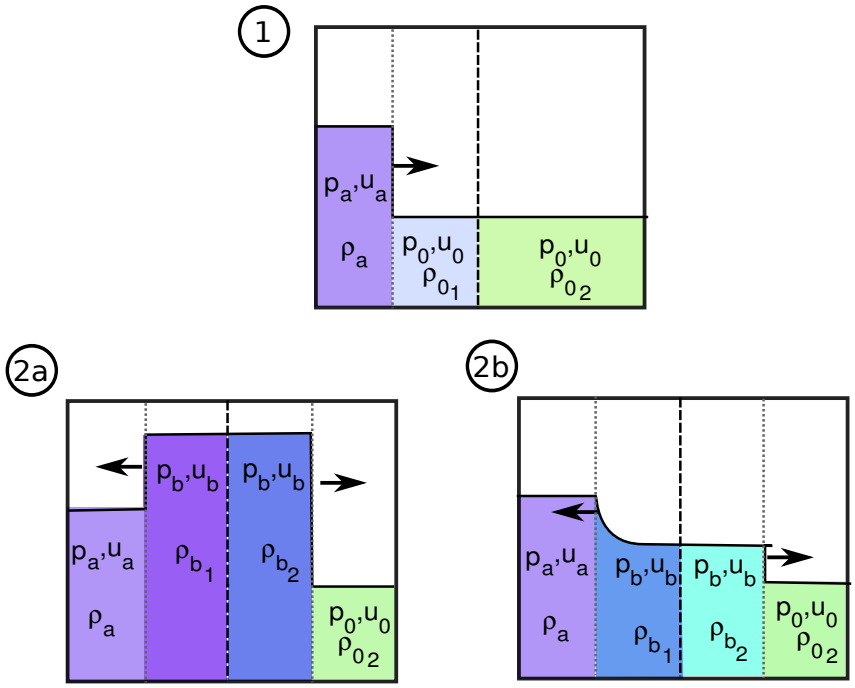

Figure 3.10: Shocks pressure profiles in the interaction of a shock wave with a contact discontinuity: 1- before the interaction , 2- after the interaction with a) the case of a reflected shock wave and b) the case of a reflected rarefaction wave.

The polar curve of the incoming shock is

$$H_{o1} \ : \ m = \left(\frac{2(z-1)^2}{\gamma^2(z+1) + \gamma(z-1)} \right)^{\frac{1}{2}}. \tag{3.71}$$

As the sound velocity is not the same across the discontinuity , the polar curve of the transmitted shock is

$$H_{o2} \ : \ m = \sqrt{x} \left(\frac{2(z-1)^2}{\gamma^2(z+1) + \gamma(z-1)} \right)^{\frac{1}{2}}. \tag{3.72}$$

The polar curves of the incoming shock and of the transmitted shock pass both through the point O. However, the slopes of those curves differ by a factor of $\sqrt{x}$. One polar curve is over the other polar curve. If the density of the right medium is higher than the density of the left medium $x < 1$, the point A is on the lower polar curve and the point B must fit on the upper curve. In this case, the reflected wave is a shock wave and the two points A and B are linked by a third polar curve. The equation of the reflected shock polar curve (H_a) is (3.66) with $s_a = 1$.

The point B is at the intersection of the curve H_a and the curve H_{o2}.

Now if $x > 1$, the point A is on the upper polar curve and the point B is on the lower curve. A reflected shock propagating into the medium A would be represented by a polar curve emerging from A that would never reach the point B. In this case, the transmitted wave is a

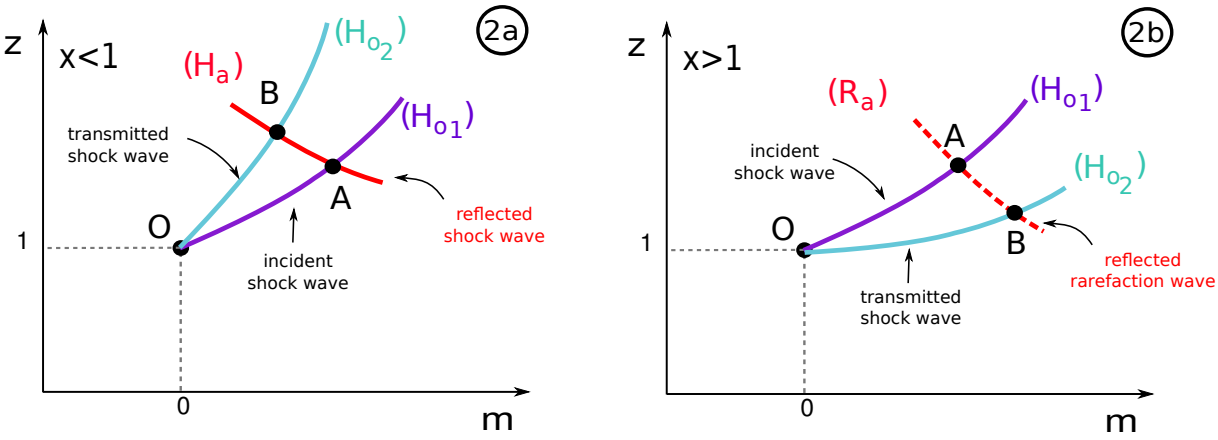

Figure 3.11: Polar curves of the interaction of a shock A propagating into the state O with a contact discontinuity surface. The transmitted shock is in the state B. The reflected wave may be a shock or a rarefaction wave depending on the density ratio x.

rarefaction wave. According to (3.34) we have

$$u_a - \frac{2}{\gamma - 1} c_a = u - \frac{2}{\gamma - 1} c. \tag{3.73}$$

As the rarefaction wave is an isentropic transformation $c/c_a = (p/p_a)^{(\gamma-1)/2\gamma}$.

Then using the dimensionless quantities, all the possible states along the rarefaction wave fulfill the equation

$$R_a \ : \ m = \frac{c_a}{c_{01}} \frac{2}{\gamma - 1} \left[\left(\frac{z}{z_a} \right)^{\frac{\gamma-1}{2\gamma}} - 1 \right] + m_a. \tag{3.74}$$

The state B in this case is at the intersection of the curve R_a and the curve H_{o2}. Figure 3.11 shows two examples of the graphical resolution of the problem, one in the case $x < 1$ and one in the case $x > 1$.

We calculated the shock pressure amplification $\chi_{CD} = z_b/z_a$ depending on the density ratio x and on the incoming shock strength z_a. The results are presented in Figure 3.12.

The transmitted shock pressure is lower than the incident shock pressure if $x > 1$ and higher than the incident shock pressure is $x < 1$. For a high density ratio at the interface and a low incident shock strength, the shock pressure amplification factor depends mainly on the incident shock strength. On the contrary, for a high incident shock strength, the shock pressure amplification factor depends only on the density ratio at the interface.

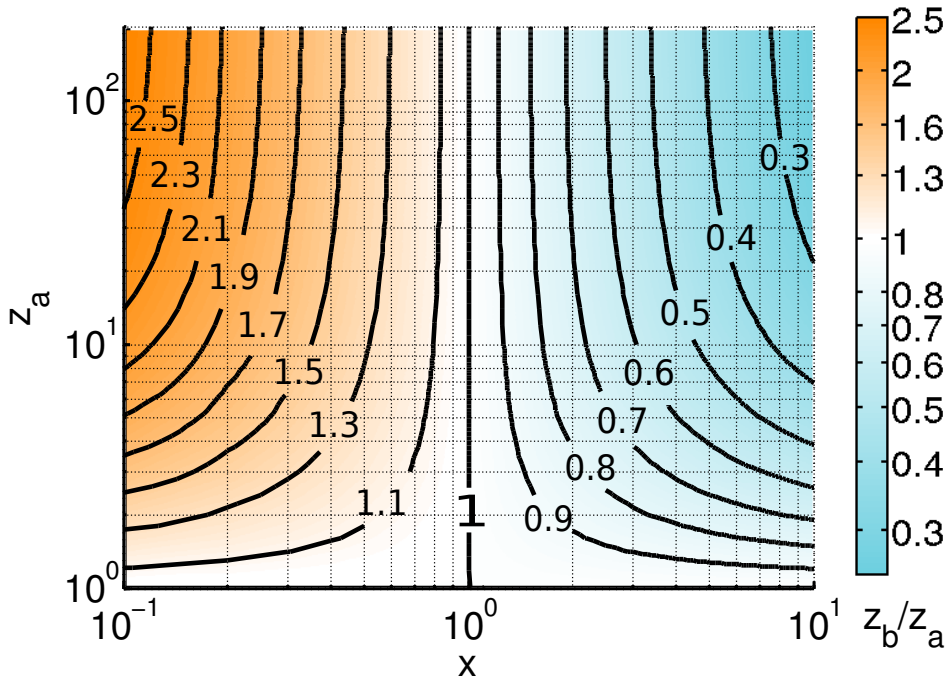

Figure 3.12: Shock pressure amplification $\mathcal{X}_{CD} = z_b/z_a$ through the interaction with a contact discontinuity surface with $\gamma = 5/3$

3.3.4.3 Overtaking shocks

The case of a shock overtaking another shock results in a transmitted shock wave. For $\gamma \leq 5/3$ the reflected wave is always a rarefaction wave. For $\gamma > 5/3$ the reflected wave may be a shock wave or a rarefaction wave. Figure 3.13 shows schematically the pressure profiles before and after the interaction between the two shocks.

The initial medium is again represented by the point $O = (1, 0)$ is the plane (z, m). The point A representing the state behind the first shock is placed on the polar curve (H_o) of equation (3.65). The point B representing the state behind the second shock is placed on the polar curve emerging from A of equation (3.66) with $s_a = 1$.

When the two shocks coalesce, a contact discontinuity surface is created. Again the pressure and velocity must be continuous. The states behind the transmitted wave and the reflected wave rely on the same point C in the plane (z, m). The transmitted shock is propagating in the unperturbed medium, the point C must be on the polar curve (H_0). The reflected wave propagates in the medium B, thus the point C must also be on a shock polar curve or an isentropic rarefaction transformation curve emerging from the point B. If the (H_o) curve is over the point B (case (a) in Figure 3.14) the point C is linked to the point B by a rarefaction wave transformation of equation

$$R_b = -\frac{c_b}{c_0}\frac{2}{\gamma - 1}\left(\left(\frac{z}{z_b}\right)^{\frac{\gamma-1}{2\gamma}} - 1\right) + m_b \tag{3.75}$$

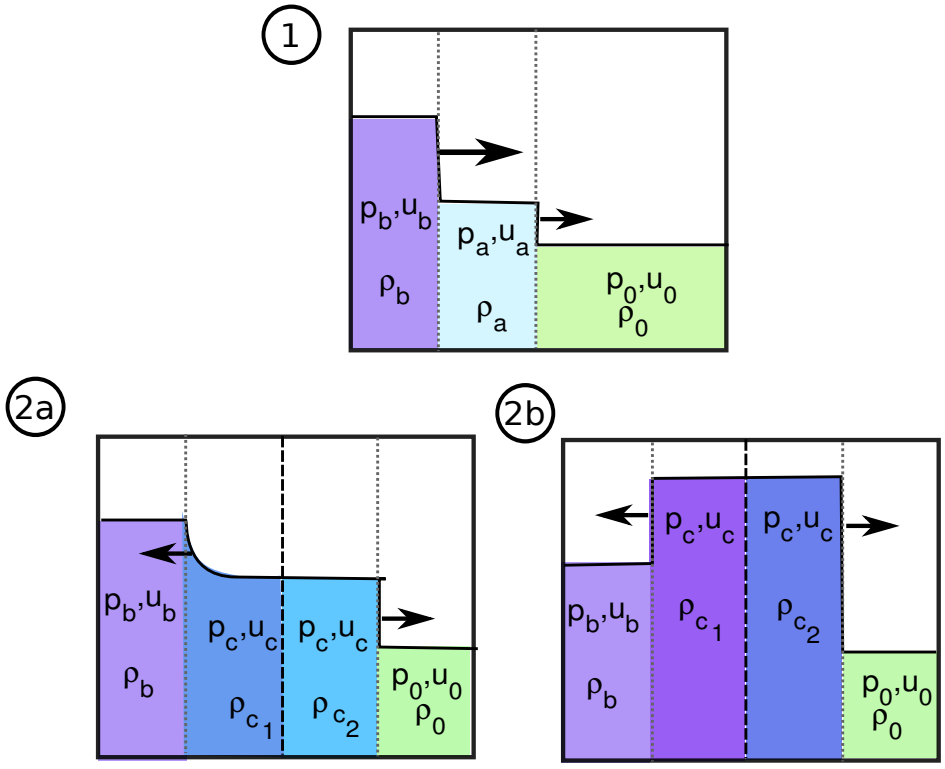

Figure 3.13: Shock pressure profiles in the coalescence of two shock waves : 1- before the interaction , 2- after the interaction with a) the case of a reflected rarefaction wave and b) the case of a reflected shock wave .

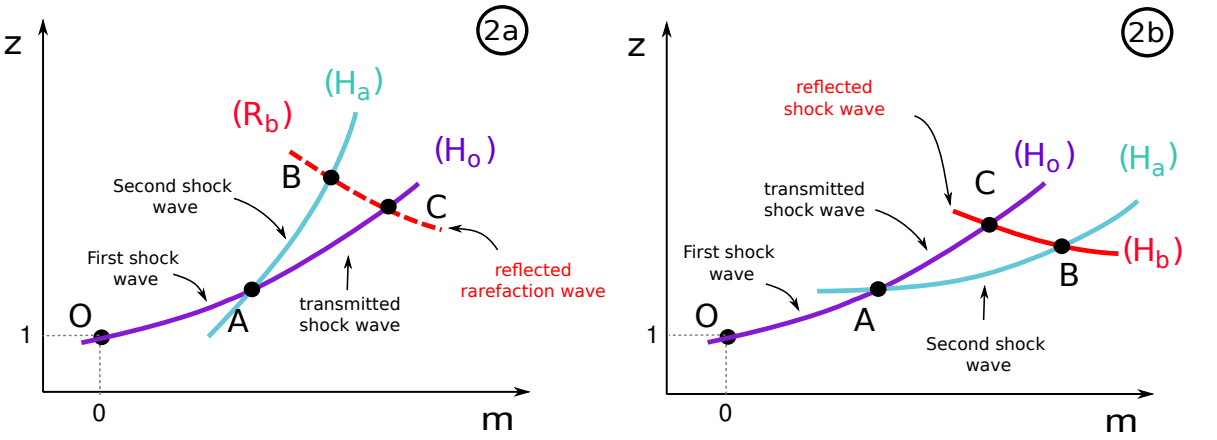

Figure 3.14: Polar curves of a shock A propagating into the state O overtaken by a faster shock B. The transmitted shock is in the state C. The reflected wave may be a shock or a rarefaction wave depending on the polytropic coefficient γ.

with

$$\frac{c_b}{c_0} = \frac{c_a}{c_0}\left(\frac{z_b}{z_a}\frac{\gamma(\frac{z_b}{z_a}+1)-(\frac{z_b}{z_a}-1))}{\gamma(\frac{z_b}{z_a}+1)+(\frac{z_b}{z_a}-1)}\right)^{\frac{1}{2}} \tag{3.76}$$

and

$$m_b = -\frac{c_a}{c_0}(\frac{z_b}{z_a}-1)\left(\frac{2}{\gamma^2(\frac{z_b}{z_a}+1)+\gamma(\frac{z_b}{z_a}-1)}\right)^{\frac{1}{2}} + m_a. \tag{3.77}$$

If the (H_o) curve is below the point B (case (b) in Figure 3.14), the point C is linked to the point B by a polar shock curve of equation

$$H_b \ : \ m = -\frac{c_b}{c_0}(\frac{z}{z_b}-1)\left(\frac{2}{\gamma^2(\frac{z}{z_b}+1)+\gamma(\frac{z}{z_b}-1)}\right)^{\frac{1}{2}} + m_b. \tag{3.78}$$

The configuration depends on γ, z_a and z_b. Figure 3.15 and Figure 3.16 show the shock pressure amplification factor when it overtakes a first shock for $\gamma = 5/3$ and $\gamma = 3$ receptively. For $\gamma = 5/3$, the reflected wave is a rarefaction wave and the pressure is lower after the coalescence. In the case of $\gamma = 3$, there is a region where the reflected wave is a shock wave (for $z_b/z_a < 4$). In this region, the amplification factor is higher than unity. For $z_b/z_a > 8$ the reflected wave is a rarefaction wave. For $4 < z_b/z_a < 8$, the reflected wave is either a shock or a rarefaction wave depending on z_a. In the case of high first shock strength $z_a \gg 1$, the amplification factor depends only on the second shock strength and γ.

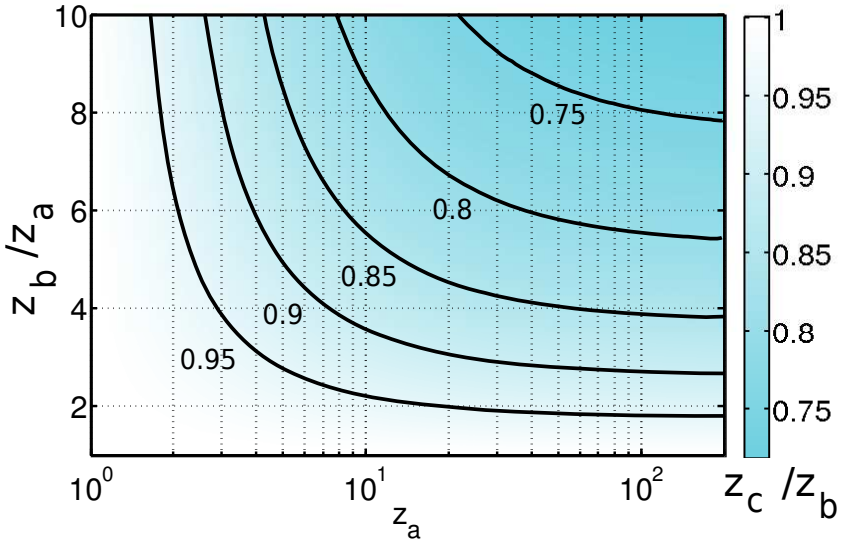

Figure 3.15: Shock pressure amplification $\mathcal{X}_{coal} = z_c/z_b$ when the shock overtakes another shock in a medium with $\gamma = 5/3$. It depends on the first shock strength z_a and on the second shock strength z_b/z_a.

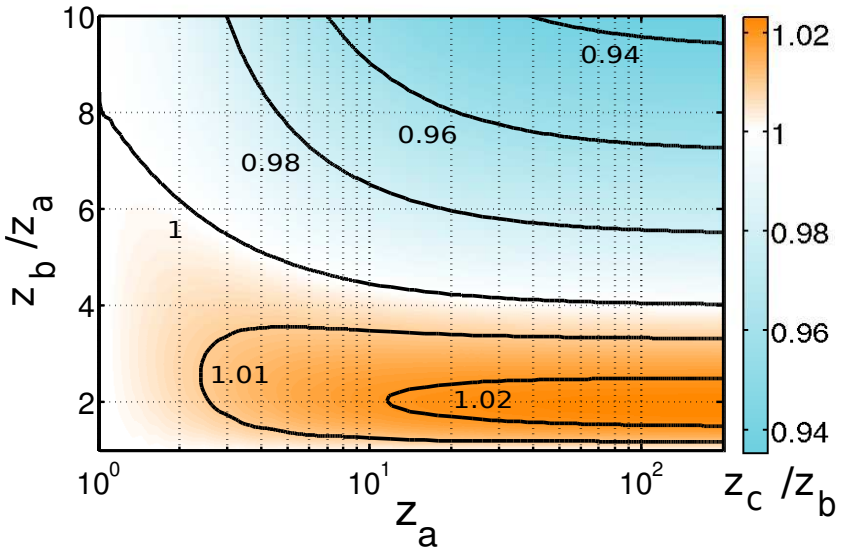

Figure 3.16: Shock pressure amplification $\mathcal{X}_{coal} = z_c/z_b$ when the shock overtakes another shock in a medium with $\gamma = 3$. It depends on the first shock strength z_a and on the second shock strength z_b/z_a.

3.3.4.4 Interaction with a rarefaction wave

Let us consider a shock of a given strength, propagating from the left to the right. It encounters a rarefaction wave also of a given strength propagating from the right to the left. The transmitted wave is a shock wave and the reflected wave is a rarefaction wave. Figure 3.17 sketches the interaction process.

Both incoming waves propagate in the initial flow represented by the point $O = (1, 0)$ in the plane (z, m). The state A of the shock wave relies on the polar curve (H_o) of equation (3.65). The state behind the rarefaction wave relies on the isentropic transformation curve R_o of equation

$$R_o \ : \ m = \frac{2}{\gamma - 1}\left(z^{\frac{\gamma-1}{2\gamma}} - 1\right). \tag{3.79}$$

The locus of all the possible states for the transmitted shock (H_b) is defined by the equation

$$H_b \ : \ m = \frac{c_b}{c_0}(\frac{z}{z_b} - 1)\left(\frac{2}{\gamma^2(\frac{z}{z_{a,b}} + 1) + \gamma(\frac{z}{z_b} - 1)}\right)^{\frac{1}{2}} + m_b, \tag{3.80}$$

where the abscissa m_b is given by (3.79)

$$m_b = \frac{2}{\gamma - 1}\left(z_b{}^{\frac{\gamma-1}{2\gamma}} - 1\right) \tag{3.81}$$

and the sound velocity c_b is expressed according to (3.73)

$$\frac{c_b}{c_0} = z_b{}^{\frac{(\gamma-1)}{2\gamma}}. \tag{3.82}$$

All possible states behind the reflected rarefaction wave (R_a) are defined by the equation (3.74). The velocities and pressures behind the two generated waves after the interaction are the same and represented by the point C in the plane (z, m). The point C is the intersection of (H_b) and (R_a) (see figure 3.18).

The resulting shock pressure amplification factor $\mathcal{X}_R = z_c/z_a$ is plotted in Figure 3.19. For a given rarefaction wave, higher is the strength of the incident shock, lower is the amplification factor.

In this section, the basic equations describing a shock wave are given. They allow to describe the flow quantities jump at the shock front. The description of the flow behind a shock wave is done by coupling the hydrodynamic equation presented in the previous section with the Rankine-Hugoniot relations at the shock front. In most of the cases, the problem is hard to solve and simplifications are needed. The next section gives several approaches for the description of a shock wave in a spherical geometry which is of a particular interest for the shock ignition analysis.

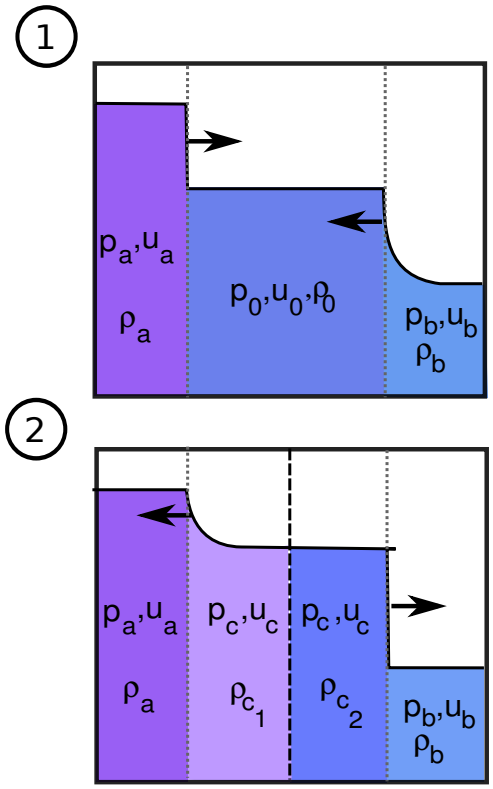

Figure 3.17: Pressure profiles in the interaction of a shock wave and a rarefaction wave: 1- before the interaction , 2- after the interaction.

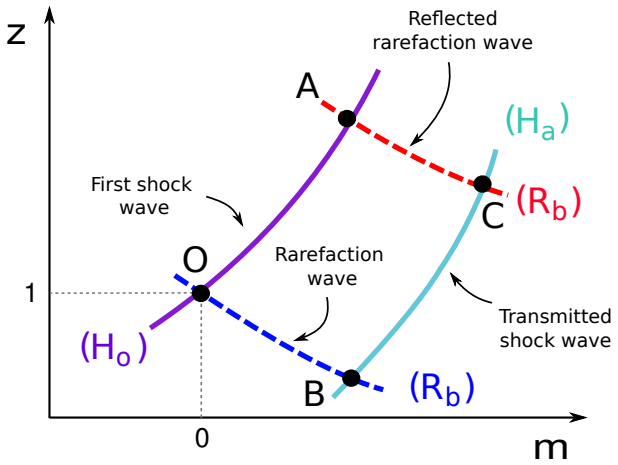

Figure 3.18: Polar curves of a shock A interacting with a rarefaction wave B. The transmitted shock is in the state C. The reflected wave is a rarefaction wave.

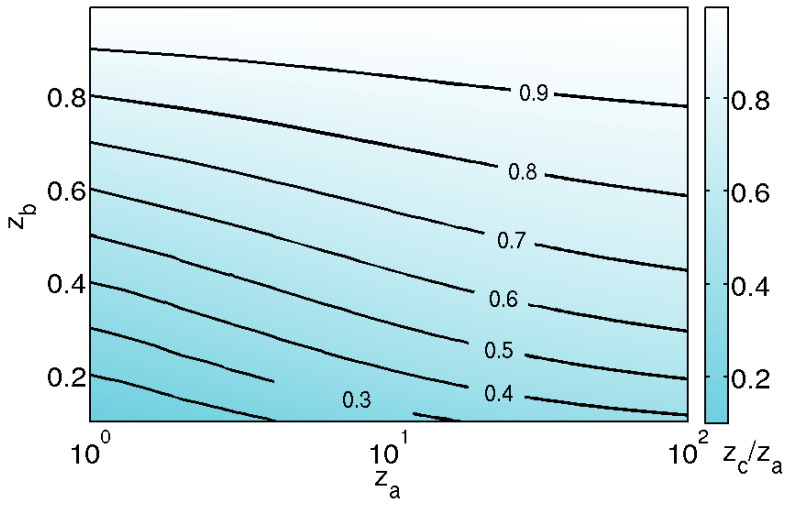

Figure 3.19: Shock strengthening in the interaction with a rarefaction wave for $\gamma = 5/3$

3.4 Spherical shock wave

Spherical converging shock waves have been a subject of interest since a long time. The very high density and temperature at the moment of the collapse could be used to ignite nuclear or chemical reactions. A lot of papers have been published on this subject. We propose here a short review of the main results on this topic.

As the converging shock wave is a strongly non-linear phenomenon, it is difficult to describe it with an analytical solution. One may simplify the problem by making strong assumptions. It is possible for example to assume that the problem is invariant under a defined transformation. Such solutions are called *self-similar* solutions and they may exist under specific boundary and initial conditions. It is also possible to neglect the flow behind the shock. Then the quantities can be described along the shock front. Some authors prescribe a specific form of the solution to simplify the problem. In any case, there is no analytical solution describing a converging shock in a general case. We present in this section some of the methods stated above.

3.4.1 Self-similar solution

A set of equations could present symmetry properties and be invariant under particular transformations [Sédov, 1977, Coggeshall and Axford, 1986, Hydon, 2000]. Transformation examples with a physical meaning are translation, stretching, rotation or projection. A basic example is the equation of a circle, which is invariant under a rotation around its center. By considering solutions invariant under a set of transformations, one could make an assumption concerning form of the solutions and simplify the set of equations. Basically, the set of partial differential equations (3.24) could be reduced to a system of ordinary differential equations.

The solutions of the hydrodynamic equations (3.24) could be represented in a 5 dimensional space : r, t, ρ, c and u. An infinitesimal transformation generator is a linear combination of the

partial derivatives in this space. Finding the transformations for which a set of equations is invariant is considered in the Lie group theory. Here we expose only the transformation leading to the scale invariant solutions [Atzeni and Meyer-Ter-Vehn, 2004]

$$U = U_{st} + a_{sr}U_{sr} + a_{s\rho}U_{s_\rho}, \tag{3.83}$$

which is a combination of the time stretching

$$U_{st} = t\partial_t - u\partial_u - c\partial_c, \tag{3.84}$$

space stretching

$$U_{sr} = r\partial_r + u\partial_u + c\partial_c - (j+1)\rho\partial_\rho, \tag{3.85}$$

and density stretching

$$U_{s\rho} = \rho\partial_\rho. \tag{3.86}$$

The form of the self-similar solution under the transformation of the generator $U = \xi_r\partial_r + \xi_t\partial_t + \xi_u\partial_u + \xi_c\partial_c + \xi_\rho\partial_\rho$ is found by integrating the characteristic equations

$$\frac{\mathrm{d}r}{\xi_r} = \frac{\mathrm{d}t}{\xi_t} = \frac{\mathrm{d}u}{\xi_u} = \frac{\mathrm{d}c}{\xi_c} = \frac{\mathrm{d}\rho}{\xi_\rho}. \tag{3.87}$$

Using the generator (3.83), the characteristic equations become

$$\frac{\mathrm{d}r}{a_{sr}r} = \frac{\mathrm{d}t}{t} = \frac{\mathrm{d}u}{(a_{sr}-1)u} = \frac{\mathrm{d}c}{(a_{sr}-1)c} = \frac{\mathrm{d}\rho}{(a_{s\rho}-(j+1)a_{sr})\rho}. \tag{3.88}$$

This leads to the solutions in the form :

$$\xi = \frac{(r/r_0)}{(t/\tau)^\alpha}, \tag{3.89a}$$

$$\rho(r,t) = \rho_0(r/r_0)^k G(\xi), \tag{3.89b}$$

$$u(r,t) = u_0\frac{r/r_0}{t/\tau}U(\xi), \tag{3.89c}$$

$$c(r,t) = u_0\frac{r/r_0}{t/\tau}C(\xi). \tag{3.89d}$$

The new functions U, C and G depend on only one independent variable ξ called the self-similar coordinate. The parameters α and k should be found to fulfill the boundary conditions. The parameters r_0 , τ, u_0 and ρ_0 are characteristic problem values in unit of length, time, velocity and density respectively.

In this way the set of partial differential equations (4.1) could be transformed into a set of ordinary differential equations. The function $G(\xi)$ has an analytical expression. The functions

U and C can be integrated from two equations of the form

$$\frac{\mathrm{d}U}{\mathrm{d}C} = \frac{\Delta_1(U,C,\alpha)}{\Delta_2(U,C,\alpha)}, \quad \frac{\mathrm{d}\ln\xi}{\mathrm{d}C} = \frac{\Delta(U,C)}{\Delta_2(U,C,\alpha)} \tag{3.90}$$

with Δ, Δ_1 and Δ_2 non-linear functions.

The boundary conditions must be invariant under the similarity transformation. After the transformation, the boundary conditions become initial conditions and apply for constant values of ξ. Thus shock position or material boundary positions follow lines of a constant ξ.

As the shock front corresponds to a fixed value of ξ, the relation (3.89a) gives the converging shock front position

$$R_s(t) = R_s(\tau)\left(\frac{t}{\tau}\right)^{\alpha}, \tag{3.91}$$

with $R_s(\tau)$ the shock position at a given time τ. The shock pressure $p = \gamma\rho c^2$, can be expressed using (3.89)

$$p_s(R_s) = p_s(R_0)\left(\frac{R_s}{R_0}\right)^{2(1-1/\alpha)}, \tag{3.92}$$

with $p_s(R_0)$ the shock pressure at a given position R_0.

The equations become singular where Δ, Δ_1 and Δ_2 vanish or become infinite. The plane (U,C) is divided in two parts by the *sonic line* of equation $U + C = 1$ where $\Delta = 0$. If the solution crosses this line, it must pass through a singular point where the three functions Δ, Δ_1 and Δ_2 vanish in order to have $\mathrm{d}\ln\xi/\mathrm{d}C \neq 0$. Otherwise the solution is double valuated for one value of ξ which is not physical.

It exists an infinity of solutions depending on the value of the parameter α [Oppenheim et al., 1972]. Figure 3.20 shows the solutions (U,C) obtained for several values of α with $\gamma = 5/3$. The unique solution of a given problem depends on the initial and boundary conditions. When $\alpha = 1$ the shock has a constant velocity. The Taylor–Sedov explosion [Taylor, 1946, Sédov, 1946] from a point-like source with a given energy is described with $\alpha = 0.4$. The curves in the zone ① are attracted by the singular point $(U = 1, C = \infty)$. The arrows indicate the direction of increasing ξ. In this zone the coordinate ξ is increasing toward the shock position. This means that the solution corresponds to an explosion. Also, the limit $C \mapsto \infty$ corresponds to an infinitely high temperature, thus it corresponds to the explosion driven by a hot piston. In the same way we can see that the curves in the zone ② describe a shock driven by a cold piston $(C \mapsto 0)$. The curves in the zone ③ stop at singular points where U and C are finite. As ξ tends to infinity in those points, those implosions are driven from infinity by an infinite temperature and an infinite velocity. In the zone ④, the curves go toward the point $P_4 = (0,0)$ which corresponds to a finite boundary conditions far from the origin. They cross the sonic line where the solutions become singular. Thus those solutions are not physical, except from the particular solution with $\alpha = 0.69$ which is the Guderley's solution.

Guderley [Guderley, 1942] was the first to use this self-similar solution to describe a converging shock. He assumed that the shock strength is high and that the upstream sound velocity is

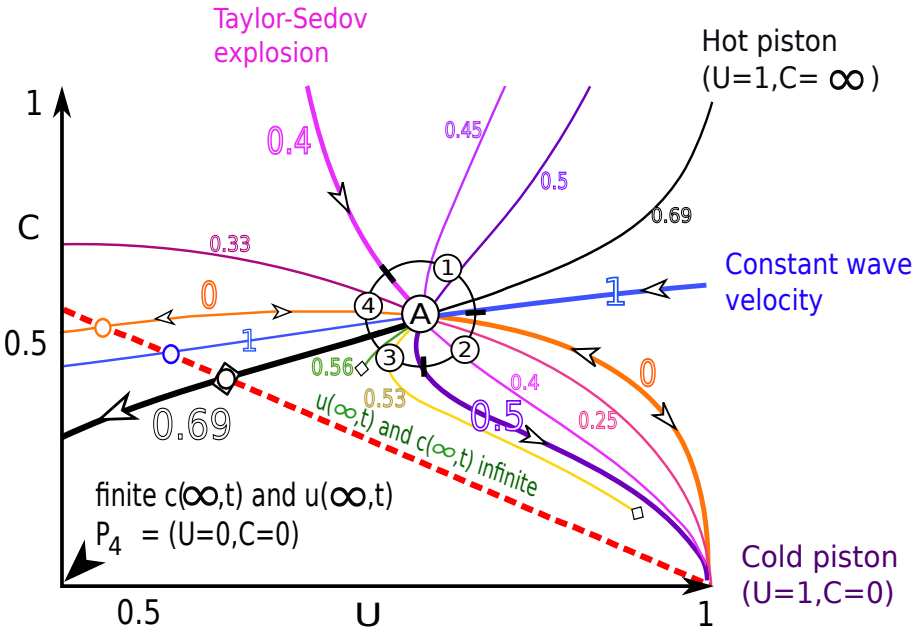

Figure 3.20: Physical meaning of the solution depending on the parameter α. The point A represent the state behind a shock. The arrows indicate the direction of increasing ξ.

negligible. Moreover, he considered that the upstream density is homogeneous with $k = 0$. He obtained the boundary conditions represented by the point A in Figure 3.20:

$$C(\xi_s) = \frac{2\gamma(\gamma-1)}{(\gamma+1)^2}, \quad G(\xi_s) = \frac{\gamma+1}{\gamma-1}, \quad U(\xi_s) = \frac{1-\gamma}{\gamma+1} \tag{3.93}$$

with ξ_s being the value of ξ at the shock front.

In the problem of Guderley, the shock is generated by a piston having a finite velocity and a finite temperature far from the origin. The solution links the point A to the point $P_4 = (0, 0)$ in Figure 3.20. It must cross the sonic line where the equations are singular. This is possible only through one point, where the both numerator and denominator vanish in the equations. The exponent α cannot be determined by the dimensional considerations alone. It must be iteratively calculated so that the solution does not undergo any singular behavior apart from the shock position. The problem consists then to solve a non-linear eigenvalue problem, and the solution is qualified as a self-similar solution of the second kind. For $\gamma = 5/3$, the value of the parameter α is $\alpha = 0.688$.

The parameter α value was calculated with an increasing accuracy by several authors [Lazarus and Richtmyer, 1977, Lazarus, 1981, Butler, 1954, Brushlinskii and Kazhdan, 1963, Stanyukovich, 1960]. In particular, Lazarus [Lazarus, 1981] gives a complete analysis of the self-similar solutions describing a strong convergent shock or of a cavity implosion in cylindrical and spherical geometries. He describes each singular point and explores several values of the parameter α depending on γ. He also describes more exotic problems like several shock fronts or problems

including a free surface.

The solution of Guderley has been extended to more general problems. For instance, the propagation of a shock wave in a non uniform medium was studied in Refs. [Yousaf, 1985, Ramu and Rao, 1993, Toqué, 2001] and the vibrational relaxation of a diatomic gas - in Ref. [Sharma and Radha, 1995].

Other authors tried to evaluate the parameter α by using physical or mathematical assumption. Mishkin and Fujimoto [Fujimoto and Mishkin, 1978] assumed that it exists a pressure maximum behind the converging shock and used this argument to find a value for α. Chisnell [Chisnell, 1997], proposed an approximate analytical solution based on a simple trial function of the form $C_T = f(U, \alpha, \gamma)$. This function is defined to keep the limit behavior of the Guderley solution in the vicinity of P_4 and to avoid the singularity in P_3. He also imposed a positive gradient of the solution $C(U)$ in P_3 and the boundary conditions in A.

A phenomenological method was used by Chisnell [Chisnell, 1957] and Chester [Chester, 1954] to study the dynamics of a converging shock wave. They consider that the shock is propagating into a channel divided into infinitesimal layers of varying area section or density. The incident shock refracts at the discontinuity surfaces. The conservation laws across the shocks and contact discontinuities give a relation between the shock Mach number and the cross-section area or the density variation. The results obtained with this method were also found by Whitham [Whitham, 1958] but with another approach. The author approximated the shock dynamics by using conservation equations in the characteristic form and by assuming that the shock follows a characteristic path. The main limitation of these methods is that the influence of the flow behind the shock is neglected. This approximation is called the "freely propagating shock wave" or the "CCW" (Chester - Chisnell - Whitham) approximation and will be expanded on below.

3.4.2 Freely propagating shock wave

Whitham considers a shock propagating into a tube of a varying cross-section area $A(x)$ initially at rest and homogeneous. He uses the characteristic form of the conservation equations (3.24). The C^+ characteristic reads

$$\mathrm{d}p + \rho c \,\mathrm{d}u + \frac{\rho c^2}{u + c} \frac{\mathrm{d}A}{A} = 0 \tag{3.94}$$

on $\mathrm{d}x/\,\mathrm{d}t = u + c$.

Whitham assumes that the shock position is close to the C^+ characteristic. The Rankine–Hugoniot relations (3.61) are injected into the characteristic equation (3.94). This leads to an equation for M_s as a function of the tube area A

$$\frac{1}{A} \frac{\mathrm{d}A}{\mathrm{d}M_s} = -g(M_s) \tag{3.95}$$

where $g(M_s)$ is the following function

$$g(M_s) = \frac{M_s}{M_s^2 - 1}\left(1 + \frac{2}{\gamma + 1}\frac{1 - \mu^2}{\mu}\right)\left(1 + 2\mu + \frac{1}{M_s^2}\right) \tag{3.96}$$

with $\mu = \sqrt{\frac{(\gamma-1)M_s^2+2}{2\gamma M_s^2-(\gamma-1)}}$ the downstream relative shock Mach number.

This function can be integrated numerically a first time to obtain the shock velocity as a function of the position and a second time to obtain the shock position as a function of time. Once this is known, the flow quantities just behind the shock are evaluated with the Rankine–Hugoniot relations.

In the *freely propagating shock wave* approximation, the interaction of the shock with the downstream flow is neglected. This assumption is better suited for imploding shock waves than for the expanding ones. Chisnell, in a more accurate model, evaluated the influence of the geometrical effects on the downstream flow and the influence of the downstream flow on the shock. He found out that for the imploding shock wave, the Witham model is quite accurate and that the correction could be neglected. However, the CCW approximation is not sufficiently accurate in the case of a varying density in front of the shock. Indeed, Hayes [Hayes, 1968] found a discrepancy of 15% between the computed shock dynamics equation and the self-similar solution in the case of a diverging spherical shock in an exponential density profile. Similarly, Sakurai [Sakurai, 1960] found an error of about 10% in the case of a power-law initial density profile. By using the Guderley's self-similar solution, Yousaf [Yousaf, 1978] included the overtaking disturbance behind the shock in the CCW approximation. He also calculated a correction to the shock dynamics equation for an exponential and a power-low density profiles in front of the shock citeYousaf85.

Whatever the initial conditions of a converging shock wave are, the flow approaches asymptotically the self-similar solution in the neighborhood of the collapse point. To describe a flow with specific boundary conditions in a domain larger than the vicinity of the center of implosion one needs to consider non self-similar solutions.

3.4.3 Quasi-self similar solutions

Van Dyke et al. [Dyke and Guttmann, 1982] described a converging shock driven by a piston by using analytical series. The zeroth order term corresponds to a plane problem and the high order terms account for the spherical effects. In the same way, the counter pressure upstream the shock appears through the Mach number in the boundary conditions and deviates the flow from the self-similar solution. Oshima [Oshima, 1960] described a diverging shock wave with three approximations depending on the Mach number : strong, intermediate and weak shock. For intermediate Mach numbers, the author used successive instantaneous self-similar solutions of a constant Mach number and obtained a "quasi–self-similar" solution. The parameter α is calculated for each instantaneous step for a given Mach number. The similarity relations are

also modified. For example, the function G is expressed as the product of two functions

$$G(\xi, M_s) = X(\xi)Y(M_s). \tag{3.97}$$

By implementing this separation of variables, the Euler's partial differential equations were transformed into a system of ordinary differential equations where the shock Mach number appears as a parameter. Oshima defined $\lambda = \frac{\mathrm{d}\ln M_s}{\mathrm{d}\ln R_s}$ as the amplification factor which depends on the shock Mach number. For a given Mach number, the equations are integrated in the same way as the self-similar solutions presented above (Section 3.4.1). The parameter λ plays the same role as the parameter α in the Gudelrey's solution. It is calculated iteratively for a given Mach number. As the Mach number varies with time, the time is discretized. At each step, the problem is solved, the shock trajectory is found and the Mach number of the next time step is computed.

Lee [Lee, 1967] applied the same method for a converging shock and Axford [Axford and Holm, 1981] extended this method to a more general equation of state.

3.4.4 Series form solutions

Sakurai [Sakurai, 1953] proposed another method to describe a diverging shock wave with a finite upstream pressure. He expressed the solution in a power series of the shock Mach number M_s^{-2}. The zeroth order term of his solution corresponds to the self-similar solution of Taylor–Sedov for a point-like explosion. The mathematical proof of existence of this solution has been demonstrated by Takahashi [Takahashi, 2009]. The series form generalization of the Guderley imploding shock problem was suggested by Hunter [Hunter, 1960] and performed later by Welsh [Welsh, 1967] in the context of a cavity collapse. However, in the Welsh work, only the converging phase was studied.

In a same way, Ponchaut [Ponchaut et al., 2006] extended the self-similar Guderley's solution by using the solutions in a series form. Higher order terms allowed him to describe a shock of intermediate Mach number. He also calculated the solution for a small Mach number and by merging these two solutions with the characteristic method, obtained an "universal" solution [Hornung et al., 2008] for imploding shock waves.

3.5 Conclusion

In this chapter, we gave a number of basic results which are useful for the development of the theory in subsequent chapters. We stated the governing equations for an ideal compressible gas flow which are the conservation of mass, of momentum and of energy. They are expressed in several useful forms : Eulerian, Lagrangian, and characteristics form. Also the particular case of a homogeneous isentropic implosion is presented. This ideal case can be used to describe the shell implosion and will be employed in Chapter 5.

Basic equations governing shock waves were next presented. The most important are the

Rankine–Hugoniot relations which are the starting point for many analysis in this thesis. The compression behind a shock is limited. A better compression of the matter is achieved by several weak shock waves. Then, the compression is nearly isentropic. In ICF implosion, the entropy in the target must be minimized (see Section 2.3.1). The optimal laser pulse would generate an ablation pressure that follows the Kidder law (3.59) given in Section 3.2. However, for technical reasons, this isentropic compression is often approached with several shock waves. The laser pulse consists then in three or four "pickets" instead of the continuous ramp described in 2.3.1. Nevertheless, in this thesis, the ideal case of a homogeneous isentropic compression will be considered.

The interaction of a shock wave with a discontinuity cannot be described analytically (except for specific cases). However it can be solved graphically. We presented maps where the shock pressure amplification through the interaction with a discontinuity can be read. This will be useful in Chapter 5 and in Chapter 6 where such interactions are analyzed.

Lastly, the mathematical methods that can be used to describe the shock wave propagation in a spherical geometry were outlined. The series extension of a self-similar solution and the "CCW" shock dynamics approaches will both be revisited in the next two chapters.

4 Coupling of the ignitor shock with the hot-spot

Contents

In this chapter we focus on the propagation of the ignitor shock in the target hot-spot at the end of the implosion. The shell is considered as a piston and we assume that the inner radius of the shell follows a particle trajectory. The aim is to define the ignition conditions for shock ignition.

We describe the flow in the hot-spot as the ignitor shock converges and diverges in it (Section 4.1). The final state of the hot-spot is related to the initial conditions when the shock just enters in the hot-spot. The initial shock Mach number is shown to be an important parameter. The effect of the initial shock Mach number on the shock coupling to the hot-spot is analyzed in Section 4.2. By requesting ignition conditions at the exit time of the shock, an ignition criterion based on the initial conditions of the shock and of the hot-spot are expressed in Section 4.3.

4.1 Spherical shock wave with a finite Mach number

It is possible to use the self-similar solution of Guderley to describe the converging and the diverging phase of a spherical shock. However, as it is explained in Section 3.4.1 the boundary conditions have to remain invariant under the self-similar transformation. The boundary condition in the present problem are the Rankine–Hugoniot relations at the front shock. The self-similar solution of Guderley applies only for an infinite Mach number. This means that the upstream sound velocity is neglected compared to the shock velocity. Figure 4.1 shows the evolution of the pressure ratio at the shock front as it propagates in a typical imploded target. We can see that it remains moderate in the shell and fall to about 1.5 when the shock enters the hot-spot. Then it increases due to the convergence effects at the very center of the hot-spot. This means that while describing the shock propagation through the whole hot-spot, the initial pressure, and therefore the initial sound velocity, cannot be neglected. We present in this Section a description of the flow induced by a shock wave of a finite initial Mach number M_{s0} in a homogeneous gas sphere. Our approach is based on the method developed by Sakurai [Sakurai, 1953] and Ponchaut [Ponchaut et al., 2006]. We calculate a linear correction of the Guderley's solution and analyze the physical meaning of the finite Mach number correction terms.

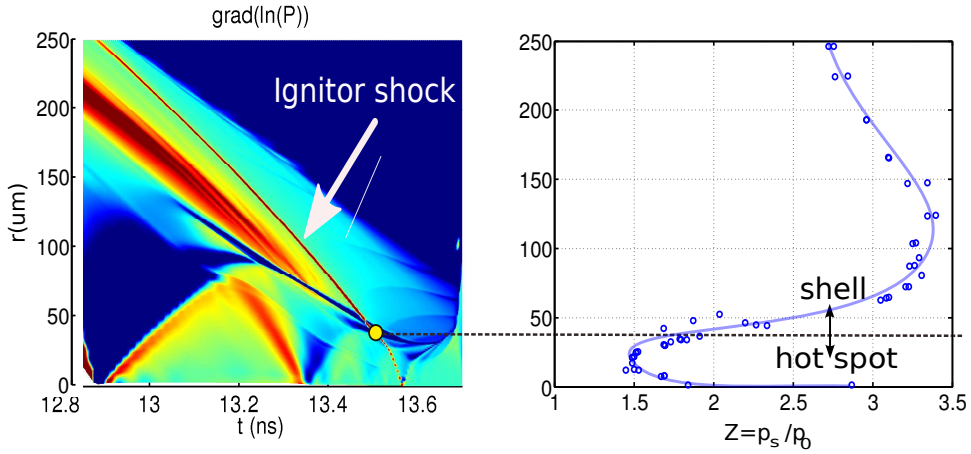

Figure 4.1: Pressure gradient evolution during the deceleration phase of the shell (left panel) and evolution of the pressure ratio along the ignitor path (right panel).

4.1.1 Basic equations

In this study we consider the converging phase, the rebound and the diverging phase of a shock wave in a homogeneous sphere at rest. We use a 1D spherical formalism. The independent variables are the radius r and the time t. The flow is characterized by the density $\rho(r,t)$, the fluid velocity $u(r,t)$ and the local sound speed $c(r,t)$ related to the pressure $p(r,t)$ by the ideal gas equation of state $c^2 = \gamma p/\rho$, where γ is the specific heat ratio. The specific entropy is defined as $s = p/\rho^\gamma$.

The conservation laws of mass, momentum and energy are expressed by the Euler's equations (3.24) without dissipative effects:

$$\partial_t \rho + \partial_r(\rho u) + \frac{2\rho u}{r} = 0, \tag{4.1a}$$

$$\rho \partial_t u + \rho u \partial_r u + \frac{1}{\gamma}\partial_r(c^2\rho) = 0, \tag{4.1b}$$

$$\partial_t c + u\partial_r c + \frac{\gamma-1}{2} c \partial_r u + (\gamma-1)\frac{uc}{r} = 0. \tag{4.1c}$$

We consider a shock traveling into a medium initially at rest with a uniform density ρ_0 and a sound speed c_0.

The shock trajectory $R_s(t)$ is a unknown of the problem. The reference time $t = 0$ is chosen at the collapse, thus $R_s(0) = 0$. At this time the shock velocity is infinite. The initial shock velocity U_{s0}, at the reference position R_0 and the time $-t_{conv}$, defines the initial shock Mach number $M_{s0} = U_{s0}/c_0$.

The flow is driven by a piston of trajectory $R_p(t)$ which coincides with a particle path starting at the position R_0. We consider $R_p(t)$ as the trajectory of the imploding shell. We define $R_p(t_{div})$ the position of the shock when it exits from the compressed sphere and collides with the piston.

The entire domain (r,t) is divided into four sub-domains $(\mathcal{D}_I, \mathcal{D}_{II}, \mathcal{D}_{III}, \mathcal{D}_{IV})$ represented

in Figure 4.2. In the following, we indicate the number of the domain with a subscript in the flow quantities if a relation is valid on only one domain, otherwise the function has no subscript.

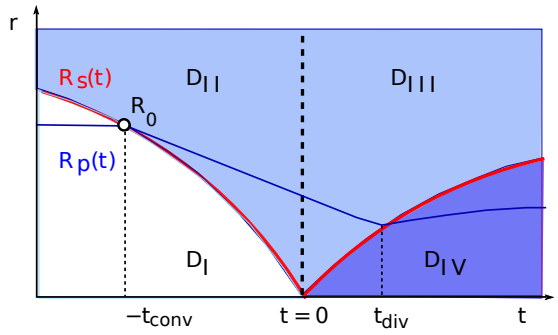

Figure 4.2: Sub-domains, shock path and particle path in the (r,t) plane: $\mathcal{D}_I$ - upstream in the converging phase, $\mathcal{D}_{II}$-downstream in the converging phase, $\mathcal{D}_{III}$-upstream in the diverging phase, $\mathcal{D}_{IV}$-downstream in the diverging phase.

The domain $\mathcal{D}_I$ corresponds to the upstream flow ahead the converging shock. The gas in this domain is unperturbed and

$$u_I(r,t) = 0, \tag{4.2a}$$
$$\rho_I(r,t) = \rho_0, \tag{4.2b}$$
$$c_I(r,t) = c_0. \tag{4.2c}$$

The domain $\mathcal{D}_{II}$ corresponds to the gas downstream the converging shock. It is accelerated toward the origin ($u_{II} < 0$). The discontinuities of the flow quantities at the shock front are described by the Rankine–Hugoniot relations (3.61)

$$\frac{\hat{\rho}_{II}}{\hat{\rho}_I} = \frac{\gamma+1}{\gamma-1}\left[1 + \frac{2}{\gamma-1}{M_s}^{-2}\right]^{-1}, \tag{4.3a}$$
$$\hat{u}_{II} = \frac{2}{\gamma+1}U_s\left[1 - {M_s}^{-2}\right], \tag{4.3b}$$
$$\frac{\hat{p}_{II}}{\hat{p}_I} = \frac{2\gamma}{\gamma+1}{M_s}^2\left[1 + \frac{1-\gamma}{2\gamma}{M_s}^{-2}\right], \tag{4.3c}$$

where the hat signifies that the functions are evaluated on the shock position $R_s(t)$.

The domain $\mathcal{D}_{III}$ corresponds to the region upstream the diverging shock. This is the same imploding flow driven by the converging shock as in the domain $\mathcal{D}_{II}$. Thus, we impose a continuity condition on the flow quantities at the boundary between $\mathcal{D}_{II}$ and $\mathcal{D}_{III}$ at the collapse time $t = 0$:

$$\rho_{II}(r,0) = \rho_{III}(r,0), \tag{4.4a}$$
$$u_{II}(r,0) = u_{III}(r,0), \tag{4.4b}$$
$$c_{II}(r,0) = c_{III}(r,0). \tag{4.4c}$$

The domain $\mathcal{D}_{IV}$ is downstream the diverging shock. The matter is moving away from the origin ($u_{III} \geqslant 0$). The post-shock density, velocity and pressure are again expressed with the Rankine–Hugoniot jump relations

$$\frac{\hat{\rho}_{IV}}{\hat{\rho}_{III}} = \frac{\gamma+1}{\gamma-1}\left[1 + \frac{2}{\gamma-1}\left(\frac{\hat{c}_{III}}{U_s - \hat{u}_{III}}\right)^2\right]^{-1}, \tag{4.5a}$$

$$\frac{\hat{u}_{IV} - U_s}{\hat{u}_{III} - U_s} = \frac{\gamma-1}{\gamma+1} + \frac{2}{\gamma+1}\left(\frac{\hat{c}_{III}}{U_s - \hat{u}_{III}}\right)^2, \tag{4.5b}$$

$$\frac{\hat{p}_{IV}}{\hat{p}_{III}} = \frac{2\gamma}{\gamma+1}\left(\frac{U_s - \hat{u}_{III}}{\hat{c}_{III}}\right)^2 - \frac{\gamma-1}{\gamma+1}. \tag{4.5c}$$

Finally, we add the condition of a spherical symmetry at the center, requiring the fluid velocity to vanish there, thus

$$u(0,t) = 0. \tag{4.6}$$

The expressions given above provide a mathematical formulation of the problem. We proceed in the next section with the construction of a solution in a series form to obtain ordinary differential equations (ODE).

4.1.2 Transformation into a system of ordinary differential equations

In this part we proceed in a change of variables and give a form to the solution. The partial differential are transformed into ordinary differential equation and can be integrated easily.

4.1.2.1 Change of variables

Independant variables Following the work performed by Sakurai [Sakurai, 1953], we introduce new independent variables defined by

$$x(r,t) = \frac{r}{R_s(t)}, \quad y(t) = \frac{c_0}{U_s(t)}. \tag{4.7}$$

The variable x represents the relative position with respect to the shock front. It varies from 0 at the center to infinity and is equal to 1 at the shock position. The variable y relates the inverse of the shock velocity normalized by the initial sound speed. During the converging phase, it is equal to the inverse of the shock Mach number $M_s(t)$. Therefore $|y(t)| \leqslant 1$ for $t \leqslant 0$.

The domain (r,t) transformed into the domain (x,y) is then represented in Figure 4.3.

By using the relations

$$\partial_r = \frac{1}{R_s}\partial_x, \tag{4.8}$$

$$\partial_t = -\frac{\dot{R}_s}{R_s}x\partial_x - \frac{\ddot{R}_s}{\dot{R}_s}y\partial_y, \tag{4.9}$$

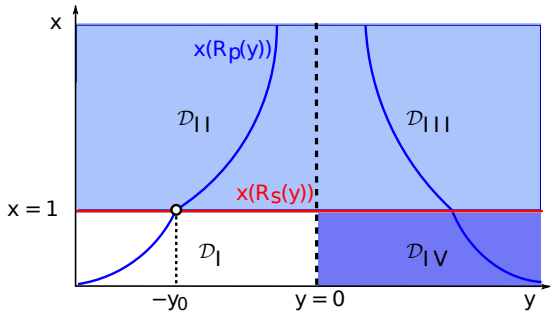

Figure 4.3: Sub-domains, shock path and particle path in the (x, y) plane.

the hydrodynamic equations (4.1) read

$$\partial_x(\rho u) + \frac{2\rho u}{x} = \dot{R}_s(x\partial_x + \Lambda y\partial_y)\rho, \tag{4.10a}$$

$$\rho u\partial_x u + \frac{\partial_x(c^2\rho)}{\gamma} = \dot{R}_s(x\partial_x + \Lambda y\partial_y)u, \tag{4.10b}$$

$$u\partial_x c + \frac{(\gamma-1)}{2}c\left(\partial_x u + \frac{2u}{x}\right) = \dot{R}_s(x\partial_x + \Lambda y\partial_y)c, \tag{4.10c}$$

with

$$\Lambda(y) = \frac{\ddot{R}_s R_s}{\dot{R}_s^2} = -\frac{\mathrm{d}\ln|y|}{\mathrm{d}\ln R_s}, \tag{4.11}$$

usually referred to as the *self-amplification factor* of the shock wave. Note that $\Lambda(y) \propto \mathrm{d}U_s/\mathrm{d}R_s$ accounts for the acceleration of the shock and depends only on y, that is, on time.

Dependant variables New dimensionless dependent variables are also defined:

$$u(x, y) = c_0\frac{x}{y}\mathcal{U}(x, y), \tag{4.12a}$$

$$c(x, y) = c_0\frac{x}{|y|}\mathcal{C}(x, y), \tag{4.12b}$$

$$\rho(x, y) = \rho_0\mathcal{G}(x, y), \tag{4.12c}$$

$$p(x, y) = p_0\left(\frac{x}{y}\right)^2\mathcal{P}(x, y), \tag{4.12d}$$

$$s(x, y) = s_0\left(\frac{x}{y}\right)^2\mathcal{S}(x, y), \tag{4.12e}$$

with $p_0 = c_0^2\rho_0/\gamma$, $s_0 = p_0/\rho_0^\gamma$, $\mathcal{P} = \mathcal{C}^2\mathcal{G}$ and $\mathcal{S} = \mathcal{C}^2\mathcal{G}^{(1-\gamma)}$.

The system of equations becomes:

$$-((1-\mathcal{U})x\partial_x + \Lambda y\partial_y)\mathcal{G} + \mathcal{G}x\partial_x\mathcal{U} + 3\mathcal{G}\mathcal{U} = 0, \tag{4.13a}$$

$$(\Lambda - (1-\mathcal{U}))\mathcal{G}\mathcal{U} - \mathcal{G}((1-\mathcal{U})x\partial_x + \Lambda y\partial_y)\mathcal{U} + \frac{1}{\gamma}(2 + x\partial_x)\mathcal{G}\mathcal{C}^2 = 0, \tag{4.13b}$$

$$-((1-\mathcal{U})x\partial_x + \Lambda y\partial_y)\mathcal{C} + (\Lambda - 1)\mathcal{C} + \frac{\gamma-1}{2}Cx\partial_x\mathcal{U} + \frac{3\gamma-1}{2}\mathcal{U}\mathcal{C} = 0. \tag{4.13c}$$

Boundary conditions The boundaries between the four domains are shown as straight lines in Figure 4.3. The conditions of symmetry apply for $x = 0$, the conditions of continuity for $y = 0$ and the shock jumps appear for $x = 1$. Concerning the converging shock wave, the jump relations (4.3) depend only on y and can be expressed as series assuming $y \ll 1$:

$$\mathcal{G}_{II}(1,y) = \frac{\frac{\gamma+1}{\gamma-1}}{1+\frac{2}{\gamma-1}y^2} = \frac{\gamma+1}{\gamma-1}\left[1 - \frac{2}{\gamma-1}y^2 + o(y^4)\right], \tag{4.14a}$$

$$\mathcal{U}_{II}(1,y) = \frac{2}{\gamma+1}(1-y^2), \tag{4.14b}$$

$$\mathcal{C}_{II}(1,y)^2 = \frac{1}{\mathcal{G}_{II}(1,y)}\left(\frac{2\gamma}{\gamma+1} - \frac{\gamma-1}{\gamma+1}y^2\right) = \frac{2\gamma(\gamma-1)}{(\gamma+1)^2}\left[1 - \frac{4\gamma-(\gamma-1)^2}{2\gamma(\gamma-1)}y^2 + o(y^4)\right]. \tag{4.14c}$$

In the case where the shock Mach number M_s is infinite, the variable y is zero and the boundary conditions on the converging shock front are constant. Then the system of equations could be invariant under similarity transformations and the Guderley's solution applies. Now, we assume that the initial shock Mach number M_{s0} is finite but sufficiently high, $y_0 = M_{s0}^{-1} < 1$. Then the upstream pressure affects the flow through the y dependent terms in the Rankine–Hugoniot relations (4.14). As only even powers of y are present, the series converge quickly and the major influence of the shock Mach number is contained in the first order term. The dependence of the density and the entropy on the shock Mach number is shown in Figure 4.4. The first order correction agrees well with the full Rankine–Hugoniot expression for the shock Mach number higher than 5.

The condition on the velocity in the center (4.6) means that $\mathcal{U}(0,y)$ has to be finite.

The condition of continuity (4.4a) between the domains $\mathcal{D}_{II}$ and $\mathcal{D}_{III}$ becomes:

$$\lim_{x\to\infty,y\to 0}\mathcal{G}_{II}(x,y) = \lim_{x\to\infty,y\to 0}\mathcal{G}_{III}(x,y), \tag{4.15a}$$

$$\lim_{x\to\infty,y\to 0}\frac{x}{y}\mathcal{U}_{II}(x,y) = \lim_{x\to\infty,y\to 0}\frac{x}{y}\mathcal{U}_{III}(x,y), \tag{4.15b}$$

$$\lim_{x\to\infty,y\to 0}\frac{x}{y}\mathcal{C}_{II}(x,y) = \lim_{x\to\infty,y\to 0}\frac{x}{y}\mathcal{C}_{III}(x,y). \tag{4.15c}$$

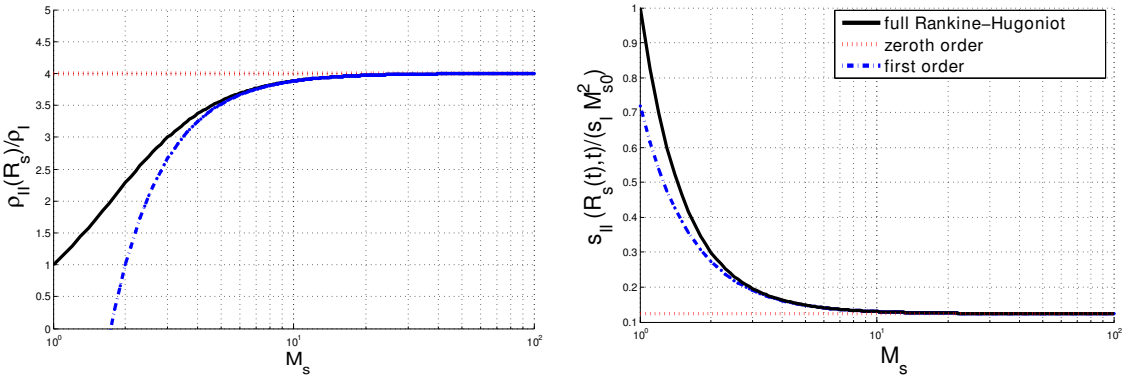

(a) (b)

Figure 4.4: Effect of the shock Mach number on the downstream density (a) and entropy (b) at the shock front for a gas with $\gamma = 5/3$.

Finally the boundary conditions between the domains $\mathcal{D}_{III}$ and $\mathcal{D}_{IV}$ are given by:

$$\mathcal{G}_{IV}(1,y) = \mathcal{G}_{III}(1,y)\frac{\frac{\gamma+1}{\gamma-1}}{1+\frac{2}{\gamma-1}\left(\frac{\mathcal{C}_{III}(1,y)}{1-\mathcal{U}_{III}(1,y)}\right)^2}, \tag{4.16a}$$

$$\mathcal{U}_{IV}(1,y) = 1 + (\mathcal{U}_{III}(1,y)-1)\left(\frac{\gamma-1}{\gamma+1} + \frac{2}{\gamma+1}\left(\frac{\mathcal{C}_{III}(1,y)}{1-\mathcal{U}_{III}(1,y)}\right)^2\right), \tag{4.16b}$$

$$\mathcal{C}_{IV}(1,y)^2 = \mathcal{C}_{III}(1,y)^2\frac{\mathcal{G}_{III}(1,y)}{\mathcal{G}_{IV}(1,y)}\left(\frac{2\gamma}{\gamma+1}\left(\frac{1-\mathcal{U}_{III}(1,y)}{\mathcal{C}_{III}(1,y)}\right)^2 - \frac{\gamma-1}{\gamma+1}\right). \tag{4.16c}$$

We can notice that the unknown shock velocity do not appear anymore in the boundary conditions.

4.1.2.2 Series form solution

Form of the solution Using the perturbative approach as proposed by Ponchaut [Ponchaut et al., 2006] and Sakurai [Sakurai, 1953], we account for the first order correction to the Guderley's solution

$$\mathcal{G}(x,y) = G(x)\left[1+y^2G_1(x)+o(y^4)\right], \tag{4.17a}$$

$$\mathcal{U}(x,y) = U(x)\left[1+y^2U_1(x)+o(y^4)\right], \tag{4.17b}$$

$$\mathcal{C}(x,y) = C(x)\left[1+y^2C_1(x)+o(y^4)\right], \tag{4.17c}$$

$$\mathcal{P}(x,y) = P(x)\left[1+y^2P_1(x)+o(y^4)\right], \tag{4.17d}$$

$$\mathcal{S}(x,y) = S(x)\left[1+y^2S_1(x)+o(y^4)\right], \tag{4.17e}$$

where $P(x) = C^2(x)^2G(x)$, $S(x) = C^2(x)G(x)^{(1-\gamma)}$, $P_1(x) = 2C_1(x) + G_1(x)$ and $S_1(x) = 2C_1(x) + (1-\gamma)G_1$.

We also express the shock amplification factor in a series form :

$$\Lambda(y) = \lambda\big[1 + y^2\lambda_1^{\pm} + o(y^4)\big]. \tag{4.18}$$

The constant λ has a unique value because the equations must be continuous at the time of the shock rebound. On the contrary, the factor $\lambda_1^{\pm}$ has no reason to be the same before and after the shock rebound. Here, the superscript $-$ denotes the converging phase and the superscript $+$ denotes the diverging phase.

The series form solution is valid in the domain $y \in [0, y_0]$ with y_0 the inverse of the initial shock Mach number $y_0 < 1$.

Zeroth order equations By injecting the expressions (4.17) into the hydrodynamic equations (4.1), we obtain two systems of ordinary differential equations (ODE) by term-wise subtraction. The zeroth order part gives a nonlinear system of equations

$$\mathbf{A_0}\mathbf{Y}' = \mathbf{F_0}(\mathbf{Y}, \lambda), \tag{4.19}$$

with

$$\mathbf{Y} = \begin{pmatrix} G \\ U \\ C \end{pmatrix},$$

$$\mathbf{A_0} = \begin{pmatrix} U-1 & G & 0 \\ 0 & U - 1 - \dfrac{C^2}{\gamma(U-1)} & 2\dfrac{C}{\gamma} \\ 0 & \dfrac{\gamma-1}{2}C & U-1 \end{pmatrix} \tag{4.20}$$

and

$$\mathbf{F_0} = \begin{pmatrix} -3GU \\ -U(\lambda + U - 1) + \frac{C^2}{\gamma}(\dfrac{3U}{U-1} + 2) \\ -C(\lambda - 1) - \dfrac{3\gamma-1}{2}UC \end{pmatrix}. \tag{4.21}$$

The prime $[.]'$ denotes the differentiation with respect to $\ln x$.

The first equation can be integrated independently using the relation

$$[\ln(S(x))]' = \frac{2\lambda}{1-U} - 2, \tag{4.22}$$

then we get

$$G = G_0\left[\frac{x^{1-\lambda}C(x)}{(1-U(x))^{\frac{\lambda}{3}}}\right]^{\frac{3\mu}{3+\mu\lambda}}, \tag{4.23}$$

with $\mu = 2/(\gamma - 1)$ and G_0 a constant which must be determined in each domain.

The last two equations can be expressed as ratios of the determinants using the Cramer's rule :

$$\frac{\mathrm{d}U}{\mathrm{d}C} = \frac{\Delta_1(U,C,\lambda)}{\Delta_2(U,C,\lambda)}, \quad \frac{\mathrm{d}\ln x}{\mathrm{d}C} = \frac{\Delta(U,C)}{\Delta_2(U,C,\lambda)}, \tag{4.24}$$

with

$$\Delta(U,C) = \det\begin{pmatrix} A_{2,2} & A_{2,3} \\ A_{3,2} & A_{3,3} \end{pmatrix} = (1-U)^2 - C^2, \tag{4.25}$$

$$\Delta_1(U,C) = \det\begin{pmatrix} F_2 & A_{2,3} \\ F_3 & A_{3,3} \end{pmatrix} = -U^3 + (2-\lambda)U^2 + (\lambda + 3C^2 - 1)U + 2C^2\lambda/\gamma, \tag{4.26}$$

$$\Delta_2(U,C) = \det\begin{pmatrix} A_{2,2} & F_2 \\ A_{2,3} & F_3 \end{pmatrix} = C\left[-\gamma U^2 + \left(1 + \left(1 + \frac{\lambda}{2}\right)\gamma - \frac{3}{2}\lambda\right)U + (\lambda - 1) + C^2\right] + \frac{C^3\lambda}{(U-1)\gamma} \tag{4.27}$$

First order equations Hereafter, the first order linear system can be written in the matrix form :

$$\mathbf{A_1}\begin{pmatrix} G_1 \\ U_1 \\ C_1 \end{pmatrix}' + \mathbf{B_1}\begin{pmatrix} G_1 \\ U_1 \\ C_1 \end{pmatrix} + \lambda_1^{\pm}\mathbf{D_1} = \mathbf{0}, \tag{4.28}$$

with

$$\mathbf{A_1} = \begin{pmatrix} U-1 & U & 0 \\ \frac{C^2}{\gamma} & U(U-1) & 2\frac{C^2}{\gamma} \\ 0 & \frac{\gamma-1}{2}CU & C(U-1) \end{pmatrix}, \tag{4.29}$$

$$\mathbf{B_1} = \begin{pmatrix} -2\lambda & U' + 3U/(1-U) & 0 \\ 0 & (1-2)\lambda U + (2U-1)(U+U') & 2((1-U)(U+U') - \lambda U) \\ 0 & C' - C(\lambda - 1) & -2\lambda C \end{pmatrix} \tag{4.30}$$

and

$$\mathbf{D_1} = \begin{pmatrix} 0 \\ \lambda U \\ \lambda C \end{pmatrix}. \tag{4.31}$$

This system can be decoupled by using the variables

$$\mathbf{Z}_1 = (X_1, W_1, Z_1)^t = \mathbf{M}(G_1, U_1, C_1)^t, \tag{4.32}$$

where the transfer matrix is

$$\mathbf{M} = \begin{pmatrix} -(U-1) & U(\nu-1) & \nu\mu(U-1) \\ 0 & 1 & 0 \\ 0 & -U & -\mu(U-1) \end{pmatrix}, \tag{4.33}$$

with $\nu = (2\lambda - 3)/(1 - \mu\lambda(\gamma - 2))$.

We obtain then a first independent equation

$$X_1' = \frac{2\lambda + U'}{U - 1} X_1 - \lambda_1 \mu \nu \lambda, \tag{4.34}$$

which can be integrated using Eq. (4.22) :

$$X_1 = (U - 1)\left(x_{10}(xS)^{-2} + \frac{\lambda_1 \nu \mu}{2} \right), \tag{4.35}$$

with x_{10} a constant.

The two other equations

$$W_1' = \frac{1}{D}\left[f_1 X_1 + f_2 W_1 + f_3 Z_1 + f_4 \lambda_1 \right], \tag{4.36}$$

$$Z_1' = \frac{2\lambda - 3}{\nu(U - 1)} U W_1 + \frac{2\lambda + U'}{U - 1} Z_1 + \lambda_1 \mu \lambda, \tag{4.37}$$

with

$$\begin{aligned}
f_1 &= -2\lambda C^2 \\
f_2 &= f_1(U(\gamma - 1) + 1) + C^2(3U + U') - \gamma(U - 1)^2(\lambda U - (U' + U)(2U - 1)) \\
&\quad - (C' + C)(U - 1) + gU \\
f_3 &= f_1(\nu - 1 + \gamma) + g \\
f_4 &= \lambda(U - 1)(\gamma U + 2(1 - U)) \\
g &= \gamma(U - 1)(\lambda U + (U + U')(U - 1))(\gamma - 1) \\
D &= \gamma(U - 1)(C^2 - (U - 1)^2)U
\end{aligned}$$

must be integrated numerically.

Boundary conditions The boundary condition (4.14) on the domain $\mathcal{D}_{II}$ is expressed for each order:

Zeroth order solution:

$$G_{II}(1) = \frac{\gamma + 1}{\gamma - 1}, \tag{4.38a}$$

$$U_{II}(1) = \frac{2}{\gamma + 1}, \tag{4.38b}$$

$$C_{II}^2(1) = \frac{2\gamma(\gamma - 1)}{(\gamma + 1)^2}. \tag{4.38c}$$

First order solution:

$$G_{1,II}(1) = \frac{2}{1-\gamma}, \tag{4.39a}$$

$$U_{1,II}(1) = -1, \tag{4.39b}$$

$$C_{1,II}(1) = \frac{(\gamma^2 - 6\gamma + 1)}{4(1-\gamma)\gamma}. \tag{4.39c}$$

The boundary conditions (4.16) on the shock front after the rebound are:

Zeroth order solution:

$$G_{IV}(1) = G_{III}(1)\frac{(\gamma+1)\,(U_{III}(1)-1)^2}{(\gamma-1)\,(U_{III}(1)-1)^2 + 2\,C_{III}^2(1)}, \tag{4.40a}$$

$$U_{IV}(1) = \frac{(U_{III}(1)-1)\,((\gamma-1)\,U_{III}(1)+2) + 2\,C_{III}^2(1)}{(\gamma+1)\,(U_{III}(1)-1)}, \tag{4.40b}$$

$$C_{IV}(1) = \frac{\left(2\,\gamma\,(U_{III}(1)-1)^2 - C_{III}^2(1)\,(\gamma-1)\right)\left((\gamma-1)\,(U_{III}(1)-1)^2 + 2\,C_{III}^2(1)\right)}{(U_{III}(1)-1)^2\,(\gamma+1)^2}. \tag{4.40c}$$

First order solution:

$$G_{1,IV}(1) = -\frac{2\mu C^2}{(U-1)^2 + \mu\,C^2}C_{1,III}(1) + \frac{2\mu U\,C^2}{(U-1)\,((U-1)^2 + \mu\,C^2)}U_{1,III}(1) + G_{1,III}(1), \tag{4.41a}$$

$$U_{1,IV}(1) = \frac{U\left((U-1)^2 - \mu\,C^2\right)U_{1,III}(1) + 2\mu\,C^2\,(U-1)\,C_{1,III}(1)}{(U-1)\,((U-1)\,(U+\mu) + \mu\,C^2)}, \tag{4.41b}$$

$$\begin{aligned} C_{1,IV}(1) = {} & 2C^2\Big(\frac{\mu(C^2(\gamma-1) - \mu\gamma(U-1)^2) - (U-1)^2}{((\gamma-1)(U-1)^2 + \mu C^2)(C^2(\gamma-1) - \mu(U-1)^2\gamma)}\Big)C_{1,III}(1). \\ & - \frac{2\mu U(\gamma(U-1)^4 + C^4))}{(U-1)((U-1)^2 + \mu C^2)(C^2(\gamma-1) - \mu\gamma(U-1)^2)}U_{1,III}(1) - G_{1,III}(1) \end{aligned} \tag{4.41c}$$

When the shock rebounds at the origin at $t = 0$, the slope of $R_s(t)$ is not symmetric. It can be proven that

$$\lim_{t\to 0}\frac{R_s(|t|)}{R_s(-|t|)} = \beta \tag{4.42}$$

with β a constant (See section 4.1.5.1).

Then, for any radius, we have

$$-\lim_{t\to 0}\frac{y(-|t|)}{y(|t|)} = \lim_{t\to 0}\frac{x(r,-|t|)}{x(r,|t|)} = \beta. \tag{4.43}$$

The continuity condition(4.15) becomes :

$$\lim_{x\to\infty} G_{II}(x) = \lim_{x\to\infty} G_{III}(x) \tag{4.44a}$$

$$\lim_{x\to\infty} U_{II}(x) = \lim_{x\to\infty} U_{III}(x) \tag{4.44b}$$

$$\lim_{x\to\infty} C_{II}(x) = \lim_{x\to\infty} C_{III}(x) \tag{4.44c}$$

and

$$\lim_{x\to\infty} G_{1,III}(x) = \beta^2 \lim_{x\to\infty} G_{1,II}(x) \tag{4.45a}$$

$$\lim_{x\to\infty} U_{1,III}(x) = \beta^2 \lim_{x\to\infty} U_{1,II}(x) \tag{4.45b}$$

$$\lim_{x\to\infty} C_{1,III}(x) = \beta^2 \lim_{x\to\infty} C_{1,II}(x). \tag{4.45c}$$

4.1.3 Analysis of the singular points

Let us first describe the trajectory of the zeroth order solution $U(C)$. We remind that this is the solution of Guderley, that is to say the curve with $\alpha = 0.68$ in the Figure 3.20, presented in the previous Chapter. The point A in Figure 4.5 is the point representing the initial downstream state just behind the incoming shock wave. It is given by the zeroth order of the Rankine–Hugoniot relations (4.14).

Far from the origin the solution must be finite thus U and C must tend to zero when x tends to infinity. Then the solution curve links the point A to the point $P_4 = (0, 0)$. However the subsonic flow near P_4 is separated from the super-sonic flow in A by the *sonic line* of equation $\Delta = 0$ (see red dashed line in Figure 4.5). In this case $x(C)$ admits an extremum in this point which signifies that the physical quantities are double valued there, which is not acceptable. There is only one value $\lambda = -0.45$ that allows the solution to intersect the sonic line without any singular behavior of the flow quantities. The intersection then takes place in the singular point P_3 where $\Delta_1 = \Delta_2 = \Delta = 0$.

With this value of λ the solution in the domain $\mathcal{D}_{II}$ is described by the curve (A, P_4) intersecting the sonic line in P_3. As the solution must be continuous at the collapse time, the solution for $t > 0$ is integrated from P_4. We get the curve (P_4, S_1) which corresponds to the flow in the domain $\mathcal{D}_{III}$. The state at the center is described by the point P_6 where $U = U_6$ is finite and C infinite. This leads to a flow velocity $u(0, t) = 0$ consistent with the symmetry condition and an infinite temperature. The solution is integrated from this point to the point S_2. This branch of the curve corresponds to the solution in the domain $\mathcal{D}_{IV}$. The unique set of points S_1 and S_2 is chosen to fulfill the Rankine–Hugoniot jump conditions at the diverging shock front. The path of the zeroth order solution in the plane (U, C) is presented in Figure 4.5.

The equations of the first order solution are singular where

$$D = \gamma\,(U-1)\left(C^2 - (U-1)^2\right)U = 0. \tag{4.46}$$

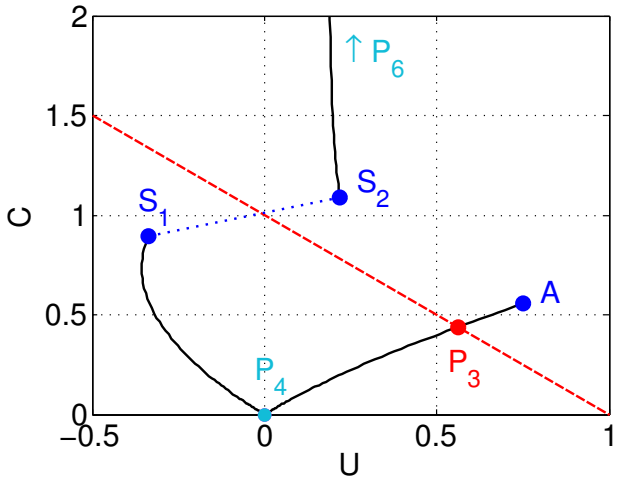

Figure 4.5: Zeroth order solution in the (U,C) plane: the black line shows the solution path, the red dashed line is the sonic line, the dashed blue line represents the diverging shock jump in the solution, the blue dots are given by the Rankine Hugoniot shock jump relations, the cyan dots represent the attractive singular points and the red dot–the repulsive singular point.

This condition is fulfilled in the points P_3 and P_4. The equations are also singular in the point P_6 where C tends to infinity.

Here, we describe in detail the solution near each singular point presented above and explain how the parameters $\lambda_1^{\pm}$ are constrained.

4.1.3.1 Converging shock jump relation

The zeroth order values of the flow quantities at the converging shock front are given by the relations (4.38) and (4.39). Theses boundary conditions depend only on the polytropic coefficient γ.

The values of the flow quantities at the front shock position can be expressed in the form

$$q(R_s(t),t) = q_0\left(\frac{R_s(t)}{R_0}\right)^{n_r}\left[1+y_0^2\left\{a_1\left(\frac{R_s(t)}{R_0}\right)^{-2\lambda}+b_1\right\}\right]. \tag{4.47}$$

The values of the coefficients for the case of $\gamma = 5/3$ are given in Table 4.1.

q	q_0	a_1	b_1	n_r	-2λ
$\rho(R_s(t),t)/\rho_0$	4	-3	0	0	
$u(R_s(t),t)/U_{s0}$	0.75	-0.3112	-0.689	-0.4527	
$c(R_s(t),t)/U_{s0}$	0.56	2.089	-0.689	-0.4527	0.9054
$p(R_s(t),t)/(\rho_0 U_{s0}^2)$	0.75	1.18	-1.378	-0.9054	
$s(R_s(t),t)/(\rho_0^{(1-\gamma)}U_{s0}^2)$	0.072	6.18	-1.378	-0.9054	

Table 4.1: Series coefficients in the expression for the flow quantities on the converging shock trajectory in the case of $\gamma = 5/3$.

For the case of $\gamma = 5/3$, the maximal compression ratio is 4 in the converging phase if the shock Mach number is infinite. The finite shock Mach number correction decreases the downstream density, velocity and pressure. In contrast, the signs of the sound velocity and entropy corrections are not defined. They are positive at the beginning of the converging phase and they become negative as the shock approaches the center. The upstream pressure affects mainly the density and the entropy with changes of respectively 3% and 4.8% at the reference position R_0 , if the initial shock Mach number is $M_{s0} = 10$.

4.1.3.2 Sonic line

The sonic line is defined by the equation $\Delta = 0$ which leads to $C = \pm(U - 1)$. By requesting that Δ_1 and Δ_2 vanish simultaneously, we obtain a quadratic equation

$$-2\gamma U^2 + U\left(2\gamma - (2-\gamma)\lambda\right) + 2\lambda = 0, \tag{4.48}$$

which is fulfilled in the point P_3 with the coordinates

$$U_3 = 1 - C_3, \quad C_3 = -\frac{\gamma\lambda - 2\gamma - 2\lambda + \sqrt{\lambda^2(\gamma-2)^2 + 4\gamma(2+\gamma)\lambda + 4\gamma^2}}{4\gamma}. \tag{4.49}$$

The choice of the parameter λ is limited. First, the point P_3 should be real. That is possible in the following range of λ:

$$\lambda \in]-\infty; -\frac{2\gamma(\sqrt{\gamma}+\sqrt{2})^2}{(\gamma-2)^2}] \cup [-\frac{2\gamma(\sqrt{\gamma}-\sqrt{2})^2}{(\gamma-2)^2}; \infty[\qquad \text{if } \gamma \neq 2, \tag{4.50}$$

$$\lambda > -\frac{1}{2} \qquad \text{if } \gamma = 2. \tag{4.51}$$

Another restriction on λ follows from the request that the internal energy E_i contained in a given sphere of radius $r = a$ at $t = 0$ is finite. As

$$E_i = 4\pi \int_0^a \frac{p}{\gamma - 1} r^2 \, \mathrm{d}r \propto \alpha^2 t^{\frac{3+2\lambda}{1-\lambda}} \int_0^{a/R_s(t)} G(x) C^2(x) x^4 dx \tag{4.52}$$

we impose $\lambda \geqslant -3/2$.

Moreover, λ must be negative because the shock is accelerating in the converging phase.

Finally, for $\gamma \neq 2$ we obtain the following restricted region of the parameter λ:

$$\max(-\frac{3}{2}, -\frac{2\gamma(\sqrt{\gamma}-\sqrt{2})^2}{(\gamma-2)^2}) \leq \lambda \leq 0. \tag{4.53}$$

In particular, for $\gamma = 5/3$ this gives $\lambda \in [-0.455, 0]$.

The slope of the integral curve $U(C)$ in the point P_3 is obtained by means of the l'Hôpital

rule, given by

$$\frac{\mathrm{d}C}{\mathrm{d}U} \approx \frac{\frac{\partial \Delta_2}{\partial U}|_{U_3,C_3} + \frac{\mathrm{d}C}{\mathrm{d}U}\frac{\partial \Delta_2}{\partial C}|_{U_3,C_3}}{\frac{\partial \Delta_1}{\partial U}|_{U_3,C_3} + \frac{\mathrm{d}C}{\mathrm{d}U}\frac{\partial \Delta_1}{\partial C}|_{U_3,C_3}}. \tag{4.54}$$

The numerical integration is started from P_3 using this analytic value of the derivative. Then, the parameter λ is calculated iteratively by requesting the solution to pass through the point A (see Figure 4.5).

The correction terms must be finite in the point P_3. We impose a relation between W_1 and Z_1 in P_3 (see Section 4.1.2.2 for the definition of the functions W_1 and Z_1) so that W_1' stays finite.

$$W_1 = \frac{f_1 X_1 + f_3 Z_1 + f_4 \lambda_{1,c}}{f_2}|_{U=U_3,C=C_3}. \tag{4.55}$$

The parameter λ_1^- is calculated iteratively to fulfill this relation.

The derivative W_1' can be expressed analytically in the limit of P_3

$$W'_{1,3} = (\gamma - 1)\frac{(U_3 - 1)}{U_3} Z_{1,3}, \tag{4.56}$$

and is used for numerical integration of W_1 from the point P_3.

The comparison of the values of λ and λ_1^- with the values found in the literature is given in Table 4.2.

q	Present study	Lazarus	Ponchaut	Welsh
β	0.74095	0.74026	0.7453564	–
λ	-0.4526927	-0.45269273	-0.452693	-0.452692
λ_1^-	-1.3776	–	-1.38846	-1.3884
λ_1^+	-6.6048	–	-6.58806	–

Table 4.2: Solution parameters values and comparison with the literature data [Lazarus, 1981, Ponchaut et al., 2006, Welsh, 1967].

4.1.3.3 Solution at the collapse time

The collapse takes place in the point P_4 where $U = 0$, $C = 0$ and $x \to \infty$. In the vicinity of P_4 we have $U = -\mathrm{sign}(t)\mathcal{M}_0 C$, $U = u_0^{\pm} x^{\lambda-1}$ and $G = g_0$. The coefficient $\mathcal{M}_0^{\pm}$ represents the zeroth order Mach number of the flow. The coefficient $u_0^{\pm}$ is different in the domain $\mathcal{D}_{II}$ and $\mathcal{D}_{III}$. The continuity equation (4.44) gives

$$\lim_{x\to\infty} u_0^- x_{II}^{\lambda-1} = \lim_{x\to\infty} u_0^+ x_{III}^{\lambda-1}. \tag{4.57}$$

This is fullfilled if $u_0^+ = u_0^- \beta^{\lambda-1}$.

The numerical integration of the equations gives $u_0^- = 0.5148$, $\mathcal{M}_0 = 0.9563$ and $g_0 = 9.55$.

The first order solutions G_1, U_1 and C_1 are all proportional to $x^{-2\lambda}$ with respectively the factors $g_{4,1} = -10.959$, $u_{4,1} = -1.8542$ and $c_{4,1} = 3.889$. The first order functions diverge as x

tends to ∞, but any singular behavior of the global solution is avoided since $y \mapsto 0$ when $t \mapsto 0$.

Using those values, the flow quantities can be expressed in the laboratory frame in the limit $t \ll 1$. For $0 < r < R_0$, the flow quantities at the collapse time are of the form

$$q(r,t) = q_0 \left(\frac{r}{R_0}\right)^{n_r} \left[1 + y_0^2 \left\{ a_1 \left(\frac{r}{R_0}\right)^{-2\lambda} + b_1 \right\}\right]. \tag{4.58}$$

The values of the constants for $\gamma = 5/3$ are given in Table 4.3.

q	q_0	a_1	b_1	n_r	-2λ
$\rho(r,0)/\rho_0$	9.55	-10	0	0	0.905
$u(r,0)/(U_{s0})$	0.51	-1.9	-0.689	-0.4527	
$c(r,0)/(U_{s0})$	0.53	3.8	-0.689	-0.4527	
$\mathcal{M}(r,0) = u(r,0)/c(r,0)$	0.9564	-5.7	0	0	

Table 4.3: Series coefficients in the expression for the flow quantities at the collapse time in the case of $\gamma = 5/3$.

Whereas the self-similar solution is characterized by a uniform density $\rho = 9.55\rho_0$ and a constant Mach number of the flow $\mathcal{M} = \mathcal{M}_0$ at the collapse time, the linear corrections imply a density decreasing with the radius and a variable flow Mach number. These quantities are both the most affected by the initial shock Mach number. The correction at the radius R_0 is of 10% for the density and of 5.7% for the flow Mach number, when the initial shock Mach number is 10. Also, the corrections increase the speed of sound for radius near R_0 but decrease it near the center.

4.1.3.4 State of the flow near the center after the collapse

The flow near the center is described by the solution $U(C)$ near the point $P_6 = (U_6, \infty)$. Its coordinate U_6 cancels the derivative $\mathrm{d}U/\mathrm{d}C$ as C tends to ∞ and its value is $U_6 = -2\lambda/3\gamma$. Then $G = g_6 x^n$ and $C = c_6 x^m$ with $n = -6\lambda/(2\lambda + 3\gamma)$ and $m = (-3\gamma + \lambda)/(2\lambda + 3\gamma)$. Making use of the validity domain for λ given in (4.53) we find that $n > 0$ and $m < -1$, which means that C tends to ∞, as expected, when x tends to zero and G tends to zero. In the case of $\gamma = 5/3$, $U_6 = 0.1811$, $c_6 = 1.0528$ and $g_6 = 29.04$.

To fulfill the symmetry condition $u(0,t) = 0$ the correction U_1 must be finite in the point P_6. This is possible if the derivatives W_1' and Z_1' tend to zero at this point. This allows us to express a relation between W_1 and Z_1 in P_6

$$Z_1 = \left(\frac{2\lambda}{3\gamma} + 1\right)\left[\frac{W_1}{\nu} + \frac{\lambda_1^+}{\gamma - 1}\right]. \tag{4.59}$$

The parameter λ_1^+ is then constrained by this relation and can be calculated iteratively. Its value is reported in Table 4.2. The first order functions G_1, U_1,C_1 tend to constant values in P_6, which are respectively $g_{6,1} = -4.008$, $u_{6,1} = 5.47$and $c_{6,1} = -4.028$ (with $\gamma = 5/3$).

The flow quantities in the limit $r \mapsto 0$ and $t > 0$ can be expressed in the form

$$q(r,t) = q_0 \left(\frac{r}{R_0}\right)^{n_r} \left(\frac{t}{R_0/U_{s0}}\right)^{n_t} \left[1 + y_0^2 \left\{ a_1 \left(\frac{t}{R_0/U_{s0}}\right)^{\frac{2\lambda}{\lambda-1}} + b_1 \right\}\right]. \tag{4.60}$$

q	q_0	a_1	b_1	n_r	n_t	$2\lambda/(\lambda-1)$
$\rho(r,t)/\rho_0$	29.8	-11.4	0.3145	0.6633	-0.4566	0.6232
$u(r,t)/(U_{s0})$	12.5	15.4	0	1	-1	
$c(r,t)/(U_{s0})$	0.6763	-8.42	-0.631	-33.17	-0.0833	
$p(r,t)/(U_{s0}^2\rho_0)$	13.64	-15.3	-0.9483	0	-0.623	

Table 4.4: Series coefficients in the expression for the flow quantities near the center after the collapse in the case of $\gamma = 5/3$.

The first order corrections do not modify the radial profiles but only affect the dependence on time. In the center, both the density and the velocity vanish whereas the temperature ($T \propto c^2$) becomes infinite. This divergence is due to the fact that the heat conductivity was neglected in the present study. This does not undermine the physical meaning of the solution as the pressure stays finite. Moreover, the sound speed depends mainly on the radius with the power $n_r = -33$ whereas its dependence on the time is to the power $n_t = -0.08$. Conversely, the pressure at the neighborhood of the center does not depend on the radius ($n_r = 0$). The pressure at the center falls down faster with time if the initial shock Mach number decreases. With the initial shock Mach number $M_{s0} = 10$ and at the time $t = R_0/3U_{s0}$, its correction is of 8.6%.

4.1.3.5 Diverging shock position

The diverging shock discontinuities fulfill the full Rankine–Hugoniot relations (4.5).

The zeroth order condition in $x = 1$ is given by the relations in equation (4.40). The positions of points S_1 and S_2 in the plane (U, C) are determined according to these relations.

The computation of x along the curve $S_1 - P_4$ allows then to calculate the parameter β according to (4.24) and knowing that $x = 1$ in S_1 :

$$\beta = \exp\left(-\int_{P_4}^{S_1} \frac{\Delta(U,C)}{\Delta_2(U,C,\lambda)}\,\mathrm{d}C\right). \tag{4.61}$$

Adding the first order term, the quantities just behind the shock have the form

$$q(R_s(t),t) = q_0 \left(\frac{R_s(t)}{R_0}\right)^{n_r} \left[1 + y_0^2 \left\{ a_1 \left(\frac{R_s(t)}{R_0}\right)^{-2\lambda} + b_1 \right\}\right]. \tag{4.62}$$

The state just behind the diverging shock depends only on time. The first order correction gives a dependence on the initial Mach number. If the shock Mach number is infinite, the compression behind the diverging shock is constant, and in particular for $\gamma = 5/3$, its value is 32. In the case of a finite initial shock Mach number the density behind the diverging shock

q	q_0	a_1	b_1	n_r	-2λ
$\rho(R_s(t),t)/\rho_0$	32.3	-20	0	0	
$u(R_s(t),t)/U_{s0}$	0.142	18.45	-0.689	-0.4527	
$c(R_s(t),t)/U_{s0}$	0.705	3.993	-0.689	-0.4527	0.9054
$p(R_s(t),t)/(\rho_0 U_{s0}^2)$	9.61	-12	-1.38	-0.9054	
$s(R_s(t),t)/(\rho_0^{(1-\gamma)} U_{s0}^2)$	0.029	21.3	-1.38	-0.9054	

Table 4.5: Series coefficients in the expression for the flow quantities on the diverging shock trajectory in the case of $\gamma = 5/3$.

decreases with time and the correction when $M_{s0} = 10$ and $R_s = R_0/3$ is 7.4%. In the same conditions the velocity, the speed of sound and the entropy are increased by 6.1%, 0.7% and 6.5% whereas the pressure is decreased by 5.8%.

4.1.4 Results in the frame (x, y)

The solution $U(C)$ is obtained by integrating numerically $\mathrm{d}U/\mathrm{d}C$ between the singular points analyzed in the last section. The analytical values of the derivative are used in the vicinity of the singular points to help the numerical resolution. We use the *ODE45* function resolution proposed by Matlab with the accuracy $\epsilon = 10^{-6}$ and $\epsilon = 10^{-5}$ respectively for the zeroth order solution and for the first order solution. This function uses a Runge–Kutta scheme of the fourth order. To find iteratively the parameters λ, λ_1^- and λ_1^+ we used the function *fzero* which allows to find the zero of an error function. We defined this error function as the quadratic distance between the numerical value of the solution near the singular point and the analytical solution at the singular point.

The zeroth and first order solutions as functions of x are represented in Figure 4.6. The function C_{IV} tends to infinity whereas the function G_{IV} tends to zero when x tends to zero meaning that the temperature is infinite and that the density vanishes in the center during the diverging phase. This is because the dissipative effects have been neglected. Also the first order corrections are infinite when x tends to infinity. We will see in the next section that it is not inconsistent as y tends to zero in this limit. Thus the flow quantities stay finite.

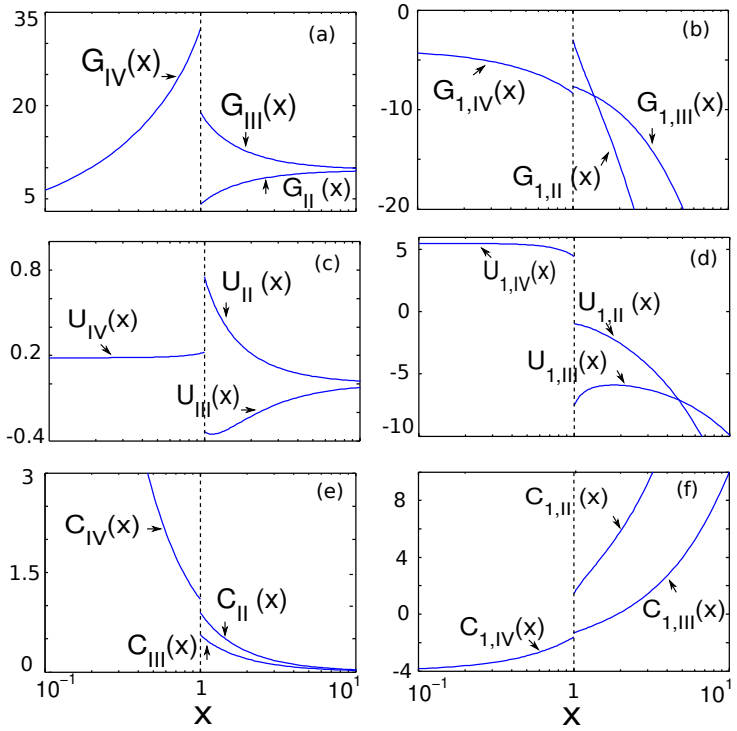

Figure 4.6: Reduced functions of the zeroth order (a-c) and the first order (d-f) solutions for $\gamma = 5/3$.

4.1.5 Results in the frame (r, t)

To express the solution in the (r, t) frame, the shock pass must be expressed. We first express the shock trajectory in the (r, t) frame then present an overview of the flow in the laboratory frame.

4.1.5.1 Shock path

We are looking for the trajectory of the shock in the plane (r, t) using the series form expression of the shock amplification factor Λ (4.18).

The relation between the shock position and the amplification factor Λ is given by

$$\mathrm{d}\ln R_s = -\frac{1}{\Lambda}\,\mathrm{d}\ln|y|. \tag{4.63}$$

by using the serie form (4.18) we obtain

$$\mathrm{d}\ln R_s = -\frac{1}{\lambda}\frac{1}{y}(1-\lambda_1 y^2 + o(y^4))\,\mathrm{d}y. \tag{4.64}$$

the integration gives

$$\ln(\frac{R_s}{\kappa^{\pm}}) = \ln(|y|^{-\frac{1}{\lambda}}) + \frac{\lambda_1^{\pm}}{2\lambda}y^2 + o(y^4), \tag{4.65}$$

with $\kappa^{\pm}$ an integration constant *a priori* different for $y < 0$ and $y > 0$.

Then the position of the shock can be expressed as a function of y:

$$R_s(y) = \kappa^{\pm}|y|^{-\frac{1}{\lambda}}(1 + \frac{\lambda_1^{\pm}}{2\lambda}y^2 + o(y^4)). \tag{4.66}$$

It can be seen here that λ must be negative so that the position of the shock vanishes when $y = 0$.

By inversion of the series, we express y as a function of R_s:

$$y(R_s) = \text{sign}(t)(\frac{R_s}{\kappa^{\pm}})^{-\lambda}(1 + \frac{1}{2}\lambda_1^{\pm}(\frac{R_s}{\kappa^{\pm}})^{-2\lambda} + o((\frac{R_s}{\kappa^{\pm}})^{-4\lambda})). \tag{4.67}$$

Then by integrating $\frac{\mathrm{d}t}{\mathrm{d}R_s} = \frac{y}{c_0}$ we get:

$$|\frac{t}{\tau^{\pm}}| = (\frac{R_s}{\kappa^{\pm}})^{1-\lambda}(1 + \frac{\lambda_1}{2}\frac{1-\lambda}{1-3\lambda}(\frac{R_s}{\kappa^{\pm}})^{-2\lambda} + o((\frac{R_s}{\kappa^{\pm}})^{-\lambda})) \tag{4.68}$$

with $\tau^{\pm} = (\frac{\kappa^{\pm}}{(1-\lambda)c_0})$.

A last series inversion gives

$$\frac{R_s}{\kappa^{\pm}} = |\frac{t}{\tau^{\pm}}|^{\frac{1}{1-\lambda}}(1 - \frac{\lambda_1}{2}\frac{1}{1-3\lambda}|\frac{t}{\tau^{\pm}}|^{-\frac{2\lambda}{1-\lambda}} + o(|\frac{t}{\tau^{\pm}}|^{-\frac{4\lambda}{1-\lambda}})). \tag{4.69}$$

By writing $\lambda = \frac{\alpha-1}{\alpha}$ the last expression becomes

$$R_s(t) = \kappa^{\pm}|\frac{t}{\tau^{\pm}}|^{\alpha}(1 + \frac{\lambda_1}{2}\frac{\alpha}{2\alpha-3}|\frac{t}{\tau^{\pm}}|^{2(1-\alpha)} + o(|\frac{t}{\tau^{\pm}}|^{4(1-\alpha)})). \tag{4.70}$$

The zeroth order expression corresponds to the shock position given by Guderley and the first order expression is the one proposed by Ponchaut.

The contraction of the shock surface leads to an increasing shock velocity as the shock radius decreases. The factor $\lambda \propto \mathrm{d}U_s/\mathrm{d}R_s$ is negative and numerical resolution of the problem gives $\lambda = -0.45$, $\lambda_1^- = -1.38$ and $\lambda_1^+ = -6.6$ (see Table 4.2). This means that the shock amplification factor is smaller for a finite shock Mach number. It increases and tends to λ when the shock converges to the center. After the shock rebound, it decreases with the increasing shock radius.

Here the constants $\kappa^{\pm}$ and $\tau^{\pm}$ are series in power of y_0^2. The constant κ^- is determined by using the initial condition $U_s(t_0) = U_{s0}, R_s(t_0) = R_{s0}$ in the expression (4.67) :

$$\kappa^- = R_0 y_0^{\frac{1}{\lambda}}[1 - y_0^2\frac{\lambda_1^-}{2\lambda}]. \tag{4.71}$$

The value of the constant κ^+ depends on the numerical evaluation of $U(x)$. We can notice that

$$\left(\frac{\kappa^+}{\kappa^-}\right)^{\frac{\lambda}{\lambda-1}} = \lim_{t\to 0}\frac{R_s(|t|)}{R_s(-|t|)} = \lim_{U\to 0}\frac{x_{II}(U)}{x_{III}(U)} = \beta, \tag{4.72}$$

constant	$a_0^{\pm}$	$a_1^{\pm}$	b_1	$\frac{1}{1-\lambda}$	$-\frac{2\lambda}{1-\lambda}$
converging phase	1.29	0.369	-0.476	0.688	0.623
diverging phase	0.956	3.23			

Table 4.6: Series coefficients in the expression for the shock trajectory.

where β is a constant.

This ratio is also linked to the variable y with

$$\beta = -\lim_{t\to 0} \frac{y(-|t|)}{y(|t|)}. \tag{4.73}$$

We note $\kappa^{\pm} = \theta^{\pm}\kappa^{-}$ with $\theta^{-} = 1$ and $\theta^{+} = \beta^{(1-1/\lambda)}$.

By replacing $\kappa^{\pm}$ and $\tau^{\pm}$ in (4.70) and neglecting the high order term we obtain R_s in the form

$$\frac{R_s(t)}{R_0} = a_0^{\pm}\left|\frac{t}{\frac{R_0}{U_{s0}}}\right|^{\frac{1}{1-\lambda}}\left[1 + y_0^2\left\{a_1^{\pm}\left|\frac{t}{\frac{R_0}{U_{s0}}}\right|^{-\frac{2\lambda}{1-\lambda}} + b_1\right\}\right], \tag{4.74}$$

with $a_0^{\pm} = \theta^{\pm}\left(\frac{1-\lambda}{\theta^{\pm}}\right)^{\frac{1}{1-\lambda}}$, $a_1^{\pm} = -\frac{\lambda_1^{\pm}}{2-6\lambda}\left(\frac{1-\lambda}{\theta^{\pm}}\right)^{-\frac{2\lambda}{1-\lambda}}$ and $b_1 = \frac{\lambda_1^{-}}{2(1-\lambda)}$.

Numerical values of the constants in this expression are given in Table 4.6 for the case of $\gamma = 5/3$.

The shock velocity is lower after the collapse ($a_0^{+} < a_0^{-}$) because it propagates inside a moving inward material. The effect of the initial shock Mach number on the collapse time is relatively weak for the case of $\gamma = 5/3$. It is barely visible during the converging phase as the correction coefficient a_1^{-} is low (see Figure 4.7), but during the diverging phase the correction coefficient a_1^{+} is ten times larger.

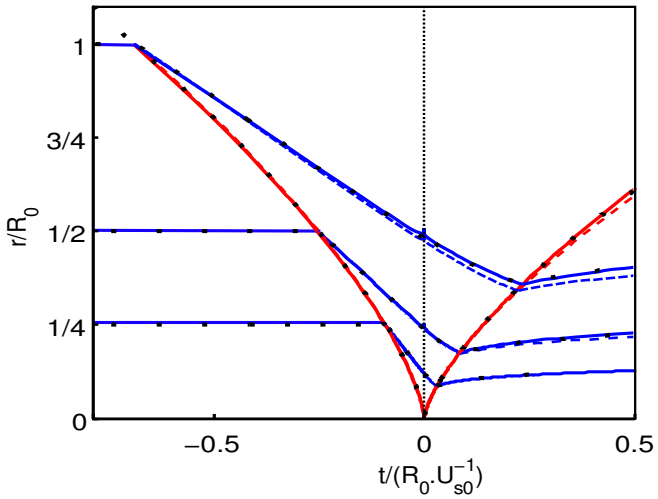

Figure 4.7: Shock and particle trajectories (respectively in red and blue) for the case of the initial shock Mach number $M_{s0} = 7$ (solid lines) and the infinite shock Mach number (dashed lines). Results from numerical simulations are represented in black dots.

4.1.5.2 Overview of the flow in Eulerian form

The effect of the initial shock Mach number on the radial profiles of fluid and sound speed, pressure and density is demonstrated in Figure 4.8. The profiles for $\gamma = 5/3$ are given at two time moments during the imploding phase and at two time moments during the diverging phase. The time dependencies of the density, pressure and velocity are given for two radial positions in Figure 4.9.

During the implosion phase, the absolute value of the flow velocity is decreasing monotonously with radius (Figure 4.8(c)) and the pressure admits a maximum behind the shock (Figure 4.8(b)). The downstream flow, perturbed by the imploding shock has a negative velocity. The density is increasing monotonously behind the shock as the flow converges for large shock Mach numbers, but it admits a maximum for lower shock Mach numbers. The convergence effect on the shock pressure manifests itself in the increasing shock amplitude near the center (Figure 4.8(b)). During the diverging phase, the velocity downstream the diverging shock is positive whereas the upstream velocity is still negative. The effect of the shock Mach number on the density and pressure amplitudes is rather visible. The pressure is almost constant in the entire zone behind the diverging shock. In general, the initial upstream pressure makes the incoming shock less efficient. The final density and pressure are then lower than those predicted by the Guderley's solution. It also induces a delay in the diverging phase as it can be seen in Figure 4.9.

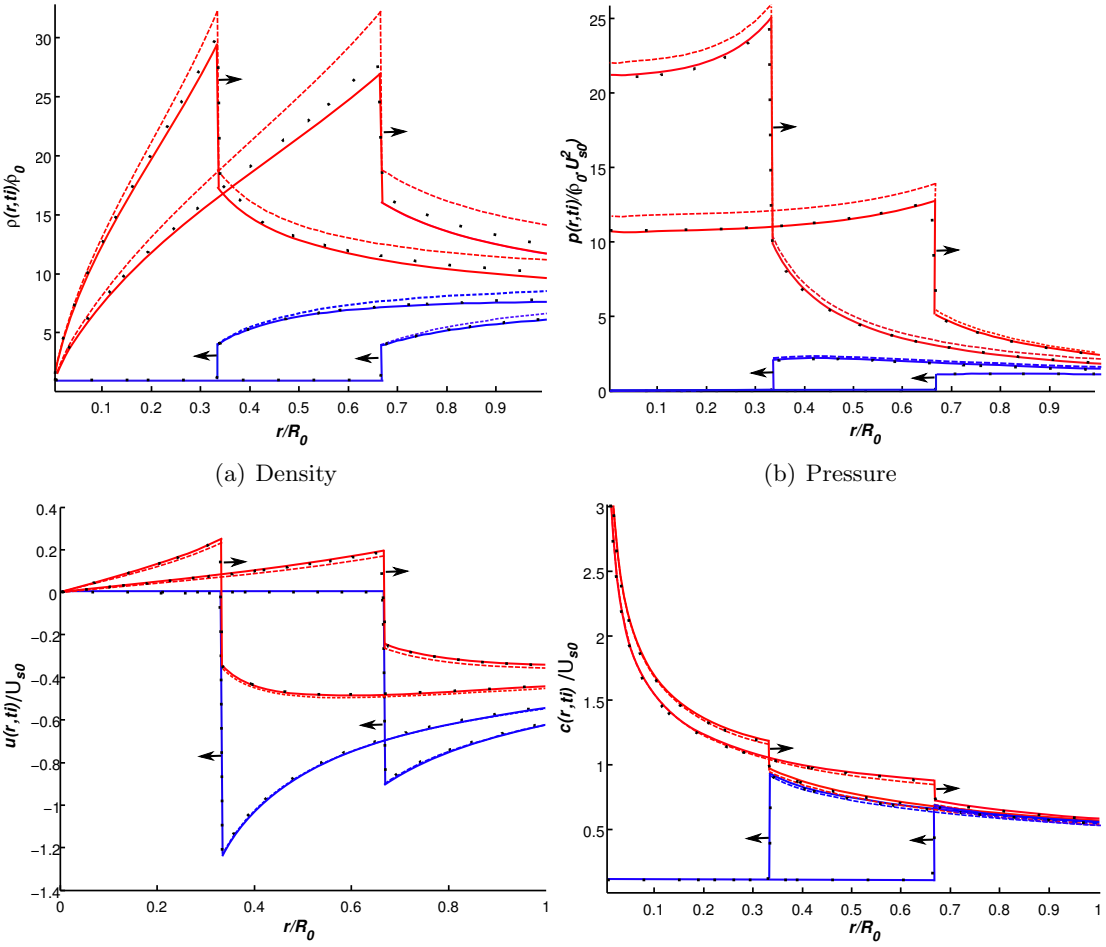

(a) Density

(b) Pressure

(c) Fluid velocity

(d) Sound velocity

Figure 4.8: Flow profiles of the density (a), pressure (b), fluid (c) and sound (d) velocities during the converging (blue curves) and the diverging (red curves) phases for $\gamma = 5/3$. The results are presented for the initial shock Mach numbers $M_{s0} = \infty$ and $M_{s0} = 10$ respectively in dashed and solid lines. Results of numerical simulations are presented with black dots.

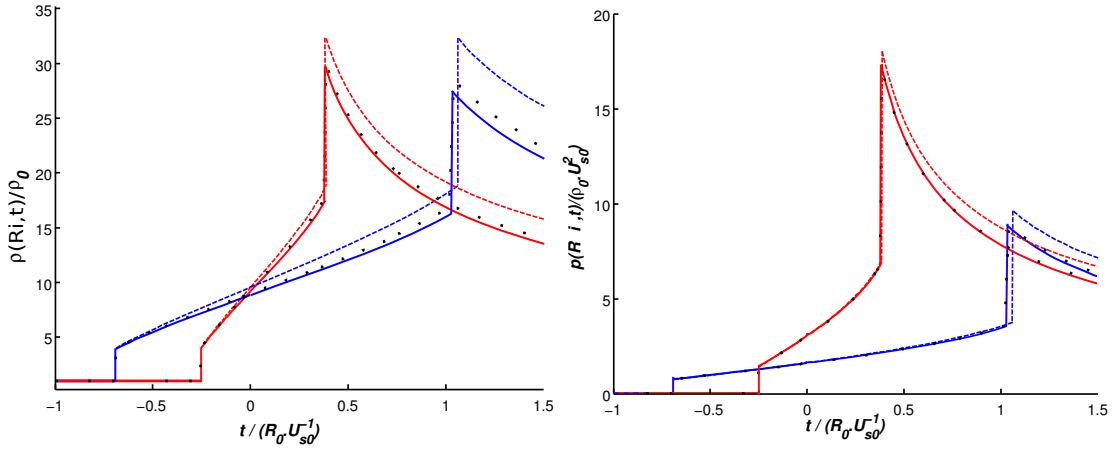

(a) Density (b) Pressure

Figure 4.9: Flow density (a) and pressure (b) at a given radius $r = (2/3)R_0$ and $r = (1/3)R_0$ as functions of time for $\gamma = 5/3$. The results are presented for the initial shock Mach number $M_{s0} = \infty$ and $M_{s0} = 10$ respectively in dashed and solid lines. Results of numerical simulations are presented with black dots.

4.1.6 Results in the Lagrangian frame

The quantities can be expressed along a particle path. In a first part we express analytically the particle path using the entropy conservervation along the particle path. Then we present the flow in the Lagragian form.

4.1.6.1 Particle path

We consider a particle initially at the position R_i. We note $y = \tilde{y}(x)$ the relation between x and y along the particle path $R_p(t)$. Then we express the position of the particle as a function of x :

$$R_p(x) = \kappa^{\pm} R_{p0}(x) \left[1 + \tilde{y}(x)^2 R_{p1}(x)\right]. \tag{4.75}$$

Knowing that $R_s(t) = R_p(t)/x$ and using (4.67) we get the expression

$$\tilde{y}(x) = \left(\frac{R_{p0}(x)}{x}\right)^{-\lambda} \left[1 + \left(\frac{R_{p0}(x)}{x}\right)^{-2\lambda} \left\{\frac{{\lambda_1}^{\pm}}{2} - \lambda R_{p1}(x)\right\}\right]. \tag{4.76}$$

As the fluid is adiabatically compressed, the entropy $s(x, y)$ (4.17e) is constant along the particle path in the domains $\mathcal{D}_{II}$ and $\mathcal{D}_{III}$. This gives the equation $s_{II}(x) = s_{III}(x) = s_{II}(1)$, that is

$$\left(\frac{x}{\tilde{y}(x)}\right)^2 S(x)\left[1 + \tilde{y}(x)^2 S_1(x)\right] = \left(\frac{1}{y_i}\right)^2 S_{II}(1)\left[1 + y_i^2 S_{1,II}(1)\right], \tag{4.77}$$

valid in the domains $\mathcal{D}_{II}$ and $\mathcal{D}_{III}$, where y_i is the value of y when the shock is at the initial particle position R_i (4.67).

By solving the equation (4.77) we obtain the expression for $R_{p0}(x)$ and $R_{p1}(x)$:

$$R_{p0}(x) = \frac{R_i}{R_0} x^{1-\lambda} y_0^{-1/\lambda} \left[\frac{S_{II}(1)}{S(x)}\right]^{\frac{1}{2\lambda}}, \tag{4.78}$$

$$\begin{aligned} R_{p1}(x) =& \frac{1}{2\lambda}\big(\lambda_1^{\pm} - S_1(x) \\ &+ x^{-2}\frac{S_{II}(1)}{S(x)}\left[S_{II,1}(1) - \lambda_1^{-} + \lambda_1^{-}\frac{R_i}{R_0}^{2\lambda}\right]\big). \end{aligned} \tag{4.79}$$

When $x = 1$, the particle is at the shock position. It is then possible to express the launching time of the converging shock t_{conv}, the time t_{div} when the diverging shock collides with the piston and the final radius R_d as series of the form $q = q_0(1+y_0^2 q_1)$. The coefficients values are presented in Table 4.7 for the case of $\gamma = 5/3$.

q	q_0	q_1
$t_{conv}/(R_0/U_{s_0})$	0.688	0.264
$t_{div}/(R_0/U_{s_0})$	0.224	2.13
R_d/R_0	0.342	2.26

Table 4.7: Series coefficients in the expression for the collapse time t_{conv}, the diverging time t_{div} and the final radius R_d.

For the case of an infinite shock Mach number, the diverging time t_{div} and the final radius R_d are about a third of the converging time t_{conv} and the initial radius R_0. The corrections of first order for a finite initial shock Mach number are mainly visible in the diverging time and the final radius. For instance, t_{div} and R_d are modified by 2 % whereas the collapse time is modified by only 0.3 % for the initial shock Mach number of 10. The effect of the initial shock Mach number on the particle path is illustrated in Figure 4.7.

4.1.6.2 Overview of the flow in Lagrangian form

The flow quantities are represented along a particle path of the initial radius R_0 in Figure 4.10. The time moment when the particle crosses the converging and the diverging shocks are considered as the same for the infinite Mach number and for the initial Mach number of 5. They are represented with blue vertical lines. The entropy is constant along the particle path. The Mach number effect is the most visible for the density and the pressure.

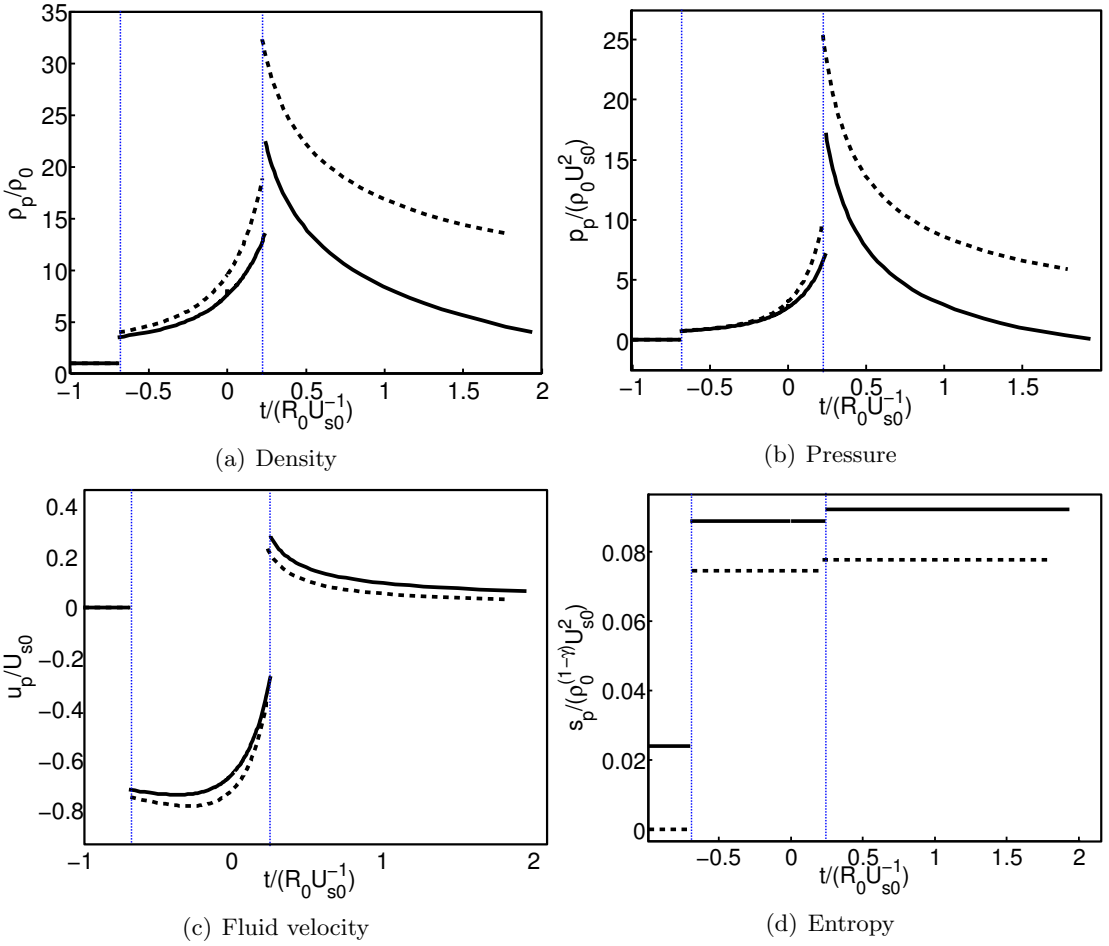

(a) Density

(b) Pressure

(c) Fluid velocity

(d) Entropy

Figure 4.10: Flow profiles of the density (a), pressure (b), fluid velocity (c) and entropy(d) along a particle path for $\gamma = 5/3$. The results are presented for the initial shock Mach numbers $M_{s0} = \infty$ and $M_{s0} = 5$ respectively with dashed and solid lines. The vertical blue lines represent the time moments when the particle interacts with the converging and the diverging shocks.

4.1.7 Discussion

Our simplified approach highlights the isolated effect of the converging shock upstream pressure on the entire flow both during the converging and the diverging phase of the shock. As the solution is in a series form on the parameter M_{s0}^{-2}, it is valid only for the shock Mach number sufficiently high.

The semi-analytical results are compared with numerical simulations using the hydrodynamic Lagrangian code CHIC [Maire et al., 2007] in a 1-D spherical configuration. The self-similar Guderley's problem corresponds to an infinitely weak perturbation at an infinite radius. A possible way to simulate this problem, in a finite size simulation domain, is to impose the piston pressure and trajectory found with the model as a boundary condition. However, this implies a characteristic length to the simulation and thus invalidates the hypothesis of self-similar solution. Instead, we excite a converging shock with a piston having a constant velocity at a very large radius compressing a gas with a non zero initial pressure p_0. The shock starts with a low Mach number $M = 1.5$, converges and is amplified by the geometrical effect. Then, it tends asymptotically to the Guderley's solution and "forgets" the boundary conditions for a sufficiently small radius $r \ll R_0$. We expect the present model to agree with the simulation for the distances where the shock Mach number is sufficiently high.

The results obtained in the numerical simulations are represented with black dots and compared with the semi-analytical results in Figures 4.8 and 4.9 with the initial shock Mach number $M_{s0} = 10$. The semi-analytical solution agrees rather well with the simulations. Discrepancies appear mainly in the density profile. This can be explained by the difference in the boundary condition and by the absence of higher order terms in the semi-analytical model. In general terms, the effects of the initial pressure predicted by the theory are consistent with simulations.

We now would like to apply this model to analyze the coupling of the ignitor shock with the pre-heated hot-spot. In this case, we assume that the shell follows a fluid particle trajectory. However, in the shock ignition scheme, the piston (imploding shell) trajectory does not necessarily coincide with the trajectory of a fluid particle. That difference can be evaluated by detailed comparison between numerical simulations and the analytical solutions. The perturbation path into the main flow due to a modification of the piston velocity follows a characteristic line of equation $\mathrm{d}r/\,\mathrm{d}t = u - c$. Several characteristics starting from different points are represented in Figure 4.11. The characteristic line plotted with a thicker green line reaches the center at $t = 0$. It divides the flow into two domains: the domain where the perturbations may affect the incoming shock and the domain where the perturbations affect only the diverging shock. This characteristic corresponds to the sonic line singularity described in Section 4.1.3. The perturbations which appear on the piston path after $t = 0$ reach the diverging shock at a time close to the exit time and have a small effect on the compressed fuel. Thus the piston trajectory should be well controlled only until the time of collapse.

According to Figure 4.10, during the shock converging time, the velocity on a particle path is approximately constant and the pressure is increasing slowly. These conditions are compatible

with the velocity and pressure profiles obtained in the typical numerical simulations of shock ignited inertial fusion targets. For example, the time t_{conv} needed to apply this pressure law with the spike laser pulse is $t_{conv} \approx 140$ ps with $R_0 = 100\,\mu$m and $U_{s0} = 500$ km.s^{-1}.

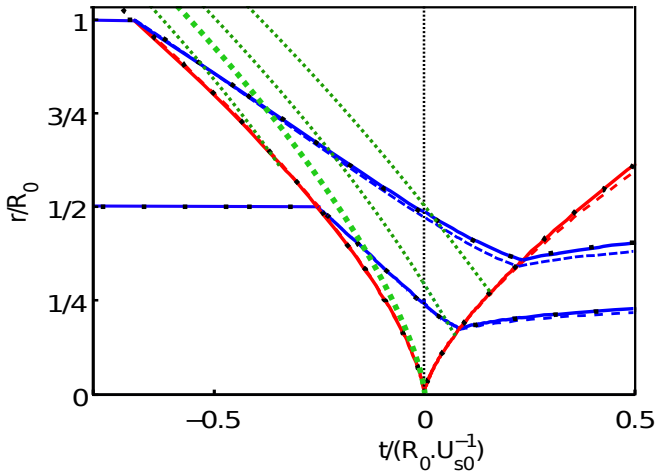

Figure 4.11: Shock and particle trajectories (respectively in red and blue) for the case of the initial shock Mach number $M_{s0} = 7$ (solid lines) and the infinite shock Mach number (dashed lines). The characteristics $\mathrm{d}r/\,\mathrm{d}t = u - c$ are represented in green dot lines.

These observations justify the use of our simplified model to express an ignition criterion for shock ignition of a compressed target.

The solution here has been constructed neglecting the heat transfer and viscosity. These phenomena dissipate energy and should further decrease the expected values of the density, pressure and temperature of the fuel behind the diverging shock. On the contrary, we expect to be near the ignition conditions during the diverging phase. Accounting for nuclear reactions will have a positive effect on the areal pressure as the fusion energy production increases the temperature of the fuel. There might be a compensation effect. Those processes are important for the study of ignition and will be accounted for in the next section.

4.2 Influence of the shock Mach number on the coupling with the hot-spot

We are interested by the state of the compressed fuel at the time moment when the diverging shock collides with the converging shell. The fusion reactions rate is proportional to the product of the fuel areal density and the temperature which corresponds to the product pR. We can assume that the fusion reactions take place only behind the diverging shock where the pressure is the highest. After the shock collapse, the pressure is almost homogeneous in the center and scales as $p \propto t^{-0.623}$. The diverging shock radius scales as $R_s \propto t^{0.688}$. Therefore, even if the

pressure behind the diverging shock decreases with time, the product pR_s increases. One may expect that the nuclear reactions ignite when the shock exits the hot-spot, that is to say, for the maximal value of the areal pressure in the hot-spot.

4.2.1 Conversion of the kinetic energy into the internal energy

The ignition efficiency is defined by the fraction of the shock kinetic energy converted into the internal energy that defines the fusion reaction rate. The temporal evolution of the internal fuel energy E_i and kinetic energy E_k in the sphere delimited by the piston are shown along with the piston work energy E_p in Figure 4.12. These quantities are defined as follows:

$$E_i(t) = 4\pi \int_0^{R_p(t)} \frac{p(r,t)}{\gamma - 1} r^2 \, \mathrm{d}r, \tag{4.80}$$

$$E_k(t) = 2\pi \int_0^{R_p(t)} \rho(r,t) u(r,t)^2 r^2 \, \mathrm{d}r, \tag{4.81}$$

$$E_p(t) = 4\pi \int_{t_0}^{t} p(R_p(\varsigma),\varsigma) R_p(\varsigma)^2 u(R_p(\varsigma),\varsigma) \, \mathrm{d}\varsigma. \tag{4.82}$$

The energy balance is respected here, that is, $E_i + E_k = E_p + E_{i0}$, with $E_{i0} = 4\pi p_0 R_0^3/3(\gamma-1)$ being the initial internal energy. The work done by the piston is converted into the flow kinetic energy during the converging phase and then it is converted into the internal energy during the diverging phase after the collapse. At the shock exit time t_{div}, the kinetic energy becomes small (few percents of the total energy).

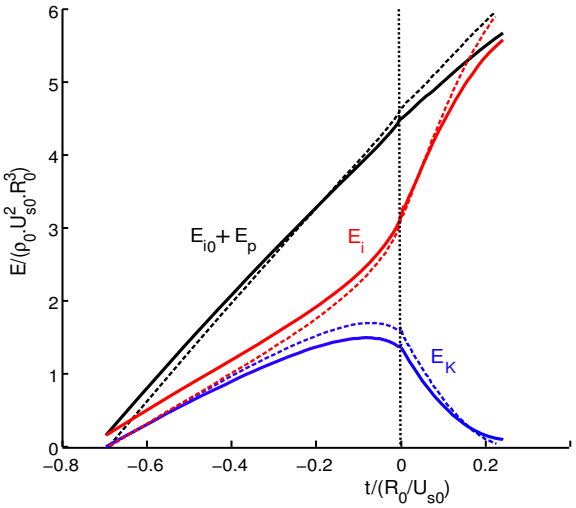

Figure 4.12: Temporal evolution of the kinetic energy E_k (blue), the work done by the piston E_p added to the initial internal energy E_{i0} (black) and the internal energy E_i (red) of the fluid inside the piston of the radius $R_p(t)$. Results are given for an infinite shock Mach number (dashed) and for $M_{s0} = 10$ (solid lines).

At the exit time t_{div}, the internal and kinetic energies can be expressed analytically:

$$E_i(t_{div}) = 4\pi \frac{\rho_0 c_0^2}{\gamma(\gamma-1)} {R_d}^3 y_d^{-2} \int_{\mathcal{D}_{IV}} P(x) x^4 \,\mathrm{d}x \left[1 + y_d^2 \frac{\int_{\mathcal{D}_{IV}} P(x) P_1(x) x^4 \,\mathrm{d}x}{\int_{\mathcal{D}_{IV}} P(x) x^4 \,\mathrm{d}x}\right], \tag{4.83a}$$

$$E_k(t_{div}) = 2\pi \rho_0 c_0^2 {R_d}^3 y_d^{-2} \int_{\mathcal{D}_{IV}} G(x) U(x)^2 x^4 \,\mathrm{d}x \left[1 + y_d^2 \frac{\int_{\mathcal{D}_{IV}} G(x) U^2(x) x^4 (G_1(x) + 2U_1(x)) \,\mathrm{d}x}{\int_{\mathcal{D}_{IV}} G(x) U^2(x) x^4 \,\mathrm{d}x}\right]. \tag{4.83b}$$

Using the data from Table 4.7 and numerical evaluation of the integrals we obtain the following expressions for $\gamma = 5/3$:

$$E_i(t_{div}) = 5.9 \rho_0 U_{s0}^2 R_0^3 [1 - 1.3 y_0^2], \tag{4.84a}$$

$$E_k(t_{div}) = 0.06 \rho_0 U_{s0}^2 R_0^3 [1 + 11 y_0^2]. \tag{4.84b}$$

We can notice in Figure 4.12 that the internal energy of a pre-heated hot-spot stays higher than the internal energy of an initially cold hot-spot until the shock collapse time $t = 0$. After that time, the internal energy in the hot-spot is lower in the pre-heated case. The finite shock Mach number decreases the deposited internal energy. A smaller amount of energy is converted into the flow kinetic energy during the converging phase. Moreover, during the diverging shock phase, a smaller amount of the kinetic energy is transferred into internal energy. This can be seen in Figure 4.12: at the moment of the shock exit time, more kinetic energy remains in the flow in the finite Mach number case.

Equation (4.83a) can be presented in a convenient form showing that the maximum internal energy of the compressed fuel is approximately twice the initial internal energy times a square of the initial shock Mach number:

$$E_i(t_{div}) = 1.6 \frac{4}{3} \pi \frac{p_0}{\gamma - 1} R_0^3 M_{s0}^2 \left[1 - 1.3 M_{s0}^{-2}\right], \tag{4.85}$$

with p_0 being the initial pressure. The correction term reduces the deposited energy by a factor of the order of ${M_{s0}}^{-2}$.

4.2.2 Influence of the Mach number on the Lawson criterion

The fuel ignition criterion is affected by the finite Mach number correction in a more significant way. The rate of fusion reactions is proportional to the fuel areal pressure $< pr >= \int p \,\mathrm{d}r$. This quantity has to be higher that a certain threshold defined by the fusion cross section. For $\gamma = 5/3$, the areal pressure reads

$$\begin{aligned} < p_d R_d > &= p_0 R_d y_d^{-2} \int_{\mathcal{D}_{IV}} P x^2 \,\mathrm{d}x \left[1 + y_d^2 \frac{\int_{\mathcal{D}_{IV}} P(x) P_1(x) x^2 \,\mathrm{d}x}{\int_{\mathcal{D}_{IV}} P(x) x^2 \,\mathrm{d}x}\right] \\ &= 7.6 \rho_0 R_0 U_{s0}^2 \left[1 - 6 y_0^2\right]. \end{aligned} \tag{4.86}$$

We compared the scaling law for the areal pressure (4.86) with simulation results and obtained a good agreement (see Figure 4.13).

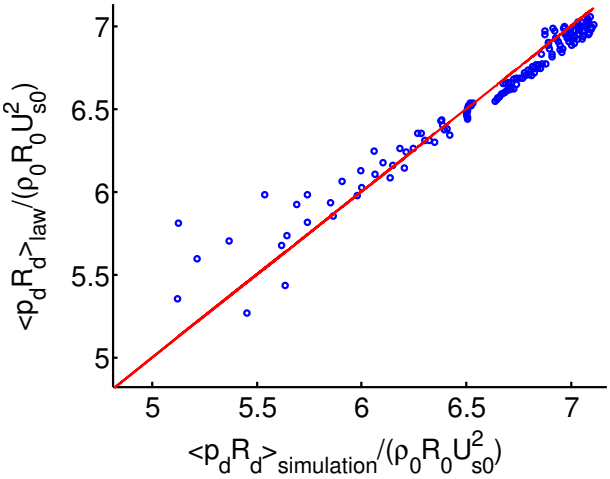

Figure 4.13: Comparison between the scaling law (4.86) and simulations results for the $< p_d R_d >$ value.

The ignition criterion can be assessed from the condition $< p_d R_d > > (pr)_{ign} = (\rho R)_{ign} T_{ign}$. Using $T_{ign} = 8$ keV and $(\rho R)_{ign} = 200$ mg.cm^{-2} (see Section 2.1.2), the areal pressure ignition threshold is $(pr)_{ign} = 1.2$ Gbar.cm.

By requiring that $< p_d R_d >= (pr)_{ign}$ in (4.86), we obtain the expression of the minimum initial shock velocity as a function of the initial hot-spot areal density for ignition:

$$(U_s)_{ign} = 0.36 \left(\frac{(pr)_{ign}}{\rho_0 R_0} \right)^{\frac{1}{2}} \left[1 + 3y_0^2 \right] . \tag{4.87}$$

The ignition threshold in the plane $(U_{s0}, \rho_0 R_0)$ is represented in Figure 4.14. When the initial temperature of the hot-spot increases, the initial shock Mach number decreases, reducing the shock efficiency. The threshold is thus affected by the initial hot-spot temperature. For example, with the initial areal density of 50 mg.cm^{-2} the minimum shock velocity needed to ignite the fuel is 600 km.s^{-1}, if the fuel is initially cold, and 800 km.s^{-1} if the initial shock Mach number is $M_{s0} = 3$.

This ignition condition can be expressed in terms of the initial ignitor shock pressure. According Table 4.1, the initial shock pressure at $R = R_0$ is

$$p_{s0} = 0.75 \rho U_{s0}^2 \left[1 - 0.2 y_0^2 \right] . \tag{4.88}$$

Therefore, the minimal initial shock pressure to reach ignition is given by the following expression:

$$(p_s)_{ign} R_0 = 0.13 (pr)_{ign} \left[1 + 5.8 y_0^2 \right] . \tag{4.89}$$

If the hot-spot is initially cold, the minimal shock pressure for ignition depends only on the hot-spot radius. For a typical hot-spot radius of 50 μm, the ignitor shock initial pressure must be greater than $(p_s)_{ign} = 31$ Gbar. We consider now that the same hot-spot is initially hot. Assuming an initial shock Mach number $M_{s0} = 4$, the minimal initial shock pressure for ignition is $(p_s)_{ign} = 43$ Gbar.

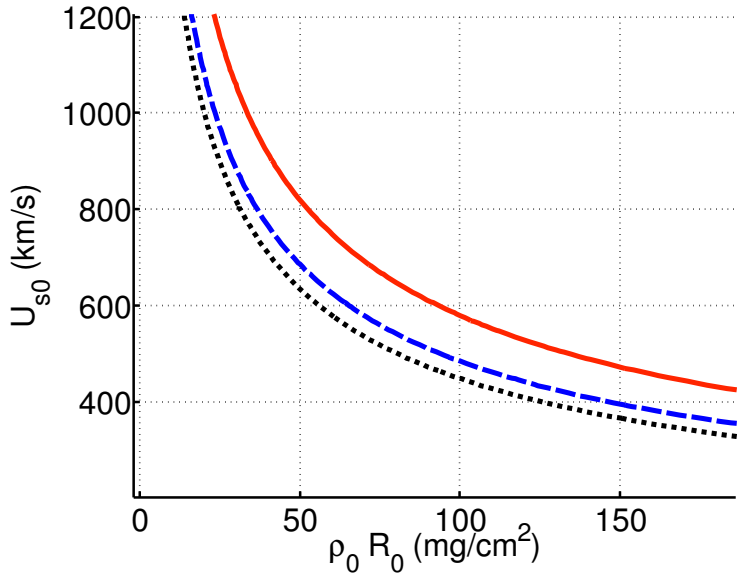

Figure 4.14: Influence of the initial temperature of the deuterium-tritium fuel on the ignition threshold according to (4.86): black dotted line - infinite initial shock Mach number, blue dashed line - initial shock Mach number of 6, red line - initial shock Mach number of 3.

Let us compare our prediction with the results given by Scherbakov [Shcherbakov, 1983]. In his study, a solid spherical DT target is first compressed to the density of 40 g.cm^{-3} with a radius of 140 μm which corresponds to the areal density of 560 mg.cm^{-2}. The temperature of the compressed target is 0.1 keV, which corresponds to an initial sound spreed $c_0 = 113$ km.s^{-1} and an initial shock pressure $p_0 = 3$ Gbar. According to (4.87), the initial velocity must be $(U_s)_{ign} \sim 250$ km.s^{-1} with an initial shock Mach number of 2.5. This is close to the 230 km.s^{-1} announced by Shcherbakov. Figure 4.14 provides a qualitative estimate of the effect of the Mach number on the ignition threshold for shock ignition. However, it can not be considered as the quantitative criterion. For that purpose, we consider in the next section the balance between the fusion energy production and the dissipative effects.

4.3 Ignition criterion

We consider that the fusion reactions start to ignite when the diverging shock exits the hot-spot. To express the ignition criterion, we use the same development as in the section 2.1.2 for the conventional ignition scheme. However, in the present case, the hot-spot is created by the ignitor

shock. The fusion reactions will be maintained if the self-heating of the hot-spot coming from alpha-particles energy deposition is larger than the hot-spot cooling due to the radiation and the electron conduction losses. Thus the ignition criterion is expressed with the relation:

$$P_\alpha > P_{brem} + P_{cond} \tag{4.90}$$

where P_α is the power deposition by the alpha-particles, P_{brem} is the radiative losses mainly due to the bremsstrahlung and P_{cond} is the conduction losses.

The term P_{mech} due to the mechanical work introduced in Section 2.1.2 is neglected here. This is because our estimate is made at the moment when the shock just exits the hot-spot, the pressure in the inner part of the shell and in the hotspot are almost equal.

We express each power contribution to the balance using the extension of the self-similar solution of Guderley. As the balance is computed at the shock exit time t_{div}, the power losses and the power gain are evaluated inside the sphere of radius R_d.

4.3.1 Alpha particle energy deposition

The fusion power carried out with the alpha-particles is integrated behind the diverging shock

$$P_\alpha = 4\pi W_\alpha \int_0^{R_d} \left(\frac{n_i}{2}\right)^2 < \sigma\nu > r^2 \, \mathrm{d}r, \tag{4.91}$$

with $W_\alpha = 5.6 \times 10^{-6}$ erg.

The particle density is expressed with the fluid density as $n = \rho/\mathrm{A}m_p$ with A = 2.5 the average atomic mass of DT and m_p the mass of a proton. The reactivity of Deuterium Tritium depends on the temperature (2.2). It can be approximated by a power law

$$< \sigma\nu > (T) = < \sigma\nu >_{10} \left(\frac{T_{[\mathrm{keV}]}}{T_{10}}\right)^\sigma, \tag{4.92}$$

where $< \sigma\nu >_{10} = 1.15 \times 10^{-16} \mathrm{cm}^3.\mathrm{s}^{-1}$ is the reactivity at the reference temperature $T_{10} = 10$ keV and $\sigma = 2$ or 3 respectively for $T > T_{10}$ and $T < T_{10}$.

Figure 4.15 presents the DT reactivity and the two power law approximations.

The temperature of an ideal gas is related to the sound velocity by

$$c = c_{10}\sqrt{\frac{T_{(\mathrm{keV})}}{T_{10}}}, \tag{4.93}$$

where $c_{10} = 1130$ km.s^{-1} is the acoustic velocity of DT at $T_{10} = 10$ keV.

The alpha-particle power reads then:

$$P_\alpha = \frac{\pi W_\alpha < \sigma\nu >_{10}}{c_{10}^{2\sigma}(Am_p)^2} \int_0^{R_d} r^2 \rho^2 c^{2\sigma} \, \mathrm{d}r. \tag{4.94}$$

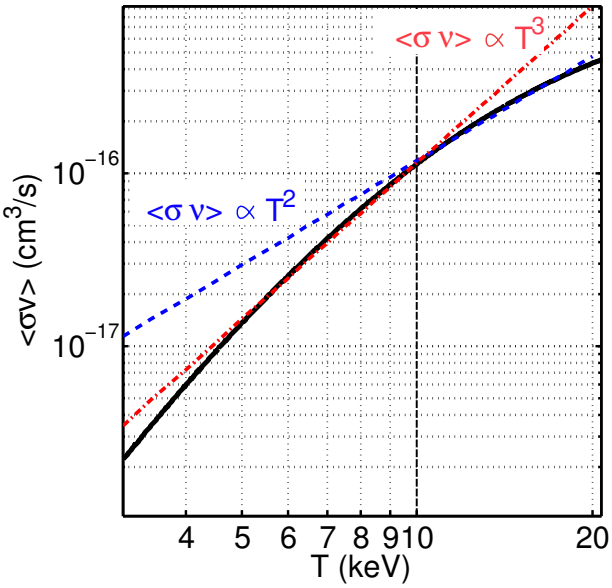

Figure 4.15: Deuterium-Tritium reactivity.

It is shown in Section 4.1.5.2 that the pressure $p = \rho c^2/\gamma$ is almost homogeneous behind the diverging shock. Thus the pressure can be taken out of the integral and its value is chosen at the shock front:

$$P_\alpha = \frac{\pi W_\alpha < \sigma\nu >_{10}}{c_{10}^{2\sigma}(Am_p)^2}\gamma^\sigma p^\sigma(R_d, t_{div}) \int_0^{R_d} r^2 \rho^{2-\sigma}\, \mathrm{d}r. \tag{4.95}$$

In the frame (x, y) and accounting for the finite Mach number corrections, this expression reads

$$P_\alpha = \frac{\pi W_\alpha < \sigma\nu >_{10}}{c_{10}^{2\sigma}(Am_p)^2} {R_d}^3 \rho_0^2 \left(\frac{c_0}{y_d}\right)^{2\sigma} P_{IV}^\sigma(1) \int_{\mathcal{D}_{IV}} x^2 G^{2-\sigma}\, \mathrm{d}x \left[1 + y_d^2\left((2-\sigma)\frac{\int_{\mathcal{D}_{IV}} x^2 G^{2-\sigma} G_1\, \mathrm{d}x}{\int_{\mathcal{D}_{IV}} x^2 G^{2-\sigma}\, \mathrm{d}x} + \sigma P_{1,IV}(1)\right)\right]. \tag{4.96}$$

According to (4.67) and Table 4.7

$$\begin{aligned} R_d &= R_{d0} R_0 \left(1 + y_0^2 R_{d1}\right), \\ y_d &= y_{d0} y_0 \left(1 + y_0^2 y_{d1}\right), \end{aligned} \tag{4.97}$$

with $R_{d0} = 0.342$, $R_{d1} = 2.26$, $y_{d0} = 0.951$ and $y_{d1} = -1.28$.

By using the numerical value of the intergal in (4.96) and the expressions of R_d and y_d in (4.97), one can express the alpha-particles power as

$$P_\alpha[10^{-7}\mathrm{W}] = \frac{W_\alpha < \sigma\nu >_{10}}{(Am_p)^2} \rho_0^2 R_0^3 \left(\frac{U_{s0}}{c_{10}}\right)^{2\sigma} P_{\alpha 0}^\sigma \left[1 + y_0^2 P_{\alpha 1}^\sigma\right] \tag{4.98}$$

with the dimensional quantities $W_\alpha, m_p, \rho_0, R_0, U_{s0}$ in CGS unit.

The coefficients $P_{\alpha 0}$ and $P_{\alpha 1}$ in (4.98) are given in Table 4.8

σ	2	3
$P_{\alpha 0}^{\sigma}$	75	134
$P_{\alpha 1}^{\sigma}$	-9.2	-11

Table 4.8: Series coefficients in the expression of the alpha-particles power.

The alpha-particles are deposited in the hot-spot if the areal density is higher than their stopping range, which depends on the temperature [Atzeni and Meyer-Ter-Vehn, 2004]

$$\rho l_\alpha(\ \mathrm{g.cm^{-2}}) = 0.025 \frac{T_{keV}^{\frac{5}{4}}}{1 + 0.008 T_{keV}^{\frac{5}{4}}}. \tag{4.99}$$

The fraction of the alpha-particles stopped in the hot-spot can be expressed as [Krokhin and Rozanov, 1973]

$$f_\alpha = \begin{cases} \frac{3}{2}\tau_\alpha - \frac{4}{5}\tau_\alpha^2, & \tau_\alpha \leq \frac{1}{2} \\ 1 - \frac{1}{4}\tau_\alpha^{-1} + \frac{1}{160}\tau_\alpha^{-3}, & \tau_\alpha > \frac{1}{2} \end{cases} \tag{4.100}$$

where $\tau_\alpha =< \rho R >_d / \rho l_\alpha$.

The hot-spot areal density is

$$< \rho R >_d = \rho_0 R_d \int_{\mathcal{D}_{IV}} G \,\mathrm{d}x \left[1 + y_d^2 \frac{\int_{\mathcal{D}_{IV}} G G_1 \,\mathrm{d}x}{\int_{\mathcal{D}_{IV}} G \,\mathrm{d}x} \right] \tag{4.101}$$

$$= 6.2 \rho_0 R_0 \left[1 - y_0^2 3.8 \right]. \tag{4.102}$$

To evaluate the fraction of the alpha-particles energy deposited in the hot-spot one needs to evaluate the temperature of the fuel as the shock exits the hot-spot.

In the frame (x, y), the temperature reads

$$\frac{T(x,y)}{T_{10}} = \left(\frac{c_0^2}{c_{10}} \right) \left(\frac{x}{y} \right)^2 C^2 \left(1 + 2 y_d^2 C_1 \right). \tag{4.103}$$

According to the corrected self-similar solution, the temperature is infinite in the center of the sphere. However, it is not important for calculation of the energy production as the fuel density is zero in the center and the mass increases with the radius. We use the value of the temperature at the shock front (at $x = 1$) which corresponds to the largest part of the fuel. By using the expression of y at the shock exit time (4.97), the temperature at the shock front R_d at the time t_{div} is

$$T_{[\mathrm{keV}]} = T_{10} T_0 \left(\frac{U_{s0}}{c_{10}} \right)^2 \left(1 + y_0^2 T_1 \right), \tag{4.104}$$

with $T_0 = 1.3$ and $T_1 = -0.4$.

As the correction term T_1 is small, the temperature is taken at the zeroth order when calculating the alpha-particle stopping range ρl_α with the expression (4.99).

Then $\tau_\alpha =< \rho R >_d / \rho l_\alpha$ is expressed in a series form by using (4.101). By injecting this expression in (4.100), the fraction of the alpha-particles stopped in the hot-spot is also expressed with a series form. It depends on the shock initial velocity U_{s0}, on the initial areal density $\rho_0 R_0$ and on the shock Mach number M_{s0} (see Figure 4.16). As the final density in the hot-spot is lower for a finite Mach number, the fraction of alpha-particles stopped in the final hot-spot is also small for a finite Mach number. The power of the alpha-particle is corrected as $P_\alpha \to f_\alpha P_\alpha$.

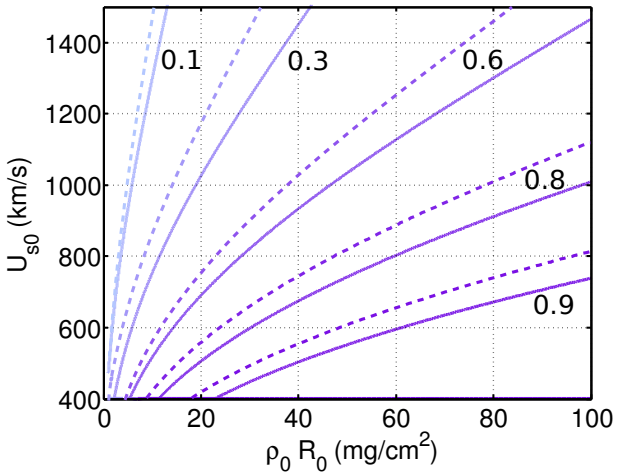

Figure 4.16: Alpha particles fraction stopped in the hot-spot: with $M_{s0} = \infty$ - dashed lines - and $M_{s0} = 4$ - solid line.

4.3.2 Conduction losses

The electron conduction losses across the surface of the hot-spot are calculated using the heat-flux given by Spitzer

$$Q_e = -\frac{K_e T^{\frac{5}{2}}}{\ln \Lambda} \nabla T, \tag{4.105}$$

with $K_e = 9.5 \times 10^{19}$ erg.s^{-1}.cm^{-1}.keV$^{-7/2}$ and $\ln \Lambda \simeq 6$ the Coulomb logarithm.

The power of conduction losses is then expressed as

$$P_{cond} = 4\pi R_d^2 Q_e. \tag{4.106}$$

In the frame (x, y), the gradient of the temperature (4.103) at the shock front writes

$$\partial_r T|_{r=R_s} = R_d^{-1}\, \partial_x T|_{x=1}\,, \tag{4.107}$$

with

$$\partial_x T = T_{10} y^{-2} 2C \left(xC + x^2 C'\right) \left[1 + y_d^2 \left(2C_1 + x^2 \frac{CC_1'}{(xC + x^2 C')}\right)\right]. \tag{4.108}$$

At the shock exit time, the temperature gradient (4.107) is calculated by replacing $x = 1$ and $y = y_d$ (4.97) in (4.108):

$$\partial_r T|_{t=t_{div},r=R_d}\,[\mathrm{keV.cm^{-1}}] = \frac{T_{10}}{R_0}\left(\frac{U_{s0}}{c_{10}}\right)^2 DT_0\left[1 + y_0^2 DT_1\right], \tag{4.109}$$

with $DT_0 = -1.9$ and $DT_1 = -13.4$.

By inserting the series form of R_s (4.97), T_0 (4.104) and ∇T (4.109) in the conduction power (4.106) we obtain

$$P_{cond}[10^{-7}\mathrm{W}] = T_{10}^{\frac{7}{2}} K_e R_0 \left(\frac{U_{s0}}{c_{10}}\right)^7 P_{c0}\left[1 + y_0^2 P_{c1}\right] \tag{4.110}$$

with $P_{c0} = 0.9$ and $P_{c1} = -9.9$.

4.3.3 Radiative losses

Assuming that the hot-spot is transparent for the thermal radiation, the radiation power is expressed using (2.13):

$$P_{brem} = 4\pi A_b \int_0^{R_d} r^2 \rho^2 T^{\frac{1}{2}}\,\mathrm{d}r \tag{4.111}$$

with $A_b = 3.05 \times 10^{23}$ erg.s^{-1}.cm^3.g^{-2}.keV$^{-1/2}$.

In the frame (x, y), this gives

$$P_{brem} = 4\pi A_b \rho_0^2 T_{10}^{\frac{1}{2}} \frac{c_0}{c_{10}} y_d^{-1} R_d^3 \int_{\mathcal{D}_{IV}} G^2 C x^2\,\mathrm{d}x \left[1 + y_d^2 \frac{\int_{\mathcal{D}_{IV}} (2G_1 + C_1)\, G^2 C x^2\,\mathrm{d}x}{\int_{\mathcal{D}_{IV}} G^2 C x^2\,\mathrm{d}x}\right]. \tag{4.112}$$

Using (4.97) and the numerical value of the integrals in (4.112) we obtain

$$P_{brem}[10^{-7}\mathrm{W}] = A_b \rho_0^2 R_0^3 \left(\frac{U_{s0}}{c_{10}}\right) T_{10}^{\frac{1}{2}} P_{r0}\left[1 + y_0^2 P_{r1}\right] \tag{4.113}$$

with $P_{r0} = 178$ and $P_{r1} = -7.2$.

It is convenient to divide the expressions (4.98),(4.113) and (4.110) by the initial radius R_0. Then the corresponding powers per unit of length depend on the initial shock velocity U_{s0}, the initial hot-spot areal density $\rho_0 R_0$ and the initial shock Mach number M_{s0}. Figure 4.17 presents the powers per unit of length for a fixed value of $\rho_0 R_0$ and two different values of the initial shock Mach number. At high initial shock velocities, the final hot-spot temperature is high and the conduction losses dominate. The dots represent the threshold $(U_s)_{ign}$ were the gain and losses are equilibrated. One can see that the finite Mach number reduces both gain and losses and increases the value of $(U_s)_{ign}$. Therefore, higher is the initial hot-spot temperature, higher is the ignition shock velocity $(U_s)_{ign}$. Interestingly, the radiation losses dominate near the ignition threshold for the chosen value of the areal density 50 mg.cm^{-2}.

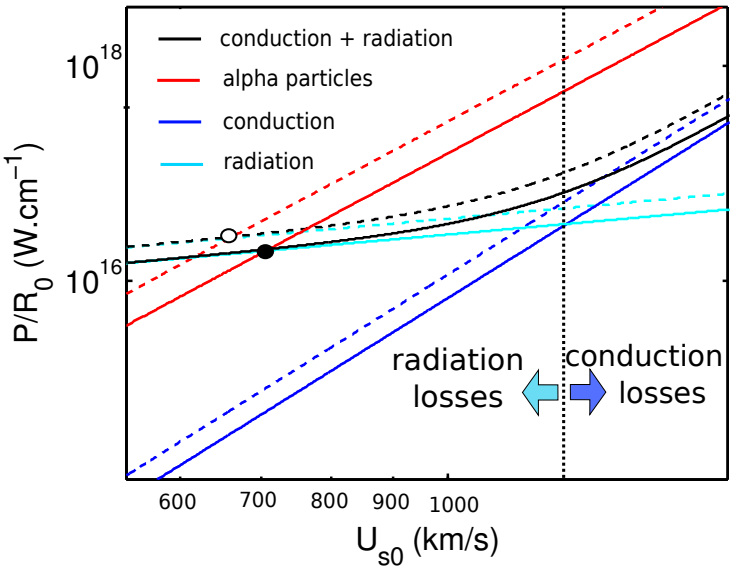

Figure 4.17: Powers of losses and gain in the hot-spot divided by the initial hot-spot radius. The initial areal density is $\rho_0 R_0 = 50$ mg.cm^{-2}. The results for $M_{s0} = \infty$ are represented with dashed line, and for $M_{s0} = 5$ with full lines.

4.3.4 Ignition Threshold

The ignition threshold is defined as the limiting curve where

$$P_\alpha = P_{brem} + P_{cond}. \tag{4.114}$$

According to (4.98), (4.110) and (4.113) the ignition shock velocity $(U_s)_{ign}$ depends on the initial areal density of the hot-spot $\rho_0 R_0$, the initial shock velocity U_{s0} and the initial shock Mach number M_{s0}.

Figure 4.18 presents the ignition threshold curves calculated under different assumptions. The ignition domain is in the top right corner of a considered threshold curve. The basic case (curve (1)) neglects the initial temperature of the hot-spot ($M_{s0} = \infty$), uses the power law of reactivity with $\sigma = 2$ and assumes that $f_\alpha = 1$. This choice of parameters corresponds to the results given in Ref. [Ribeyre et al., 2011]. We see that the minimum shock velocity needed to ignite the fuel is less than 500 km.s^{-1} for a minimum initial hot-spot areal density of less than 10 mg.cm^{-2}. The temperature behind the diverging shock front is according to (4.104) $T = 2.6$ keV. This temperature is much below the domain of validity of the reaction rate power low (4.92) with $\sigma = 2$. Thus the ignition conditions are strongly underestimated. The threshold curve (2) uses the reactivity power law with $\sigma = 3$. The minimum shock velocity is then about 600 km.s^{-1} and the fuel temperature $T = 4.3$ keV is in the range of validity of the reactivity law used.

However this curve still underestimates the ignition threshold as it does not account for the finite Mach number of the shock and the alpha-particle losses. The curve (3) presents the

ignition threshold which accounts for the fraction of alpha-particles escaping the hot-spot. For a low areal density, the alpha-particles are not stopped. This increases the minimum initial areal density to approximately 15 mg.cm^{-2}. The curve (4) presents the ignition threshold for a finite initial shock Mach number of 4 by using the corrected solution of Guderley established in this chapter. A combination of the alpha-particle losses and the hot-spot initial temperature leads to the increase of the minimum shock velocity $U_{s0} = 750$ km.s^{-1} and a minimal hot-spot areal density $\rho_0 R_0 = 20$ mg.cm^{-2}.

The ignition thresholds are compared to numerical simulations with a realistic equation of state, conduction, radiation and alpha-particles transport. The black markers represent cases where the fuel was ignited. The white markers represent cases where the fuel does not ignite after one rebound of the ignitor shock. The hot-spot areal density and the shock velocity were measured when the ignitor shock enters into the fuel. Also the strength of the shock at this time was measured. The diamond markers represent the cases where intial shock strength is very low $Z_0 < 1.5$. The circle markers represent the cases where the initial shock strength is higher $Z_0 > 3$. The square markers represent the intermediate cases. One can see that for the highest shock strengths, the simulation results agree with the ignition threshold calculated for an infinite Mach number. The simulation with very low strengths are closer to the ignition threshold calculated with an initial shock Mach number of 4. The simulations indicate a higher threshold than the curve (4). This must be due to their corresponding shock Mach number $M \sim 1.2$ which is out of the present model domain of validity.

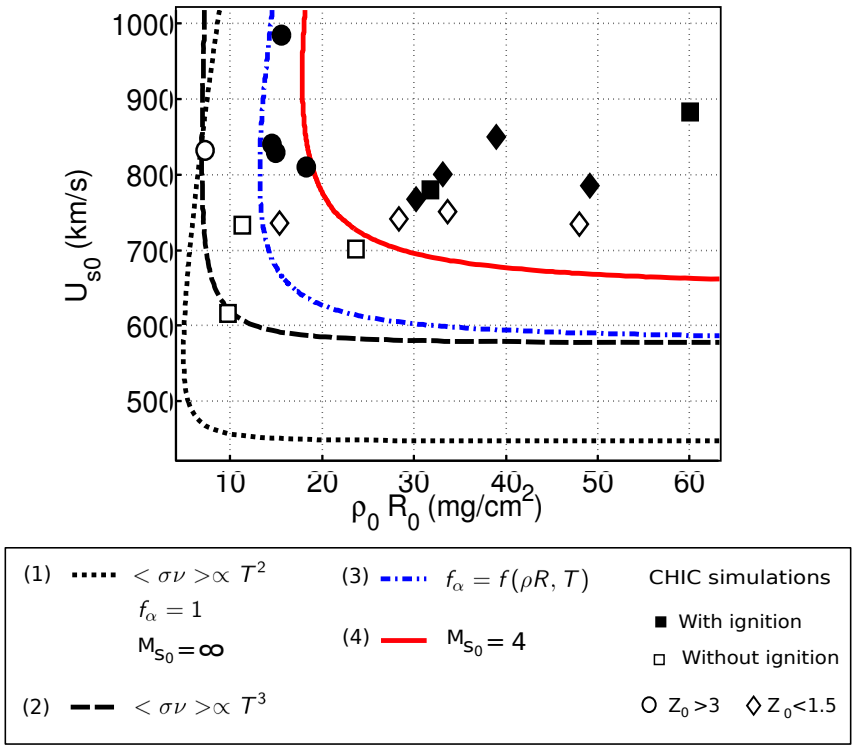

Figure 4.18: Ignition threshold in the plane $(U_{s0}, \rho_0 R_0)$.

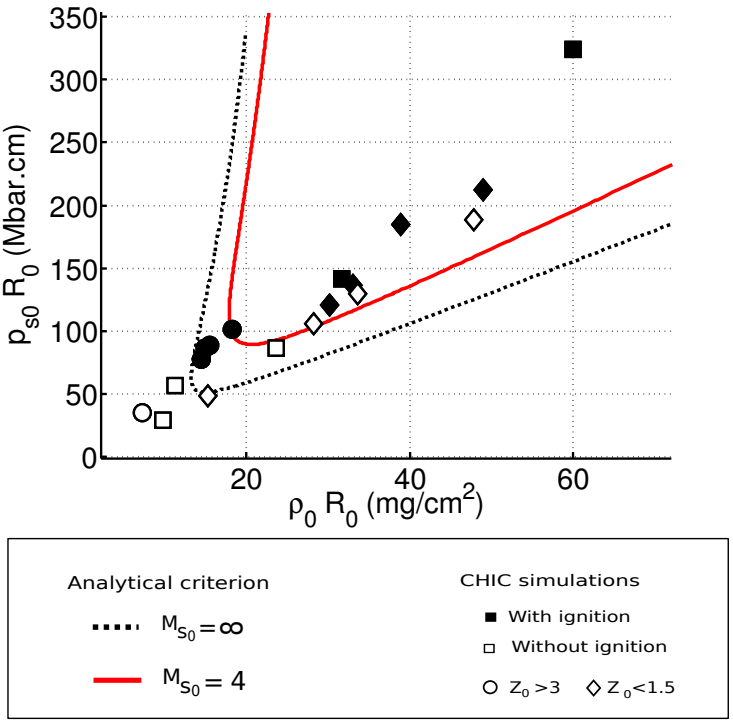

Figure 4.19: Ignition threshold in the plane $(p_{s0}R_0, \rho_0 R_0)$.

The ignition criterion can also be expressed with the initial shock pressure. By inserting the ignition shock velocity in the relation (4.88), the ignition shock pressure $(p_s)_{ign}$ is expressed as a function of the initial hot-spot areal density and radius. The product $(p_s)_{ign}R_0$ as a function of $\rho_0 R_0$ is represented in Figure 4.19.

In the previous section, the product $(p_s)_{ign}R_0$ (4.89) was defined as a function of the initial shock Mach number only. In the present approach, it depends on the initial hot-spot areal density: higher is the hot-spot density for a given hot-spot radius, higher must be the initial shock pressure for ignition. Here again we obtain a good agreement with the simulations. The circle markers, corresponding to the higher shock strengths, are closer to the infinite Mach number threshold. The diamond markers, corresponding to smaller shock strengths, are closer to the finite Mach number threshold.

According to 4.19, for a typical hot-spot radius of 50 μm, the minimal initial shock pressure is $(p_s)_{ign} = 10$ Gbar with $\rho_0 R_0 = 15$ mg.cm^{-2} for an infinite shock Mach number, and $(p_s)_{ign} = 20$ Gbar with $\rho_0 R_0 = 20$ mg.cm^{-2} for an initial shock Mach number of 4.

4.3.5 Discussion

Throughout the present study, a sufficiently high shock Mach number is assumed in order to stay within the domain of validity of the solution with only one correction term. The effective expansion parameter is M_{s0}^{-2}, so even for $M_{s0} = 4$, the value of this parameter ~ 0.06 is sufficiently small to justify the validity of our approach. Nevertheless, in the power expressions

(4.98), (4.110), and (4.113), the large coefficients in front of this small parameter indicate that significant effects are expected for lower Mach numbers. This is the case of shock ignition where numerical simulations show a shock Mach number below 3 when it enters the fuel. Although the present solution might not be sufficiently accurate in this case, it provides important qualitative trends.

One may choose to add one or two more correction terms to the Guderley solution in order to obtain a more accurate model. Another way would be to study numerically the ignition of a hot-spot with a very low initial shock Mach number. Then, the theory developed here can be used as a tool to understand the results qualitatively.

This simple model is useful for getting a physical insight on the shock ignition conditions and the possibilities for optimization. However, there are some more physical effects that need to be considered. In particular, the heat flux leaving the hot-spot induce ablation at the shell inner face surface. This feeds the hot-spot with more fuel and increases its areal density. A model taking into account the shell should be more accurate.

4.4 Conclusions

In the first part of this chapter, we analyzed the effects of the initial Mach number of a converging spherical shock wave propagating through a hot-spot at a finite pressure at rest. The Guderley's solution has been generalized to a finite shock Mach number using a first order correction over a small parameter ${M_s}^{-2}$. The shock amplification factor that was constant for an infinite shock Mach number now varies in time (and with the shock position) as $\Lambda = \lambda(1 + \lambda_1^{\pm} M_s(t)^{-2})$. The factors λ, λ_1^- and λ_1^+ are the solutions of a non linear eigen-value problem. They are calculated iteratively so that the solution does not undergo any singular behavior apart from the position of the shock. The values obtained for the correction terms are consistent with those found in the literature [Ponchaut et al., 2006, Welsh, 1967]. We recover the expression of the shock wave position given by Ponchaut [Ponchaut et al., 2006] by integrating the shock amplification factor. In this study, we consider that the flow is driven by a piston following a particle path. The conservation of entropy on the particle path, except across the shock, allows to express the particle trajectory analytically. It is then possible to write the expression of the radius and the time where the diverging shock encounters the piston. This time corresponds to the moment when the ignition is expected. Scaling laws are expressed in that time and are a straightforward way to evaluate the finite shock Mach number effect on the final hot-spot conditions.

It appears that the self-similar solution overestimates the density and pressure at the ignition threshold. The initial temperature decreases significantly the compressibility of the fluid. The flow quantities are more affected by the finite shock Mach number during the diverging phase. This is explained by the fact that the shock wave encounters a flow that is already perturbed by the finite Mach number. Therefore, the small changes in the boundary condition during the converging phase are amplified during the diverging phase. This is clearly visible in the Lagrangian representation of the solution in Figure 4.10.

This analytical solution gives us a possibility to evaluate the effect of a fuel preheating during the compression phase on the efficiency of the ignitior shock wave for the shock ignition scheme.

We used the corrected solution of Guderley to define an analytical criterion for SI which takes into account the initial temperature of the hot-spot. The ignition criterion $P_\alpha > P_{brem} + P_{cond}$, with the expressions (4.98),(4.113) and (4.110) is obtained by taking into account the radiative and thermal energy losses from the hot-spot and the alpha-particle energy deposition. We obtain a relation between the initial areal density of the hot-spot and the initial shock velocity depending on the initial shock Mach number. The shock velocity must be higher than $U_{s0} = 750$ km.s^{-1} with $< \rho R >_0 = 20$ mg.cm^{-2} to ignite the fuel. If we consider a hot-spot of 50 μm this corresponds to a minimal shock pressure $(p_s)_{ign} = 20$ Gbar.

This may seem counter-intuitive that a pre-heated hot-spot which contains more internal energy initially is harder to ignite. Figure 4.12 shows that for a given initial shock velocity, the final internal energy is lower if the initial hot-spot is preheated. The shock Mach number as it enters the hot-spot is therefore a dominant parameter for shock ignition.

We demonstrated that the preheat of the hot-spot leads to a modification of more than 20% in the ignition criterion. Such a strong variation may have strong effect on the driver energy and the target energy gain, that are crucial parameters for the inertial fusion power plant.

5 Ignitor shock amplification in the shell

Contents

In a typical HiPER implosion, the hot-spot radius near stagnation is of about 50 μm. Then the ignition criterion presented in Chapter 4 requires a minimal ignitor shock pressure of 20 Gbar as it enters the hot-spot. Generating such an ablation pressure is very challenging and not realistically feasible nowadays. Therefore, the amplification of the shock pressure in the imploding shell is a key element for shock ignition.

The converging shock description developed in the previous chapter applies for an initial medium at rest. It cannot be applied for the shock propagation through an imploding shell. Indeed, as the shell is accelerated or decelerated, the shock is propagating in a non-inertial frame. Moreover, the upstream density and pressure gradients must be accounted for. The shell is imploding as the shock propagates through it and an overall pressure increase contributes to the shock pressure amplification. Lastly, the collision of the shock with the diverging first shock plays an important role [Lafon et al., 2013] in the current shock ignition scenario.

We propose a quantitative theoretical description of the shock propagation in the imploding shell in Section 5.1. Also, the role of the various physical effects in the ignitor shock pressure amplification and strengthening are analyzed in Section 5.2.

5.1 Shock amplification mechanisms

In this section, we present the physical processes influencing the ignitor shock pressure p_s and strength Z as it propagates through an accelerated or decelerated spherical shell. We assume in this study a one dimensional spherical flow depending on the radius r and time t. The shock is generated at the outer radius of the shell r_{out} at the time t_i with an initial pressure p_{si}. The function $R_s(t)$ defines its position. The shock propagates first into an accelerated medium. It eventually collides with the returning primary shock coming from the assembly phase. We define p_{c1} and p_{c2} respectively the ignitor shock pressure before and after the collision. After the collision, the shock propagates into a decelerating medium until it reaches the inner face of the shell r_{in} at the time t_f with the final pressure p_{sf}. Figure 5.1 presents the shell profile and the ignitor shock position at its generation (a), before the collision (b), after the collision (c) and at the inner face of the shell (d).

The shock strength Z is defined as the ratio of the upstream pressure and the downstream pressure at the shock front $Z = p(R_s^+, t)/p(R_s^-, t)$. The strengthening factor of the shock is the ratio of the final strength of the shock Z_f and its initial strength Z_i. We define the amplification factor of the shock $\mathcal{X}$ as the final shock pressure at the inner face of the shell over the initial shock pressure near the ablation front $\mathcal{X} = p_{sf}/p_{si}$.

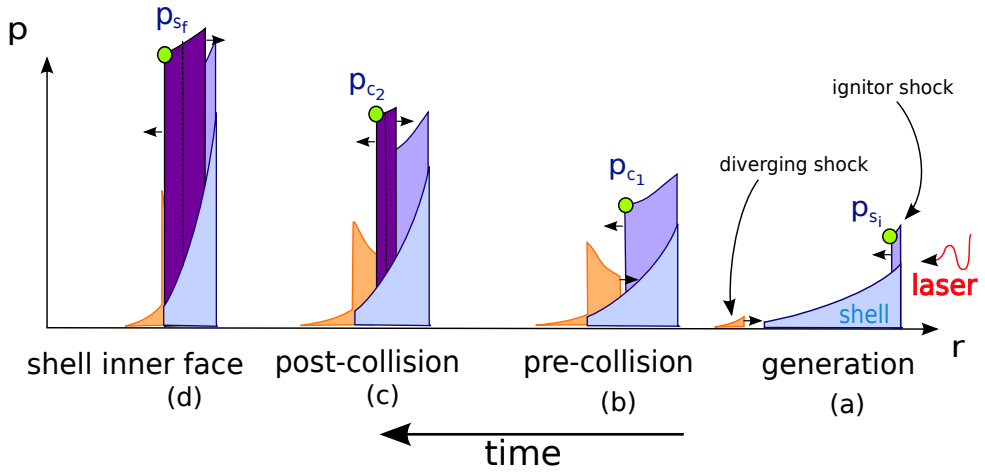

Figure 5.1: Pressure profiles at four different steps in the ignitor shock propagation : (a) the ignitor shock is generated as the returning shock diverges, (b) state before the shocks collision, (c) state after the shocks collision, (d) the ignitor shock reaches the shell inner surface

During the shell implosion, the shell pressure increases with time. We describe in a first part the shell implosion in order to express this overall pressure amplification $\mathcal{X}_{imp}$. Then we study the shock pressure amplification in the shell comoving frame $\mathcal{X}_{shell}$ in a second part. Finally we describe the shock pressure amplification in the collision $\mathcal{X}_{coll}$. The total shock amplification factor is $\mathcal{X} = \mathcal{X}_{imp}\mathcal{X}_{shell}\mathcal{X}_{coll}$.

5.1.1 Shell implosion

A simple model is introduced to describe the shell during the ignitor shock propagation. This allows to define a reference frame comoving with the shell. The relation between the shell comoving frame and the laboratory frame gives the overall time dependent pressure amplification factor $\mathcal{X}_{imp}$.

5.1.1.1 Shell description

We write $X = \{r, t\}$ the inertial Cartesian frame which corresponds to the laboratory frame. We consider the compression of a medium - called the shell - included between the radius r_{in} and r_{out} at the reference time $t = 0$.

Let $R_p(r_0, t)$ be the position at the time t of the fluid particle initially at the position $r_0 \in [r_{in}, r_{out}]$ at $t = 0$. The spatial domain of the shell is $\mathcal{D}(t) = \{R_p(r_{in}, t) < r < R_p(r_{out}, t), t \in \mathbb{R}\}$ with $\mathcal{D}(0) = [r_{in}, r_{out}]$. The aim of this section is to express the shell quantities $p(r, t)$, $\rho(r, t)$ and $u(r, t)$ for all couples (r, t) included in $\mathcal{D}(t) \times \mathbb{R}$.

By following the approach of Kidder [Kidder, 1976], we consider a homogeneous compression of the shell. This particular flow has been presented in Section 3.2.

We remind that every elementary volume scales in the same way with time

$$\mathrm{d}^3 R_p = h^3(t)\,\mathrm{d}^3 r_0, \tag{5.1}$$

where $h(t)$ is a time dependent dimensionless factor, with $h(0) = 1$.

It is also assumed that the flow is isentropic,

$$\frac{p(r,t)}{\rho^\gamma(r,t)} = \frac{p_0}{\rho_0^\gamma} = \alpha_0, \tag{5.2}$$

where α_0 is the shell adiabat, p_0 and ρ_0 are the initial pressure and density.

The density, velocity and pressure can be expressed in the Cartesian frame X using the time scaling function $h(t)$ as follows

$$\forall (r,t) \in \mathcal{D}(t) \times \mathbb{R}, \quad \rho(r,t) = h(t)^{-3}\rho_0\left(h(t)^{-1}r\right), \tag{5.3a}$$

$$p(r,t) = h(t)^{-3\gamma}p_0\left(h(t)^{-1}r\right), \tag{5.3b}$$

$$u(r,t) = \dot{h}(t)h(t)^{-1}r. \tag{5.3c}$$

The temporal function $h(t)$ is obtained by integrating the equation

$$-h^{3\gamma-2}\ddot{h} = \pm\frac{1}{\tau^2}, \tag{5.4}$$

with τ an arbitrary constant in units of time. The right hand side sign determines if the imploding flow is accelerating $\ddot{h}(t) < 0$ or decelerating $\ddot{h}(t) > 0$.

The spatial profiles $\rho_0(r)$, $p_0(r)$ and $c_0(r)$ fulfill the equation

$$-\frac{1}{\rho_0 r_0}\frac{\mathrm{d}p_0}{\mathrm{d}r_0} = \pm\frac{1}{\tau^2}. \tag{5.5}$$

.

By integrating (5.5) we get the initial spatial profiles of the shell

$$\forall r_0 \in \mathcal{D}(0), \quad p_0(r_0) = p_{out}\left[1 - \frac{\gamma-1}{2}\mathcal{K}\left(1 - \left(\frac{r_0}{r_{out}}\right)^2\right)\right]^{\frac{\gamma}{\gamma-1}}, \tag{5.6a}$$

$$\rho_0(r_0) = \rho_{out}\left[1 - \frac{\gamma-1}{2}\mathcal{K}\left(1 - \left(\frac{r_0}{r_{out}}\right)^2\right)\right]^{\frac{1}{\gamma-1}}, \tag{5.6b}$$

$$c_0(r_0) = c_{out}\left[1 - \frac{\gamma-1}{2}\mathcal{K}\left(1 - \left(\frac{r_0}{r_{out}}\right)^2\right)\right]^{\frac{1}{2}}, \tag{5.6c}$$

with p_{out}, $\rho_{out} = (p_{out}/\alpha_0)^{1/\gamma}$ and $c_{out}^2 = \gamma p_{out}/\rho_{out}$ the pressure, density and sound velocity at the external radius r_{out} and initial time $t = 0$.

The shell parameter $\mathcal{K} = \pm(r_{out}/c_{out}\tau)^2$ defines how sharp are the shell density and pressure

profiles. The smaller this parameter is, the longer is the implosion and the lower are the density and pressure gradients. The sign of $\mathcal{K}$ is positive in the accelerating case and negative in the decelerating case.

In case of the accelerating shell, the parameter $\mathcal{K}$ has a maximum value for which the flow quantities are zero at the shell inner surface :

$$\forall \gamma \neq 1, \quad \mathcal{K}_{\max} = \frac{2}{\gamma - 1}\left(1 - \left(\frac{r_{in}}{r_{out}}\right)^2\right)^{-1}. \tag{5.7}$$

5.1.1.2 Shell comoving frame

Let us consider the non-inertial reference frame $\tilde{X} = \{\tilde{r}, \tilde{t}\}$ introduced by Martel and Shapiro [Martel and Shapiro, 1998] which homogeneously contracts. It is defined by the transformation $\Lambda : (r, t) \mapsto (\tilde{r}, \tilde{t})$ with

$$\tilde{r} = a(t)^{-1} r, \tag{5.8a}$$

$$\mathrm{d}\tilde{t} = a(t)^{-(\vartheta+1)}\,\mathrm{d}t, \tag{5.8b}$$

with $a(t)$ a function of time positive and twice differentiable and ϑ a constant parameter.

Hereafter, we denote with a tilde a quantity expressed in the non-inertial reference frame $\tilde{X}$. The transformation Λ stretches the time and the length. The density is also stretched in the reference frame $\tilde{X}$ as

$$\tilde{\rho} = a(t)^{\delta} \rho, \tag{5.9}$$

with δ another free parameter.

The pressure is then transformed according to dimensional arguments with the relation

$$\tilde{p} = a(t)^{2\vartheta+\delta} p \tag{5.10}$$

and the velocity in $\tilde{X}$ is

$$\tilde{u} = a(t)^{(\vartheta-1)}\,(au - \dot{a}r)\,. \tag{5.11}$$

We consider that in the laboratory frame, no external volume force acts on the flow (that is to say $f = 0$). The conservative equations (3.24) in the Cartesian frame X are expressed in the non-inertial frame $\tilde{X}$ by

$$\partial_{\tilde{t}}\tilde{\rho} + \partial_{\tilde{r}}(\tilde{\rho}\tilde{u}) = -\frac{2\tilde{\rho}\tilde{u}}{\tilde{r}} + (\delta - 3)a^{\vartheta}\dot{a}\tilde{\rho}, \tag{5.12a}$$

$$\partial_{\tilde{t}}\tilde{u} + \tilde{u}\partial_{\tilde{r}}\tilde{u} + \frac{1}{\tilde{\rho}}\partial_{\tilde{r}}(\tilde{p}) = a^{\vartheta}\dot{a}\tilde{u}(\vartheta - 1) - r a^{2\vartheta+1}\ddot{a}, \tag{5.12b}$$

$$\partial_{\tilde{t}}\tilde{p} + \tilde{u}\partial_{\tilde{r}}\tilde{p} + \tilde{\rho}\tilde{c}^2(\partial_{\tilde{r}}\tilde{u} + 2\frac{\tilde{u}}{\tilde{r}}) = a^{\vartheta}\dot{a}\tilde{p}(\delta + 2\vartheta - 3\gamma). \tag{5.12c}$$

This new reference frame possesses free parameters which could be chosen to fit a contracting

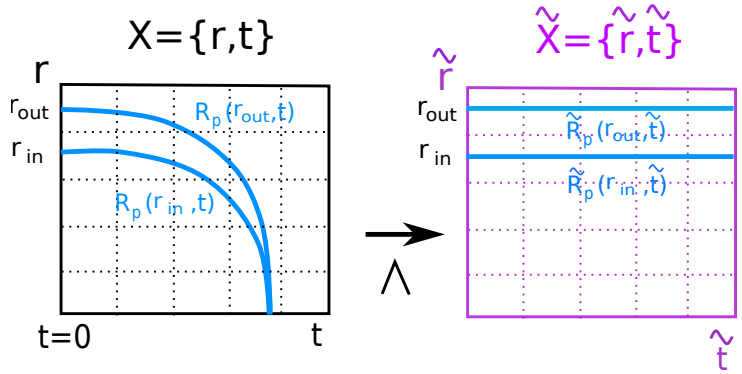

Figure 5.2: Transformation Λ from the laboratory frame to the shell comoving frame

flow. In our case we impose that $a(t) = h(t)$, $\gamma = 5/3$, $\vartheta = 1$ and $\delta = 3$ to follow the imploding shell. This case corresponds to a spherical fully ionized plasma, which is compatible with the ICF imploding shell problem.

The set of equations (5.12) becomes

$$\partial_{\tilde{t}}\tilde{\rho} + \partial_{\tilde{r}}(\tilde{\rho}\tilde{u}) = -\frac{2\tilde{\rho}\tilde{u}}{\tilde{r}}, \tag{5.13a}$$

$$\partial_{\tilde{t}}\tilde{u} + \tilde{u}\partial_{\tilde{r}}\tilde{u} + \frac{1}{\tilde{\rho}}\partial_{\tilde{r}}(\tilde{p}) = \tilde{f}, \tag{5.13b}$$

$$\partial_{\tilde{t}}\tilde{p} + \tilde{u}\partial_{\tilde{r}}\tilde{p} - \tilde{c}^2(\partial_{\tilde{r}}\tilde{\rho} + \tilde{u}\partial_{\tilde{r}}\tilde{\rho}) = 0, \tag{5.13c}$$

where the equation of state $\tilde{c}^2 = \gamma\tilde{p}/\tilde{\rho}$ applies. These equations are the same as in the Cartesian frame X except from the source term in the momentum equation $\tilde{f} = -\tilde{r}h^3\ddot{h}$. This non-inertial term, is a volume force in the reference frame $\tilde{X}$ due to the acceleration of the flow in the laboratory frame X.

By inserting (5.3) into (5.9)-(5.11), we express the shell density pressure and velocity in the reference frame $\tilde{X}$:

$$\forall(\tilde{r},\tilde{t}) \in \mathcal{D}(0)\times\mathbb{R}, \quad \tilde{\rho}(\tilde{r},\tilde{t}) = \rho_0(\tilde{r}), \tag{5.14a}$$

$$\tilde{p}(\tilde{r},\tilde{t}) = p_0(\tilde{r}), \tag{5.14b}$$

$$\tilde{u}(\tilde{r},\tilde{t}) = 0. \tag{5.14c}$$

The shell flow in the laboratory frame becomes stationary in the non-inertial frame $\tilde{X}$ (figure 5.2). Hereafter we call $\tilde{X}$ the *shell comoving frame*.

5.1.1.3 Pressure amplification factor due to the implosion $\mathcal{X}_{imp}$

We now consider an imploding shock of pressure p_s at the position $R_s(t)$ moving with the negative velocity $-U_s(t)$ into the imploding shell. It is generated at $t = t_i$ at the outer shell position $R_p(r_{out}, t_i)$. We limit our study to the shock propagation into the shell, thus for $R_s(t) \in \mathcal{D}(t)$.

The shock position and velocity in the comoving frame are

$$\tilde{R}_s(\tilde{t}) = h(t)^{-1} R_s(t), \tag{5.15a}$$

$$\tilde{U}_s(\tilde{t}) = hU_s(t) + \dot{h}(t) R_s(t). \tag{5.15b}$$

In the comoving frame, the shock is propagating into a stationary medium of pressure p_0 and density ρ_0. Indeed, for all $\tilde{r} \in [r_{in}, \tilde{R}_s(\tilde{t})]$ the conditions (5.14) apply.

Shock strengthening and shock pressure amplification The strength of the shock in the comoving frame $\tilde{Z}$ is equal to the strength of the shock in the laboratory frame Z. Indeed by definition

$$Z = \frac{p(R_s^+, t)}{p(R_s^-, t)} = \frac{h(t)^{-5}\tilde{p}(\tilde{R_s}^+, \tilde{t})}{h(t)^{-5}\tilde{p}(\tilde{R_s}^-, \tilde{t})} = \frac{\tilde{p}_s(\tilde{R}_s)}{p_0(\tilde{R}_s)} = \tilde{Z}, \tag{5.16}$$

where R_s^+ is the position just downstream the shock front and R_s^- is the position just upstream the shock front.

For this reason, the strengthening of the shock between r_{in} and r_{out} in the shell comoving frame $\tilde{X}$ is the shock strengthening in the laboratory frame X between its generation at $R_p(r_{out}, t_i)$ and its exit of the shell at $R_p(r_{in}, t_f)$.

Concerning the shock pressure amplification between the initial time t_i and the final time t_f, we have

$$\mathcal{X} = \frac{p_{sf}}{p_{si}} = \frac{p(r_{in}^+, t_f)}{p(r_{out}^+, t_i)} = \frac{h^{-5}(t_f)\tilde{p}(\tilde{r}_{in}^+, \tilde{t}_f)}{h^{-5}(t_i)\tilde{p}(\tilde{r}_{out}^+, \tilde{t}_i)} = \left(\frac{h(t_i)}{h(t_f)}\right)^5 \frac{\tilde{p}_{sf}}{\tilde{p}_{si}}. \tag{5.17}$$

We call the implosion amplification factor $\mathcal{X}_{imp}$ the amplification due to the overall pressure amplification in time

$$\mathcal{X}_{imp} = \left(\frac{h(t_i)}{h(t_f)}\right)^5, \tag{5.18}$$

and $\mathcal{X}_{shell}$ the shock amplification due to the shock dynamics in the shell comoving frame

$$\mathcal{X}_{shell} = \frac{\tilde{p}_{sf}}{\tilde{p}_{si}}. \tag{5.19}$$

The amplification factor $\mathcal{X}_{imp}$ cannot be expressed easily. It depends on the shock time of propagation in the shell and on the overall shell pressure evolution. Nevertheless, we give two estimates of this factor depending on the implosion phase in which the shock propagates.

Factor $\mathcal{X}_{\mathbf{imp}}$ estimation in the accelerating shell case If the shock reaches the shell inner surface at a time t_f smaller than the deceleration time t_d, the shock propagates in an accelerated medium only. Let us assume that the scale factor $h(t)$ follows the law (3.51) $h(t) = \sqrt{1-(t/\tau)^2}$. The constant τ is the time of implosion and can be estimated by $\tau = R_{sb}/\mathrm{u_{imp}}$ where R_{sb} is the shell radius at the beginning of the acceleration phase and $\mathrm{u_{imp}}$ is the implosion velocity. If the shock is launched at mid-time of the implosion $t_s = \tau/2$ we have $h(t_s) = \sqrt{3/4}$. The

shock time of propagation in the shell is about $\Delta t \sim \Delta R_{sb}/(U_{si} - \mathrm{u_{imp}})$ with ΔR_{sb} the shell thickness and U_{si} the initial shock velocity. Under the assumption of a strong shock (3.61), $(U_{si} - \mathrm{u_{imp}})^2 \sim 3p_{si}/4\rho_i$ with ρ_i being the shell density at the shock launch time t_s. The scale factor when the shock reaches the shell inner surface is

$$h(t_s + \Delta t) = \sqrt{1 - \left(\frac{1}{2} + \frac{\Delta R_{sb}}{(U_{si} - \mathrm{u_{imp}})} \frac{\mathrm{u_{imp}}}{R_{sb}}\right)^2} = \sqrt{1 - \left(\frac{1}{2} + \frac{\mathrm{u_{imp}}}{IFAR} \left(\frac{4}{3}\frac{\rho_i}{p_{si}}\right)^{\frac{1}{2}}\right)^2}, \qquad (5.20)$$

where $IFAR = R_{sb}/\Delta R_{sb}$ is the maximal shell aspect ratio (see Section 2.3.2).
The shell density ρ_i at the time t_s, depends on the density at the beginning of the acceleration phase ρ_{sb} and on the scale factor at the spike time $h(t_s)$: $\rho_i = \rho_{sb} h(t_s)^{-3}$.

As a numerical example, let us consider $\rho_{sb} = 5$ g.cm^{-3}. Then the shell density when the ignitor shock is launched is $\rho_i = 8$ g.cm^{-3}. If the initial shock pressure is $p_{si} = 300$ Mbar, the relative velocity $(U_{si} - \mathrm{u_{imp}})$ is 70 km.s^{-1}. We take a shell thickness $\Delta R_{sb} = 20\,\mu$m and a shell inner radius $R_{sb} = 800\,\mu$m which gives an $IFAR = 40$.
Now taking an implosion velocity $\mathrm{u_{imp}} = 280$ km.s^{-1}, we find that the shock pressure amplification $\mathcal{X}_{imp} = [h(t_s + \Delta t)/h(t_s)]^{-5} = 1.5$.
During the approximate time of propagation $\Delta t = 290$ ps, the pressure amplification in the accelerated shell $\mathcal{X}_{imp}$ is around 1.5.

Factor $\mathcal{X}_{\mathbf{imp}}$ estimation in the decelerating shell case If $t_f > t_d$, the shock collides with the returning shock and then propagates in a decelerated medium downstream the returning shock. The pressure in this inner part of the shell follows the hot-spot pressure increase during the deceleration phase. The scale factor $h(t)$ is now $h(t) = \sqrt{1 + ((t - t_{stag})/\tau)^2}$ and the constant τ is estimated by $\tau = R_{stag}/\mathrm{u_{imp}}$ where R_{stag} is the shell radius at stagnation. Let us choose that $R_{stag} \sim R_{sb}/20$ and $t_f = t_{stag}$. In this case, the scale factor h when the shock reaches the shell radius r_i is $h(t_f - t_{stag}) = h(0) = 1$. The shock time of propagation Δt in the decelerated part of the shell depends on the relative velocity of the shock and on the shell thickness. We evaluate the shock velocity when it reaches the shell inner surface by $U_{sf} \simeq \sqrt{3p_{sf}/4\rho_f}$. The shell density at stagnation is around $\rho_f = 1000$ g.cm^{-3} and the shock velocity as it reaches the inner shell surface must be around $p_{sf} = 20$ Gbar (see Section 4.4). Then the relative shock velocity is $U_{sf} = 50$ km.s^{-1}. The shock time of propagation in the decelerated part of the shell depends also on the distance traveled. This is a small fraction of the thickness ΔR_{sb}, let say $\Delta R_{sb}/4$. Then the time of propagation is $\Delta t = \Delta R_{sb}/4U_{sf} = 100$ ps.
The scale factor at the time Δt is

$$h(-\Delta t) = \sqrt{1 + \left(\frac{\Delta R_{sb}}{4(U_{sf})} \frac{20\mathrm{u_{imp}}}{R_{sb}}\right)^2} = \sqrt{1 + \frac{1}{12}\frac{\mathrm{u_{imp}^2}}{IFAR^2}\frac{\rho_f}{p_{sf}}}. \qquad (5.21)$$

Using the same implosion parameter as in the previous part we have $\mathcal{X}_{imp} = [h(t_s + \Delta t)/h(t_s)]^5 \simeq 15$.

Even if the shock propagates a short time in the decelerated part of the shell, the overall pressure amplification near the stagnation time is significant and $\mathcal{X}_{imp}$ is ten times higher than in the previous case.

We develop in the next section a shock dynamics model in the shell comoving frame to express the factor $\mathcal{X}_{shell}$.

5.1.2 Shock dynamics in the shell comoving frame

Several phenomena could contribute to the change in the shock strength. A piston with a constant velocity pushing a homogeneous planar medium launches a shock with a constant strength. In a cylindrical or spherical geometry, the mass and the momentum conservation leads to the shock strengthening as it propagates toward the origin. This is referred to the geometrical effect. If the shock strength is not constant, the downstream flow is not homogeneous leading to the propagation of compression waves toward the shock. This interaction between the shock and the flow behind it affects the shock dynamics. Lastly, the shock strength depends on the upstream flow profile. The combination of all these contributions induces a non-linear behavior of the shock and explains the difficulty to describe it analytically.

A review of the methods existing to describe a converging shock is given in Section 3.4. Whitham [Whitham, 1958] proposed an approximate expression for the shock strength using the conservation equations in the characteristic form and by assuming that the shock follows a characteristic path. The main limitation of this method is that the influence of the flow behind the shock is neglected. This approximation is called the "freely propagating shock wave" or the "CCW" (Chester - Chisnell - Whitham) approximation.

In this section we use the characteristics approach to derive the shock dynamics equation in the shell comoving frame valid in a spherical geometry with the upstream isentropic profiles p_0 and ρ_0. We show that in our case, the CCW approximation applies as the advancing waves behind the shock have a weak influence on the shock dynamics.

5.1.2.1 Shock dynamics equation in a general case of an inhomogeneous upstream flow

Shock dynamics equation The flow unperturbed by the shock is at rest with the monotonous profiles of density and pressure defined previously (5.14). As the initial quantities are at an equilibrium state, we have the condition:

$$\frac{1}{\tilde{\rho}_0}\partial_{\tilde{r}}(p_0) = \tilde{f}. \tag{5.22}$$

At the shock front $\tilde{R}_s$, the Rankine–Hugoniot relations (3.61) apply. These relations are

invariant with respect to the choice of the reference frame and read

$$\frac{\tilde{p}}{\tilde{p}_0}\Big|_{\tilde{r}=\tilde{R}_s} = Z, \tag{5.23a}$$

$$\frac{\tilde{u}}{\tilde{c}_0}\Big|_{\tilde{r}=\tilde{R}_s} = s\left(\frac{2(Z-1)^2}{\gamma^2(Z+1)+\gamma(Z-1)}\right)^{\frac{1}{2}}, \tag{5.23b}$$

$$\frac{\tilde{\rho}}{\tilde{\rho}_0}\Big|_{\tilde{r}=\tilde{R}_s} = \frac{\gamma(Z+1)+(Z-1)}{\gamma(Z+1)-(Z-1)}, \tag{5.23c}$$

where s is the sign of the shock velocity.

Using the same approximation as Whitham [Whitham, 1958], we assume that the characteristic C_+ path is close to the shock path $\tilde{R}_s(t)$. We remind that the characteristic C_+ of the Euler's equation (3.27) reads

$$\frac{\mathrm{d}\tilde{p}}{\mathrm{d}x} + \tilde{\rho}\tilde{c}\frac{\mathrm{d}\tilde{u}}{\mathrm{d}x} + \frac{\tilde{\rho}\tilde{c}}{\tilde{u}+\tilde{c}}\left[\frac{j\tilde{u}\tilde{c}}{\tilde{r}} - \tilde{f}\right] = 0 \text{ on } C_+ : \frac{\mathrm{d}x}{\mathrm{d}\tilde{t}} = \tilde{u}+\tilde{c}\,. \tag{5.24}$$

The pressure and velocity variations $\mathrm{d}\tilde{p}$ and $\mathrm{d}\tilde{u}$ along C_+ are calculated using the Rankine–Hugoniot relations (5.23). This gives the approximate shock dynamics equation :

$$A\frac{\mathrm{d}\tilde{p}_0}{\tilde{p}_0} + B\frac{\mathrm{d}\tilde{c}_0}{\tilde{c}_0} + C\frac{\mathrm{d}Z}{Z} + jD\frac{\mathrm{d}\tilde{R}_s}{\tilde{R}_s} - E\frac{\tilde{f}}{\tilde{c}_0^2}\,\mathrm{d}\tilde{R}_s = 0, \tag{5.25}$$

where

$$A = Z, \tag{5.26}$$

$$B = \frac{m}{n}(Z-1), \tag{5.27}$$

$$C = Z\left[1+\frac{1}{2}\frac{m}{n}\left(1+\frac{2\gamma}{\gamma(Z+1)+(Z-1)}\right)\right], \tag{5.28}$$

$$D = \frac{\gamma m^2(Z-1)}{\gamma(Z-1+mn)+(Z-1)}, \tag{5.29}$$

$$E = \frac{\gamma(\gamma+1)}{2}\frac{m}{n}\frac{\gamma(Z+1)+(Z-1)}{\gamma(Z-1+mn)+(Z-1)}, \tag{5.30}$$

$$m = [Z(\gamma+1)]^{1/2}, \tag{5.31}$$

$$n = \left[\frac{Z\gamma^2+\gamma^2+2\gamma-Z+1}{2\gamma}\right]^{1/2}. \tag{5.32}$$

Using the equilibrium relation (5.22) and $\mathrm{d}c_0/c_0 = (\mathrm{d}p_0/p_0 - \mathrm{d}\rho_0/\rho_0)/2$ we have

$$\mathrm{d}\ln Z = \mathcal{S}_p\,\mathrm{d}\ln p_0 + \mathcal{S}_\rho\,\mathrm{d}\ln\tilde{\rho}_0 - j\mathcal{S}_r\,\mathrm{d}\ln\tilde{R}_s. \tag{5.33}$$

with

$$\mathcal{S}_p = \left[\frac{2E-\gamma(2A+B)}{2\gamma C}\right], \quad \mathcal{S}_\rho = \left[\frac{B}{2C}\right], \quad \mathcal{S}_r = \left[j\frac{D}{C}\right]. \tag{5.34}$$

Correction of the equation In the *freely propagating shock wave* approximation, the interaction of the shock with the downstream flow is neglected.

The hydrodynamic code CHIC has been used to evaluate the accuracy of the shock dynamics equation (5.36). The density and pressure are initialized with various initial profiles and a zero initial velocity. The volume force needed to keep an equilibrium with the initial pressure profile is taken into account. The shock is launched by applying a constant velocity at the outer edge of the shell as a boundary condition. We integrated the shock dynamics equation (5.33) and compared the results with numerical simulations. Figure 5.3 presents the CHIC simulation results (circles) and the numerical integration of the equation (5.33) (lines). In the case (a), the shock propagates into a homogeneous sphere. Only the third term in the right hand side of (5.33) is present. In the case (b) a constant volume force $\tilde{f}$ is considered. The density is kept homogeneous. The pressure gradient is constant $\partial_{r_0}(p_0) = \tilde{f}\rho_0$ and the geometry is planar ($j = 0$). Only the first term in the right hand side of equation (5.33) is present. The case (c) is the same as the case (b) but in a spherical geometry. In the case (d), the shock is propagating in a constant density gradient, without a pressure gradient. Only the second term of the right hand side of equation (5.33) is present. The CHIC simulation results are superposed to the numerical integration of (5.33) for all the cases except the case (d). It appears that only the density gradient term needs to be corrected. Yousaf [Yousaf, 1978, Yousaf, 1985] calculated its corrections by using the exact self-similar solution in specific density and pressure profiles. To stay general, we add an arbitrary correction term ω to the density term $\mathcal{S}_\rho \to (1+\omega)\mathcal{S}_\rho$ in the shock dynamics equation. This parameter must be adjusted depending on the initial medium profile considered. It has been adjusted to the value 0.1 in the particular case of the shell profiles (5.6). Figure 5.4 presents comparison between the simulation results and the numerical solution of (5.33) with $\omega = 0.1$ for various shell thicknesses and parameters $\mathcal{K}$.

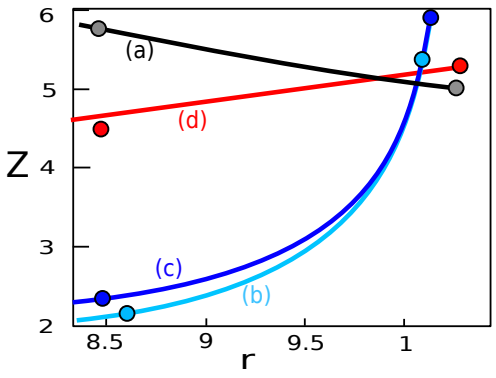

Figure 5.3: Shock strength evolution for various upstream flows : (a) homogeneous spherical geometry, (b) pressure gradient and volume force, (c) pressure gradient and volume force in spherical geometry, (d) density gradient. The circles represent the CHIC simulation results.

This validates the equation (5.33), with the correction $\mathcal{S}_\rho \to (1+0.1)\mathcal{S}_\rho$, for studies of the ignitor shock dynamics in the imploding shell.

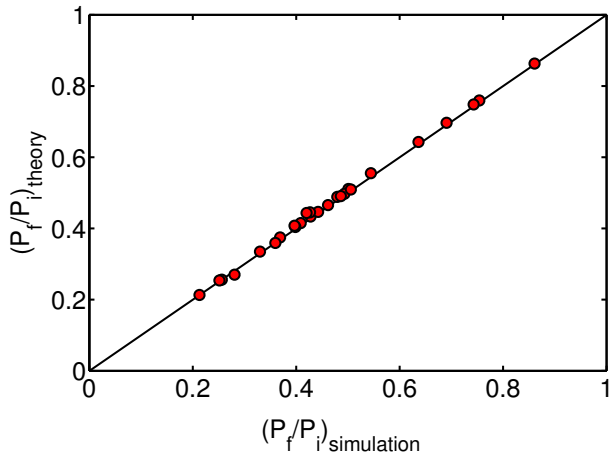

Figure 5.4: Comparison between the CHIC simulation results and the numerical integration of the shock dynamics equation for various imploding shell parameters. The correction factor value here is $\omega = 0.1$.

5.1.2.2 Shock dynamics in the shell

Shock dynamics equation in the shell comoving frame : We apply the shock dynamics equation to the shell profile expressed previously (5.14) in the spherical geometry $j = 2$. According to (5.5) and (5.6) we have

$$\frac{\tilde{r}}{p_0}\frac{\mathrm{d}p_0}{\mathrm{d}\tilde{r}} = -\gamma\left(\frac{\tilde{r}}{r_{out}}\right)^2 \mathcal{K}\left[\left(1-\frac{\gamma-1}{2}\mathcal{K}\left(1-\left(\frac{\tilde{r}}{r_{out}}\right)^2\right)\right)\right]^{-1}, \tag{5.35a}$$

$$\frac{\tilde{r}}{\tilde{\rho}_0}\frac{\mathrm{d}\tilde{\rho}_0}{\mathrm{d}\tilde{r}} = \frac{1}{\gamma}\frac{\tilde{r}}{p_0}\frac{\mathrm{d}p_0}{\mathrm{d}\tilde{r}}. \tag{5.35b}$$

The shock dynamics equation in the shell is then

$$\frac{\mathrm{d}\ln Z}{\mathrm{d}\ln(\tilde{r}/r_{out})} = -(\gamma\mathcal{S}_p + (1+w)\mathcal{S}_\rho)\frac{\mathcal{K}\left(\frac{\tilde{r}}{r_{out}}\right)^2}{\left(1+\frac{1-\gamma}{2}\mathcal{K}\left(1-\left(\frac{\tilde{r}}{r_{out}}\right)^2\right)\right)} - \mathcal{S}_r. \tag{5.36}$$

In the right hand side, the first term is the accelerated shell profile contribution to the shock strengthening and the second term is the contribution of the converging effect. The solution of this equation depends on three parameters : the shell parameter $\mathcal{K}$, the final radius reached by the shock r_{in} and the initial shock strength Z_i.

Convergence effect : The contribution of the geometrical effect to the shock strengthening in the shock dynamics equation (5.36) is plotted in Figure 5.5. It depends mainly on the shell parameter $\mathcal{K}$ and on the radius $\tilde{r}/r_{out}$. In the case of $\mathcal{K} = 0$, the acceleration is zero and the density and pressure profiles are flat, thus only the convergence effect contributes to

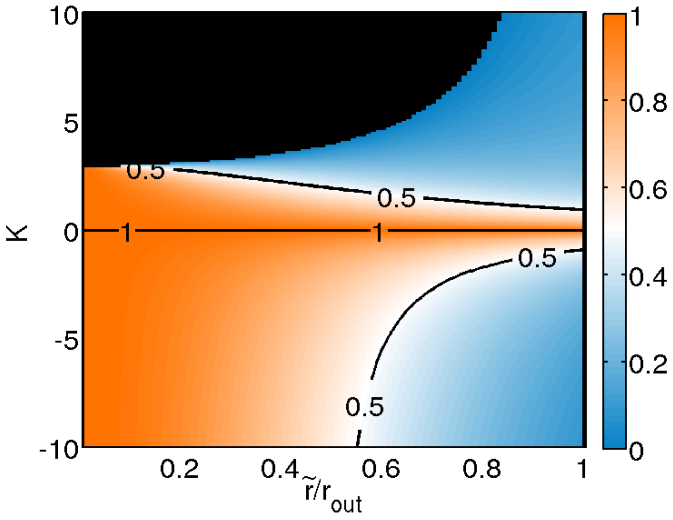

Figure 5.5: Contribution of the geometrical effect in the shock strengthening: $|\mathcal{S}_r \,\mathrm{d}\ln\tilde{R}_s|/(|\mathcal{S}_\rho \,\mathrm{d}\ln\tilde{\rho}_0) + \mathcal{S}_p \,\mathrm{d}\ln\tilde{p}_0)| + |\mathcal{S}_r \,\mathrm{d}\ln\tilde{R}_s)|$.

the shock strengthening. The geometrical effect is predominant for $|\mathcal{K}| < 1$ and near the center ($\tilde{r}/r_{out} < 0.2$). This confirms that one can neglect the downstream density and pressure gradients in the hot-spot. However in the shell, we expect $\tilde{r}/r_{out} < 0.7$ and the effects of pressure and density profiles are not negligible.

Analytical asymptotic equation for high Z : In the limit $Z \gg 1$, the analytical solution of the shock dynamics equation is

$$\frac{Z}{Z_i} = \left(1 + \mathcal{K}\frac{(\gamma-1)}{2}\left(\left(\frac{\tilde{r}}{r_{out}}\right)^2 - 1\right)\right)^{\mu}\left(\frac{\tilde{r}}{r_{out}}\right)^{\nu}, \tag{5.37}$$

with $\mu = \left(\frac{(1+\omega)}{2\sqrt{\frac{\gamma-1}{2\gamma}}+1} - \gamma\right)/(\gamma-1) = -1.6$ for $\gamma = 5/3$ and $\nu = -4\gamma/\left(2+\gamma+\gamma\sqrt{\frac{2\gamma}{\gamma-1}}\right) = -0.9$ for $\gamma = 5/3$. We recover the Guderley's law $Z \propto (\tilde{r}/r_{out})^{-0.9}$ when $\mathcal{K} = 0$ or $\tilde{r}/r_{out} \ll 1$.

Shock strengthening dependence on $\mathbf{r_{in}/r_{out}}$, $\mathcal{K}$ and $\mathbf{Z_i}$: The numerical solutions to the shock dynamics equation (5.36) for several values of parameters $\mathcal{K}$ and Z_i are shown in Figure 5.6. The analytical solution valid for a high Z is represented with dashed line. The results from the numerical simulations CHIC with a volume force are represented with crosses in Figure 5.6 (a). We observe a very good agreement.

The influence of the shell parameter $\mathcal{K}$ is shown in Figure 5.6 (a) where the shock initial strength is $Z_i = 100$. The analytical solution (5.37) is superposable with the numerical integration of the shock dynamics equation (5.36). The shock strength increases as the shock reaches the inner face of the shell if $\mathcal{K}$ is positive and it decreases if $\mathcal{K}$ is negative. At $r_{in}/r_{out} = 0.85$,

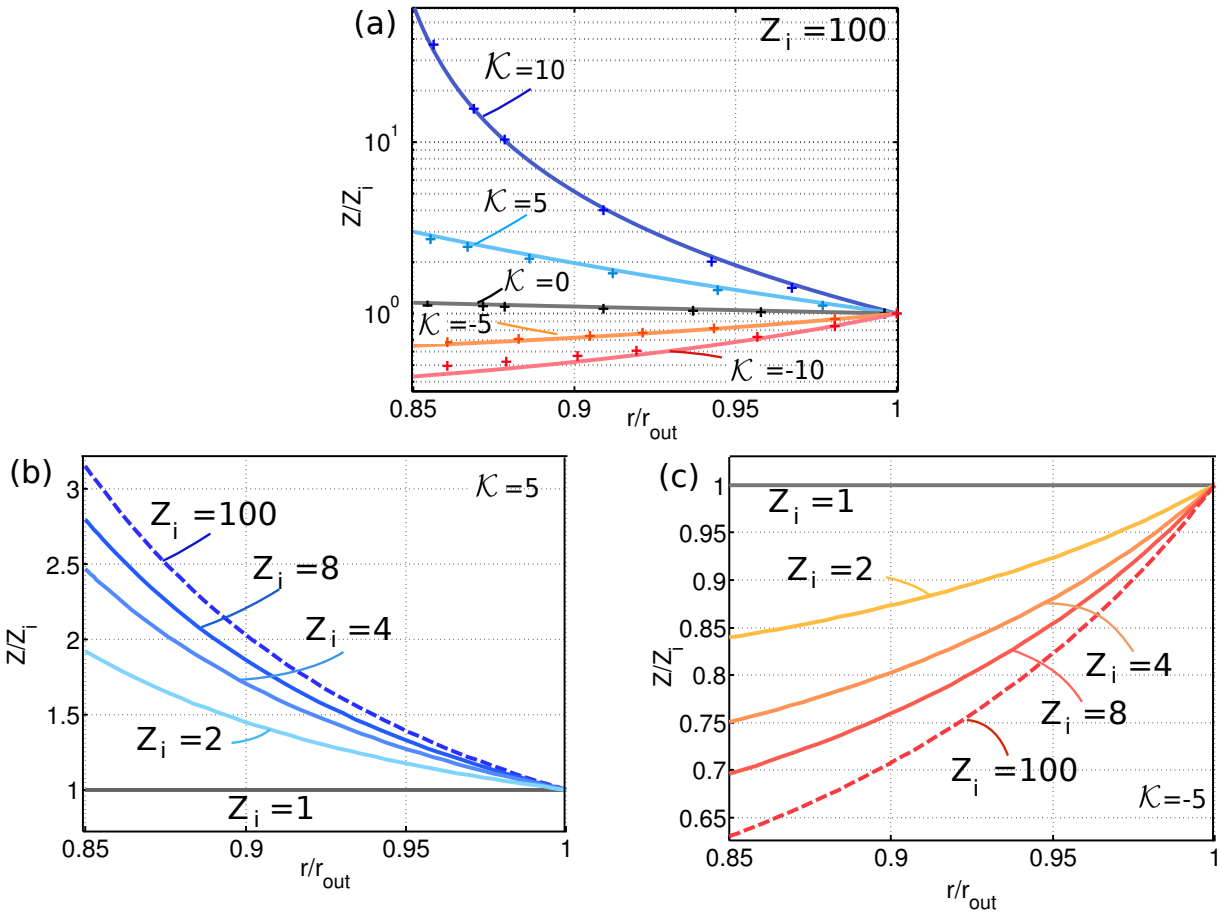

Figure 5.6: Shock strengthening Z/Z_i dependence on the radius for several values of the shell parameter $\mathcal{K}$ (a) and the initial shock strength Z_i (b). The analytical solution (5.37) is represented with dashed lines. The results from hydrodynamic simulations CHIC are represented with crosses (a).

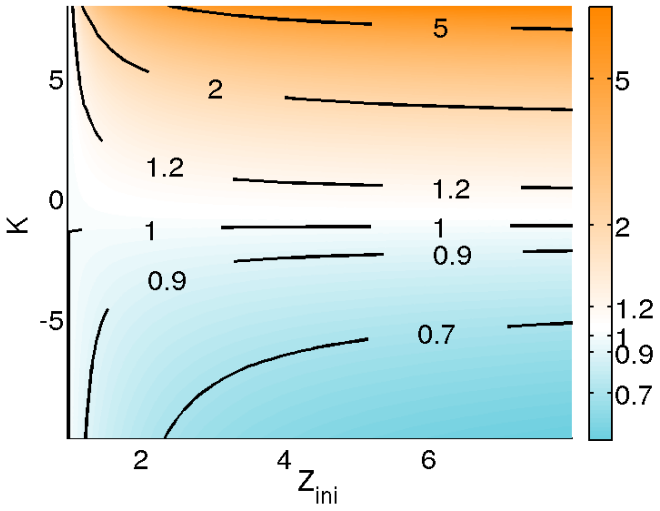

Figure 5.7: Shock strengthening Z_f/Z_i dependence on $(\mathcal{K}, Z_i)$ with a fixed value $r_{in}/r_{out} = 0.8$.

the shock strength is 80 times higher with $\mathcal{K} = 10$ than with $\mathcal{K} = 0$.

Figure 5.6 (b - c) demonstrates the influence of positive (b) and negative $\mathcal{K}$ (c) on the shock strength amplification. For Z_i close to 1, the shock initial strength is weak and the shock strength amplification is also weak. When Z_i increases, the change in the shock strength become more noticeable and tends to the solution (5.37) valid for $Z \gg 1$. The approximation (5.37) seems to be valid for Z_i higher than 8. Then the strength evolution depends only on the shell parameter $\mathcal{K}$ and on the radius ratio r_{in}/r_{out}.

This is rather convenient to plot the map of the shock strengthening Z_f/Z_i in the plane $(\mathcal{K}, Z_i)$ for a given radius ratio of the shell r_{in}/r_{out} (Figure 5.7). The important result here is that the shock strength increases as it propagates in an accelerated medium and decreases as it propagates in a decelerated medium.

5.1.2.3 Pressure amplification factor in the shell $\mathcal{X}_{\text{shell}}$

The shock pressure amplification factor as it propagates through the shell, in the comoving frame, reads

$$\mathcal{X}_{\text{shell}} = \frac{\tilde{p}_{s_f}}{\tilde{p}_{s_i}} = \frac{Z_f}{Z_i}\frac{p_0(r_{in})}{p_0(r_{out})} = \frac{Z_f}{Z_i}\left[1 + \frac{1-\gamma}{2}\mathcal{K}\left(1 - \left(\frac{r_{in}}{r_{out}}\right)^2\right)\right]^{\frac{\gamma}{\gamma-1}}. \tag{5.38}$$

Figures 5.8, 5.9 and 5.10 show the shock pressure amplification $\mathcal{X}_{\text{shell}}$ in the shell comoving frame, as a function of Z_i, r_{in}/r_{out} and $\mathcal{K}$. Figure 5.8 shows that the shock pressure remains constant on the isocontour $\mathcal{X}_{shell} = 1$. This isocontour corresponds to a shell parameter $\mathcal{K} \approx 1$ and has a weak dependence on the initial shock strength Z_i. Above this isocontour, $\mathcal{X}_{shell}$ is below unity. Thus in an accelerated shell, if $\mathcal{K} > 1$ the shock pressure decreases. For a small shell parameter $|\mathcal{K}| \approx 0$ the shock pressure increases slowly by convergence effect. In the

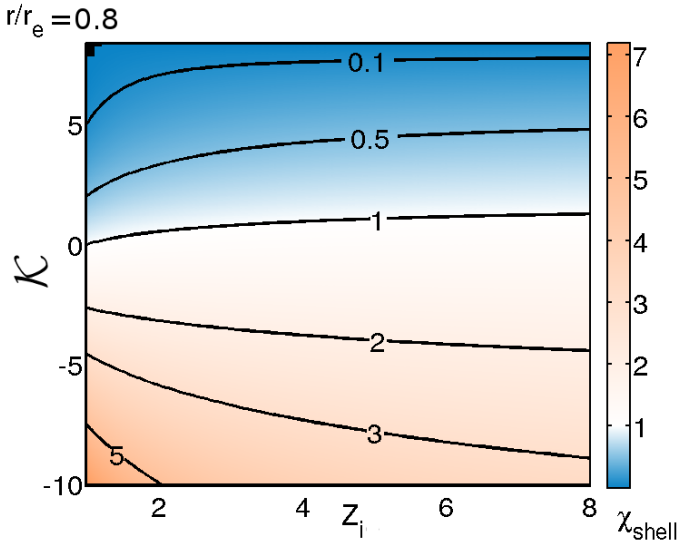

Figure 5.8: Shock pressure amplification $\mathcal{X}_{\text{shell}} = \tilde{p}_{s_f}/\tilde{p}_{s_i}$ in the shell comoving frame as a function of $(\mathcal{K}, Z_i)$ for a fixed value $r_{in}/r_{out} = 0.8$.

decelerating case $\mathcal{K} < 0$, the shock pressure is amplified. This amplification increases with the depth traveled by the shock and is higher for a small initial shock strength Z_i (figure 5.9 (b)). For a short propagation distance $r_{in}/r_{out} > 0.8$ and for the initial strength $Z_i > 2$, there is a weak influence of Z_i on the shock pressure amplification.

We demonstrated that the shell pressure and density profiles have an effect on the shock pressure amplification in the shell. Assuming an isentropic compression of the shell and radius ratio of about $r_{in}/r_{out} = 0.8$, the shock pressure increases in the case of a decelerating shell, remains almost constant in a stationary shell and decreases in an accelerated shell. On the contrary, the strength of the shock $Z = p_s/p_0$ increases in an accelerated medium and decreases in a decelerated medium.

In the shock ignition scheme, the ignitor shock encounters a diverging shock coming from the target center which modifies its pressure and strength. This effect is analyzed in the next section.

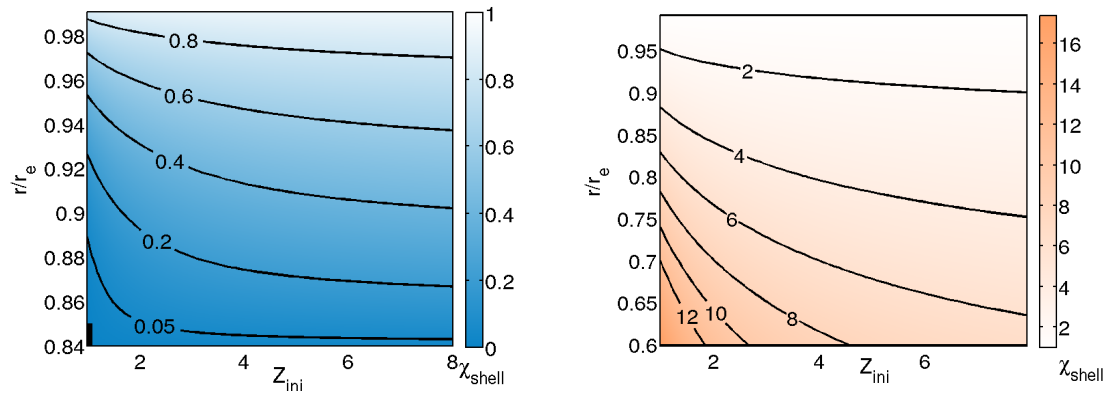

(a) (b)

Figure 5.9: Shock pressure amplification $\mathcal{X}_{\rm shell} = \tilde{p}_{s_f}/\tilde{p}_{s_i}$ in the shell comoving frame as a function of$(r_{in}/r_{out}, Z_i)$ for $\mathcal{K} = 10$ (a) and $\mathcal{K} = -10$ (b).

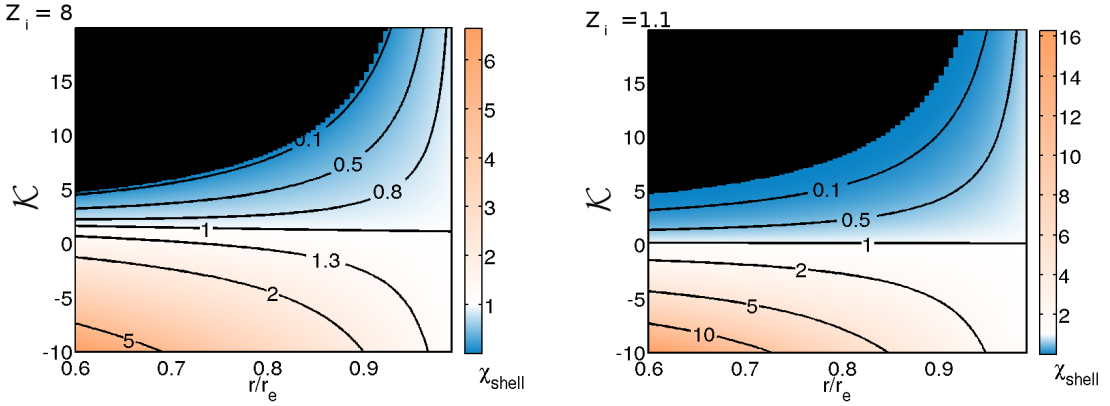

(a) (b)

Figure 5.10: Shock pressure amplification $\mathcal{X}_{\rm shell} = \tilde{p}_{s_f}/\tilde{p}_{s_i}$ in the shell comoving frame as a function of $(\mathcal{K}, r_{in}/r_{out})$ for $Z_i = 8$ (a) and $Z_i = 1.1$ (b).

5.1.3 Shock pressure amplification and strengthening in a shock collision

A collision between two shocks with opposite velocities generates two new shocks propagating in opposite directions. The flow behind the two transmitted shocks has a higher pressure and a lower velocity than the flows behind the two incoming shocks. The collision converts the kinetic energy of the incoming shocks into the internal energy and thus enhances the transmitted shock pressure. A graphical method to calculate the transmitted shock pressure is presented in Section 3.3.4.1.

Let us now apply these results to the ignitor shock with the pressure p_{c1} colliding with the returning shock of a pressure p_r. The converging shock just after the collision has the pressure p_{c2}. We assume that the collision is instantaneous, thus the amplification factor is the same in the shell comoving frame as in the laboratory frame

$$\mathcal{X}_{coll} = \frac{p_{c2}}{p_{c1}} = \frac{\tilde{p}_{c2}}{\tilde{p}_{c1}}. \tag{5.39}$$

We calculate the shock amplification factor $\mathcal{X}_{coll} = p_{c2}/p_{c1}$ and the shock strengthening Z_{c2}/Z_{c1} with the method explained in 3.3.4.1. The results are presented in Figure 5.11.

If the returning shock has a strength $Z_r < 3$, the amplification of the shock pressure in the collision is below 2 and it depends weakly on the ignitor shock strength Z_{c1}. On the contrary, for a strong returning shock with $Z_r > 5$, the shock pressure amplification depends strongly on the incoming shock strength Z_{c1}. The shock pressure amplification is higher for weaker incoming shocks.

Concerning the change in the shock strength, it is decreasing. This effect is more significant if both shocks have high strengths.

With Z_r and Z_{c1} below 10, the following analytical formula approximates well the shock amplification :

$$\mathcal{X}_{coll} \approx \left(\frac{Z_{c1} + Z_r}{1 + Z_{c1} Z_r} \right)^{\frac{1}{2}} Z_r. \tag{5.40}$$

In the limit of strong shocks, two approximate expressions were proposed: in [Lafon et al., 2013] the post collision shock pressure is given by $p_{c2} = 3(p_{c1} + 0.9 p_r)$ and in [Schurtz et al., 2010] another relation $p_{c2} = (p_{c1}^2 + p_r^2 + 10 p_{c1} p_r)/(p_{c1} + p_r)$ was proposed. With both approximations, if $p_{c1} = p_r$, the amplification is equal to 6. This is in agreement with the results given in Section 3.3.4.1 in the strong shocks limit and with $\gamma = 5/3$.

We compare in figure 5.12 the shock pressure amplification in collision obtained from the exact Rankine–Hugoniot relations, from the hydrodynamic code CHIC simulations and from the three analytical approximations. Theses results concern the collision of two shocks with strengths varying from 2 to 10. The asymptotic approximations for strong shocks are less accurate than the analytical approximation (5.40). However, this latter is not valid in the limit of very strong shocks.

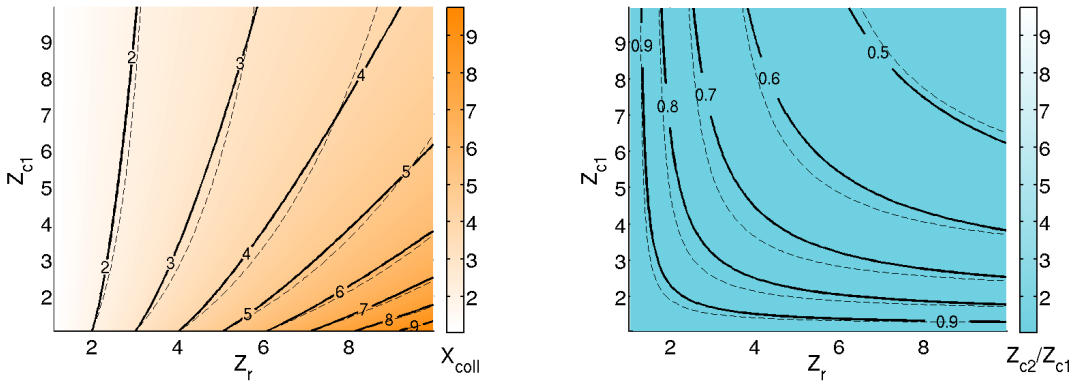

(a) (b)

Figure 5.11: Shock pressure amplification (a) and strengthening (b) in the shock collision with $\gamma = 5/3$. The dashed lines represent the isocontours of the approximate analytical solution (5.40).

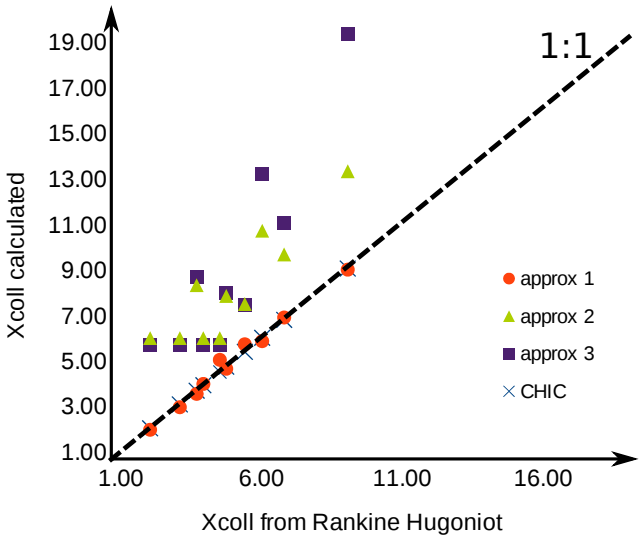

Figure 5.12: Plot of the calculated shock pressure amplification through collision versus the exact Rankine–Hugoniot results. The dashed line represents the ratio 1:1. The simulation results are represented with crosses. The approximation 1 (red dots) is based on (5.40). The approximation 2 (green triangles) uses $p_{c2} = 3(p_{c1} + 0.9p_r)$. The approximation 3 (blue squares) uses $p_{c2} = (p_{c1}^2 + p_r^2 + 10p_{c1}p_r)/(p_{c1} + p_r)$.

5.1.4 Partial conclusions

We defined in this section three amplification factors which apply to a converging shock when it propagates into an imploding shell. The total amplification is written as:

$$\mathcal{X} = \mathcal{X}_{imp}\mathcal{X}_{shell}\mathcal{X}_{coll}. \tag{5.41}$$

The amplification factor $\mathcal{X}_{imp}$ accounts for the overall shell pressure amplification during the shock propagation. It depends on the assembly phase of the target, on the time of shock launching and on the shock velocity. A rough estimate of this factor indicates an overall pressure amplification during the shock propagation $\mathcal{X}_{imp} \simeq 1.5$ for typical implosion parameters in the shell acceleration phase. However, this factor could be higher if the shock collides with the reflected first shock and propagates after that through a decelerating shell near the stagnation time. Then, even if the shock traveling time in the decelerated shell is short, the overall pressure amplification factor is $\mathcal{X}_{imp} \simeq 15$ for typical implosion parameters.

The factor $\mathcal{X}_{shell}$ accounts for the shock pressure amplification in the shell comoving frame. It depends on the shell spatial profile, on the initial shock strength and on the shell aspect ratio. The shell spatial profile is characterized by the parameter $\mathcal{K}$. If the shell is accelerated, $\mathcal{K}$ is positive and the pressure and density gradients are positive. If the shell is decelerated, $\mathcal{K}$ is negative and the pressure and density profiles are negative. For $|\mathcal{K}| < 1$, the shock pressure is mainly amplified due to the convergence effect and follows the self-similar solution (3.92). If $|\mathcal{K}| > 1$, the shell spatial profile effect is significant. The shock pressure decreases in an accelerated shell whereas it increases in a decelerated shell.

The shell starts to decelerate when the returning shock is entering in the shell. Therefore, if the ignitor shock enters the hot spot during the deceleration phase, it collides with the returning shock. The shock pressure amplification through this collision is $\mathcal{X}_{coll}$. If the returning shock is weak, the amplification factor is about $\mathcal{X}_{coll}$=2. For a stronger returning shock, the collision amplification factor is more significant.

The ignitor shock pressure evolution in the shell depends thus on several processes. We presented in this section maps of the amplification factors depending on the shell parameters ($\mathcal{K}$, r_{in}/r_{out}), on the initial strength of the ignitor shock Z_i and on the strength of the returning shock Z_r. The results obtained here, in the context of shock ignition, could be applied to any shock propagating into an isentropic homogeneously imploded medium.

We analyze in the next section the effect of the assembly phase parameters and the ignitor shock initial strength on the shock amplification in the case of a HiPER shock ignition target.

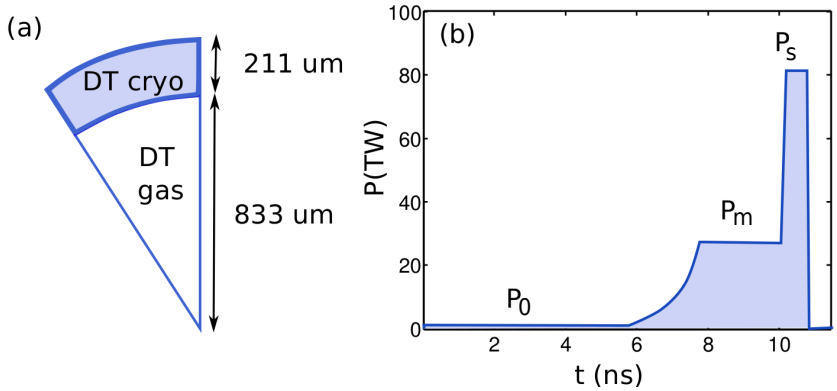

Figure 5.13: HiPER baseline target (a) and laser pulse temporal shape (b)

5.2 Shock pressure amplification and strengthening in shock ignition scheme

The shock dynamics theory is applied here for the analysis of the shock amplification in the hydrodynamic simulations of a shock ignition implosion. The simulations are performed with the hydrodynamic code CHIC in spherical geometry. The domain is discretized with 280 meshes in the radial direction. The laser energy deposition is described by one ray and its energy is totally deposited at the critical density n_c. The hydrodynamic simulations are performed with an ideal gas equation of state.

We use the HiPER target baseline [Atzeni et al., 2008, Ribeyre et al., 2009] implosion design. The target of an outer radius $R_0 = 1044\,\mu$m is composed by a shell of cryogenic D-T with a thickness $\Delta R_0 = 211\,\mu$m and a central part filled with gas of D-T (figure 5.13). The initial density of the shell is $\rho_{cryo} = 0.25$ g.cm^{-3} and the initial density of the gas is $\rho_{gas} = 1$ mg.cm^{-3}. The initial aspect ratio of the target is $\mathcal{A}_0 = (R_0 - \Delta R_0)/\Delta R_0 = 4$. The laser pulse has the shape presented in figure 5.13. The power in the prepulse $P_0 = 0.5$ TW is chosen to produce a shell adiabat $\alpha_0 = 0.7$ at the beginning of the acceleration phase. The power in the main pulse $P_m = 10$ TW is chosen to obtain the implosion velocity $u_{imp} = 280$ km.s^{-1}. At the time $t_s = 10.5$ ns a laser spike with the power $P_s = 80$ TW launches the ignitor shock. This power involves a laser intensity $I_s = 7 \times 10^{15}$ W.cm^{-2} on the target surface. The shock pressure amplification depends on the initial shock strength and on the shell radial profile. These implosion parameters can modify the shock pressure amplification. In a first part we analyze the influence of the spike parameters t_s and I_s, in a second part we analyze the influence of the main implosion parameters.

5.2.1 Analysis of the shock pressure amplification factor

We consider the time interval of the shock launch 9.9 ns $< t_s <$ 10.8 ns and the spike intensity range 2.10^{15} W.cm^{-2} $< I_s <$ 8.10^{15} W.cm^{-2}. These intervals are chosen according to the ignition window of the HiPER target [Ribeyre et al., 2009]. To evaluate the shock amplification,

one needs to know the shell parameters $\mathcal{K}$ and r_{in}/r_{out} as well as the initial shock strength Z_i.

5.2.1.1 Shock initial strength and shell parameters

Initial shock strength The initial strength of the shock depends on the outer pressure of the shell $p_e(t_s)$ and on the absorbed spike intensity I_s. The outer pressure is measured in a simulation without laser spike. Then, the initial strength is evaluated by using the ablation pressure law (2.17) for DT and a laser wavelength $\lambda_L = 351$ nm :

$$Z_{ini}(t_s) = \frac{119\big(I_s[10^{15}\ \mathrm{W.cm^{-2}}]\big)^{\frac{2}{3}}}{p_e(t_s)}. \tag{5.42}$$

The initial shock strength evaluation is represented in figure 5.14. As $p_e(t)$ increases with time, the strength of the launched shock with a given laser intensity decreases while the time t_s increases.

Shell profile The shock pressure amplification depends strongly on the shell profile which evolves with time. Figure 5.15 presents the evolution of the pressure gradient over density and the acceleration evolution in a simulation without laser spike. Those two quantities compensate each other and the equilibrium condition (5.22) is clearly visible here. At the time $t_d = 11.1$ ns, the returning shock enters the shell. For $t < t_d$ the shell is accelerated with positive pressure and density gradients. This corresponds to a positive shell parameter $\mathcal{K}$. For $t > t_d$, the shell is decelerated and the shell parameter $\mathcal{K}$ is negative. The shell is divided into two parts: the part $\mathcal{S}_{acc}$ at the outer side of the returning shock with a positive pressure gradient, and the part $\mathcal{S}_{dec}$ at the inner side of the returning shock with a negative pressure gradient.

The ignitor shock is generated at the outer radius location at the time t_s. It collides eventually with the returning shock at the time t_c. Then, it reaches the inner face of the shell at the time t_f. We calculate the shock amplification through the two zones.

The ignitor shock initial pressure p_{si} is first amplified in the zone $\mathcal{S}_{acc}$. It reaches the pressure p_{sf} at the inner radius of the shell r_{in} if no collision occurs, or it attains the pressure p_{c1} before the collision at the time t_c. The shock pressure amplification in $\mathcal{S}_{acc}$ is $\mathcal{X}_1 = p_{sf}/p_{si}$ in the first case and $\mathcal{X}_1 = p_{c1}/p_{si}$ in the second case. If $t_f > t_d$, the collision amplifies the shock pressure by a factor $\mathcal{X}_{coll} = p_{c2}/p_{c1}$, with p_{c2} being the shock pressure after the collision. The shock is further amplified in the decelerating zone $\mathcal{S}_{dec}$ by the factor $\mathcal{X}_2 = p_{sf}/p_{c2}$. If the ignitor shock reaches the inner shell face before the time t_d, there is no returning shock and we set $p_{c2} = p_{c1} = p_{sf}$, $t_f = t_c$ in order to have $\mathcal{X}_{coll} = 1$ and $\mathcal{X}_2 = 1$.

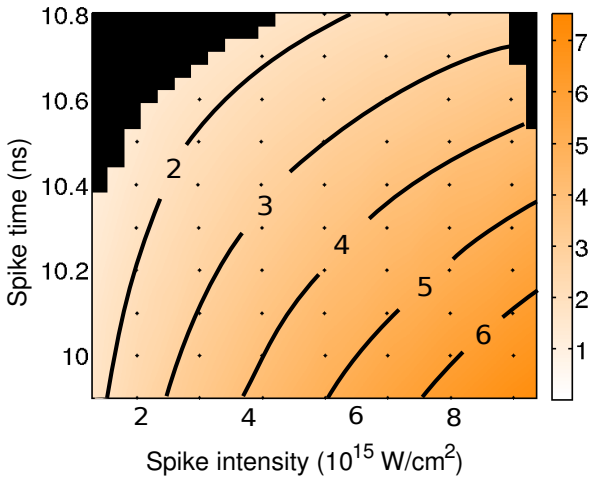

Figure 5.14: Dependence of the ignitor shock initial strength Z_i on the laser spike intensity and spike time t_s.

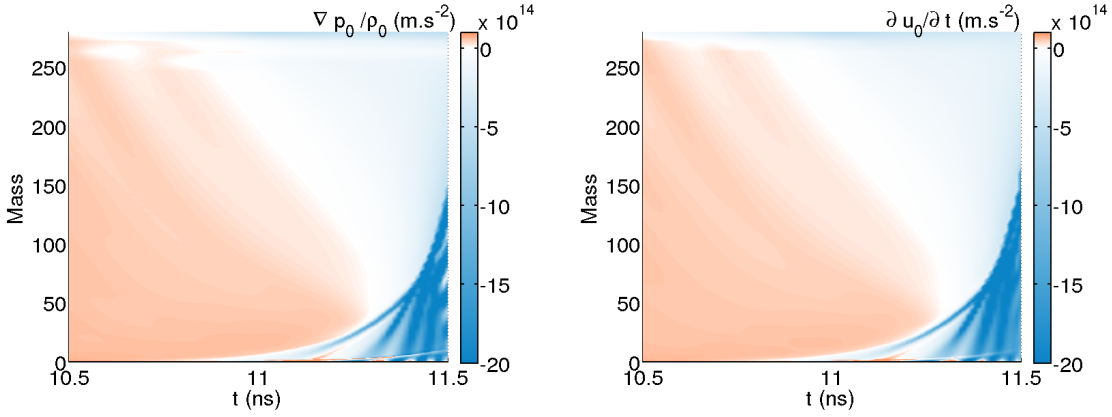

(a) (b)

Figure 5.15: HiPER shell pressure gradient over density (a) and acceleration (b) evolution at the end of the compression phase

5.2.1.2 Pressure amplification factors

Implosion amplification factor $\mathcal{X}_{\mathbf{imp}}$ The amplification factors $\mathcal{X}_1$ and $\mathcal{X}_2$ are partially due to the overall pressure increase in both zones $\mathcal{S}_{acc}$ and $\mathcal{S}_{dec}$ of the shell. The mean pressures in $\mathcal{S}_{acc}$ and $\mathcal{S}_{dec}$ are measured in the simulation without spike (figure 5.16 (a)). The slope of the curves gets steeper at a later time and is steeper in $\mathcal{S}_{dec}$ than in $\mathcal{S}_{acc}$. The overall pressure amplification factor is evaluated as a ratio of pressures averaged on the shell thickness at the time t_f and t_s $\mathcal{X}_{imp} =< p(t_f) >_{shell} / < p(t_s) >_{shell}$. The factor $\mathcal{X}_{imp}$ is higher if the shock propagation time is longer - which corresponds to a low shock velocity - and close to the stagnation time when the mean pressure $< p(t) >$ increases rapidly. Figure 5.16 (b) shows the shell overall pressure amplification $\mathcal{X}_{imp}$ during the shock path, depending on the shock initial strength and time. The dashed line in panel (b) delimits the zone where the shock undergoes a collision. Below this curve, the amplification factor $\mathcal{X}_{imp}$ is lower than 5. As soon as the shock enters in the decelerating part of the shell (in the upper part of the graph), $\mathcal{X}_{imp}$ increases quickly and reaches 100. For a given spike time, $\mathcal{X}_{imp}$ is higher for a lower intensity as the shock velocity is lower. We notice a good agreement with the estimates of $\mathcal{X}_{imp}$ given in Section 5.1.1.3.

Shell amplification factor $\mathcal{X}_{\mathbf{shell}}$ The shock amplification in the shell comoving frame depends on the initial strength of the shock, on the shell parameters $\mathcal{K}$ and on the shell radius ratio r_i/r_e in $\mathcal{S}_{acc}$ and $\mathcal{S}_{dec}$. The whole shell implosion does not follow a fully isentropic homogeneous compression. However, this assumption can be applied for shorter time intervals. We assume here that the isentropic model is describing the imploding shell during the ignitor shock propagation time.

The shell parameter $\mathcal{K}$ is calculated to fit the outer and inner pressure of each part $\mathcal{S}_{acc}$ and $\mathcal{S}_{dec}$ in the simulation without spike. Its evolution with time is plotted in the figure 5.17(a). Its mean value during shock propagation time is calculated for several spike time t_s and intensity I_s. It depends mainly on the spike time t_s.

In the same way, the inner radius of the shell r_{in}, the outer radius of the shell r_{out}, and the position of the returning shock R_r are measured in a simulation without spike and are represented in the figure 5.17(b). The mean dimensionless ratio r_i/r_e during the shock propagation is calculated in $\mathcal{S}_{acc}$ and $\mathcal{S}_{dec}$. The curve $(\mathcal{K}, r_i/r_e)$ is plotted in figure 5.18 (a).

In the accelerated shell part $\mathcal{S}_{acc}$, the shell parameter $\mathcal{K}$ is positive. According to Figure 5.10 (a), $\mathcal{X}_{shell}$ varies from 0.2 to 1 as the radius r_i/r_e varies from 0.9 to 0.6 and as the shell parameter $\mathcal{K}$ varies from 20 to 0. Thus the shock pressure decreases in $\mathcal{S}_{acc}$. In the decelerated part of the shell, Figure 5.8 indicates that the maximal amplification factor is $\mathcal{X}_{shell} = 2.5$ considering a shell parameter $\mathcal{K} = -8$ at the radius $r_i/r_e = 0.8$. By combining the amplifications in $\mathcal{S}_{acc}$ and $\mathcal{S}_{dec}$, the total amplification factor in the shell comoving frame $\mathcal{X}_{shell}$ varies from 0.2 to 2 as it is presented in figure 5.18 (b). We observe a weak dependence of $\mathcal{X}_{shell}$ on the initial shock strength Z_i as the spike intensity influence is low. The amplification in the shell comoving frame $\mathcal{X}_{shell}$ has a positive effect only for a very late spike time t_s.

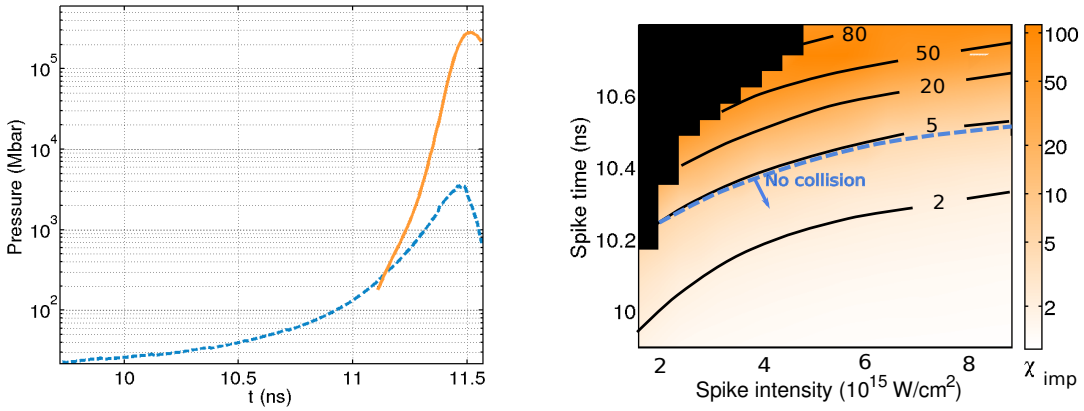

(a) (b)

Figure 5.16: Mean pressure in the shell in a HiPER simulation without spike (a) and ignitor shock pressure amplification due to the shell compression (b).

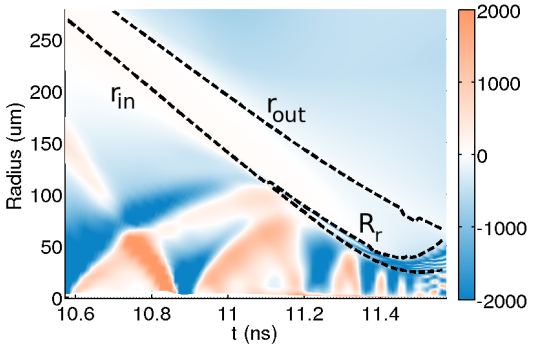

Figure 5.17: Shell outer/inner and returning shock position at the end of the compression phase

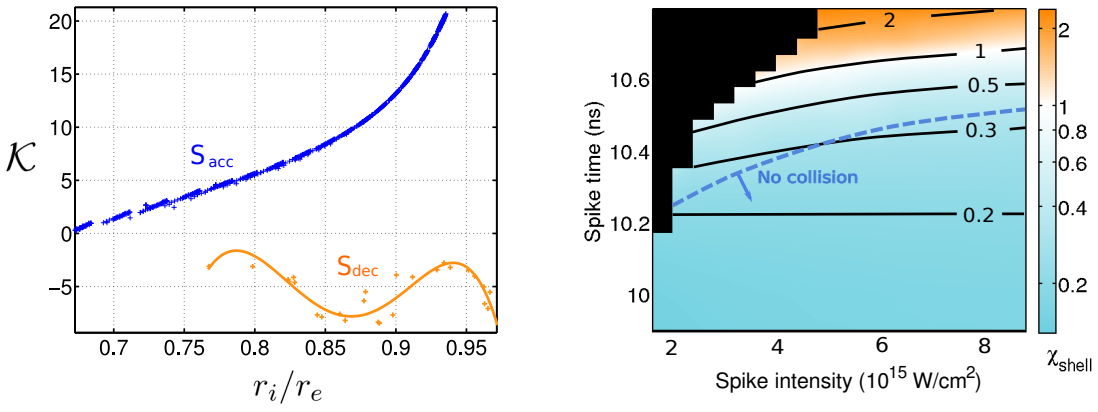

(a) (b)

Figure 5.18: Evolution of the shell parameter $\mathcal{K}$ and r_i/r_e in a HiPER simulation without spike (a) and ignitor shock pressure amplification due to the shell profile (b).

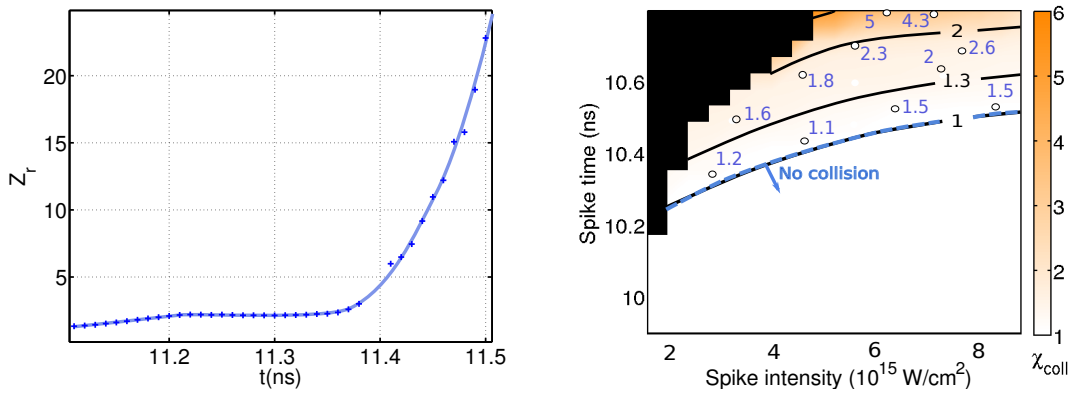

(a) (b)

Figure 5.19: Evolution of the returning shock strength in the HiPER simulation without spike (a) and ignitor shock amplification due to the shock collision (b).

Collision amplification factor $\mathcal{X}_{\text{coll}}$ The amplification factor due to the shock collision is calculated from the ignitor shock strength and the returning shock strength before the collision. The strength of the returning shock is measured in a simulation without spike and represented in Figure 5.19 (a). In the spike parameters domain considered here, the time of collision is in the range [11.1 ns, 11.43 ns]. In this range of interest, the strength of the returning shock is around 2 until 11.4 ns and then increases quickly up to 25. The shock strength before the collision is evaluated using the shock dynamics model in the same way it was done for $\mathcal{X}_{shell}$ (see Section 5.2.2.1). As the returning shock strength is known (Figure 5.19 (a)), the shock pressure amplification in the collision $\mathcal{X}_{coll}$ is calculated with the method explained in Section 3.3.4.1.

The theoretical shock pressure amplification in the collision is presented in Figure 5.19 (b). The comparison with the simulation results is not straightforward because the collision in the simulation is not instantaneous. The shock amplification in simulation is calculated with the ratio of the shock pressure after and before the collision divided by the overall pressure enhancement factor $\mathcal{X}_{imp}$ during the time of collision. The comparison of the model and the simulation results presented in Figure 5.19 (b) shows a good agreement. If the collision takes place before 11.4 ns - when the returning shock strength is weak $Z_r \simeq 2$ - Figure 5.11 indicates that the shock amplification is below a factor of 2. It becomes significant only for a very late time as the strength of the returning shock increases. It reaches the maximum value of 6.

Total pressure amplification factor The total pressure amplification of the shock is given by $\mathcal{X} = p_{sf}/p_{si} = \mathcal{X}_{imp}\mathcal{X}_{shell}\mathcal{X}_{coll}$. It is represented in figure 5.20 where the white dots represent the shock amplification measured in simulations with spike. We obtain a very good agreement between the theory and the simulations results.

The unity isocontour is close to the dashed line delimiting the domain where the ignitor shock undergoes a collision with the returning shock. For earlier spike times, the shock propagates only

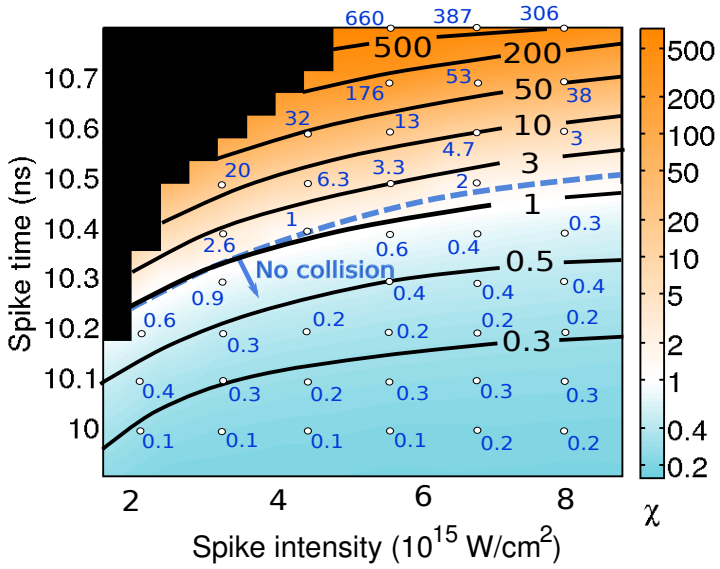

Figure 5.20: Shock pressure amplification dependence on the spike time t_s and the spike intensity I_s. The white dots represent simulation results.

in an accelerating medium. The positive pressure gradient, which compensate the acceleration force in the shell comoving frame, induces a decrease of the shock pressure. Moreover, in this zone, the shell overall pressure is increasing slowly which is not sufficient to compensate the shock pressure decrease in the shell comoving frame. Therefore, the total amplification factor is below unity when $t_f < t_d$.

For time later than the isocontour of unity, the shock pressure amplification increases quickly and reaches a value of 500. This huge modification of the amplification factor $\mathcal{X}$ is visible on a variation of 400 ps of the spike time t_s from 10.4 ns to 10.8 ns. In this domain, the shock collides with the returning shock. The collision factor is of about 2-6 and does not explain the high value of the total amplification factor. After the collision, the shock propagates into a decelerated medium with a sharp negative pressure gradient. This increases the shock pressure by a factor 2 for very late times. The main reason of such a high total shock amplification factor is the quick increase of the overall shell pressure near the stagnation time. Indeed, close to the stagnation time, several shocks and compression waves coming from the hot-spot enters into the shell and increase its mean pressure. This explains the pressure amplification in the range of 50-80.

5.2.1.3 Conclusion

The theoretical analysis and the numerical simulations show that the higher shock pressure amplification is obtained for later spike times. As the pressure amplification is higher for late time, a shock with a low initial velocity can be better amplified. This means that an initially weak shock is more amplified than a strong shock. However, the initial shock strength has a

weak influence in comparison with the shock timing.

In practice the shock cannot be launched too late. The target needs to be confined during a time long enough for the fusion reactions to ignite and for the burn wave to propagates in the fuel. So a late spike time results in a lower fusion gain (see Section 2.1.1). Moreover, the shock is less efficient if it enters into a hot-spot with a high pressure. Indeed, as we demonstrated in Chapter 4, the ignitor shock strength is another critical parameter for the shock ignition. We analyze this quantity in the next section.

5.2.2 Analysis of the shock strengthening

The shock strength does not depend on the overall pressure amplification. It is affected by the shock dynamics in the shell comoving frame and by the shock collision.

5.2.2.1 Spike parameters influence on the shock strength

Dependence of the ignitor shock strengthening on the laser intensity and the spike launch time is presented in Figure 5.21. The main amplification of the shock strength takes place in the accelerated shell part $\mathcal{S}_{acc}$ (panel (a)). The shock strength is lowered in the collision with the returning shock (panel (b)). The shock strength decreases further more in the shell decelerated part $\mathcal{S}_{dec}$ (panel (c)). The total shock strengthening as a function of the spike parameters (t_s, I_s) is obtained by combining the previous maps (panel (d)).

We represented also the total shock strengthening in the plane (t_f, I_s), where t_f is the time when the shock enters in the hot spot in Figure 5.22. It appears that the shock strengthening depends mainly on the time t_f when the shock reaches the shell inner surface. The results from simulations with spike are represented with white dots. The later the shock arrives at the shell inner surface, the lower is its final strength.

Even if the shock pressure amplification is stronger for late spike times, the final strength of the shock is weaker.

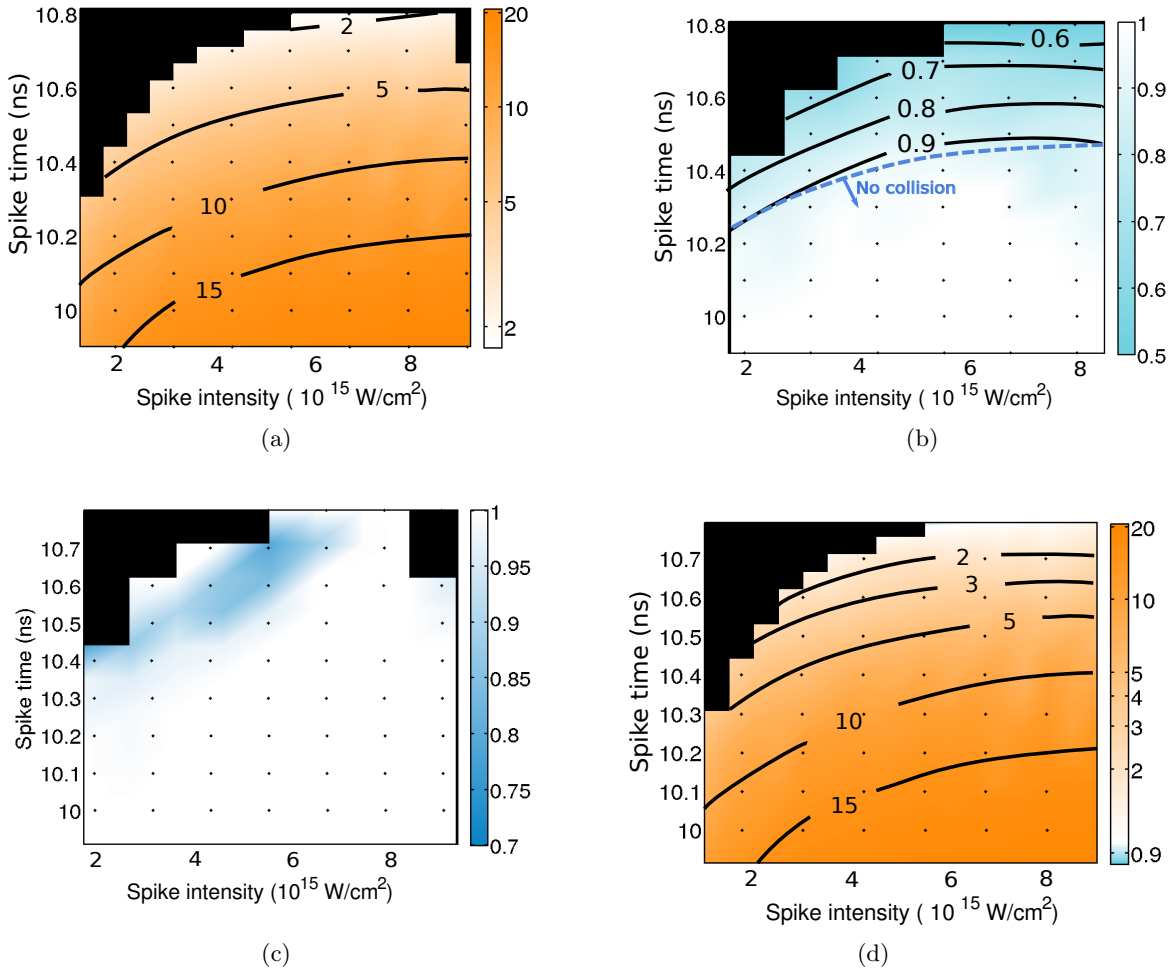

Figure 5.21: Shock strengthening in the accelerated part of the shell (a) in the shock collision (b), in the decelerated part of the shell (c) and total shock strengthening (d).

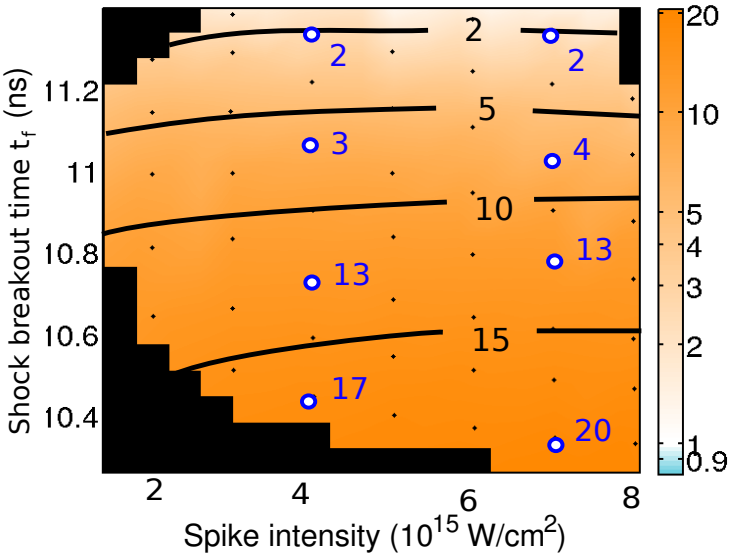

Figure 5.22: Shock strengthening depending on the shock breakout time t_f and on the laser intensity I_s. The white dots represent simulation results.

5.2.2.2 Assembly phase parameters influence on the shock strength

To quantify the shock strengthening in the shell accelerated part $\mathcal{S}_{acc}$, one needs to evaluate the shell parameter $\mathcal{K}$ which is time dependent. Indeed, the target implosion does not follow a homogeneous compression as it is assumed in the simplified model. Here, we assume that the shell is compressed homogeneously during the shock propagation time in the shell. The shell parameter $\mathcal{K}$ and the radius ratio r_{in}/r_{out} will be evaluated at the time t_s.

Relation between the shell parameter and the shell aspect ratio According to the shell profile description (Section 5.1.1.1), the shell parameter during the acceleration phase is $\mathcal{K} = (r_{out}/c_{out}\tau)^2$ where τ is defined by

$$-\frac{1}{\rho_0}\frac{\mathrm{d}p_0}{\mathrm{d}r_0} = \pm\frac{r_0}{\tau^2}. \tag{5.43}$$

In this expression, τ may be related to the acceleration $\ddot{r}_{out}$ of the shell. Let us estimate τ as $\tau = \sqrt{r_{out}/\ddot{r}_{out}}$. We have

$$\mathcal{K} = \frac{r_{out}\ddot{r}_{out}}{c_{out}^2}. \tag{5.44}$$

The shell mass is related to the shell aspect ratio as $\mathrm{M} = 4\pi\rho R^2/\mathcal{A}^3$. Using the Newton's law $\mathrm{M}\ddot{R} = -4\pi pR^2$ we have

$$\mathcal{A} = \gamma\frac{R\ddot{R}}{c^2}. \tag{5.45}$$

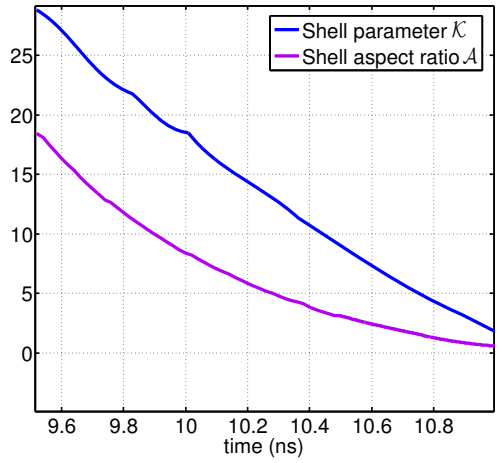

Figure 5.23: Shell parameter $\mathcal{K}$ and shell aspect ratio $\mathcal{A}$ in the reference simulation without spike

The expression of the shell parameter $\mathcal{K}$ and shell aspect ratio $\mathcal{A}$ during the acceleration phase are similar. According to the section 2.3.2, they decrease during the acceleration phase. In the reference simulation without spike we measured the shell aspect ratio and the shell parameter of the accelerated part of the shell. Their evolution with time is shown in Figure 5.23. It appears that indeed those two quantities are almost proportional to each other. The factor of proportionality is $\simeq 0.7$.

Based on this observation, we present in Figure 5.24 (a) the shock strengthening dependence on the initial shock strength and the shell parameter $\mathcal{K}$. The radius ratio $r_{in}/r_{out} = \mathcal{A}/(\mathcal{A}+1)$ is related to the shell parameter with $\mathcal{A} = 0.7\mathcal{K}$. This plot can be compared with the shock strengthening calculated directly with the shell parameters. The Figure 5.21 (a) is reproduced in Figure 5.24 (b) in the plane (t_s, Z_i). We can notice the similarity between those two maps in Figure 5.24 panel (a) and (b).
In conclusion, the shell parameter $\mathcal{K}$ is almost proportional to the shell aspect ratio $\mathcal{A}$ during the acceleration phase. This fact allows us to establish a relation between the shock time of launch and the shock strengthening.

Relation between the shell parameter and the shell Mach number To confirm the relation between the shell parameter and the shell aspect ratio, we performed a set of simulations where the laser pre-pulse power P_0 is varied between 0.4 and 0.7 TW and the laser main pulse power P_m is varied between 10 and 40 TW. This allowed us to vary the shell adiabat et acceleration and to cover a maximal shell Mach number $\mathcal{M}_0$ in the range from 7 to 11. We remind here that the shell maximal Mach number is defined as $\mathcal{M}_0 = \mathrm{u_{imp}}/c_{if}$ (see Section 2.3.2).
For each simulation, the shell parameter $\mathcal{K}$, the shell aspect ratio $\mathcal{A}$ and the shell Mach number $\mathcal{M}$ are measured from the beginning of the acceleration phase to the stagnation. Figure 5.25 (a) presents the evolution those quantities as a function of the shell radius obtained from a typical run. The position corresponding to the beginning and the end of the acceleration phase are

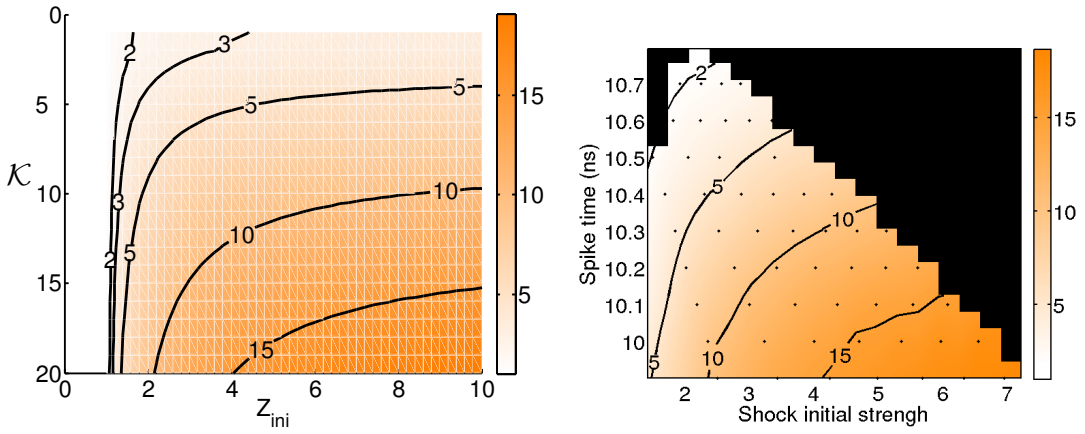

(a) (b)

Figure 5.24: Estimate of the shock strengthening by assuming $\mathcal{A} = 0.7\mathcal{K}$ (a) and calculation of the shock strengthening using the shell parameters in the simulation without spike (b).

indicated with dashed lines.

In each simulation, the maximum shell Mach number $\mathcal{M}_0$ and the shell parameter $\mathcal{K}_{sb}$ at the radius R_{sb} are measured. Their values are reported in Figure 5.25 (b). It appears that $\mathcal{K}_{sb}$ scales as the square of the maximal shell Mach number $\mathcal{K}_{sb} \propto \mathcal{M}_0^2$ as does the IFAR (2.38).

As the shell converges, the shell aspect ratio decreases and the shell Mach number increases. At some point, $\mathcal{A} \simeq \mathcal{M}$. We conclude from observation of Figure 5.25 (a), that the assumption $\mathcal{K} \propto \mathcal{A}$ is valid only before this moment.

At the end of acceleration phase (time t_d), the first shock enters in the shell at the radius R_d and the shell starts to decelerate. The parameter $\mathcal{K}$ is equal to zero at this point.

According to this analysis, the shell parameter $\mathcal{K}$ evolves monotonically with the shell radius from $\mathcal{K}_{sb} \propto \mathcal{M}_0^2$ at R_{sb} to 0 at R_d. Therefore, the shock strengthening in the shell accelerated part can be enhanced by increasing the shell Mach number. However, the strength of the shock is decreased after the collision with the returning shock. The returning shock strength dependance on the shell Mach number should be known to estimated the overall shock strenghening as a function of $\mathcal{M}_0$.

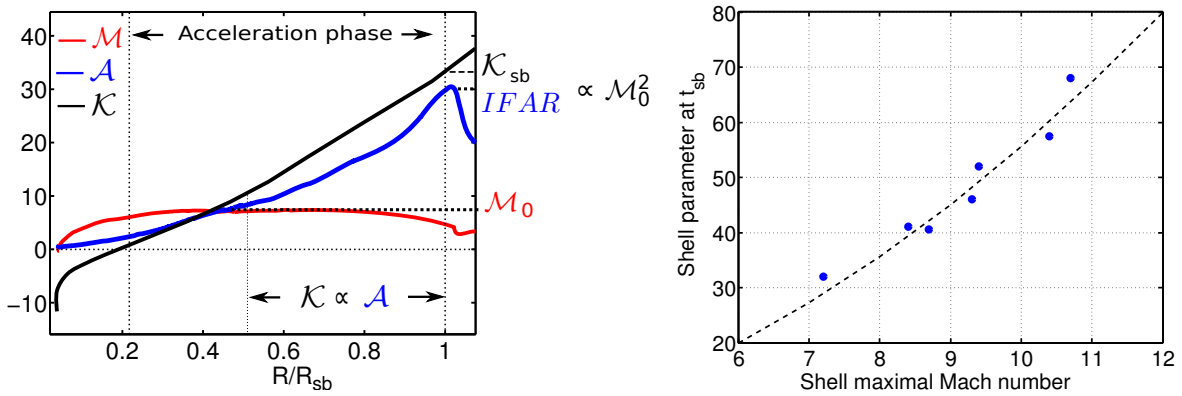

(a) (b)

Figure 5.25: Evolution of the shell parameter $\mathcal{K}$, aspect ratio $\mathcal{A}$ and Mach number $\mathcal{M}$ as a function of the shell position R in a simulation without spike (a) and relation between the shell parameter $\mathcal{K}_{sb}$ at the beginning of the acceleration phase t_{sb} and the maximal shell Mach number $\mathcal{M}_0$ (b). The dashed line in panel (b) follows the relation $\mathcal{K}_{sb} \propto \mathcal{M}_0^2$

5.3 Conclusions

In order to ignite the fusion reactions in a hot-spot with an areal density higher than 20 mg.cm^{-2}, the ignitor shock pressure p_s must attain a level of tens of Gbar at the shell/fuel interface and have a sufficiently high strength Z (see Chapter 4). It is therefore desirable that both the ignitor shock pressure amplification and the shock strength are maximized. For that, one needs to understand the shock dynamics in the imploding shell.

The shock dynamics depends on the medium where the shock propagates. The shell is described with a Kidder like model where the compression is assumed to be homogeneous. This allows to define a non-inertial reference frame which follows the shell flow. Then the shock amplification factor can be expressed as $\mathcal{X} = \mathcal{X}_{imp}\mathcal{X}_{shell}$ where $\mathcal{X}_{shell}$ corresponds to the shock pressure amplification in the shell comoving frame and $\mathcal{X}_{imp}$ is the pressure amplification in the imploding shell itself. The ignitor shock must enter in the hotspot close the stagnation phase where its areal density is sufficiently large for ignition to be possible. It must therefore at some point propagate through a decelerated medium. The deceleration phase starts as a diverging shock wave coming from the assembly phase enters in the shell. The ignitor shock collides with this returning shock. This process leads to a third amplification factor $\mathcal{X}_{coll}$ which is the pressure amplification in the collision with the returning shock.

The factor $\mathcal{X}_{imp}$ accounts for the overall pressure amplification in the shell due to its implosion. This overall pressure raise is faster near the stagnation phase. The influence of the factor $\mathcal{X}_{imp}$ on the ignitor shock pressure is therefore dominant near the stagnation. It can reach high values of order 100. Also, the amplification factor $\mathcal{X}_{imp}$ is higher if the shock propagation time in the shell $\Delta t \sim \Delta R_{sb}/(U_{si} - \mathrm{u_{imp}})$ is longer. For that one can either reduce the initial shock velocity $U_{si} \propto \sqrt{p_{si}/\rho_i}$ (by increasing the shell density ρ_i at the spike time moment) or increase

the shell thickness at the spike time or increase the implosion velocity. On the other side, the shock must have time to propagate in the shell. If the implosion velocity is too high, the shock relative velocity ($U_{si} - \mathrm{u_{imp}}$) might be small. Then the spike time t_s can be too close to the beginning of the acceleration phase t_{sb}. In this case, the laser pulse is the same as in the conventional scheme and there is no shock ignition anymore. The maximal shock propagation time in the shell may also be limited by the laser energy available. This point should be analyzed deeper from a design point of view.

The factor $\mathcal{X}_{shell}$ depends on the shell density $\tilde{\rho}_0$ and pressure $\tilde{p}_0$ profiles and on converging effects. The shock dynamics equation in the shell comoving frame can be written in the form $\mathrm{d}\ln Z = \mathcal{S}_p\,\mathrm{d}\ln p_0 + (1+\omega)\mathcal{S}_\rho\,\mathrm{d}\ln\tilde{\rho}_0 - j\mathcal{S}_r\,\mathrm{d}\ln\tilde{R}_s$, where $\tilde{R}_s$ is the position of the shock. We verified the validity of this equation for a converging shock and for various pressure and density profiles. Only the density gradient term must be corrected through the coefficient ω depending on the shell profile considered. The third term represents convergence effect. It is predominant if the pressure and density gradient are low (in a homogeneous non accelerated medium) or for radius 5 times lower than the outer radius. This justifies the assumption of a homogeneous initial hot-spot in the chapter 4 dedicated to the shock propagation in the hot spot. However, in the shell, a spatial variation of the density and pressure profiles must be accounted for.

The profile of the shell is characterized by the parameter $\mathcal{K}$, which is positive in the accelerated part of the shell and negative in the decelerated part of the shell. The factor $\mathcal{X}_{shell}$ depends on the shell parameter $\mathcal{K}$, on the ratio of its inner and outer radius r_{in}/r_{out} and on the initial shock strength Z_i. In an accelerated shell ($\mathcal{K} > 0$) the pressure decreases whereas the shock strength increases and in a decelerated shell ($\mathcal{K} < 0$) the opposite behavior occurs. Higher are r_{in}/r_{out} and Z_i, more influent is the parameter $\mathcal{X}_{shell}$.

The amplification factor $\mathcal{X}_{coll}$ depends on the strength of the ignitor shock Z_{c1} and on the strength of the returning shock Z_r before the collision. No exact analytical expression exists but it can be evaluated by using a graphical resolution or with an approximate expression. For Z_{c1} and Z_r below 10, we propose the expression (5.40) which is sufficiently accurate in the domain of interest.

The theoretical model of shock propagation through a converging shell is applied to a typical HiPER implosion. The shock pressure amplification is predicted using parameters measured in a simulation without spike. Then, the predicted shock pressure amplification is compared to the results from simulations with spike. A good agreement between the simulation results and the shock dynamics model is obtained. This means that the theory developed here includes all important processes influencing the shock dynamics. In the HiPER implosion, the pressure amplification factor varies from 0.1 to 500 if the spike time varies within 1 ns. The shock pressure amplification is very sensitive to the shock timing. It is maximal when the shock enters in the hot-spot at the stagnation time.

The strength of the shock need also to be maximized. It can be calculated in the shell comoving frame. The shock strength is mostly affected by two steps: (a) the accelerated shell pressure and density profiles upstream the returning shock and (b) the shock collision. In the

step (a) the shock strength increases. The strengthening depends strongly on the spike time. It is minimal when the ignitor shock enters in the hot-spot at the stagnation time. This lower limit can be increased if the density and pressure gradients in the accelerated shell are significant. For that one can increase the implosion velocity or reduce the shell adiabat. In the step (b), the shock strength is reduced in the collision with the returning shock. Increasing the implosion velocity would increase the returning shock strength and the two effects in (a) and (b) might compensate each other.

Further studies are needed to link the assembly phase parameters to the shock pressure amplification and strengthening. However, our analysis based on the assembly parameters of a typical HiPER implosion showed that the shock pressure amplification can be higher than 50 if the shock is launched sufficiently late. The ignition conditions expressed in Chapter 4 indicate that the shock pressure when it enters in the hot-spot must be of the order 20 Gbar. Therefore, to reach ignition, an initial shock pressure of more than 400 Mbar is needed. This is in agreement with the literature. The question now is: is it possible to generate such a pressure? The next chapter is devoted to the analysis of an experimental campaign where the ablation pressure is measured in SI relevant conditions.

6 Shock generation and experiments

Contents

In this chapter, we discuss experimental results concerning the ablation pressure and the shock generation in shock ignition relevant conditions. We review briefly the past experimental studies on this topic in Section 6.1. In Section 6.2, we expose the experimental setup considered in this study. In Section 6.3, we explain how the ablation and the shock pressure can be inferred from the experimental data. In Section 6.4, we analyze two representative shots. The influence of the hot electrons in the shock generation is discussed in 6.5.

The results exposed in this chapter are obtained in the framework of a collaboration between the american team (LLE Rochester,USA) and the CELIA team.

6.1 Experiments of shock generation

The crucial issue of the shock ignition scheme is the possibility of generating an ablation pressure higher than 300 Mbar in a large pre-plasma with a laser pulse in the intensity regime where the parametric instabilities dominate. In Section 2.2.3, we saw that the ablation pressure in the classical collisional absorption regime, can be expressed as [Dautray and Watteau, 1993]

$$p_a(\text{ Mbar}) = 11.8\big(I_{abs}[10^{14}\text{ W.cm}^{-2}]\big)^{\frac{2}{3}}(\lambda_L[\,\mu\text{m}])^{-\frac{2}{3}}\left(\frac{\text{A}}{2\text{Z}}\right)^{\frac{1}{3}}, \tag{6.1}$$

with I_{abs} being is the absorbed laser intensity and λ_L being the laser wavelength.

According to this law, the absorbed intensity needed to generate 300 Mbar pressure in the plastic ablator is 4.7×10^{15} W.cm^{-2}. Assuming an absorption coefficient of 60 % means that the incident intensity must be higher than 7.8×10^{15} W.cm^{-2}. Considering a laser wavelength of 351 nm, this gives an irradiance of $I_L\lambda_L^2 = 10^{15}$ W.cm^{-2}.μm^2. This is above the threshold of non-linear processes (see Section 2.2.1). In this regime, the reflectivity will increase due to the Stimulated Raman Scattering (SRS) and the Stimulated Brillouin Scattering (SBS). Moreover the SRS along with the laser beam filamentation (FI) and two plasmon decay (TPD) are the sources of hot electrons.

A direct measurement [Fratanduono et al., 2011] of the ablation pressure during a ramp compression of carbon has been accomplished at laser intensities up to 7×10^{13} W.cm^{-2} with a 351 nm light. The ablation pressure scaling law found is

$$p_a(\text{Mbar}) = 42(\pm3)\big(I_{abs}[10^{15}\text{ W.cm}^{-2}]\big)^{0.71(\pm0.01)}. \tag{6.2}$$

In 1980 [Drake et al., 1984], experiments showed that the yield of hot electrons generated by SRS instability increases strongly with the laser intensity approaching 10^{15} W.cm^{-2}. Klimo [Klimo et al., 2010] performed PIC simulations of the laser interaction with intensities in the range $10^{15}-10^{16}$ W.cm^{-2} with a plasma of temperature 5 keV and a density gradient length of 300 μm mimicking the shock ignition conditions. The overall absorption coefficient remains at the level of 60-70 % in this intensity domain. However, the non-linear processes become

important for high intensity. The dominant mechanism is the SRS. The energy is transported to the dense plasma by hot electrons with energy in the range of $20 - 40$ keV.

In 2011 and 2012 a series of planar experiments have been performed on the laser facilities LULI [Baton et al., 2012], PALS [Koester et al., 2013] and OMEGA [Hohenberger et al., 2014]. Recent experiments have been repeated on LIL facility also. The principle was to first irradiate the target with a low intensity pre-pulse to generate a pre-plasma. This generates a first shock in the target. Then, a high intensity pulse launches a second shock in the target. The shock breakout time at the rear side of the target is measured and is compared to the results of 2D simulations. This allows to infer the ablation pressure. The target (see Figure 6.1) is constituted of a layer of plastic (on the laser side), a layer of high Z material and a layer of α-quartz (LULI and OMEGA) or aluminum (PALS). The first layer is the ablator material in which the ablation pressure is evaluated. The second layer stops the X-rays (which are undesirable for the shock diagnostics) and gives information about the hot electrons population via the K_α X-ray emission. The third layer allows to measure the shock velocity with the optical interferometry setup VISAR (LULI and OMEGA) or the thermal emission with the SOP (PALS).

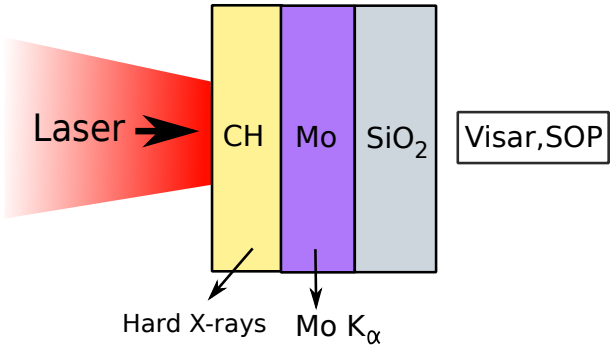

Figure 6.1: Schematic of the planar experimental setup for ablation pressure measurement(adapted from [Theobald et al., 2013]).

The maximal ablation pressures obtained in those experiments is 70 Mbar on OMEGA, 40 Mbar on LULI and 90 Mbar on PALS. The data corresponding to these results are presented in Table 6.1. The ablation pressures inferred in the experiments are below the law (6.1) prediction (see Figure 6.2). The ablation pressure for intensities near 10^{15} W.cm^{-2} is closer to the pressure predicted by the experimental scaling (6.2). However, the results from the PALS experiment with the intensity of 9×10^{15} W.cm^{-2} is still too low (see Figure 6.2).

This may be due to 2D effects, where the energy is dissipated in the lateral direction, and to non-linear effects which lead to back scattering. Theses experiments show a reflectivity at the level of 10 % dominated by the SBS mechanism and reflection from the critical surface. The conversion efficiency in hot electrons is low. As predicted by Klimo, the energy of the hot electrons is below 100 keV but their number is lower than expected.

Experimental data are lacking in the shock ignition intensity regime. To overcome the 2D effects, a spherical geometry is needed. We present in this chapter the results of the experimental

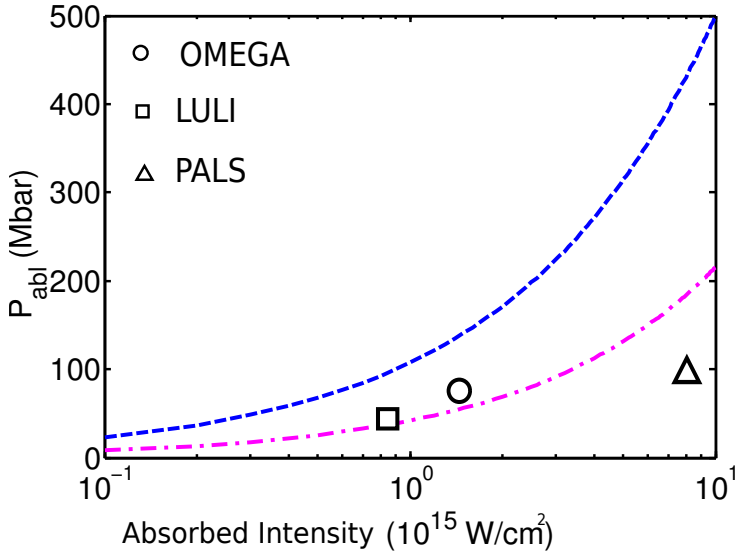

Figure 6.2: Ablation pressure versus the incident intensity in the planar experiments done on OMEGA (circle), LULI (square) and PALS (triangle). The scaling law (6.1) is represented in blue dashed line and the experimental scaling (6.2) is represented in magenta dot dashed line.

	Pre-pulse				Pre-plasma		
	I_L (W.cm^{-2})	λ_L (nm)	$\varnothing(\mu$m)	t (ns)	T (eV)	$L_{n\|n_c/4}$ (μm)	$L_{n\|n_c/10}$ (μm)
PALS	7×10^{13}	1315	900	0.250	175	4-25	20 - 65
LULI	7×10^{13}	530	400	2			
OMEGA	20×10^{13}	351	900	1.5			

	Spike-pulse				Results			
	I_L (W.cm^{-2})	λ_L (nm)	$\varnothing(\mu$m)	t (ns)	P_{abl} (Mbar)	BSL (%)	he (%)	he (keV)
PALS	9×10^{15}	438	100	0.250	60-100	< 10	1	50
LULI	10^{15}	530	100	2	40	10-15	-	50
OMEGA	1.49×10^{15}	351	600	0.5	75	< 3	< 2	20-70

Table 6.1: Condition of planar experiments on laser plasma interaction in the shock ignition relevant regime.

campaign conducted on the OMEGA laser facility to measure the ablation pressure in the spherical geometry with an intensity of $\simeq 5 \times 10^{15}$ W.cm^{-2}.

6.2 The "Strong Spherical Shock" experiments objectives and setup

A campaign of experiments called the "Strong Spherical Shock" has been performed since 2013 on the OMEGA laser. The aim of this campaign is to measure the ablation pressure with a peak laser intensity pertinent for shock ignition and in a target covered with a pre-plasma [Theobald et al., 2013].

6.2.1 OMEGA laser facility

The OMEGA laser facility at the Laboratory for Laser Energetics (LLE) in Rochester (USA) is a 60 beams neodynium:glass laser with a wavelength of 351 nm. It allows to conduct ICF experiments in a direct drive scheme with a total energy of 30 kJ with a peak power up to 45 TW. The 60 laser beams are distributed symmetrically around a spherical target chamber as it is shown in Figure 6.3. The target chamber is equipped with target diagnostics ports which are also represented in Figure 6.3. The system repetition rate is of one shot every 45 minutes which allows a productive program of experiments in one day.

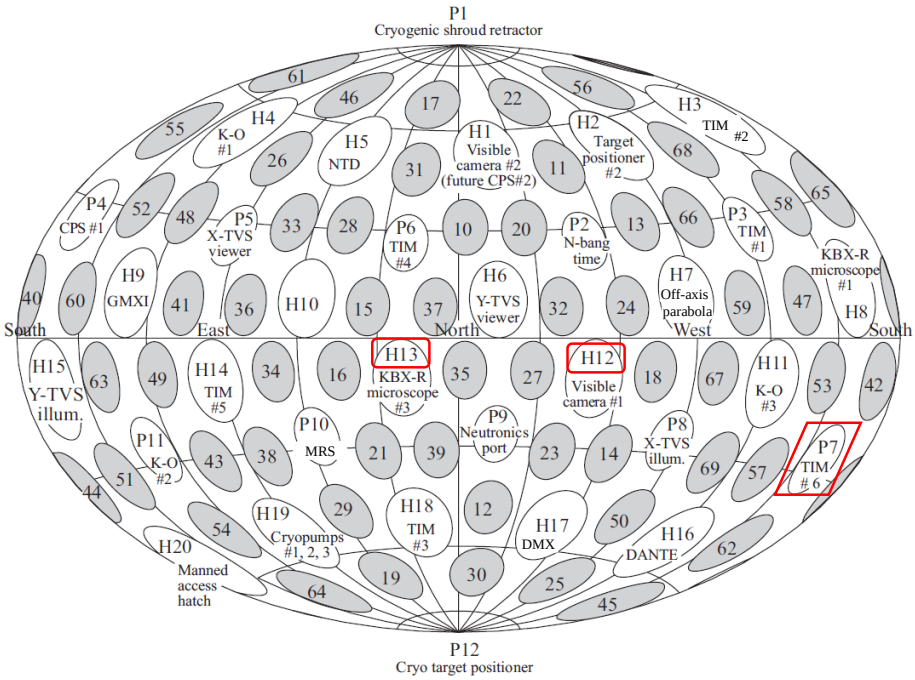

Figure 6.3: Schematic location of the laser beam ports (in gray) and diagnostics ports on the target chamber

6.2.2 Target and laser pulse

In this campaign the target used is a solid ball of CH doped with 5% of titanium covered with a CH ablator of 50 μm thickness (see Figure 6.4(a)). In order to obtain the highest achievable intensity, the target diameter is small 430 μm. The target is irradiated by the 60 beams of OMEGA with the laser pulse shape illustrated in Figure 6.4(b). A pre-pulse of about 800 ps duration is used to create a pre-plasma. Then a 1 ns spike pulse with 22-27 kJ of energy is used to generate a shock.

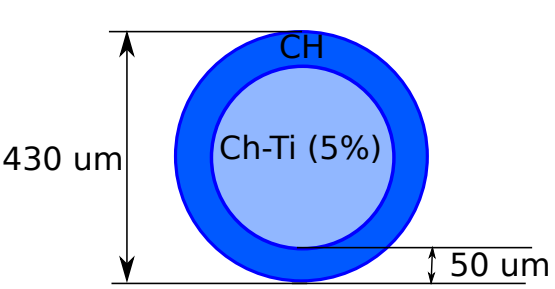

(a) Target

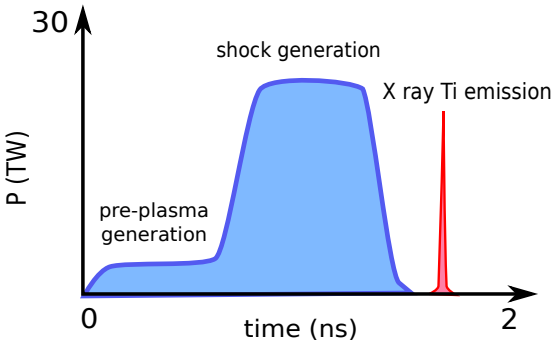

(b) Laser pulse shape

Figure 6.4: Target (a) and laser pulse (b) sketches used in the SSS campaign

6.2.3 Laser beams

The beam spot on the target can be smoothed with three smoothing techniques. The Smoothing by Spectral Dispersion (SSD) moves the speckles positions in the beam spot during the time of irradiation. A polarization smoothing is done with a Distributed Phase Rotator (DPR) optics. This is coupled to the Distributed Phase Plates (DPP) which produce multiple speckle pattern in the focal spots on the target. The phase-plates designs have an irradiance envelope with a super Gaussian profile $I_L(r) \propto exp(-r/r_0)^n$ where r_0 is the radius of the beam focal spot. The "SG4" phase plates combined with the SSD and polarization smoothing produce an intensity profile with $n = 4$. This currently allows to obtain the most uniform spherical irradiation (uniformity better than 2 % on the target). There are also other phase plates with 100, 200, 300 and 800 μm diameter spots.

For the SSS campaign, small phase-plates (elliptic of radii 105 μm and 145 μm and circular of radius 150 μm) where chosen to increase the on-target intensity up to 6×10^{15} W.cm^{-2}. For several shots in the SSS campaign, the SSD was removed to increase the laser on target intensity.

6.2.4 Shock timing measurement

The shock generated by the main pulse converges and reaches a high pressure in the center (see section 4.1). It rebounds from the target center and the matter behind the diverging shock reaches a temperature of hundred of eV. The excited titanium atoms emit a flash of X-rays when the shock collapse.

The X-ray framing camera (XRFC) [Bradley et al., 1992] detects and amplifies the X-ray light and converts it to visible light which is recorded. A set of typically 16 pinholes (10 μm diameter) provides a sequence of 16 images of the target with a given spatial ($\sim 12\,\mu$m) and an absolute timing error of $\pm$50 ps. The images are recorded with a microchannel plates (MCPs) covered with a gold film to convert the photons into electrons. The electron signal is amplified in the channels in an electric potential and converted in optical photons in a phosphor plate at

the rear side of the MCP. Finally, the optical signal is recorded with a film or a CCD camera. Filters can be added in front of the detector to select the range of recorded X-ray energies.

Another diagnostic is the streaked X-ray spectrometer (SXS) [Millecchia et al., 2012] which allows to measure the signal with a 35 picoseconds temporal resolution.

In the SSS campaign, the X-ray emission is detected with a spatial, temporal and spectral resolution with the X-ray framing camera (XRFC) and the streaked X-ray spectrometer (SXS). The time of convergence of shock convergence is deduced from the time delay of the X-ray flash.

6.2.5 Laser-plasma interaction analysis

The Full-Aperture Backscatter Stations (FABS) are used to characterize the backscattered light from the target. There are two FABS installed in the ports of the beams 25 and 30. They measure the backscattered light energy and temporally resolved spectra in the domains of SRS ($\lambda = 400 - 700$ nm) and SBS ($\lambda = 350 - 352$ nm). Knowing the incident and the backscattered laser power, the laser power absorbed in the target is evaluated with the temporal resolution of 100 ps. The temporally resolved spectra provide the information of non-linear processes occurring during the laser plasma interaction. In particular, the SRS and TPD signals are related to the acceleration of electrons.

The most reliable method of characterization of the hot electrons population is to measure the K_α line emission from a layer where the hot electrons deposit their energy. However, this requires a specific layered target. This makes the shock dynamics more complex and is not employed in this experiment. Another signal related to hot electrons in a plasma is the Bremsstrahlung emission produced in scattering of hot electrons with ions. This radiation is characterized by a continuous spectrum of X-ray which contains informations about hot electrons number and energies. This does not require any specific target design.

In the SSS campaign, the hot electron temperature is inferred from the imaging diagnostics HERIE (High Energy Radiography Imager on EP) and the X-ray spectrometer BMXS (Bremsstrahlung MeV X-ray Spectrometer) [Chen et al., 2008]. The measurements are completed by the time resolved four-channel hard X-ray detector (HXRD) [Stoeckl et al., 2001].

6.3 Ablation and shock pressure evaluation

It is not possible to measure directly the pressure in the laser plasma interaction experiments. However, the pressure can be inferred from the shock time of convergence, as the shock initial velocity depends on its initial pressure (see Chapter 5). Here, we first give a rough analytical estimate of the initial shock pressure. Then we explain how this pressure can be inferred more precisely from the simulation.

6.3.1 Estimate of the initial shock pressure

Let us use the previous analytical work to predict the initial shock pressure as a function of the flash time. We define R_{out} the radius of the outer part of the ablator and R_{in} the radius of the inner part of the ablator at the initial time.

The first shock launched by the pre-pulse has a very high Mach number as the upstream medium is cold. Considering the ablator as an ideal mono-molecular gas, it is compressed in the shock by a factor of about 4. The shock generated by the spike pulse first propagates in the pre-compressed CH of density $\rho_{out} = 4\rho_{CH}$. During the time interval of ~ 1 ns between pre-pulse and the main pulse, the first shock has already crossed the ablator. Therefore, the second shock is generated at the radius $R = R_{in} + (R_{out} - R_{in})/4$. As the velocity of the second shock is much higher, we may consider that the two shocks merge near the CH/CHTi interface. Assuming that the shock velocity is approximately constant because the converging effects are small in this part of the target, the second shock velocity is $U_{sout} = \sqrt{4p_{si}/3\rho_{out}}$, with p_{si} the initial pressure of the spike shock. Then the propagation time of the spike shock in the CH is $\Delta t_{CH} = (R_{out} - R_{in})4U_{sout}$, which in the dimensional units reads:

$$\Delta t_{CH}(\text{ns}) = \frac{(R_{out} - R_{in})}{40}\sqrt{3\frac{\rho_{CH}}{p_{si}}}. \tag{6.3}$$

where the radius is in μm, the density is in g.cm^{-3} and the pressure is in Mbar.

The spike shock pressure is modified by the convergence effect, the interaction with the interface CH/ CHTi and the coalescence with the first shock. We can expect from the self-similar solution (3.92) that the shock pressure amplification due to converging effects in the CH is $\mathcal{X}_{conv} = (R_{in}/R_{out})^{-0.9} = 1.07$. The first shock strength is infinite and the expected second shock strength is below 5. Thus according to Figure 3.15, the amplification factor in the shock coalescence $\mathcal{X}_{coal}$ is between 0.8 and 1 . The density ratio between CH and CHTi is $x = 0.7$. Again assuming that the strength of the shock is below 5, Figure 3.12 predicts a pressure amplification through the contact discontinuity $\mathcal{X}_{CD}$ between 1 and 1.2. All together those effects might compensate each other and we assume that the shock pressure is constant in the CH.

The propagation time of the shock from the CH/CHTi interface to the target center is calculated using the Guderley's solution. One can refer to the zeroth order expression of the converging time in Table 4.7. In the dimensional units have

$$\Delta t_{CHTi}(\text{ns}) = \frac{R_{in}}{14.5}\sqrt{\frac{3}{4}\frac{\rho_{CHTi}}{p_{si}}}. \tag{6.4}$$

Adding these two time intervals 6.3 and 6.4, the initial shock pressure can be expressed using the formula

$$p_{si}(\text{Mbar}) = \frac{3}{\Delta t^2}\left[\frac{(R_{out} - R_{in})}{40}\sqrt{\rho_{CHTi}} + \frac{R_{in}}{30}\sqrt{\rho_{CHTi}}\right]^2, \tag{6.5}$$

where Δt (in ns) is the duration between the spike time and the flash time.

6.3.2 Estimate of the initial shock pressure with simulations

The initial shock pressure and the ablation pressure can be inferred by constraining radiative hydrodynamic simulations with the experimental observables: the X-ray flash time and the absorbed laser energy. In the hydrodynamic code, the electron heat flux is limited and the value of the flux limiter is constrained by the experimental evaluation of the absorbed energy. A good agreement between the simulated and the experimental time of shock collapse gives confidence in the simulation. Then, the ablation pressure and the initial shock pressure are inferred from the simulation results.

To interpret the experiments we used the radiative hydrodynamic code CHIC [Maire et al., 2007]. The laser beam irradiation on the target is calculated using the experimental laser pulse and a 3D ray-tracing package (Section 2.2.1). The focal spots have a super-Gaussian profile with the radius of 150 μm. The laser absorption is calculated assuming the inverse Bremsstrahlung process (Section 2.2.1). Then the shock evolution was simulated in the spherical geometry including the radiative effects. The electron heat-flux is treated in the flux limited Spitzer–Härm approximation. We used a SESAME equation of state, a Thomas–Fermi ionization and multi-group radiative diffusion with LTE opacities. The details about the simulation parameters are given in Appendix A.

6.4 Analysis of two representative shots

We consider here in details the results and analysis of two representative shots with and without SSD beam smoothing.

6.4.1 Shot with the laser beam Smoothing by Spectral Dispersion

6.4.1.1 Experimental results

The shot # 69133 was performed with the temporal beam smoothing SSD. The external target radius is $R_{out} = 215\,\mu$m and the radius of the interface CH/CHTi is $R_{in} = 165\,\mu$m. The incident and absorbed laser power is presented in Figure 6.5. The total incident energy is 17 kJ. The measured absorption coefficient is 52 %.

The X-ray flash time is measured with the XRFC diagnostics. Figure 6.6 shows the results of the shot # 69133. For early times, the X-rays emitted from the hot corona when the laser is on is visible. At the end of the laser pulse the temperature of the corona decreases and the signal disappears. After some time, a small bright spot appears in the center. This is the titanium flash which occurs at $t_{flash} \sim 1.62$ ns. The size of the emitting zone is of about 15 μm. The duration of the flash is less than 50 ps.

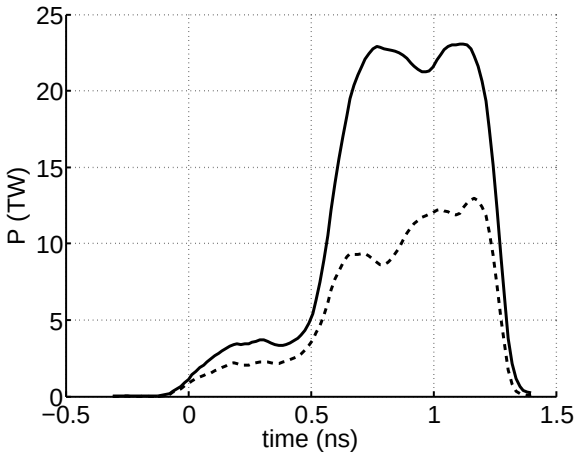

Figure 6.5: Experimental temporal profiles of the incident power (solid line) and absorbed power (dashed line) in the shot # 69133.

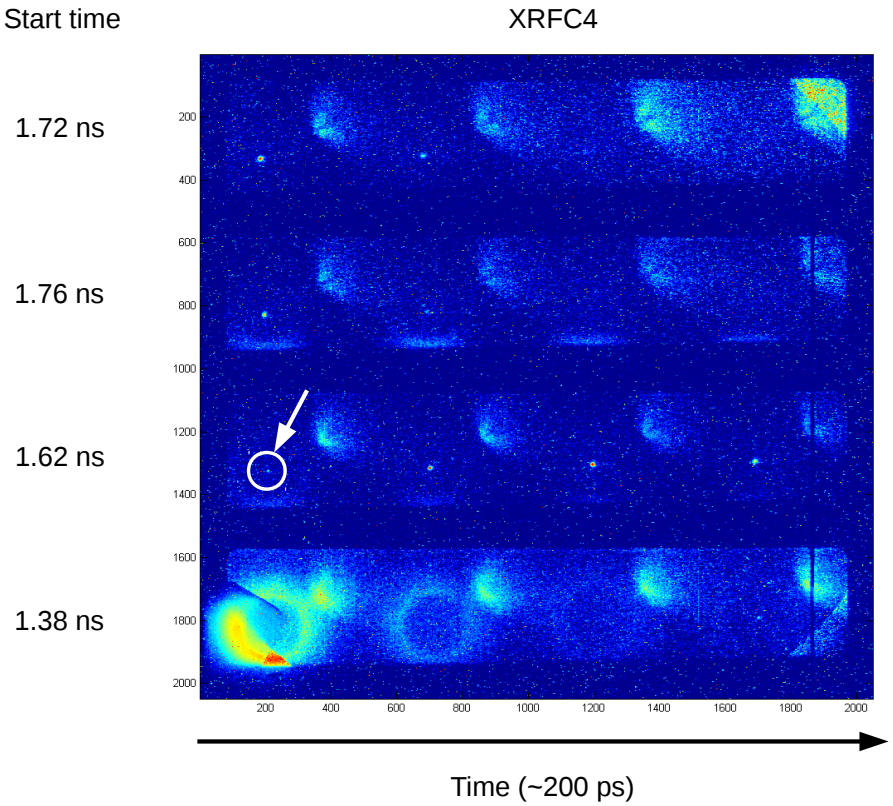

Figure 6.6: XRFC records in the shot # 69133. The arrow indicates the titanium X-ray flash from the center of the target.

6.4.1.2 Analytical estimate of the shock pressure

According to Figure 6.5 the spike time is $t_s = 600$ ps, therefore the experimental time of collapse is $\Delta t = t_{flash} - t_s = 1.02$ ns. Using equation (6.5), the analytical estimate gives a first approximation of the ablation pressure $p_{si} = 172$ Mbar.

During the spike pulse, the absorbed power is $P_s = 12$ TW. The absorbed intensity is evaluated by $I_{abs} = P_s/4\pi R_{out}^2 = 2 \times 10^{15}$ W.cm^{-2}. The theoretical ablation (6.1) pressure is 170 Mbar. This is in agreement with the initial shock pressure inferred from the shock collapse time.

6.4.1.3 Simulations

We conduct a more detailed analysis with numerical simulations.

Variation of the flux limiter Figure 6.7 presents the absorbed power and Table 6.2 shows the absorption and the time of shock collapse obtained in the simulations with several values of the flux limiter f. We also performed a simulation with the non local model of electron conduction. The absorption is of 75 % and the shock collapse time is 1.45 ns.

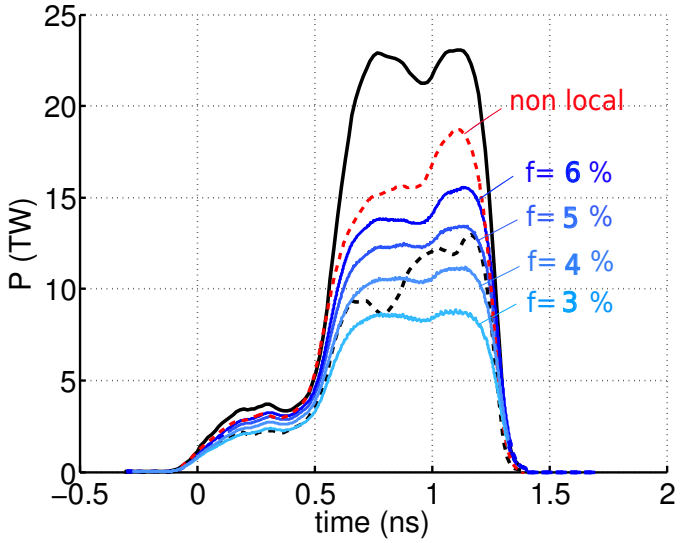

Figure 6.7: Laser incident power at the target surface (solid line), experimental absorbed power (dashed line) and simulated absorbed power (blue lines) depending on the flux limiter.

f (%)	η (%)	t_c (ns)
6	69	1.58
5	**62**	**1.67**
4	52	1.77
3	43	1.89

Table 6.2: Time of the shock collapse t_c and total absorption coefficient η depending on the flux limiter f.

We can see that the simulation with the flux limiter of 5 % recovers the experimental shock time of collapse and shows an absorption coefficient in agreement with the experiment.

Hydrodynamic analysis Figure 6.8 shows the pressure evolution in time and mass coordinate of the simulation with the flux limiter of 5 %.

Shocks pressure A first shock is generated in the CH during the pre-pulse ❶. The spike shock is generated at 600 ps ❸. During this time the first shock has reached the CH-Ti interface ❷. As the density of the CH-Ti is higher than the density of the CH, a shock is reflected. This shock interacts with the spike shock at 700 ps ❹. Thus, the spike shock is unperturbed by the upstream flow for only 100 ps. It reaches the CH/CHTi interface in ❺ and merges with the first shock in ❻. A shock is transmitted with a lower pressure and a shock is reflected. This one reaches the outer radius of the target at 1.1 ns and interferes with the ablation pressure.

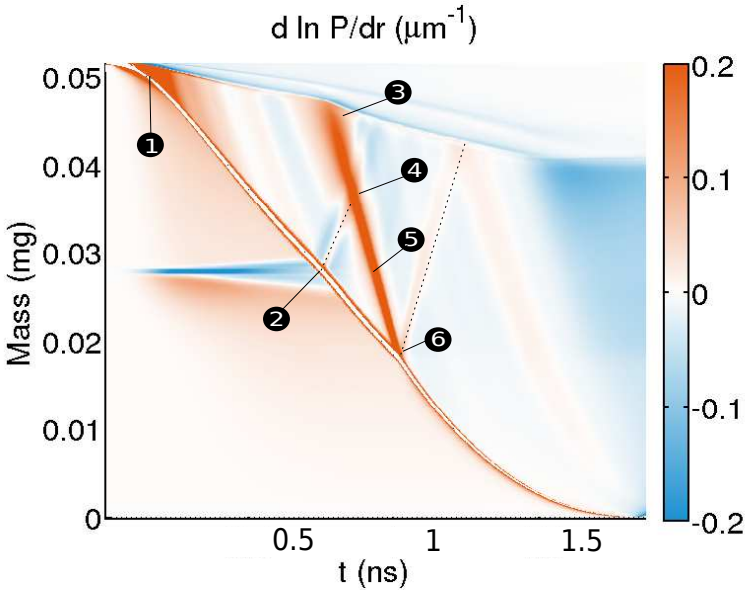

Figure 6.8: Simulated pressure gradient depending on time and mass coordinate for the shot 69133.

Figure 6.9 shows the pressure at the shock fronts and at the ablation front. The pressure evolution can be interpreted using the shock theory presented in Section 3.3. We reported in Table 6.3 the shock pressure at some particular points in the simulation and the corresponding theoretical pressure amplification.

We give somes detail about how the theoretical values are obtained.

The first shock is propagating in a cold matter, thus we assume that it has an infinite strength $Z \gg 1$.

The pressure amplification factor $\mathcal{X}_{conv}$ is due to the convergence effect. It depends on the shock position and is calculated using the self-similar law (3.92) with $\alpha = 0.688$: $p_s \propto R_s^{-0.9}$.

The pressure amplification factor $\mathcal{X}_{coll}$ is due to the collision with a counter-propagating shock. It can be evaluated using the relation (5.40) $\mathcal{X}_{coll} = Z_r(Z_{c1} + Z_r)^{1/2}(1 + Z_{c1}Z_r)^{-1/2}$ where Z_{c1} is the strength of the shock and Z_r is the strength of the counter-propagating shock.

The pressure amplification factor $\mathcal{X}_{coal}$ is due to the coalescence of the shock with an upstream shock. It depends on the strength of both shocks and can be read in Figure 3.15.

The pressure amplification factor $\mathcal{X}_{CD}$ is due to the interaction of the shock with a contact discontinuity surface. It depends on the density ratio at the contact discontinuity surface and on

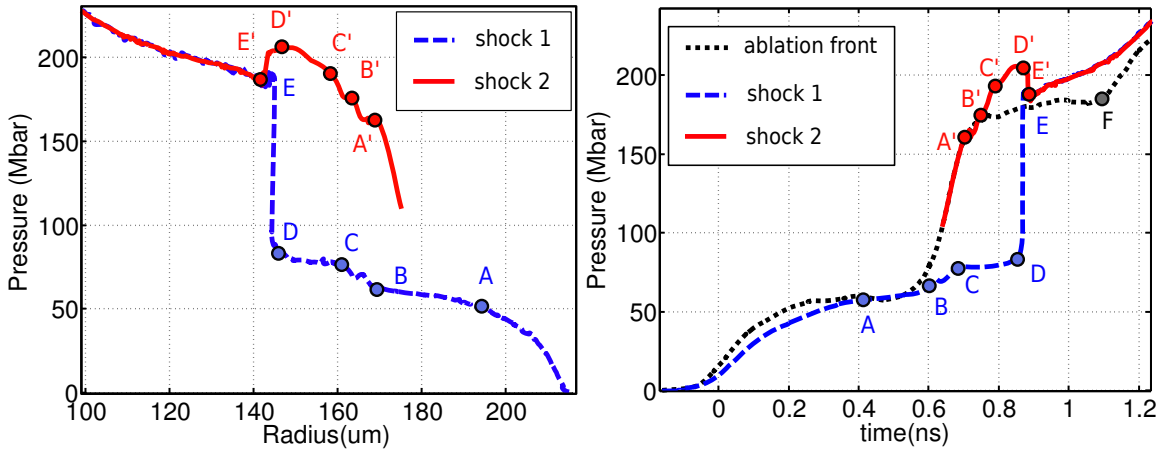

(a) Ablation pressure

(b) Shock pressure

Figure 6.9: Pressure evolution at the shock fronts in the simulation of the shot 69133. Panel (a) - evolution in space, panel (b) - evolution in time.

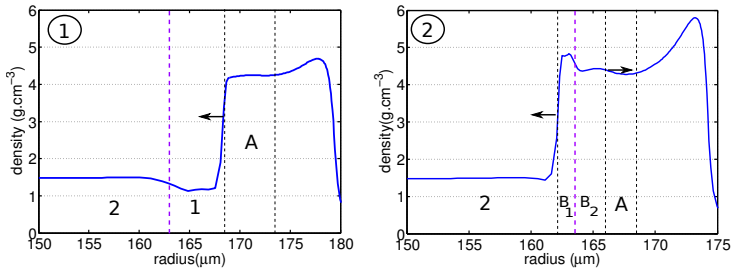

Figure 6.10: Density profile before (left panel) and after (right panel) the interaction of the first shock with the contact discontinuity.

the shock strength. The initial densities of the CH and the CHTi are respectively 1.05 g.cm^{-3} and 1.47 g.cm^{-3}. The density ratio $x = 0.7$ is used for the calculation of the first shock pressure amplification through the CD interaction. The value of this amplification factor can be read in Figure 3.12.

The density profile near the CH/CHTi interface before and after the shock interaction is presented in Figure 6.10. The density $\rho_1 = 1.05$ mg.cm^{-3} is the CH density and the density $\rho_2 = 1.47$ mg.cm^{-3} is the CHTi density. The density factor at the interface before the interaction is $x = \rho_1/\rho_2 = 0.7$. The strength of the incoming shock is infinite. The density in A is therefore $\rho_A = 4\rho_1$. After the collision, the transmitted shock strength is also infinite and $\rho_{B1} = 4\rho_2$. The reflected shock strength is according to Figure 3.12 $z_b/z_a = 1.2$. Then, according to (5.23c), $\rho_{B2} \simeq 1.1\rho_A$. Therefore, the density ratio at the interface after the shock interaction is $x = \rho_{B1}/\rho_{B2} = 1.1 \times 4\rho_1/4\rho_2 = 0.8$.

The pressure amplification of the spike shock at the CD interface is read in Figure 3.12 with the value $x = 0.8$.

Points	Event	Pressure in simulation (Mbar)	Theory
A	Generation ❶	$P_A = 55$	$P_A \sim$ ablation pressure
A-B	Convergence	$P_B = 1.15 P_A = 63$	$\mathfrak{X}_{conv} = (R_B/R_A)^{-0.9} = 1.15$
B-C	CD interaction ❷	$P_C = 1.2\, P_B = 76$	$\mathfrak{X}_{CD}(x = 0.7, Z \gg 1) = 1.2$
C-D	Convergence	$P_D = 1.1\, P_C = 83$	$\mathfrak{X}_{conv} = (R_C/R_D)^{-0.9} = 1.1$
A'	Generation ❸	$P_{A'} = 162$	$P_{A'} \sim$ ablation pressure
A'-B'	Collision ❹	$P_{B'} = 1.2 P_{A'} = 178$	$\mathfrak{X}_{coll}(Z_{c1} = \frac{P_{A'}}{P_B}, Z_r = \frac{P_C}{P_B}) = 1.15$
B'-C'	CD interaction ❺	$P_{C'} = 1.1\ P_{B'} = 195$	$\mathfrak{X}_{CD}(x = 0.8, Z = \frac{P_{B'}}{P_C}) = 1.1$
C'-D'	Convergence	$P_{D'} = 1.05\, P_{C'} = 205$	$\mathfrak{X}_{conv} = (R_{C'}/R_{D'})^{-0.9} = 1.1$
D'-E'	Shock coalescence ❻	$P_{E'} = 0.9\ P_{D'} = 189$	$\mathfrak{X}_{coal}(Z_a \gg 1, Z_b = \frac{P_{D'}}{P_D}) = 0.9$

Table 6.3: Comparison of the shocks pressure evolution in the simulation of the shot # 66133 with the theory.

Ablation pressure Concerning the evolution of the ablation pressure, it is directly linked to the laser power. The measured absorbed power of the pre-pulse is 2.5 TW. The position of the critical density during the pre-pulse is around $R_{nc} = 220\,\mu$m in the simulation. The absorbed intensity is thus $I_{abs} = 4.1 \times 10^{14}$ W.cm^{-2}. If we apply the scaling law (6.1), the expected ablation pressure is 60 Mbar. During the spike pulse, the measured absorbed power is 12 TW and the critical density position in the simulation is 210 μm which gives $I_{abs} = 2.16 \times 10^{15}$ W.cm^{-2}. The expected ablation pressure is 180 Mbar. We can see in Figure 6.9(b) that the pressure at the ablation front follows well the scaling law. In the point F the ablation pressure raises. This is due to the second reflected shock perturbation.

Conclusion The simulation with a 5 % flux limiter recovers both the experimental absorbed energy and the shock collapse time. The ablation pressure during the spike is 180 Mbar with an absorbed intensity of 2.16×10^{15} W.cm^{-2}. The generated shock pressure before any perturbation coming from the upstream flow is 162 Mbar. This result is close to the analytic prediction (6.5). The discrepancy can be explained by the shock pressure perturbation by the reflected shock wave at the CH/CHTi interface. The maximal shock pressure before the coalescence of the first and second shock is 205 Mbar. It comes from an amplification through the collision with the reflected shock, through the interaction with the CH/CHTi interface and with the convergence effect.

6.4.2 Shot without laser beam Smoothing by Spectral Dispersion

6.4.2.1 Experimental results

In the shot # 71597, the SSD smoothing was removed. This increases the level of the intensity fluctuations on the target surface, but also increases the average incident intensity. This is in order to explore possibilities of further increased ablation pressure. The external radius is $R_{out} = 215.2\,\mu$m and the radius of the interface CH/CHTi is $R_{in} = 169\,\mu$m. The incident and absorbed laser power are presented in Figure 6.5. The total incident energy is 26 kJ. The absorption coefficient is 36.3 %. The titanium flash occurs at $t_{flash} \approx 1.98$ ns as it can be seen in Figure 6.12.

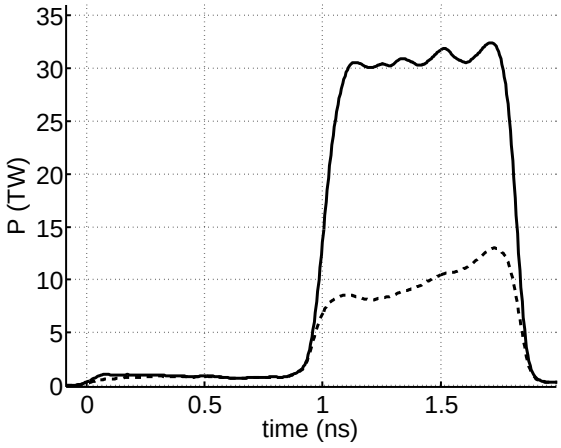

Figure 6.11: Experimental incident power (solid line) and absorbed power (dashed line) of the shot # 71597.

The spike time is $t_s = 1.1$ ns, therefore the experimental time of shock collapse is $\Delta t = t_c - t_{flash} = 0.88$ ns. The analytical formula (6.5) predicts the initial shock pressure $p_{si} = 249$ Mbar.

The mean absorbed power during the spike is $P_s = 9.5$ TW. The absorbed intensity during the spike is evaluated by $I_{abs} = P_s/4\pi R_{out}^2 = 1.6 \times 10^{15}$ W.cm^{-2}. The scaling law (6.1) predicts the ablation pressure of 147 Mbar which is not consistent with the measured shock collapse time.

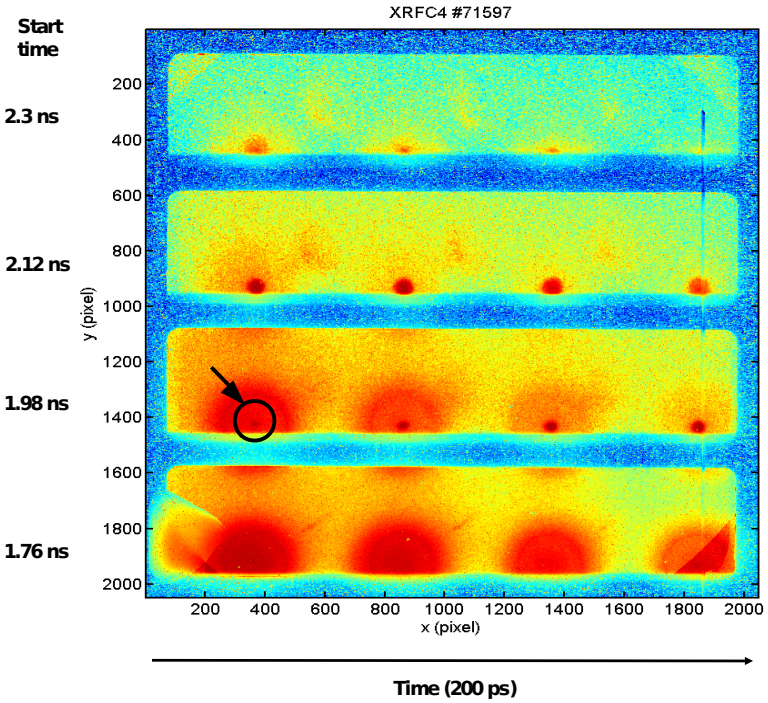

Figure 6.12: XRFC record of the shot # 71597. The arrow indicates the titanium X-ray flash from the center of the target.

6.4.2.2 Simulations

The estimated initial shock pressure is too high compared to the predicted ablation pressure with the scaling laws (6.5) and (6.1) assuming the collisional laser absorption. Let us see what are the results of numerical simulations.

Variation of the flux limiter and non local model Figure 6.13 presents the time evolution of the absorbed power and Table 6.4 shows the time of shock collapse obtained in the simulations with several values of the flux limiter f.

For any value of the flux limiter, the simulated time of collapse is larger than the experimental value. Moreover, the flux limiter value of 3 % which fits the experimental absorbed energy corresponds to the largest time of collapse. Here, the simulations do not agree with the experimental results. In this shot, the incident laser intensity on the target is 40 % higher than in the previous shot while the experimental absorbed intensity is lower. Thus collisional absorption alone is not consistent with the experiment and the non-linear processes must be considered. The latter enhances reflection and possibly leads to the generation of supra-thermal electrons. If the mean free path of the hot electrons is larger than the size of the conduction zone, a non local model should be better suited to simulate this experiment than the flux limited model (see

Section 2.2.2). Indeed, the simulation performed with the non-local model [Schurtz et al., 2000] implemented in the CHIC code gives a time of shock collapse closer to the experimental result: 1.9 ns. However, this is achieved due to the absorption coefficient of 70 % which is much too high (see red line on Figure 6.13) compared to the experiment. As the heat conduction is larger with the nonlocal model, the corona temperature is lower. Then inverse Bremsstrahlung absorption coefficient (2.15) is higher. Thus the non local model alone does not allow to interpret the experimental results as it does not accounts to the parametric processes in the laser-plasma interaction.

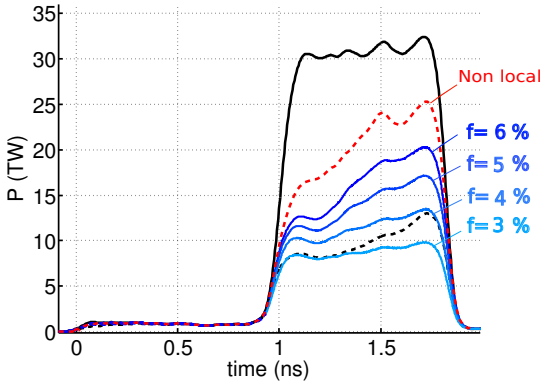

Figure 6.13: Laser incident power (solid line), experimental absorbed power (dashed line) and simulated absorbed power (dotted lines) depending on the flux limiter.

f (%)	η (%)	t_c (ns)
6	57	2.07
5	49	2.16
4	41	2.26
3	42	2.39

Table 6.4: Time of the shock collapse t_c and total absorption coefficient η depending on the flux limiter f.

Artificial increase of the ablation pressure The ablation pressure in the experiment seems to be higher than the ablation pressure obtained in the simulation with the same amount of absorbed energy.

In order to evaluate the ablation pressure leading to the experimental shock time of collapse, we increase artificially the absorbed laser power in the spike. Figure 6.14 shows the input laser laws generated from the experimental absorbed power with a mean power in the spike from 10 TW to 40 TW. As we want to impose the absorbed energy in this set of simulations, we do not use the ray-tracing. Only one ray is used and all input energy is deposited at the critical density n_c. We choose a flux limiter of 5 %.

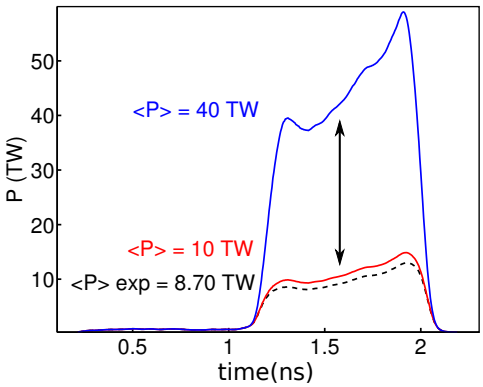

Figure 6.14: Rescale of the experimental absorbed power of the shot # 71597. The mean spike power is varied from 10 TW to 40 TW.

In each run with a given value of the laser spike mean power, the pressure at the ablation front and its position as well as the pressure and position of the spike shock front are measured. Then the pressure as a function of position is

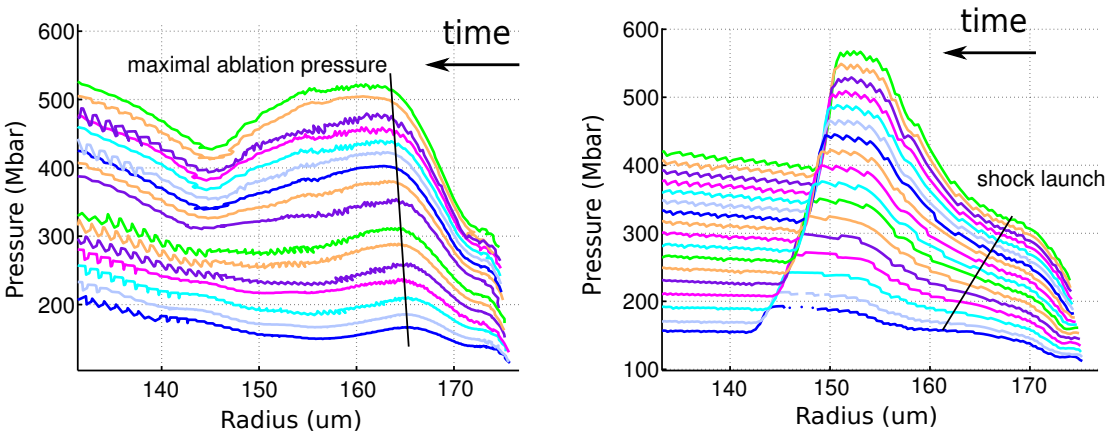

(a) Ablation pressure

(b) Shock pressure

Figure 6.15: Pressure at the ablation front (a) and at the shock front (b) obtained in the simulations with increasing mean spike power from 10 TW to 22 TW.

plotted in Figure 6.15 where the time is considered as a parameter. Each curve corresponds to one run. The shock and ablation fronts propagate from higher radii to lower radii. Therefore, the pressures evolution at the fronts can be read from the right to the left. In panel (b) the shock generation phase corresponds to the zone where the second derivative of $p_s(R_s)$ at the right from the straight black line. During this phase, the shock pressure is coupled to the ablation pressure. When the shock is launched in the target, the pressure increases by the converging effects $p_s \propto R_s^{-0.9}$ and the second derivative of $p_s(R_s)$ is positive. Therefore, we define the initial shock pressure as the pressure at the inflection point. The maximal ablation pressures and initial shock pressures at the inflection point $p(R_s)$ curves are indicated with black lines.

Figure 6.16 presents the relation between the measured maximal ablation pressure (black diamonds), the initial shock pressure (black circles) and the time of shock collapse. In the same plot, the corresponding mean absorbed power in the spike used in the simulation is represented with red squares. The experimental shock time of collapse 1.98 ns corresponds to an ablation pressure of 300 Mbar and a initial shock pressure of 225 Mbar. In this case the mean spike power absorbed is 19 TW. The analytical formula (6.5) is represented with the black dashed line. It underestimates the initial shock pressure for a short time of collapse. This is explained by the fact that we neglected the shock pressure modification at the CH/CHTi interface and the collision with the reflected shock. This approximation is valid only for a weak spike shock strength. Nevertheless, the pressure estimate is in satisfactory agreement with the simulation results. The experimental error in measuring the shock collapse time is 50 ps. According to Figure 6.16 that corresponds to an uncertainty of 50 Mbar in the ablation pressure and of 25 Mbar in the initial shock strength.

According to the simulation, the experimental shock collapse time is recovered with the ablation pressure of 300 Mbar. This pressure will be called the *apparent* ablation pressure, that is to say, the ablation pressure needed to recover the experimental shock timing in the

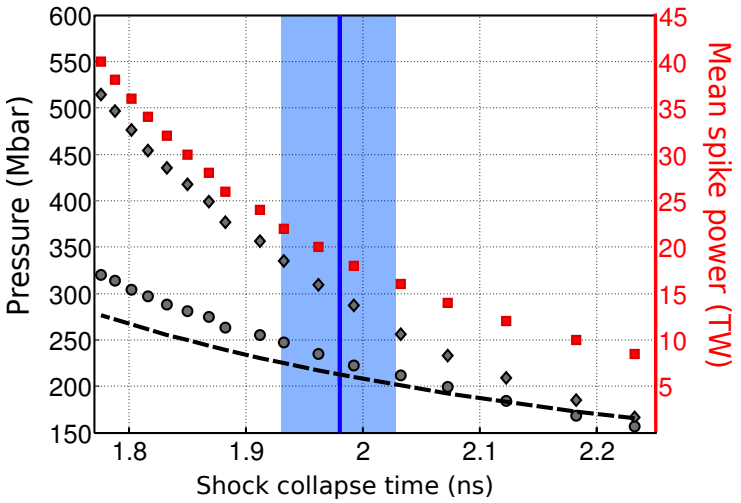

Figure 6.16: Maximal ablation pressure (black diamonds), initial shock pressure (black circles) and mean spike power (red squares) depending on the shock collapse time. The analytical relation between the shock collapse time and the initial shock pressure (6.5) is represented with the black dashed line. The experimental time of collapse is indicated with the blue line. The experimental error bar is represented by the blue zone.

hydro-radiative simulation code with the thermal electron flux limited at 5 %.

The current model of laser energy absorption by inverse Bremsstrahlung process implemented in our code does not allow to recover both the *apparent* ablation pressure and the experimental absorption coefficient. The PIC simulations of Klimo [Klimo et al., 2010] indicates that the laser energy absorption process is dominated by the stimulated Raman scattering but not the inverse Bremsstrahlung at such incident laser intensity. In this case, a part of the absorbed energy is carried by the hot electrons. We will show in the next section that both the experimental absorbed energy and the shock collapse time can be recovered in the simulations by taking into account the hot electron energy deposition.

Hot-electron energy deposition Let us now revise the model of absorption. We use as input the experimental absorbed laser power. However, we assume that a part η_{he} of the absorbed energy is converted into hot electrons. For the sake of simplicity, let us consider that those hot electrons are mono-energetic. They deposit their energy behind the critical density on the distance defined by the stopping range ρl_{he} which depends on their energy. Thus we combine two processes of energy deposition: 1-a local deposition at the position of critical density R_{nc} and 2- a volume deposition from R_{nc} to $R_{\rho l_{he}}$ where $\int_{R_{\rho l_{he}}}^{R_{nc}} \rho \, \mathrm{d}R = \rho l_{he}$. We suppose that the hot electron energy per unit of mass is homogeneously deposited along the stopping range. In this model, there are two free parameters: the fraction of energy carried by hot electrons η_{he} and their stopping range ρl_{he}.

Such a simple model of hot electron energy deposition is introduced to the code CHIC. At each time step a fraction η_{he} of the absorbed energy is distributed homogeneously over the

distance defined by the hot electron stopping range. In the simulations, we measured the shock collapse time in different set of parameters $(\rho l_{he}, \eta_{he})$. The map obtained is represented in Figure 6.17. The area where the simulations fit the experiment, taking a 50 ps margin of error on the shock collapse time, is hatched. The experimental value of the shock collapse time can be recovered by converting 15-20 % of the absorbed energy into hot electrons with the stopping range of $6 - 10$ mg.cm^{-2} which corresponds to the electron energy from 60 to 100 keV in a CH [Ribeyre et al., 2013a]. As we will show in Section 6.5, these parameters are in agreement with the experimental data.

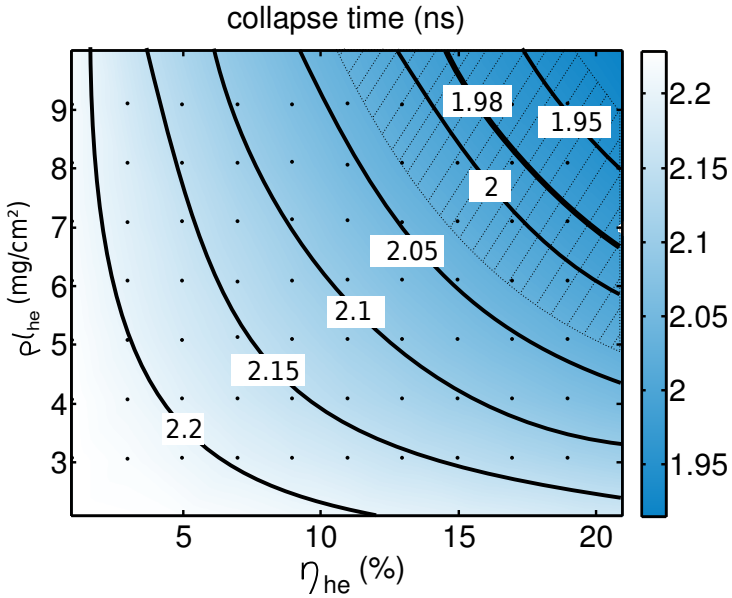

Figure 6.17: Shock collapse time dependence on the hot electron conversion efficiency and on their stopping range.

6.4.2.3 Hydrodynamic analysis

To understand how the shock collapse time can be decreased by the hot electrons whereas the absorbed energy remains fixed, we compare the results of two simulations: one without hot electrons and one with 15 % of absorbed energy converted into hot electrons with a stopping range of 10 mg.cm^{-2} corresponding to the energy of 100 keV (see Figure 6.23).

Figure 6.18 presents the pressure gradient evolution in the two simulations. In the case with hot electrons, 85 % of the absorbed energy is deposited at the critical density and transported to the ablation front by thermal electrons and the remaining 15 % of the absorbed energy is deposited in volume in the hot electron stopping range. A discontinuity surface is created at the limit of the hot electron stopping range R_{he}. Two shocks are generated during the spike: one at the ablation front and another one deeper in the target at this contact discontinuity. Figure 6.19 shows the density, pressure and temperature profiles near the contact discontinuity position R_{he} at the end of the spike raise. The temperature and density profiles are similar to the profiles at

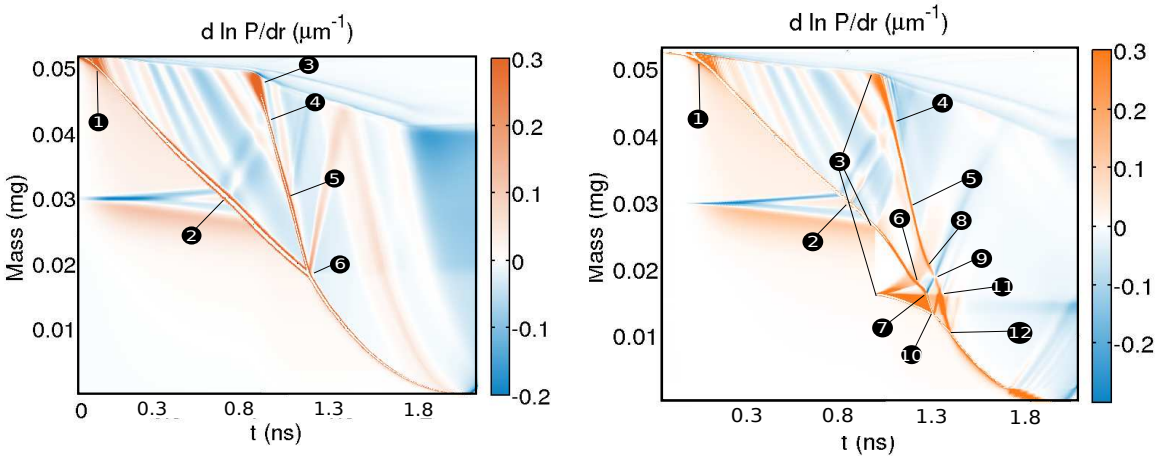

(a) Without hot electrons

(b) With hot electrons

Figure 6.18: Maps of the pressure gradient in the simulations of the shot # 71597 with and without hot electrons. The absorbed energy of 9.4 kJ is taken from the experiment. In the simulation with hot electrons conversion efficiency is $\eta_{he} = 15\%$ and stopping range is $\rho l_{he} = 10$ mg.cm^{-2}.

the ablation front. We will call this discontinuity surface "the hot electron ablation front".

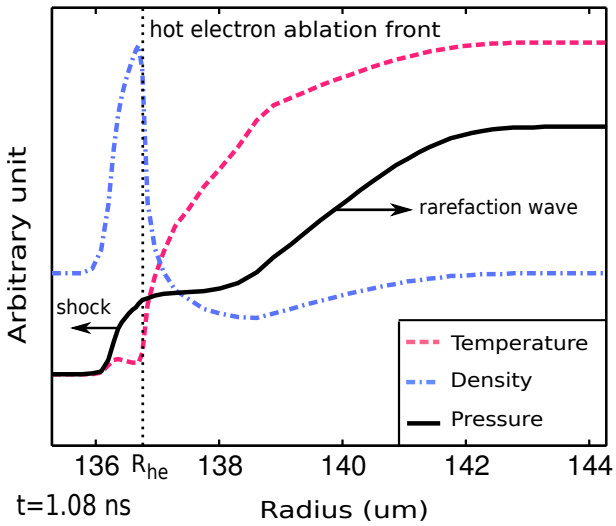

Figure 6.19: Density, temperature and pressure profiles near the hot electron ablation front at t=1.08 ns. The hot electrons parameters are: $\eta_{he} = 15\%$ and $\rho l_{he} = 10$ mg.cm^{-2}.

Case without hot electrons The case without hot electrons is similar to the shot # 69133. The pressure at the ablation front and at the shock front are represented in Figure 6.20. We reported in Table 6.5 the shock pressure at some particular points in the simulation and the corresponding theoretical pressure amplification. A first shock is generated ❶ during the prepulse. Its pressure increases with the ablation pressure and reaches 20 Mbar. It propagates in the CH and interacts with the CH/CHTi interface ❷. A shock wave is reflected with a low

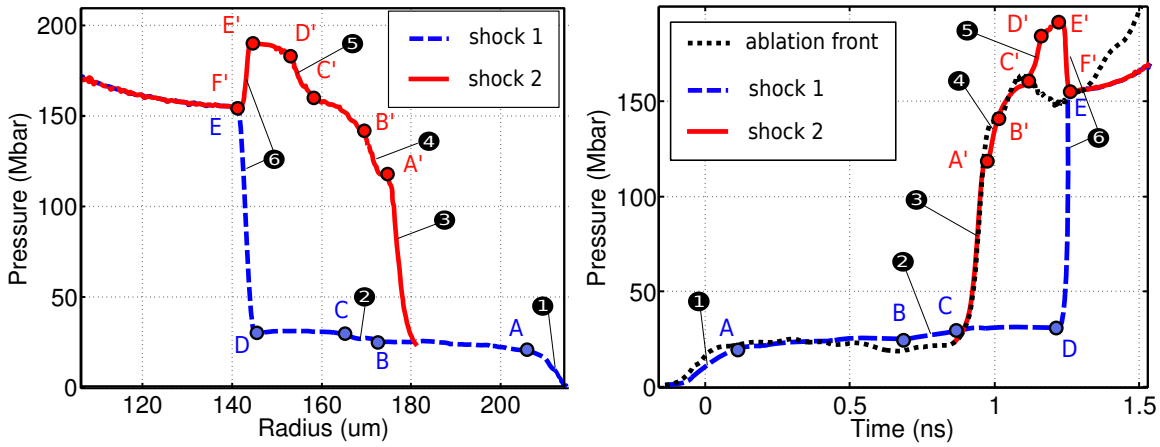

(a) (b)

Figure 6.20: Pressure evolution at the shock fronts and at the ablation front in a simulation of the shot # 71597 without hot electrons. Panel (a) - evolution in space, panel (b) - evolution in time.

strength $Z = 1.2$. The second shock is generated by the laser spike ❸. Its initial pressure in the point A' is 120 Mbar. It interacts with the first reflected shock wave ❹. Then, the shock pressure is still alimented by the ablation pressure raise: it increases between the points B' and C'. The shock interacts with the interface CH/CHTi ❺. Lastly, the spike shock overtakes the first shock ❻.

Points	Event	Pressure in simulation (Mbar)	Theory
A	Generation ❶	$P_A = 21$	$P_A \sim$ ablation pressure
A-B	Convergence	$P_B = 1.19 P_A = 25$	$\mathfrak{X}_{conv} = (R_B/R_A)^{-0.9} = 1.2$
B-C	CD interaction ❷	$P_C = 1.2\, P_B = 30$	$\mathfrak{X}_{CD}(x = 0.7, Z \gg 1) = 1.2$
C-D	Convergence	$P_D = 1\, P_C = 30$	$\mathfrak{X}_{conv} = (R_C/R_D)^{-0.9} = 1.1$
A'	Generation ❸	$P_{A'} = 120$	$P_{A'} \sim$ ablation pressure
A'-B'	Collision ❹	$P_{B'} = 1.17 P_{A'} = 140$	$\mathfrak{X}_{coll}(Z_{c1} = \frac{P_{A'}}{P_B}, Z_r = \frac{P_C}{P_B}) = 1.13$
C'	Generation	$P_{C'} = 160$	$P_{C'} \sim$ ablation pressure
C'-D'	CD interaction ❺	$P_{C'} = 1.13\ P_{B'} = 180$	$\mathfrak{X}_{CD}(x = 0.7, Z = \frac{P_{C'}}{P_C}) = 1.1$
D'-E'	Convergence	$P_{E'} = 1.06\, P_{D'} = 190$	$\mathfrak{X}_{conv} = (R_{E'}/R_{D'})^{-0.9} = 1.06$
E'-F'	Shock coalescence ❻	$P_{F'} = 0.8\ P_{E'} = 155$	$\mathfrak{X}_{coal}(Z_a \gg 1, Z_b = \frac{P_{E'}}{P_D}) = 0.8$

Table 6.5: Shocks pressure evolution in the simulation of the shot # 71597 without hot electrons and the corresponding theoretical estimates.

Case with hot electrons The pressure evolution in the case with hot electrons is much more complicated. It is represented in Figure 6.18 (b) and 6.21.

Shocks pressure The first shock is generated in ❶. Its pressure follows the ablation pressure until it reaches the pressure $p_A = 22$ Mbar in the point A. The pressure increases slowly by convergence effects before the interaction with the interface CH/CHTi ❷. There, a low strength shock is reflected back.

The spike shock is generated near the ablation front ❸ and reaches the pressure $p_{A'} = 98$ Mbar in the point A'. The hot electrons deposit their energy in the CH and also partially in the CHTi over the distance from $r = 180\,\mu$m to $r = 140\,\mu$m. This increases the first shock pressure between the points D and E. A second ablation front is created in the CHTi at the distance $R_{he} \simeq 140\,\mu$m, where the hot electrons are stopped. It is clearly visible on Figure 6.18 (b). A rarefaction wave is generated outward and a shock wave is launched inward.

From the time 1.1 ns corresponding to the bullet ❸, three shocks are propagating into the target. The first one is the pre-pulse shock, the second one is the spike shock generated at the laser ablation front and the third one is generated at the hot electron ablation front in the CHTi.

During the laser spike the pressures of the first and the spike shocks increase quickly due to the target heating by the hot electrons. The interaction between the second shock with the first reflected shock in bullet ❹ and with the interface CH/CHTi in bullet ❺ have a weak influence on the spike shock pressure compared to the high pressure increase between the points A' and C' due to the hot electron energy deposition. The impact of the rarefaction wave generated at the hot electron ablation front, with the first shock in bullet ❻ and the spike shock in bullet

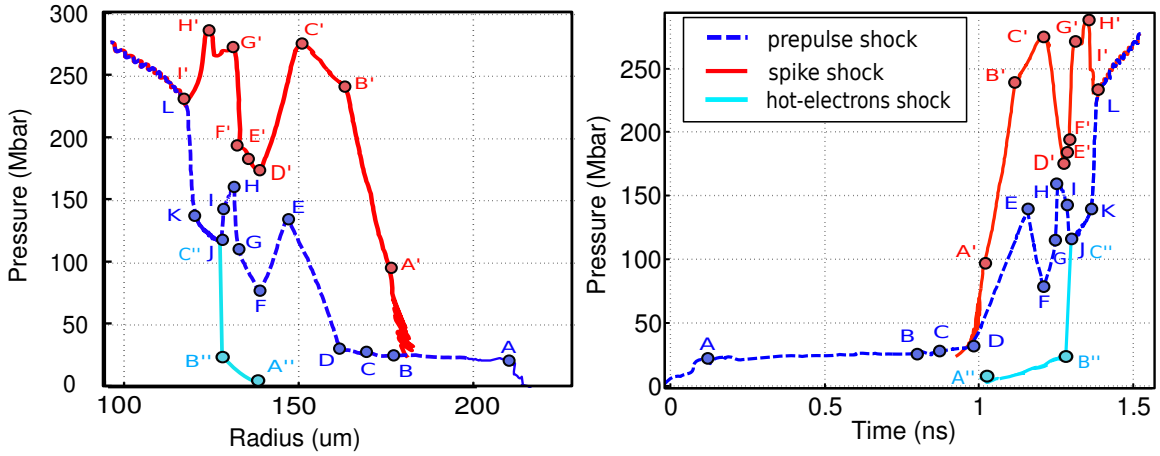

(a) (b)

Figure 6.21: Pressure evolution at the shocks fronts in the simulation of the shot 71597 wit hot electrons ($\eta_{he} = 15\%, \rho l_{he} = 10$ mg.cm^{-2}).

❽ is well visible in Figure 6.21. This corresponds to the pressure drops between the points C' and D' for the spike shock and between E and F for the first shock.

The first shock encounters the ablation front in the CHTi at R_{he} ❼. A shock wave is reflected backward, it interacts with the second shock in bullet ❾.

The third shock pressure follows initially the pressure at the hot electron ablation front up to 25 Mbar between the points A'' and B''. It is then overtaken by the first shock in bullet ❿. A rarefaction wave is reflected during this process. This rarefaction wave interferes with the second shock and reduces its pressure in F'.

The spike shock passes through the hot electron ablation surface in ⓫. Its pressure increases between the points F' and H' to level of $p_{H'} = 287$ Mbar before it overtakes the first shock in the point I' (bullet ⓬). After the coalescence the shock pressure is $p_L = 240$ Mbar.

The spike shock pressure in this case is highly sensitive to four processes: (1) the hot electron energy deposition (pressure amplification between A' and C'), (2) the rarefaction wave created at the hot electron ablation surface (❾ pressure decrease between C' and D'), (3) the shock interaction with the hot electron ablation front (❿ pressure increase between F' and G') and (4) the shock coalescence (⓬ pressure decrease between H' and I').

Table 6.6 summarizes the processes acting on the shocks pressure and compares the simulation pressure amplification to the theoretical amplification factors. The role of hot electrons processes in the pressure evolution is not theoretically characterized. In order to predict the spike pressure evolution, one needs to characterize the jump in density at the hot electron ablation front and the pressure ratio of the generated rarefaction wave. The quantities related to the hot electrons and not explained by a theory are written in red in Table 6.6. Their values are measured in the simulation.

While the target heating by hot electrons plays a significant role, the influence of the shock generated at the hot electron ablation front is not dominant. If $P_{B''}$ would be higher, the first

Points	**Event**	**Pressure in simulation (Mbar)**	**Theory**
A	Generation ❶	$P_A = 21$	$P_A \sim$ ablation pressure
A-B	Convergence	$P_B = 1.19 \times P_A = 25$	$\mathcal{X}_{conv} = (R_B/R_A)^{-0.9} = 1.2$
B-C	CD interaction ❷	$P_C = 1.2 \times P_B = 30$	$\mathcal{X}_{CD}(x = 0.7, Z \gg 1) = 1.2$
C-D	Convergence	$P_D = 1 \times P_C = 30$	$\mathcal{X}_{conv} = (R_C/R_D)^{-0.9} = 1.04$
D-E	HE heating ❸	$P_E = 133$ Mbar $Z_E = 1.5$	–
E-F	R interaction ❻	$P_F = 0.58 \times P_E = 77$	$\mathcal{X}_{rare}(Z = 0.2, Z_E)$
F-G	HE heating	$P_G = 110$ Mbar $Z_G = 3.5$	–
G-H	CD interaction ❼	$P_H = 1.48 \times P_G = 163$	$\mathcal{X}_{CD}(x = 0.2, Z_G) = 1.5$
H-I	–	$P_I = 148$ Mbar	–
I-J	shocks coalescence ❿	$P_J = 0.78 \times P_I = 148$	$\mathcal{X}_{coal}(z_a \gg 1, Z_I = P_I/P_{B''}) = 0.8$
J-K	convergence	$P_K = 1.16 \times P_J = 135$	$\mathcal{X}_{conv}(R_K/R_J)^{-0.9} = 1.07$
A'	Generation ❸	$P_{A'} = 98$	$P_{A'} \sim$ ablation pressure
A'-C'	HE heating	$P_{C'} = 276$ Mbar $Z_{C'} = 2.6$	–
C' -D'	R interaction ❽	$P_{D'} = 0.63 \times P_{C'} = 174$	$\mathcal{X}_{rare}(Z_a = 0.3, Z_C)$
D'-F'	Collision/R interaction ❾	$P_{F'} = 1.1 \times P_{D'} = 190$	$\mathcal{X}_{coll}(1.5, 1.5) = 1.5$, $\mathcal{X}_{rare}(1.5, 0.8) = 0.8$
F'-G'	CD interaction ⓫	$P_{G'} = 1.42 \times P_{F'} = 270$	$\mathcal{X}_{CD}(x = 0.2, Z = 1.5) = 1.3$
G'-H'	–	$P_{H'} = 287$	–
H'-I'	Shocks coalescence ⓬	$P_{I'} = 0.84 \times P_{H'} = 240$	$\mathcal{X}_{coal}(z_a \gg 1, P'_H/P_K = 2) = 0.95$
A"-B"	Hot electrons shock generation ❸	$P''_B = 25$	follows the "ablation" pressure

Table 6.6: Shocks pressure evolution in the simulation of the shot # 71597 with hot electrons and the corresponding theoretical estimates.

and spike pressure drops in coalescence would be less important. The quantities affected by the hot electron driven shock are denoted in blue in Table 6.6.

The values written in green in Table 6.6 are not well explained theoretically. This process of interaction of three coalescing shocks needs further theoretical analysis.

Nevertheless, one can say that at a given absorbed energy, the shock generation is more efficient with an energy deposition both at the critical density and over the hot electron stopping range. In this case, less internal and kinetic energy is wasted in the ablated matter. Also, the density is higher behind the shock, so the hot electron energy deposition increases just behind the shock. Therefore, the shock amplitude is enhanced due to the hot electron energy deposition.

Both the measured shock collapse and absorbed energy can be recovered if one takes into account the hot electrons. The hot electron stopping range is varying from 6 to 10 mg.cm^{-2} and they are carrying from 10% to 20% of the absorbed energy. The maximal shock pressure before its interaction with the rarefaction wave is 275 Mbar.

Ablation pressure Both the energy deposition and the hydrodynamic during the shock generation are strongly affected by the hot electrons. Effectively, they create a second ablation front in the target. Figure 6.22 presents the pressure evolution at the two ablation fronts. Here the ablation front is defined as the location of the density gradient length local minimum. The pressure at the thermal ablation front reaches a maximum value of 150 Mbar. The suprathermal ablation pressure due to the hot electron energy deposition increases slowly to the value of 25 Mbar. It is perturbed by the shock generated during the pre-pulse ❼ and by the shock generated at the ablation front during the spike ⓬. The ablation pressure is then raised up to 300 Mbar. This value is in agreement with the analysis presented in the previous section (Section 6.4.2.2). Indeed, Figure 6.16 shows that the *apparent* ablation pressure should be at the level of 300 Mbar to recover the experimental shock collapse time, leading to an initial shock pressure of 240 Mbar in a simulation without hot electrons.

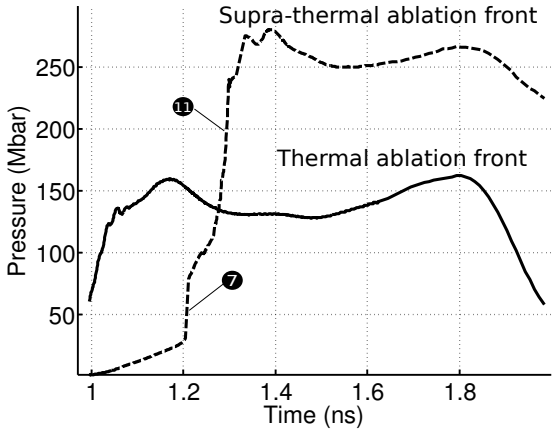

Figure 6.22: Pressure evolution at the laser driven and hot electron driven ablation fronts. The hot electrons parameters in this simulation are $\eta_{he} = 15\%$ and $\rho l_{he} = 10$ mg.cm^{-2}.

6.5 Discussion on the hot electron influence

We demonstrated in this chapter that the SSS shock timing measurements can be recovered in simulations with the hydro-radiative code CHIC if the laser beams are temporally and spatially smoothed. However, if the temporal smoothing is removed, the apparent ablation pressure needed to infer the experimental shock timing cannot be recovered using the collision absorption process (inverse Bremsstrahlung). In this case, one possibility to recover the experimental data is to include an energy deposition by hot electrons with the adjusted energy and range. According to this interpretation the hot electrons influence is negligible in the shot with SSD whereas it is more important without SSD.

6.5.1 Hot electron characterization in the experiments

Let us compare the energy carried by the hot electrons to the absorbed energy in these two shots.

In the shot # 69133, the total supra-thermal electrons energy measured is 500 J. The incident energy is 17 kJ with the experimental absorption coefficient of 52 % which means that the absorbed energy is 8.8 kJ. The hot electron energy represent 5.6 % of the absorbed energy. According to Figure 6.17, it is expected that the shock timing in the simulation would be modified by less than 60 ps if the hot electrons where accounted for. This is comparable to the experimental margin error and the hot electrons can be neglected in the simulation.

In the shot # 71597, the total measured supra-thermal electron energy measured is 2000 J. The incident energy is 26 kJ with the experimental absorption coefficient of 36.3 % which means that the absorbed energy is 9.4 kJ. The hot electrons carry 21 % of the absorbed energy. This is in agreement with the value needed in the simulations to recover the experimental shock timing.

The other free parameter adjusted in the simulation is the stopping range of the hot electrons. In the experiments, the energy distribution of hot electrons can be fitted by a Maxwellian distribution with central temperatures in the range 50-100 keV. In the CH this corresponds to a stopping range of the hot electrons between 2.7 mg.cm^{-2} and 10 mg.cm^{-2} [Ribeyre et al., 2013a] (see Figure 6.23). According to Figure 6.17, the experimental shock collapse time is recovered in the simulations with a hot electron stopping range between 5 mg.cm^{-2} and 9 mg.cm^{-2} if the energy conversion efficiency in hot electrons is 20 %. The parameters used in the simulation to interpret the experiment results are therefore consistent with the experimental data.

In this experimental campaign the observed yield of hot electrons seems to be strongly dependent on the laser beam smoothing. Both parametric instabilities TPD and SRS are dominant.

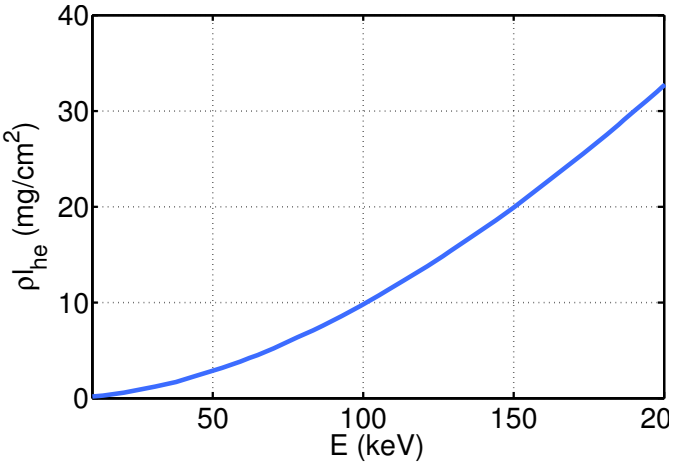

Figure 6.23: Hot electron stopping range in CH as a function of their energy [Ribeyre et al., 2013a].

6.5.2 Role of the hot electrons in shock dynamics

Let us consider how the shock dynamics is affected by the hot electrons. Figure 6.24 presents the evolution of spike pressure when varying the energy carried by the hot electrons (panel (a)) and the hot electron stopping range (panel (b)). The slope of the shock pressure at the beginning is steeper for a higher η_{he} and for a lower ρl_{he}. The influence of the total electron energy shown in panel (a) is obvious. The shock pressure increases with the quantity of energy deposited by hot electrons. The dependence of the electron stopping range is shown in panel (b). As the hot electron energy is deposited homogeneously per unit of mass, the specific energy deposited decreases as the range increases. The shock pressure increase stops as soon as the rarefaction wave interacts with it. The interaction with the rarefaction wave occurs at the same radius when the total energy is varied ($R = 150\mu m$). If the stopping range of hot electrons is shorter, the rarefaction wave is generated at a larger radius leading to an earlier interaction. Therefore, the maximal shock pressure before the interaction is higher when η_{he} or ρl_{he} increase. Later the shock pressure is affected by the interaction with the interface and by the coalescence with the first shock. Those processes seem to compensate each other and the shock pressure at the radius 100 μm is almost the same as the shock pressure before the interaction with the rarefaction wave.

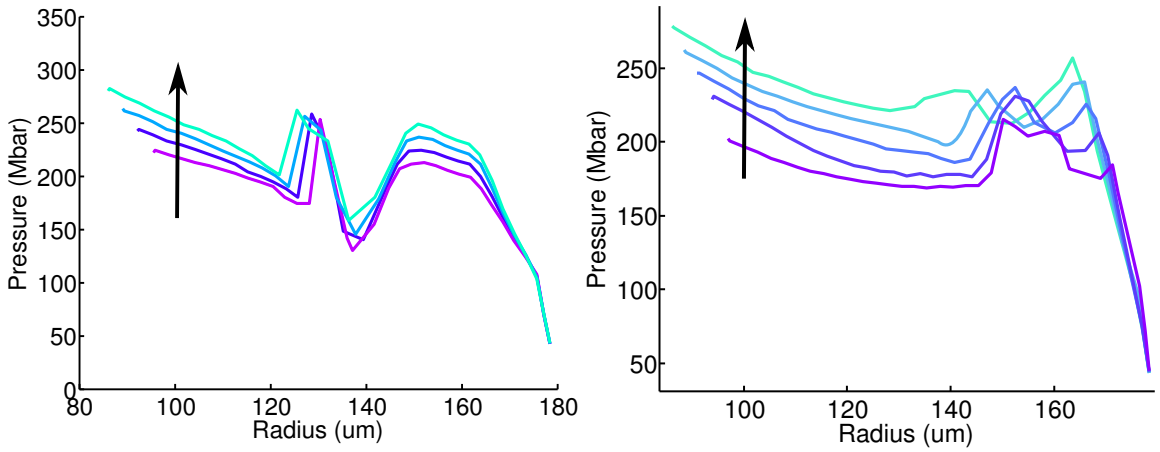

(a) (b)

Figure 6.24: Pressure evolution at the spike shock front. In panel (a) the percentage of the absorbed energy carried by the hot electrons varies from 7 % to 13 % with a constant stopping range $\rho l_{he} = 10$ mg.cm^{-2}. In panel (b) the hot electron stopping range varies from 4 to 7 mg.cm^{-2} with a constant conversion efficiency of $\eta_{he} = 15\%$.

6.6 Conclusion

In this experimental campaign, the ablation and shock pressures during the spike where studied in the spherical geometry for the shock ignition relevant laser intensity. With a temporal laser beam smoothing and an absorbed intensity of 1.7×10^{15} W.cm^{-2}, less than 5% of the absorbed energy was carried by the hot electrons. When the smoothing is removed and the laser spike power increased, the absorbed intensity remains at the same level even though the incident laser intensity is higher. The un-smoothed speckled structure of the laser beams leads to excitation of parametric instabilities and to the generation of a bigger quantity of hot electrons. With an absorbed intensity of 1.9×10^{15} W.cm^{-2}, 20% of the absorbed energy is carried by the hot electrons.

The apparent ablation pressure of these experiments evaluated in this chapter is presented in Figure 6.25. In the case where the hot electrons are not dominant, the ablation pressure follows the standard scaling law (6.1) corresponding to the collisional laser absorption. However, in the case of un-smoothed laser beams, the apparent ablation pressure is much higher than it is expected from the collisional absorption.

The real ablation pressure is lower than the apparent pressure, but the laser energy coupling to the shock is more efficient due to the presence of hot electrons, leading to a higher shock pressure than the ablation pressure.

When the hot electrons are taken into account, two shocks are generated during the spike. One is generated at the ablation front, due to the inverse Bremsstrahlung absorption. A second one is generated deeper in the target, near a second ablation front created by the hot electrons. Behind this second ablation front, a rarefaction wave is also generated and propagates outward.

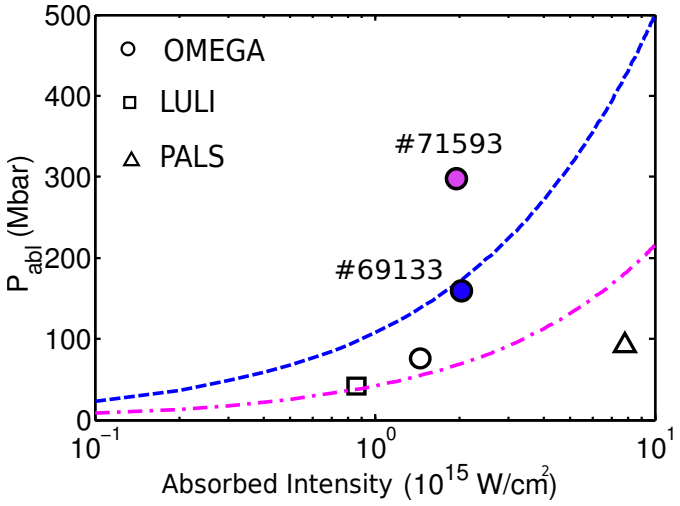

Figure 6.25: Apparent ablation pressure versus absorbed intensity for the shots # 69133 and # 71597.

The interaction between the first shock wave of gradually increasing pressure and the rarefaction wave seems to be the key point to determine the shock maximal pressure. Before the interaction, the shock pressure amplification is due to hot electron energy deposition. The pressure amplification is higher for low hot electron range and for high total hot electron energy. The time of the interaction between the rarefaction wave and the shock determines the time moment when the shock pressure amplification is stopped. This time depends on the range of the hot electrons. Larger is the range, longer is the time before the interaction.

The shock pressure is further perturbed by the interaction with the ablation front created by the hot electrons. Lastly it overtakes the hot electron driven shock. In addition to the hot electrons heating rate, the final shock pressure depends on three quantities: the strength of the rarefaction wave, the density ratio at the hot electron ablation front and on the strength of the two shocks before the coalescence.

The pressure of the shock generated by the hot electrons has been studied in References [Gus'kov et al., 2012, Ribeyre et al., 2013a, Piriz et al., 2013]. In our case, with 20 % of hot electron conversion efficiency, the dominant shock is still the shock created at the thermal ablation surface and not the shock created by the hot electrons. What is important in this case is the influence of the hot electrons on the dynamics of the spike shock.

The processes involved in the shock generation with two ablation fronts need to be analyzed more deeply, either numerically or analytically. To describe the spike shock dynamics, we suggest to use a shock dynamics equation like in Section 5.1.2 and to add a term accounting for the heating rate of the hot electrons.

In this Chapter, we assumed a homogeneous hot electron energy deposition. The shock dynamics could be different with a more realistic hot electron energy deposition and by taking into account the hot electron energy distribution. Also, we assumed that the hot electrons carry a fixed percentage of the absorbed energy during the whole spike duration. In reality, the hot

electrons may be generated only at the end of the spike pulse, where the pre-plasma temperature is high enough. This may change the shock dynamic analysis proposed here.

Moreover, the shell density profile may affect the hydrodynamic processes presented here. Let us consider the influence of the density value. If the shell density is higher, the same hot electron energy is deposited in a smaller volume, thus leading to a higher pressure increase. However, the ablation front created by the hot electrons in that case would be closer to the laser driven ablation front where the main shock is generated. Therefore, the interaction between the shock and the rarefaction wave occurs after a shorter time interval and the shock pressure amplification would be smaller. It is not obvious whether the shell density increase (like in SI conditions) would lead to the generation of a stronger shock.

The density gradient length at the quarter critical density measured in the simulations is $\sim 72\,\mu$m and $52\,\mu$m and the mean electron temperature in the corona is 1.8 keV and 720 eV, respectively, in the first and the second shot. This is rather different from the expected shock ignition conditions where the density gradient scale is $300\,\mu$m and the temperature is 3 keV in the corona.

It was demonstrated for the first time in the SSS experiments that an apparent ablation pressure close to 300 Mbar can be reached experimentally with an incident laser intensity of 7×10^{15} W.cm^{-2}. The hot electron had an important role in the getting of this result.

7 Conclusions and perspectives

The purpose of this thesis is to describe the evolution of the ignitor shock from its generation to the ignition of the fusion reactions. We summarize the work presented in this manuscript and discuss some possible future research directions relevant to this work.

Shock coupling to the hot-spot The ignitor shock must increase the hot-spot areal density and temperature up to the ignition conditions. In the flow created by a converging shock, the highest temperature and density appear behind the shock after its reflection at the center. Then, the product $\rho RT \propto pR$ increases as the shock diverges. The fusion reactions rate is proportional to the areal pressure pR. Therefore, the ignition is expected at the time when the ignitor shock exits the hot-spot. This time moment must occur before the target stagnation time. Otherwise, the fuel is no more confined and the ignition will not be followed by the combustion of cold fuel.

Condition A : The time of ignition, when the ignitor shock exits the hot-spot, must occur before the stagnation time.

To express the shock ignition conditions, one needs to describe the entire flow in the hot-spot during the convergence and the divergence phase of the ignitor shock. The hot-spot is already compressed and pre-heated when the ignitor shock enters in it. The upstream temperature T_0 is not negligible and the shock Mach number $M_{s0} = U_{s0}/c_0$ is relatively low. The ignitor shock propagation in the hot-spot is described in Chapter 4 with an extension of the self-similar solution of Guderley by adding a correction term proportional to ${M_s}^{-2}$.

The finite Mach number correction shows that the ignitor shock coupling efficiency to the hot-spot is reduced for a low initial shock Mach number.

This means that, for a given initial shock velocity, the higher the temperature is in the hot-spot, before the ignitor shock-arrival, the lower the final hot-spot pressure will be. An ignition

criterion based on the alpha-particle power gain as well as the conduction and the radiation losses is expressed in Section 4.3. This criterion gives the minimal shock velocity $(U_s)_{ign}$ and the minimal hot-spot areal density $(\rho R)_{ign}$ depending on the shock Mach number M_{s0}.

Condition B : For a given initial shock Mach number M_{s0}, the ignition conditions are $U_{s0} > (U_s)_{ign}$ and $\rho_0 R_0 > (\rho R)_{ign}$ (Figure 4.18).

For an infinite shock Mach number, the ignition conditions are $(U_s)_{ign} = 650$ km.s^{-1} and $(\rho R)_{ign} = 15$ mg.cm^{-2}. However, in a typical SI simulation, the hot-spot temperature when the ignitor shock arrives is around $2-4$ keV. The ignitor shock Mach number is therefore $M_{s0} < 3$. Our model is valid only for a shock Mach number $M_{s0} > 4$. In the limit of our model domain of validity $M_{s0} = 4$, the ignition conditions are $(U_s)_{ign} = 750$ km.s^{-1} and $(\rho R)_{ign} = 20$ mg.cm^{-2}. Both the hot-spot areal density and initial shock velocity threshold values are increased when the initial shock Mach number is finite.

Let us consider the limit case of condition (A), where the ignitor shock exits the hot-spot at the radius R_{stag} at the stagnation time. According to condition (B), the ignition is possible only if the hot-spot areal density is higher than $(\rho R)_{ign}$ when the shock enters in the hot-spot. According to Table 4.7 the radius of the shell at the shock entrance is $R_0 \sim 3R_{stag}$. Another way to express condition (B) is that the hot-spot areal density must be higher than $(\rho R)_{ign}$ when the shell radius is $R_0 \sim 3R_{stag}$.

Now let us consider that no shock is launched and that the target follows a homogeneous isentropic compression during the deceleration phase (Section 3.2). If the condition (B) is fulfilled, the hot-spot areal density at the stagnation time is $(\rho R)^{noshock}_{stag} = (R_0/R_{stag})^2 (\rho R)_{ign} \sim 9(\rho R)_{ign}$.

Condition C : The ignition with a shock is possible only if the areal density at the stagnation time without shock is $(\rho R)^{noshock}_{stag} > 9(\rho R)_{ign}$.

According to [Zhou and Betti, 2007], the hot-spot areal density at stagnation, without ignitor shock can be estimated as

$$(\rho R)^{noshock}_{stag}[\text{g.cm}^{-2}] \simeq \frac{0.31}{\alpha_{if}^{0.55}} \left(\frac{\text{u}_{\text{imp}}[\text{ cm.s}^{-1}]}{3\times 10^7}\right)^{0.62} \left(\frac{E_L[\text{kJ}]}{100}\right)^{0.27} \left(\frac{0.35}{\lambda_{[\mu\text{m}]}}\right)^{0.5}. \tag{7.1}$$

For a fixed in flight shell adiabat and compression pulse energy, the minimal implosion velocity u_{ign} for shock ignition to be possible is determined by the threshold $(\rho R)^{noshock}_{stag} = 9(\rho R)_{ign}$.

For example, with the HiPER baseline target design $\alpha_{if} \sim 1.3$, $E_L \sim 100$ kJ, $\lambda_L = 351$ nm [Atzeni et al., 2011], the minimal implosion velocity is $u_{ign} = 200$ km.s^{-1}. This value has to be compared to the limit value 250 km.s^{-1} under which no gain is observed in the simulations

[Atzeni et al., 2011, Lafon et al., 2013] (see Figure 1.16 in Section 1.4).

The condition C defines the assembly phase for the shock ignition to be possible. However, the ignitor shock must also have the minimum velocity needed. It is more significant to express condition B in terms of the minimal shock pressure when it enters the hot-spot (Figure 4.19). The condition on the shock pressure depends on the hot-spot areal density and on the hot-spot radius. For an initial shock Mach number $M_{s0} = 4$, the minimal shock pressure is given by $(P_sR)_{min} = 100$ Mbar.cm at the minimal hot-spot areal density $\rho R_{min} = 20$ mg.cm^{-2}. For a higher initial hot-spot areal density, the ignition threshold $(P_s)_{ign}R_0$ is proportional to the areal density $\rho_0 R_0$.

Condition D : For a given initial shock Mach number M_{s0}, the ignition conditions are $P_{s0}R_0 > (P_sR)_{min}(\rho_0 R_0/(\rho R)_{ign})$, $\rho_0 R_0 > (\rho R)_{ign}$ (Figure 4.19).

Let us consider the limit case where the hot-spot areal density at stagnation is $(\rho R)^{noshock}_{stag} = 9(\rho R)_{ign}$. The minimal shock pressure in this limit case is $(p_s)_0 = (P_sR)_{min}/R_0$, where R_0 is the shell radius when $\rho_0 R_0 = (\rho R)_{ign}$.
If we increase the areal density at stagnation $(\rho R)^{noshock}_{stag} > 9(\rho R)_{ign}$ without changing the convergence ratio. Then, the ignitor shock can enter the hot-spot at the shell radius $R'_0 > R_0$ where the hot-spot areal density is $\rho'_0 R'_0 = (\rho R)_{ign}$. In this case, the minimal ignitor shock pressure required for the ignition is reduced to $(P_sR)_{min}/R'_0$.

If we take $R_0 = 50\,\mu$m as a reasonable value of the hot-spot radius when $\rho_0 R_0 = (\rho R)_{ign}$, an estimate of the ignition shock pressure when it enters the hot-spot is $(p_s)_{ign} = 20$ Gbar with a shock Mach number $M_{s0} = 4$.

Nowadays, it is not possible to generate directly such a pressure, so the amplification of the shock pressure in the shell is a key process for shock ignition. It has been described in Chapter 5 of this thesis.

Shock pressure amplification in the shell We make a distinction between the shock pressure amplification $\mathcal{X}$ - which relates to the final pressure of the shock to its initial pressure - and the shock strengthening - which accounts for the change in the shock strength $Z = p_s/p_0$ where p_s is the shock pressure and p_0 is the upstream pressure.

We have demonstrated in Chapter 5, that the shock pressure amplification is not only due to the convergence effect as it is often said in the literature.

The shock pressure amplification in the shell $\mathcal{X}$ depends on three factors $\mathcal{X} = \mathcal{X}_{imp}\mathcal{X}_{shell}\mathcal{X}_{coll}$.

The factor $\mathcal{X}_{imp}$ corresponds to the overall pressure amplification in the shell during its

implosion. If the shock enters in the hot-spot close to the stagnation time, this factor is dominant and can reach values of order 50. The final pressure in the hot-spot (2.48) - without an ignitor shock - is $p_h^{noshock} \propto \mathrm{M}^{5/2}\mathrm{u}_{\mathrm{imp}}^5$. Therefore, we expect the overall pressure amplification to be more significant for a higher implosion velocity and a bigger shell mass.

The factor $\mathcal{X}_{shell}$ is calculated in the shell comoving frame. It depends on the shell density and pressure profiles, on the shell aspect ratio and on the shock initial strength. A shell parameter $\mathcal{K}$ has been defined to characterize the shell pressure gradient which is related to its acceleration.

When the shell is accelerated $\mathcal{K}$ is positive and the shock pressure decreases in the shell comoving frame. When the shell is decelerated $\mathcal{K}$ is negative and the shock pressure increases in the shell comoving frame.

Close to the stagnation time, $\mathcal{X}_{shell}$ has a positive effect on the shock pressure but it is not dominant compared to $\mathcal{X}_{imp}$. On the contrary, if the shock propagates only in an accelerated shell, $t_f < t_d$, the factor is $\mathcal{X}_{shell} < 1$. In this case, if the factor $\mathcal{X}_{imp}$ is not high enough to compensate the pressure decrease in the comoving frame, the ignitor shock pressure in the laboratory frame is not amplified.

The ignitor shock must enter the hot-spot during the shell deceleration phase.

Then, the shock collides with a diverging shock coming from the assembly phase. The amplification factor $\mathcal{X}_{coll}$ describes the shock pressure amplification through the collision. During almost all the deceleration phase, the returning shock strength is almost constant and below 3 in a typical HiPER implosion. Then the shock pressure amplification in the collision is $\mathcal{X}_{coll} \sim 2$.

These three amplification factors were computed with the implosion parameters of a typical SI implosion. It was demonstrated that an amplification of the shock pressure by a factor higher than 100 is possible.

The shock pressure amplification is very sensitive to the shock timing. It increases for later spike times.

The shock strength Z is another important parameter considered for the ignition. It depends on the shock Mach number as $Z \propto M_s^2$ and is therefore important for the shock coupling efficiency to the hot-spot according to Chapter 4.

The shock strengthening depends on : (1) the initial shock strength Z_i; (2) the shell pressure profile; (3) the shell aspect ratio $\mathcal{A}$.

The shock strengthening depends on the shock dynamics in the shell comoving frame. There is no dependency on the shock propagation time in the shell.

The shell pressure profile is characterized by the parameter $\mathcal{K}$. The shock strength increases only in the accelerated part of the shell where $\mathcal{K} > 0$. The shell parameter $\mathcal{K}$ is time dependent. Its value at the beginning of the acceleration phase t_{sb} is proportional to the square of the shell maximal Mach number $\mathcal{K}_{sb} \propto \mathcal{M}_0^2$ in typical implosion simulations. After that time, its value decreases. The earlier is launched the shock, the higher will be its strengthening. The strengthening can be improved by increasing the shell Mach number $\mathcal{M}_0^2 \propto u_{imp}^2 {p_a}^{-2/5} \alpha^{-3/5}$. One can either choose to increase the implosion velocity or to reduce the ablation pressure during the main pulse or to reduce the shell adiabat.

The shock strength is reduced in the collision with the returning shock. Therefore, if the strength of the returning shock is too high, it can inhibit the ignition. According to Ref. [Lafon et al., 2013], the returning shock strength scales as the square of the implosion velocity similarly to the scaling of the shell parameter $\mathcal{K}$. So we expect that modifying the implosion velocity would not change the shock strengthening in the shell.

If the shock is launched too early, its pressure is weakly amplified and can even decrease. If the shock is launched too late, its strength when it enters the hot-spot is too low, increasing the ignition conditions.

The time window where both the final shock strength and pressure are high enough defines the ignition window for shock ignition.

In Chapter 5, we proposed a theory that predicts quantitatively the shock strengthening and the shock pressure amplification in the shell. By using the parameters values measured in typical implosion simulations, we have obtained a good agreement with simulation results. Therefore, the proposed theory can be used to interpret simulations. To have a fully predictive model, further research is needed to express the model parameters with the assembly phase parameters. Then, one should be able to couple the theory of the shock strengthening and pressure amplification of Chapter 5 with the ignition criterion theory given in Chapter 4.

With the shell parameters considered in our analysis, the ignitor shock pressure can be amplified by a factor greater than 50 in the shell. Knowing the minimal shock pressure in order to reach ignition ($(p_s)_{ign} = 20$ Gbar), we estimate the minimal shock pressure to be 400 Mbar at its generation at the outer edge of the shell. This is in agreement with the values given in the literature. This brings us to the point assessed in Chapter 6 : the experimental shock generation with SI relevant conditions.

Shock pressure generation In Chapter 6, the ablation and shock pressures are analyzed for the shock ignition relevant experimental conditions where the laser intensities are higher than the parametric instabilities threshold. We show that generation of fast electrons may explain the high shock pressures observed in experiments.

We analyzed two shots of the Strong Spherical Shock campaign performed on the OMEGA laser facility [Theobald et al., 2013]. The ablation and shock pressures were estimated from the

delay time of the X-ray flash coming from the target center corresponding to the shock collapse. The numerical simulations are constrained by both the experimental absorption energy and the shock collapse time.

A first shot performed with an incident laser energy of 17 kJ with SSD smoothed beams can be explained by the classical Bremsstrahlung absorption. The inferred maximal ablation pressure during the spike is 180 Mbar and the initial shock pressure is 162 Mbar.

A second shot performed at higher energy (26 kJ) and without SSD showed a higher generated shock pressure. Whereas the incident laser intensity is 30 % higher than in the previous case, the absorbed intensity remained almost the same. This shot cannot be interpreted with a simulation accounting for the collisional laser energy absorption only. The experimental data can be recovered if the hot electron energy deposition is taken into account. We implemented a basic model of hot electrons in the simulation code CHIC where a mono-energetic source of hot electrons deposits homogeneously a part of the absorbed laser energy in the hot electron stopping range. The experimental shock timing is recovered with 20% of the laser absorbed energy carried by the hot electrons with energies in the range 50-100 keV.

The hot electrons must be taken into account to recover the experimental data if their energy is > 50 keV and if they carry about 20% of the laser absorbed energy.

It is shown that hot electrons produce significant changes in the shock formation dynamics.

In a simulation with hot electrons, two shocks are generated during the spike : one at the laser ablation front and one at the hot electron ablation front.

The dominant shock is generated at the thermal ablation front and is driven by both the collisional absorption and the hot electron energy deposition. Its pressure increases quickly up to 275 Mbar. The shock pressure increase is stopped by the interaction with a diverging rarefaction wave created at the hot electron ablation front. This time moment depends on the distance between the two ablation fronts, therefore on the stopping range of the hot electrons. Furthermore, the shock pressure is affected by the interaction with the hot electron ablation front and with the coalescence with the hot electron driven shock wave.

The shock pressure generation phase is highly sensitive to four processes : (1) the hot electron energy deposition, (2) the rarefaction wave created at the hot electron ablation surface, (3) the shock interaction with the hot electron ablation front and (4) the shock coalescence with the hot electron driven shock.

We discussed the experimental results assuming a homogeneous hot electron energy deposition. The shock dynamics could be different with a more realistic hot electron energy deposition and that may change the shock dynamic analysis proposed here. Moreover, the shell density

profile in an imploding shell is different from the density profile in the experiments considered here. Also, the laser/plasma interaction in the present experiments is not completely relevant to the shock ignition implosion (lower temperature and density gradient length). Therefore, the results of the SSS campaign cannot be extrapolated to the real shock ignition conditions in a straightforward manner.

In the case where the hot electron energy deposition is important, one can express the minimum shock pressure needed for ignition at the position where the laser driven shock and the hot electron shock coalesce. Then, the relevant metric for shock ignition is the *apparent* ablation pressure. It corresponds to the ablation pressure in a simulation without hot electrons to have the same shock pressure at the same position.

For the first time, it has been shown that an apparent ablation pressure of 300 Mbar can be reached experimentally.

This is close to the ignition condition of 400 Mbar evaluated by combining the results of Chapter 4 and 5. Here, more theoretical studies are needed to quantify the shock dynamics before the coalescence of the laser driven shock and the hot electron driven shock. Both hydrodynamic and kinetic approaches may be required. Also more experiments are needed to explore the analysis given here. For example the influence of the shell density may be seen by using different ablators. The hot electrons stopping range and energy should be experimentally controlled. The influence of the beam smoothing and the pre-plasma density gradient length on the hot electron generation should be understood more accurately.

More general perspectives In this thesis, we proposed two simplified analytical theories to describe the shock propagation in the hot-spot and in the shell. Those theories depend on the assembly phase through: the hot-spot areal density and temperature at the ignitor shock entrance, the shell pressure gradient and aspect ratio at the spike time, the returning shock strength. Those quantities should be expressed depending on the assembly phase parameter. Then, by coupling the two theories proposed here, one may be able to express the energy gain of the target and to optimize the target design. This should be compared to the work done in Refs. [Lafon et al., 2013, Atzeni et al., 2011, Atzeni et al., 2013].

On the NIF or LMJ facilities, the shock ignition scheme would require a depointing of the laser beams which are initially designed for indirect drive. The global laser irradiation non-uniformity as well as the focal spots non-uniformities may lead to a high hot electrons yield. This justifies the need to investigate better the shock generation in the presence of hot electrons. Also, as the shock would be non uniform, the 3D effects should be analyzed. A recent paper [Davie et al., 2014] indicates that the shock is stable even under strong perturbations.

One can consider the extreme case where the ignitor shock is generated by only two beams. According to numerical simulations [Ribeyre et al., 2009] the ignition can be reached in this case. Both analytical and numerical studies should be interesting on that topic.

We remark that in the case of a strongly non uniform laser irradiation, a self-generated magnetic fields may be advected by the ignitor shock and be amplified by the convergence effect. This may have an influence on the ignition conditions, for example by confining the alpha-particles in the hot-spot [Hohenberger et al., 2012].

The brief overview of potential future research presented in this chapter, while not exhaustive, gives an indication of non answered questions remaining in the field of shock ignition.

Appendix A

The simulation setup for the SSS campaign.

Laser beams

- wave length : 351 nm
- rays number : 500
- power law : experimental data
- focal spot : n=4 super-Gaussian of diameter 300 μm.

Mesh grid

- symmetry : cylindrical
- zone 1 dimension : 165 μm
- zone 2 dimension : 50 μm
- zone 1 meshes number : 300
- zone 2 meshes number : 200

Materials

- zone 1 : CHTi SESAME
  composition C : 27.6 %, H: 42.8 %, O : 24.3 %, Ti : 0.53 %
- zone 1 initial density : 1.47 g.cm^{-3}
- zone 2 : CH SESAME
  composition C : 50 %, H : 50 %
- zone 2 initial density : 1.05 g.cm^{-3}

Radiation

- number of groups : 30
- maximal energy : 30 keV

Flux limiter on

- value : input parameter

Bi temperature on

Conduction on

References

[LLE, 2006] (2006). Basic principles of direct-drive ignition target design. *LLE review*, 106:83–89. 50

[Alejaldre et al., 1990] Alejaldre, C., Gozalo, J. J. A., Perez, J. B., Magaña, F. C., Diaz, J. R. C., Perez, J. G., Lopez-Fraguas, A., García, L., Krivenski, V. I., Martin, R., et al. (1990). Tj-ii project: a flexible heliac stellarator. *Fusion Science and Technology*, 17(1):131–139. 8

[Anderson and Betti, 2004] Anderson, K. and Betti, R. (2004). Laser-induced adiabat shaping by relaxation in inertial fusion implosions. *Physics of Plasmas (1994-present)*, 11(1):5–8. 53, 57

[Anderson et al., 2013] Anderson, K., Betti, R., McKenty, P., Collins, T., Hohenberger, M., Theobald, W., Craxton, R., Delettrez, J., Lafon, M., Marozas, J., et al. (2013). A polar-drive shock-ignition design for the national ignition facilitya). *Physics of Plasmas (1994-present)*, 20(5):056312. 23, 27

[Anderson et al., 1958] Anderson, O. A., Baker, W. R., Colgate, S. A., Ise, J., and Pyle, R. V. (1958). Neutron Production in Linear Deuterium Pinches. *Physical Review*, 110:1375–1387. 9

[Aston, 1920] Aston (1920). The mass-spectra of chemical elements. *Philosophical Magazine and Journal of Science*, 39:611–625. 10

[Atkinson and Houtermans, 1929] Atkinson, R. D. E. and Houtermans, F. G. (1929). Zur frage der aufbaumöglichkeit der elements in sternen. *Zeitschrift für Physik*, 54:656. 10

[Atzeni, 2013] Atzeni, S. (2013). *Inertial Confinement Fusion with Advanced Ignition Schemes: Fast Ignition and Shock Ignition*. Springer. 54

[Atzeni et al., 2008] Atzeni, S., Bellei, C., Davies, J., Evans, R., Honrubia, J., Nicolaï, P., Ribeyre, X., Schurtz, G., Schiavi, A., Badziak, J., et al. (2008). Fast ignitor target studies for hiper. *Journal of Physics: Conference Series*, 112(2):022062. 161

[Atzeni et al., 2009] Atzeni, S., Davies, J., Hallo, L., Honrubia, J., Maire, P., Olazabal-Loumé, M., Feugeas, J., Ribeyre, X., Schiavi, A., Schurtz, G., et al. (2009). Studies on targets for inertial fusion ignition demonstration at the hiper facility. *Nuclear Fusion*, 49(5):055008. 23

[Atzeni et al., 2013] Atzeni, S., Marocchino, A., Schiavi, A., and Schurtz, G. (2013). Energy and wavelength scaling of shock-ignited inertial fusion targets. *New Journal of Physics*, 15(4):045004. 19, 23, 25, 27, 215

[Atzeni and Meyer-Ter-Vehn, 2004] Atzeni, S. and Meyer-Ter-Vehn, J. (2004). *The Physics of Inertial Fusion: Beam Plasma Interaction, Hydrodynamics, Hot Dense Matter*. Oxford science publications, international series of monographs on physics edition. 3, 4, 32, 33, 35, 38, 45, 46, 52, 90, 132

[Atzeni et al., 2014] Atzeni, S., Ribeyre, X., Schurtz, G., Schmitt, A., Canaud, B., Betti, R., and Perkins, L. (2014). Shock ignition of thermonuclear fuel: principles and modelling. *Nuclear Fusion*, 54(5):054008. 18

[Atzeni et al., 2011] Atzeni, S., Schiavi, A., and Marocchino, A. (2011). Studies on the robustness of shock-ignited laser fusion targets. *Plasma Physics and Controlled Fusion*, 53(3):035010. 23, 24, 25, 26, 27, 210, 211, 215

[Axford and Holm, 1981] Axford, R. and Holm, D. (1981). Converging finite-strength shocks. *Physica D: Nonlinear Phenomena*, 2(1):194 – 202. 95

[Basov et al., 1975] Basov, N., Krokhin, O., Pustovalov, V., Rupasov, A., Silin, V., Sklizkov, G., Tikhonchuk, V., and Shikanov, A. (1975). Anomalous interaction of strong laser radiation with dense plasma. *JETP*, 40:61. 11

[Batani et al., 2014] Batani, D., Baton, S., Casner, A., Depierreux, S., Hohenberger, M., Klimo, O., Koenig, M., Labaune, C., Ribeyre, X., Rousseaux, C., Schurtz, G., Theobald, W., and Tikhonchuk, V. (2014). Physics issues for shock ignition. *Nuclear Fusion*, 54(5):054009. 18

[Baton et al., 2012] Baton, S., Koenig, M., Brambrink, E., Schlenvoigt, H., Rousseaux, C., Debras, G., Laffite, S., Loiseau, P., Philippe, F., Ribeyre, X., et al. (2012). Experiment in planar geometry for shock ignition studies. *Physical review letters*, 108(19):195002. 179

[Becquerel, 1896] Becquerel, H. (1896). Sur les radiations émises par phosphorescence. *Comptes rendus de l' Académie des Sciences Paris*, 122:420. 9

[Betti et al., 2008] Betti, R., Theobald, W., Zhou, C. D., Anderson, K. S., McKenty, P. W., Skupsky, S., Shvarts, D., Goncharov, V. N., Delettrez, J. A., Radha, P. B., Sangster, T. C.,

Stoeckl, C., and Meyerhofer, D. D. (2008). Shock ignition of thermonuclear fuel with high areal densities. *Journal of Physics: Conference Series*, 112(2):022024. 23

[Betti et al., 2007] Betti, R., Zhou, C., Anderson, K., L.J., P., Theobald, W., and Solodov, A. (2007). Shock ignition of thermonuclear fuel with high areal density. *Phys Rev Lett.*, 98(15):155001. 18, 19, 23, 54

[Braams and Stott, 2002] Braams, C. and Stott, P. (2002). *Nuclear Fusion , Half a century of magnetic confinement fusion research.* Institute of Physics Publising, Bristol. 7

[Bradley et al., 1992] Bradley, D., Bell, P., Kilkenny, J., Hanks, R., Landen, O., Jaanimagi, P., McKenty, P., and Verdon, C. (1992). High-speed gated x-ray imaging for icf target experiments. *Review of scientific instruments*, 63(10):4813–4817. 182

[Brueckner and Jorna, 1974] Brueckner, K. A. and Jorna, S. (1974). Laser-driven fusion. *Rev. Mod. Phys.*, 46:325–367. 32

[Brushlinskii and Kazhdan, 1963] Brushlinskii, K. V. and Kazhdan, J. M. (1963). On auto-models in the solution of certain problems of gaz dynamics. *Russ. Math. Surv.*, 18(1). 92

[Butler, 1954] Butler, D. (1954). Converging spherical and cylindrical shocks. Technical Report 54, UK Armament Res. Estab. 92

[Canaud and Temporal, 2010] Canaud, B. and Temporal, M. (2010). High-gain shock ignition of direct-drive icf targets for the laser mégajoule. *New Journal of Physics*, 12(4):043037. 23, 24, 25, 26

[Chadwick, 1932] Chadwick, J. (1932). Possible existence of a neutron. *Nature*, 129(3252):312. 10

[Chandrasekhar, 1957] Chandrasekhar, S. (1957). *An Introduction to the Study of Stellar Structure.* Dover publications, dover books in physics,engineering edition. 70

[Chen et al., 2008] Chen, C., King, J., Key, M., Akli, K., Beg, F., Chen, H., Freeman, R., Link, A., Mackinnon, A., MacPhee, A., et al. (2008). A bremsstrahlung spectrometer using k-edge and differential filters with image plate dosimetersa). *Review of Scientific Instruments*, 79(10):10E305. 183

[Chester, 1954] Chester, W. (1954). The quasi-cylindrical shock tube. *Phil. Mag.*, 45(7):1293–1301. 93

[Chisnell, 1957] Chisnell, R. (1957). The motion of a shock wave in a channel, with applications to cylindrical and spherical shock waves. *Journal of Fluid Mechanics*, 2(03):286–298. 93

[Chisnell, 1997] Chisnell, R. F. (1997). An analytic description of converging shock waves. *Journal of Fluid Mechanics*, 354:357–375. 93

[Clery, 2013] Clery, D. (2013). *A Piece of the Sun: The Quest for Fusion Energy*. Overlook Duckworth. 10

[Coggeshall and Axford, 1986] Coggeshall, S. V. and Axford, R. A. (1986). Lie group invariance properties of radiation hydrodequations and their associated similarity solutions. *Physics of Fluids*, 29(8):1986–2420. 89

[Curie, 1898] Curie, M. (1898). Rayons émis par les composes de l'uranium et du thorium. *Comptes rendus de l' Académie des Sciences Paris*, 126:1101–1103. 9

[Dautray and Watteau, 1993] Dautray, R. and Watteau, J.-P. (1993). *La fusion thermonucléaire inertielle par laser*. Eyrolles, la fusion par confinement inertiel edition. 40, 178

[Davie et al., 2014] Davie, C. J., Bush, I. A., and Evans, R. G. (2014). Stability of shocks relating to the shock ignition inertial fusion energy scheme. *Physics of Plasmas (1994-present)*, 21(8):–. 215

[Depierreux et al., 2009] Depierreux, S., Labaune, C., Michel, D., Stenz, C., Nicolaï, P., Grech, M., Riazuelo, G., Weber, S., Riconda, C., Tikhonchuk, V., et al. (2009). Laser smoothing and imprint reduction with a foam layer in the multikilojoule regime. *Physical review letters*, 102(19):195005. 53

[Drake et al., 1984] Drake, R. P., Turner, R. E., Lasinski, B. F., Estabrook, K. G., Campbell, E. M., Wang, C. L., Phillion, D. W., Williams, E. A., and Kruer, W. L. (1984). Efficient raman sidescatter and hot-electron production in laser-plasma interaction experiments. *Phys. Rev. Lett.*, 53:1739–1742. 178

[Durrell et al., 2014] Durrell, J. H., Dennis, A. R., Jaroszynski, J., Ainslie, M. D., Palmer, K. G. B., Shi, Y.-H., Campbell, A. M., Hull, J., Strasik, M., Hellstrom, E. E., and Cardwell, D. A. (2014). A trapped field of 17.6 t in melt-processed, bulk gd-ba-cu-o reinforced with shrink-fit steel. *Superconductor Science and Technology*, 27(8):082001. 8

[Dyke and Guttmann, 1982] Dyke, M. and Guttmann, A. J. (1982). The converging shock wave from a spherical or cylindrical piston. *Journal of Fluid Mechanics*, 120:451–462. 94

[Eddington, 1920] Eddington, A. S. (1920). The internal constitution of the stars. *Observatory*, 43:353. 10

[Fratanduono et al., 2011] Fratanduono, D., Boehly, T., Celliers, P., Barrios, M., Eggert, J., Smith, R., Hicks, D., Collins, G., and Meyerhofer, D. (2011). The direct measurement of ablation pressure driven by 351-nm laser radiation. *Journal of Applied Physics*, 110(7):073110. 178

[Fujimoto and Mishkin, 1978] Fujimoto, Y. and Mishkin, E. A. (1978). Analysis of spherically imploding shocks. *Physics of Fluids*, 21(11):1933–1938. 93

[Fujioka et al., 2004] Fujioka, S., Sunahara, A., Ohnishi, N., Tamari, Y., Nishihara, K., Azechi, H., Shiraga, H., Nakai, M., Shigemori, K., Sakaiya, T., et al. (2004). Suppression of rayleigh-taylor instability due to radiative ablation in brominated plastic targets. *Physics of Plasmas (1994-present)*, 11(5):2814–2822. 53

[Gamow, 1928] Gamow, G. (1928). Zur quantentheorie der atomzertrümmerung. *Zeitschrift für Physik*, 52:510. 10

[Guderley, 1942] Guderley, V. G. (1942). Strake kugelige und zylindrische verdichtungsstöe in der nähe des kugelmittelpunktes bzw. des zylinderachse. *Luftfahrtforschung*, 19:302–312. 91

[Gus'kov et al., 2012] Gus'kov, S., Ribeyre, X., Touati, M., Feugeas, J.-L., Nicolaï, P., and Tikhonchuk, V. (2012). Ablation pressure driven by an energetic electron beam in a dense plasma. *Physical review letters*, 109(25):255004. 23, 206

[Haan et al., 2011] Haan, S., Lindl, J., Callahan, D., Clark, D., Salmonson, J., Hammel, B., Atherton, L., Cook, R., Edwards, M., Glenzer, S., et al. (2011). Point design targets, specifications, and requirements for the 2010 ignition campaign on the national ignition facility. *Physics of Plasmas*, 18(5):051001. 15

[Hahn and Strassmann, 1939] Hahn, O. and Strassmann, F. (1939). Concerning the existence of alkaline earth metals resulting from neutron irradiation of uranium. *Die Naturwissenschaften*, 27:11–15. 10

[Haines, 2011] Haines, M. G. (2011). A review of the dense z -pinch. *Plasma Physics and Controlled Fusion*, 53(9):093001. 9

[Hayes, 1968] Hayes, W. D. (1968). Self-similar strong shocks in an exponential medium. *Journal of Fluid Mechanics*, 32(02):305–315. 94

[Hazeltine and Meiss, 2003] Hazeltine, R. D. and Meiss, J. (2003). *Plasma Confinement*. Dover Books on Physics. Dover Publications. 7

[Hohenberger et al., 2012] Hohenberger, M., Chang, P.-Y., Fiksel, G., Knauer, J., Betti, R., Marshall, F., Meyerhofer, D., Séguin, F., and Petrasso, R. (2012). Inertial confinement fusion implosions with imposed magnetic field compression using the omega lasera). *Physics of Plasmas (1994-present)*, 19(5):056306. 216

[Hohenberger et al., 2014] Hohenberger, M., Theobald, W., Hu, S., Anderson, K., Betti, R., Boehly, T., Casner, A., Fratanduono, D., Lafon, M., Meyerhofer, D., et al. (2014). Shock-ignition relevant experiments with planar targets on omega. *Physics of Plasmas (1994-present)*, 21(2):022702. 179

[Hornung et al., 2008] Hornung, H. G., Pullin, D. I., and Ponchaut, N. F. (2008). On the question of universality of imploding shock waves. *Acta Mechanica*, 201(1-4):31–35. 95

[Hunter, 1960] Hunter, C. (1960). On the collapse of an empty cavity in water. *Journal of Fluid Mechanics*, 8:241–263. 95

[Hurricane et al., 2014] Hurricane, O., Callahan, D., Casey, D., Celliers, P., Cerjan, C., Dewald, E., Dittrich, T., Döppner, T., Hinkel, D., Hopkins, L. B., et al. (2014). Fuel gain exceeding unity in an inertially confined fusion implosion. *Nature*. 15

[Hydon, 2000] Hydon, P. (2000). *Symmetry Methods for Differential Equations*. Cambridge University press, cambridge texts in applied mathematics edition. 89

[Kemp et al., 2001] Kemp, A., Meyer-ter Vehn, J., and Atzeni, S. (2001). Stagnation pressure of imploding shells and ignition energy scaling of inertial confinement fusion targets. *Physical review letters*, 86(15):3336. 21, 56

[Kidder, 1976] Kidder, R. (1976). Laser-driven compression of hollow shells: power requirements and stability limitations. *Nuclear Fusion*, 16(1):3. 43, 73, 143

[Klimo et al., 2010] Klimo, O., Weber, S., Tikhonchuk, V. T., and Limpouch, J. (2010). Particle-in-cell simulations of laser–plasma interaction for the shock ignition scenario. *Plasma Physics and Controlled Fusion*, 52(5):055013. 23, 178, 195

[Koester et al., 2013] Koester, P., Antonelli, L., Atzeni, S., Badziak, J., Baffigi, F., Batani, D., Cecchetti, C., Chodukowski, T., Consoli, F., Cristoforetti, G., et al. (2013). Recent results from experimental studies on laser-plasma coupling in a shock ignition relevant regime. *Plasma Physics and Controlled Fusion*, 55(12):124045. 179

[Krokhin and Rozanov, 1973] Krokhin, O. N. and Rozanov, V. B. (1973). Escape of alpha particles from a laser-pulse-initiated thermonuclear reaction. *Soviet Journal of Quantum Electronics*, 2(4):393. 132

[Lafon et al., 2010] Lafon, M., Ribeyre, X., and Schurtz, G. (2010). Gain curves and hydrodynamic modeling for shock ignition. *Physics of Plasmas (1994-present)*, 17(5):052704. 21

[Lafon et al., 2013] Lafon, M., Ribeyre, X., and Schurtz, G. (2013). Optimal conditions for shock ignition of scaled cryogenic deuterium-tritium targets. *Physics of Plasmas (1994-present)*, 20(2):022708. 21, 22, 24, 25, 142, 158, 211, 213, 215

[Landen et al., 2012] Landen, O., Benedetti, R., Bleuel, D., Boehly, T., Bradley, D., Caggiano, J., Callahan, D., Celliers, P., Cerjan, C., Clark, D., et al. (2012). Progress in the indirect-drive national ignition campaign. *Plasma Physics and Controlled Fusion*, 54(12):124026. 15

[Lawson, 1957] Lawson, J. D. (1957). Some criteria for a power producing thermonuclear reactor. *Proceedings of the Physical Society. Section B*, 70(1):6. 5

[Lazarus, 1981] Lazarus, R. B. (1981). Self-similar solutions for converging shocks and collapsing cavities. *Society for Industrial and Applied Mathematics J. Numer. Anal.*, 18(2). 92, 112

[Lazarus and Richtmyer, 1977] Lazarus, R. B. and Richtmyer, R. D. (1977). Similarity solutions for converging shocks. 92

[Lee, 1967] Lee, B. H. K. (1967). Nonuniform propagation of imploding shocks and detonations. *AIAA Journal*, 5(11). 95

[Lindl, 1995] Lindl, J. (1995). Development of the indirect-drive approach to inertial confinement fusion and the target physics basis for ignition and gain. *Physics of Plasmas*, 2(11):3933–4024. 32, 47, 55

[Maiman, 1960] Maiman, T. H. (1960). Stimulated optical radiation in ruby. *Nature*, 187(4736):493–494. 11

[Maire et al., 2007] Maire, P., Abgrall, R., Breil, J., and Ovadia, J. (2007). A lagrangian scheme for multidimensional compressible flow problems. *SIAM Journal on Scientific Computing*, 29. 124, 185

[Malone et al., 1975] Malone, R. C., McCrory, R. L., and Morse, R. L. (1975). Indications of strongly flux-limited electron thermal conduction in laser-target experiments. *Phys. Rev. Lett.*, 34:721–724. 40

[Martel and Shapiro, 1998] Martel, H. and Shapiro, P. R. (1998). A convenient set of comoving cosmological variables and their application. *mnras*, 297:467–485. 145

[McLean, 2005] McLean, A. (2005). The iter fusion reactor and its role in the development of a fusion power plant. *Radiation Protection Management*, 22(5):27. 1, 2

[Meitner and Frisch, 1939] Meitner, L. and Frisch, O. R. (1939). Disintegration of uranium by neutrons: A new type of nuclear reaction. *Nature*, 143:239–240. 10

[Millecchia et al., 2012] Millecchia, M., Regan, S., Bahr, R. E., Romanofsky, M., and Sorce, C. (2012). Streaked x-ray spectrometer having a discrete selection of bragg geometries for omega. *Review of Scientific Instruments*, 83(10):10E107–10E107–3. 183

[Noddack, 1934] Noddack, I. (1934). über das element 93. *Angewandte Chemie*, 47(37):653–655. 10

[Nora and Betti, 2011] Nora, R. and Betti, R. (2011). One-dimensional planar hydrodynamic theory of shock ignition. *Physics of Plasmas (1994-present)*, 18(8):082710. 22

[Nuckolls, 1998] Nuckolls, J. H. (1998). Early steps toward inertial fusion energy (ife) (1952 to 1962). Technical report, Lawrence Livermore National Lab., CA (United States). 11

[Oppenheim et al., 1972] Oppenheim, A. K., Kuhl, A. L., Lundstrom, E., and Kamel, M. (1972). A parametric study of self-similar blast waves. *Journal of Fluid Mechanics*, 52:657–682. 91

[Oshima, 1960] Oshima, K. (1960). Blast waves produced by exploding wire. Technical Report 358, Aeronautical research institute, University of Tokyo. 94

[Perkins et al., 2009] Perkins, L., Betti, R., LaFortune, K., and Williams, W. (2009). Shock ignition: a new approach to high gain inertial confinement fusion on the national ignition facility. *Physical review letters*, 103(4):045004. 23

[Piriz et al., 2013] Piriz, A., Piriz, S., and Tahir, N. (2013). High pressure generation by hot electrons driven ablation. *Physics of Plasmas (1994-present)*, 20(11):112704. 23, 206

[Ponchaut et al., 2006] Ponchaut, N. F., Hornung, H., Pullin, D. I., and Mouton, C. A. (2006). On imploding cylindrical and spherical shock waves in a perfect gas. *Journal of Fluid Mechanics*, 560(3):103. 95, 98, 104, 112, 138

[Ramu and Rao, 1993] Ramu, A. and Rao, M. P. R. (1993). Converging spherical and cylindrical shock waves. *Journal of Engineering Mathematics*, 27(4):411–417. 93

[Ribeyre et al., 2013a] Ribeyre, X., Guskov, S., Feugeas, J.-L., Nicolaï, P., and Tikhonchuk, V. T. (2013a). Dense plasma heating and gbar shock formation by a high intensity flux of energetic electrons. *Physics of Plasmas (1994-present)*, 20(6):–. 23, 196, 203, 204, 206

[Ribeyre et al., 2009] Ribeyre, X., Schurtz, G., Lafon, M., Galera, S., and Weber, S. (2009). Shock ignition: an alternative scheme for hiper. *Plasma Physics and Controlled Fusion*, 51(1):015013. 20, 23, 24, 26, 161, 215

[Ribeyre et al., 2011] Ribeyre, X., Tikhonchuk, V., Breil, J., Lafon, M., , and Le Bel, E. (2011). Analytical criterion for shock ignition of fusion reaction in hot spot. *Physics of Plasma*, 18:102702. 20, 135

[Ribeyre et al., 2013b] Ribeyre, X., Tikhonchuk, V., Breil, J., Lafon, M., Vallet, A., and Le Bel, E. (2013b). Analytical criterion for shock ignition of fusion reaction in hot spot. In *EPJ Web of Conferences*, volume 59, page 03005. EDP Sciences. 20

[Rosen, 1999] Rosen, M. D. (1999). The physics issues that determine inertial confinement fusion target gain and driver requirements: a tutorial. *Physics of Plasmas (1994-present)*, 6(5):1690–1699. 45

[Sakurai, 1953] Sakurai, A. (1953). On the propagation and structure of the blast wave, i and ii. *Journal of the Physical Society of Japan*, 8(5):662. 95, 98, 101, 104

[Sakurai, 1960] Sakurai, A. (1960). On the problem of a shock wave arriving at the edge of a gas. *Communications on Pure and Applied Mathematics*, 13(3):353–370. 94

[Sangster et al., 2013] Sangster, T., Goncharov, V., Betti, R., Radha, P., Boehly, T., Casey, D., Collins, T., Craxton, R., Delettrez, J., Edgell, D., et al. (2013). Improving cryogenic

deuterium-tritium implosion performance on omegaa). *Physics of Plasmas (1994-present)*, 20(5):056317. 16

[Schmitt et al., 2010] Schmitt, A. J., Bates, J. W., Obenschain, S. P., Zalesak, S. T., and Fyfe, D. E. (2010). Shock ignition target design for inertial fusion energy. *Physics of Plasmas (1994-present)*, 17(4):042701. 23, 25, 27

[Schurtz et al., 2010] Schurtz, G., Ribeyre, X., and Lafon, M. (2010). Target design for shock ignition. *Journal of Physics: Conference Series*, 244(2):022013. 158

[Schurtz et al., 2000] Schurtz, G. P., Nicolaï, P. D., and Busquet, M. (2000). A nonlocal electron conduction model for multidimensional radiation hydrodynamics codes. *Physics of Plasmas (1994-present)*, 7(10):4238–4249. 40, 193

[Sédov, 1946] Sédov, L. (1946). Propagation of strong blast waves. *Prikl. Mat. Mech.*, 10:241–250. 91

[Sédov, 1977] Sédov, L. (1977). *Similitude et dimensions en mécanique*. Editions MIR. 89

[Sharma and Radha, 1995] Sharma, V. D. and Radha, C. (1995). Similarity solutions for converging shocks in a relaxing gas. *Int. J. Engng. Sci.*, 33(4):535–553. 93

[Shcherbakov, 1983] Shcherbakov, V. (1983). Ignition of a laser-fusion target by a focusing shock wave. *Soviet Journal of Plasma Physics*, 9:240–241. 18, 129

[Spitzer and Härm, 1953] Spitzer, L. and Härm, R. (1953). Transport phenomena in a completely ionized gas. *Phys. Rev.*, 89:977–981. 35

[Stanyukovich, 1960] Stanyukovich, S. (1960). *Unsteady Motion of Continuous Media*. Pergamon. 92

[Stoeckl et al., 2001] Stoeckl, C., Glebov, V. Y., Meyerhofer, D., Seka, W., Yaakobi, B., Town, R., and Zuegel, J. (2001). Hard x-ray detectors for omega and nif. *Review of Scientific Instruments*, 72(1):1197–1200. 183

[Tabak et al., 1994] Tabak, M., Hammer, J., Glinsky, M. E., Kruer, W. L., Wilks, S. C., Woodworth, J., Campbell, E. M., Perry, M. D., and Mason, R. J. (1994). Ignition and high gain with ultrapowerful lasers. *Physics of Plasmas (1994-present)*, 1(5):1626–1634. 17, 54

[Tabak et al., 2014] Tabak, M., Norreys, P., Tikhonchuk, V., and Tanaka, K. (2014). Alternative ignition schemes in inertial confinement fusion. *Nuclear Fusion*, 54(5):054001. 54

[Takabe et al., 1985] Takabe, H., Mima, K., Montierth, L., and Morse, R. L. (1985). Self-consistent growth rate of the rayleigh–taylor instability in an ablatively accelerating plasma. *Physics of Fluids (1958-1988)*, 28(12):3676–3682. 52

[Takahashi, 2009] Takahashi, S. (2009). An existence theorem for the point source blast wave equation. *Communications in Partial Differential Equations*, 34(1):1–23. 95

[Tamm and Sakharov, 1959] Tamm, I. E. and Sakharov, A. D. (1959). *Plasma Physics and the Problem of Controlled Thermonuclear Reactions (transl)*. Pergamon. 7

[Taylor, 1946] Taylor, G. (1946). The air wave surrounding an expanding sphere. *Proc. Roy. Soc. A.*, 186:273–292. 91

[Theobald et al., 2008] Theobald, W., Betti, R., Stoeckl, C., Anderson, K., Delettrez, J., Glebov, V. Y., Goncharov, V., Marshall, F., Maywar, D., McCrory, R., et al. (2008). Initial experiments on the shock-ignition inertial confinement fusion concept. *Physics of Plasmas (1994-present)*, 15(5):056306. 22, 26

[Theobald et al., 2013] Theobald, W., Nora, R., Lafon, M., Anderson, K., Davies, J., Hohenberger, M., Sangster, T., Seka, W., Solodov, A., Stoeckl, C., et al. (2013). Demonstration of 200-Mbar ablation pressure for shock ignition. *Bulletin of the American Physical Society*, 58. 179, 180, 213

[Theobald et al., 2012] Theobald, W., Nora, R., Lafon, M., Casner, A., Ribeyre, X., Anderson, K., Betti, R., Delettrez, J., Frenje, J., Glebov, V. Y., et al. (2012). Spherical shock-ignition experiments with the 40+ 20-beam configuration on omega. *Physics of Plasmas (1994-present)*, 19(10):102706. 22

[Toqué, 2001] Toqué, N. (2001). Self-similar implosion of a continuous stratified medium. *Shock Waves*, 11(3):157–165. 93

[Wegener, 2009] Wegener, L. (2009). Status of wendelstein 7-x construction. *Fusion Engineering and Design*, 84(2):106–112. 8

[Welsh, 1967] Welsh, R. L. (1967). Imploding shocks and detonations. *Journal of Fluid Mechanics*, pages 61–79. 95, 112, 138

[Whitham, 1958] Whitham, G. B. (1958). On the propagation of shock waves through regions of non-uniform area or flow. *Journal of Fluid Mechanics*, 4:337–360. 93, 149, 150

[Yañez et al., 2011] Yañez, C., Sanz, J., Olazabal-Loumé, M., and Ibañez, L. (2011). Linear stability analysis of double ablation fronts in direct-drive inertial confinement fusion. *Physics of Plasmas (1994-present)*, 18(5):052701. 53

[Yousaf, 1978] Yousaf, M. (1978). Motion of a strong shock wave in a medium of nonuniform density. *Physics of Fluids*, 21:217–220. 94, 151

[Yousaf, 1985] Yousaf, M. (1985). Motion of a strong shock wave in an exponential medium. *Physics of Fluids*, 28(6):1659–1664. 93, 151

[Zhou and Betti, 2007] Zhou, C. and Betti, R. (2007). Hydrodynamic relations for direct-drive fast-ignition and conventional inertial confinement fusion implosions. *Physics of Plasmas (1994-present)*, 14(7):072703. 57, 210

Publications and communications

List of publications

In preparation

- **A Vallet**, X Ribeyre, A Casner, R Nora, W Theobald, R Betti and V Tikhonchuk. Hydrodynamic analysis of strong spherical shock generation experiments on OMEGA, *In preparation.*

- **A Vallet**, X Ribeyre, and V Tikhonchuk. Shock dynamics in an imploding shell, application to shock ignition, *In preparation.*

Submitted

- R Nora, W Theobald, F Marshall, D T Michel, W Seka, B Yaakobi, M Lafon, C Stoeckl, J Delettrez, A A Solodov, A Casner, C Reverdin, X Ribeyre, **A Vallet**, J Peebles, M S Wei and R Betti. Gigabar Spherical Shock Generation on the OMEGA Laser. *Submitted to Physical Review Letters*, 2014

Published

- X Ribeyre, E Llor Aisa, **A Vallet**, P Nicolai and V Tikhonchuk. Shock Ignition Theoretical Studies: From Hot Electrons Pressure Generation To Converging Amplification Effects, *Bulletin of the American Physical Society*, 59, 2014

- W Theobald, R Nora, M Lafon, KS Anderson, JR Davies, M Hohenberger, TC Sangster, W Seka, AA Solodov, C Stoeckl, B Yaakobi, R Betti, A Casner, C Reverdin, X Ribeyre,

and **A Vallet**. Demonstration of 200-Mbar ablation pressure for shock ignition. *Bulletin of the American Physical Society*, 58, 2013.

- **A Vallet**, X Ribeyre, and V Tikhonchuk. Finite mach number spherical shock wave, application to shock ignition. *Physics of Plasmas*, 20:082702, 2013.
- X Ribeyre, V Tikhonchuk, J Breil, M Lafon, **A Vallet**, and E Le Bel. Analytical criterion for shock ignition of fusion reaction in hot spot. *EPJ Web of Conferences*, 59:03005, 2013.

List of conference presentations

- International Congress On Plasma Physics, Lisbonne - Portugal, September 2014, Oral, *Hydrodynamic modeling of shock ignition.*
- 41st EPS Conference on Plasma Physics, Berlin - Allemagne , June 2014, Poster,*Semi-analytic modeling of shock ignition.* (Best poster award)
- Guest talk DPTA/DCSA, CEA-DIF, June 2014, Oral, *Modèles hydrodynamiques et expériences dans le contexte du schéma d'allumage par choc pour la fusion par confinement inertiel.*
- LMJ-PETAL and Action COST MP1208, Bordeaux - France, March 2014, Poster, *Shock strengthening in the imploding shell for shock ignition.*
- HEDP summer school, Columbus - USA (Ohio state), July 2013, Poster, *Finite Mach number spherical shock wave - analytical criterion for shock ignition.* (Fusion Science Center Award for Excellence in Poster Presentation)
- SPIE - Laser Energy Workshop , Prague - Czech Republic , April 2013, Poster, *Study of converging spherical shock wave with a finite Mach number in the context of shock ignition.*
- Forum Lasers et Plasmas, Ile de Ré - France, September 2012 , Poster, *Study of a spherical converging shock with finite Mach number.*